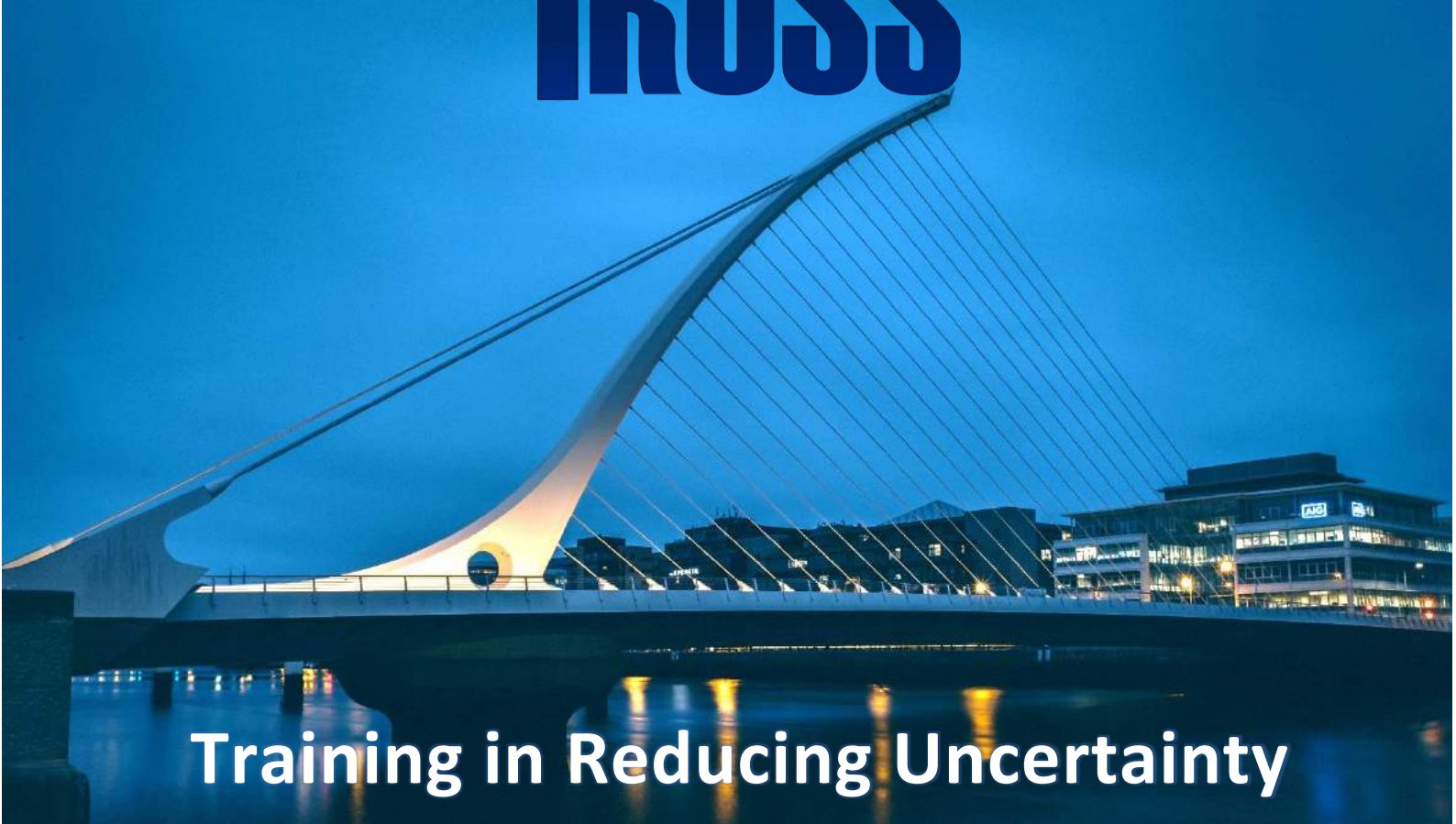




www.trussitn.eu



Training in Reducing Uncertainty in Structural Safety

WORKSHOP
29th August 2018
Dublin, Ireland



The TRUSS project has received funding from the European Union's Horizon 2020 research and innovation programme under the Marie Skłodowska-Curie grant agreement No. 642453



Training in Reducing Uncertainty in Structural Safety

WORKSHOP
29th August 2018
Dublin, Ireland



The TRUSS project has received funding from the European Union's Horizon 2020 research and innovation programme under the Marie Skłodowska-Curie grant agreement No. 642453

Contents

The TRUSS ITN project (2015-19): a Marie Skłodowska-Curie innovative training network on reducing uncertainty in structural safety.....	1-7
---	-----

RESEARCH ON BUILDINGS, ENERGY AND MARINE INFRASTRUCTURE

ESR1. A comparative study on different BFRP rebar design methodologies.....	8-12
ESR2. Statistical reliability of the screw pullout test in the assessment of in-situ concrete strength.....	13-18
ESR3. Vibration tests of an underwater free-standing 2-rack system.....	19-23
ESR4. Application of Gaussian process regression for structural analysis.....	24-30
ESR5. On the effectiveness and uncertainty of inspection methods for fatigue crack management.....	31-36
ESR6. Reduction of uncertainties associated to the dynamic response of a ship unloader.....	37-42

RESEARCH ON RAIL AND ROAD INFRASTRUCTURE

ESR7. Nothing on the road axle detection system using direct strain measurements – A case study.....	43-47
ESR8. Finding the influence line for a bridge based on random traffic and field measurements on site.....	48-52
ESR9. A machine learning classifier for condition monitoring and damage detection of bridge infrastructure...53-58	
ESR10. Vibration-based, output-only damage identification of bridge under vehicle induced excitation.....	59-64
ESR11. Fatigue testing of reinforced concrete beam instrumented with distributed optical fiber sensors.....	65-70
ESR12. Sensitivity of SHM sensors to bridge stiffness.....	71-74
ESR13. A big data approach for investigating the performance of road infrastructure.....	75-80
ESR14. Automated bridge deck evaluation through UAV derived point cloud.....	81-86

Foreword

Inspections and maintenance of infrastructure are expensive. In some cases, overdue or insufficient maintenance/monitoring can lead to an unacceptable risk of collapse and to a tragic failure as the Morandi bridge in Genoa, Italy, on 14th August 2018. An accurate assessment of the safety of a structure is a difficult task due to uncertainties associated with the aging and response of the structure, with the operational and environmental loads, and with their interaction. During the period from 2015 to 2019, the project TRUSS (Training in Reducing Uncertainty in Structural Safety) ITN (Innovative Training Network), funded by the EU H2020 Marie Skłodowska-Curie Action (MSCA) programme, has worked towards improving the structural assessment of buildings, energy, marine and transport infrastructure. Fourteen Early Stage Researchers (ESRs) have been recruited to carry out related research on new materials, testing methods, improved and more efficient modelling methods and management strategies, and sensor and algorithm development for structural health monitoring purposes. This research has been enhanced by an advanced program of scientific and professional training delivered via a collaboration between 6 Universities, 1 research institute and 11 companies from 5 European countries. The high proportion of companies participating in TRUSS ITN has ensured significant industrial expertise and has introduced a diverse range of perspectives to the consortium on the activities necessary to do business in the structural safety sector. The training has consisted of a ‘joint supervision’ by industrial and academic experts, periodic monitoring and updating of a career development plan, ‘network-wide training’ where all ESRs have been brought together to be taught transferrable skills such as communication, entrepreneurship and management skills in addition to research topics, and ‘local training’ allowing the ESR to be exposed to different working and cultural environments. A key aspect of the local training are meaningful placements, with a main host where the ESR has carried out most of the research activity during three years, and secondment periods in other Universities and companies complementing the training at the main host. This mobility, which is a fundamental characteristic of the MSCA ITN scheme, has given ESRs an opportunity to access modules at the Universities, to have exposure to large enterprises and SMEs, to experience the international dimension of the project, and to gather practical knowledge in the application of skills acquired in the taught modules. Under this umbrella, all ESRs have had placements in both research-active industry and academic participants, have conducted work placing them at the forefront of their field, and have been directly exposed to the commercial world getting ready for a subsequent professional career.

This book is a compilation of the papers presented by the TRUSS team at their 2nd workshop. The workshop has been held within the 2018 Civil Engineering Research in Ireland (CERI) national forum through interaction with the Civil Engineering Research Association of Ireland. In the introductory paper, an overall view of the project is provided. Then, ESRs report on some of their latest findings, starting by Sofia Antonopoulou (ESR1), who has reduced the uncertainty associated to the performance of Braided Fiber Reinforced Polymer (BFRP) through a comprehensive numerical and experimental campaign. Discrepancies between the true strength of reinforced concrete and the strength measured on site have been tackled via a novel testing method by Shah Nur Sourav (ESR2). Some limitations are computational, i.e., simulation time required for estimating fatigue life in large steel structures, when Rui Teixeira (ESR4) has proposed Kriging models to reduce the more expensive Monte Carlo simulations. There is also a relatively large degree of uncertainty between the dynamic response of numerical models and the true responses in complex scenarios such as submerged free-standing nuclear racks subjected to an earthquake that have been investigated by Alberto González (ESR3), or a ship unloader subjected to a moving trolley that has been analysed by Giulia Milana (ESR6). Distributed Optical Fiber Sensors (DOFS), sensors mounted in Unmanned Aerial Vehicles (UAV) and sensors in land vehicles have been further developed by Antonio Barrias (ESR11), Siyuan Chen (ESR14) and Daniel Martinez (ESR12) respectively, to efficiently gather on-site information about the structure. Algorithms able to convert on-site information into a realistic assessment of the structural condition have been proposed for bridge infrastructure by Farhad Huseynov (ESR7), Barbara Heitner (ESR8), Matteo Vagnoli (ESR9) and John James Moughty (ESR10). When managing infrastructure, questions arise on when and how to inspect it, that Guang Zou (ESR5) has addressed with advanced probabilistic methods taking the probability of detection of damage, the time taken until repair and the cost into account. Finally, Federico Perrotta (ESR13) has used field data to build a relationship between fuel consumption and road condition that allows integrating costs within the whole life cycle assessment of pavements. In summary, TRUSS proposes an advanced training and research programme at doctoral level that will qualify graduates for dealing with the challenges of an aging European infrastructure stock, thereby meeting a critical need whilst at the same time enhancing their career prospects in both industry and academia by matching their skills to the jobs of the future.

Arturo González (TRUSS Project Coordinator)
Dublin, Ireland
August 2018

The TRUSS ITN project (2015-19): a Marie Skłodowska-Curie innovative training network on reducing uncertainty in structural safety

Arturo González¹

¹Civil Engineering School, University College Dublin, Dublin 4, Ireland
email: arturo.gonzalez@ucd.ie

ABSTRACT: The structural deterioration of aging structures is often aggravated by an increase in loads that were not foreseen at the design stage and an insufficient maintenance spending as a result of the economic downturn of recent years. A management strategy guaranteeing structural safety with the best use of the resources available is clearly needed. TRUSS (Training in Reducing Uncertainty in Structural Safety, <http://trussitn.eu/>, 2015-2019) is a €3.7 million Marie Skłodowska-Curie innovative training network funded by the European Horizon 2020 Research and Innovation Programme, with the main objectives of: (1) carrying out research that will ensure structural safety levels for buildings, energy and transport infrastructure, and (2) providing training to a new generation of researchers for dealing with an aging infrastructure stock. The network is composed by 6 Universities, 11 companies and 1 research institute from 5 European countries, joining forces to identify, quantify and reduce uncertainties associated to the structural response, to the imposed loads, and to the probability of structural failure.

KEY WORDS: Structural safety; ITN; Marie Skłodowska-Curie; Infrastructure; Doctoral training.

1 INTRODUCTION

The Marie Skłodowska-Curie Innovative Training Network (ITN) TRUSS was favourably evaluated by the Research Executive Agency and invited to grant preparation in September 2014. Out of 1161 proposals, TRUSS is one the 121 successful projects funded under the H2020-MSCA-ITN-2014 call [1]. Fourteen Early Stage Researchers (ESRs) are funded within TRUSS with the purpose of providing them with a range of research skills related to structural assessment of infrastructure, and also with creative, entrepreneurial and innovative skills that will help them to convert these knowledge and ideas into products and services for economic and social benefit. The ITN scheme extends beyond the traditional academic research training setting by equipping ESRs with the right combination of research-related and transferable competences, which will enhance their career perspectives in both academic and non-academic sectors through international, interdisciplinary and inter-sector mobility [2].

The research theme of TRUSS are buildings, energy and transport infrastructure, which are key elements for supporting society in day-to-day activities. The infrastructure network is ageing and deteriorating rapidly under an increasing demand in operational and environmental loads. While an efficient infrastructure network provides economic and social benefits, infrastructure failure in terms of capacity or reliability can involve economic costs and lower quality of life. For infrastructure to remain effective and structurally safe, a management strategy that guarantees proper maintenance and best use of the resources available is needed. An optimal strategy will minimize costs while ensuring safety levels (Figure 1). However, this is a complex task due to uncertainties associated to the structural capacity and to the demand on a structure.



Figure 1. Variation of repair costs with time.

Therefore, the main objectives of TRUSS ITN are twofold:

- To develop reliable monitoring systems and structural, material and loading models to be achieved through research that will contribute to: (a) more efficient infrastructure design, assessment, monitoring and management, (b) maintain current infrastructure stock in operation while minimizing risks, and (c) reduce infrastructure costs and demand for non-renewable and carbon intensive resources while maintaining or improving safety levels.
- To offer a high-quality intersectoral and multidisciplinary training in structural safety to a new generation of ESRs through network-wide and local activities. The training programme combines taught modules with original research supported by secondments, which allows ESRs gaining experience and enhancing their career prospects in both industrial and academic sectors.

Training and secondment opportunities by the network allow ESRs to be exposed to technologies evolving rapidly, and to research and innovation in both academia and industry. Individual projects fall within two research clusters: (i)

buildings (methods for testing of strength, new materials), energy (nuclear, wind turbine towers) and marine (off-shore, ships and ships unloaders) infrastructure, and (ii) rail and road infrastructure (pavement, railway and highway bridges). A summary of all individual research projects can be found in [3]. Some fellows are focused on lab tests to reduce uncertainty associated to measurement techniques and to materials. Other fellows are concerned with the development of efficient structural monitoring systems (i.e., based on distributed optical-fiber sensing, instrumented drones and land vehicles). A third group of fellows is developing algorithms for damage detection, estimation of remaining life and structural inspection purposes.

Within this framework, the TRUSS proposal involves partnerships at a variety of levels. At the most basic level, there is a number of bilateral collaborations, centred around ESRs. Each ESR is assigned a project with a Doctoral Studies Panel (DSP) composed by experts from at least two European countries, including both academic and industrial participation. TRUSS network brings together a consortium (Figure 2) consisting of four leading European Universities with a world perspective on education (University College Dublin -UCD- and Trinity College Dublin -TCD- in Ireland, Universitat Politècnica Catalunya -UPC- in Spain, and University of Nottingham -UNOTT- in UK), and five industry beneficiaries (Arup in Ireland, Equipos Nucleares SA -ENSA-, Full Scale Dynamics Ltd -FSDL- and Lloyd's Register EMEA in UK, and Phimeca Engineering in France) with complementary specialist expertise and enthusiasm for the prospect of early exploitation of the research results. Six additional industry partners (Burgmann Packings in Ireland, COMSA and COTCA in Spain, Greenwood Engineering in Denmark, and Microlise and AECOM in UK), two Universities (Université de Nantes in France, and University of Aalborg in Denmark) and one research institute (TRL in UK) provide specialised support and secondment opportunities in specific research projects.

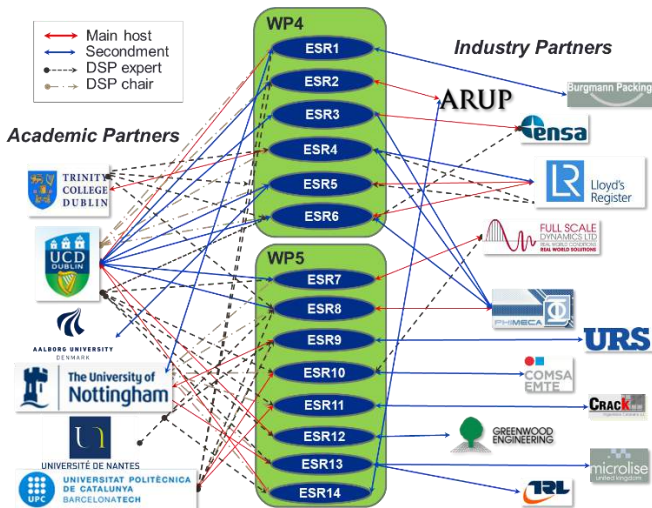


Figure 2. Main interactions at ESR level.

TRUSS is structured into five Work Packages (WPs): WP1 on Management (led by UCD), WP2 on Dissemination and Outreach (led by UPC), WP3 on Structured Training (led by UCD), and two Research WPs on buildings, energy, marine

(WP4 lead by UCD), rail and road (WP5 lead by UNOTT) infrastructures. The outputs of these WPs are reviewed next.

2 WP1 MANAGEMENT AND RECRUITMENT

WP1 deals with deal with the management, governance, recruitment and mobility of the programme. The ultimate decision body of the project is the Supervisory Board (SB), which comprises one representative of all beneficiaries and partner organizations and an ESR representative for the purpose of high-level decision-making. Up to date, WP1 has held 6 management (including SB) meetings. It is worth noting that the SB has approved the addition of two partners to the consortium: Universite de Nantes and University of Aalborg. Regarding recruitment, the total number of applicants to the 14 ESR positions was 211. The percentage distribution per gender was 85% male and 15% female. Typically, applicants would apply to more than one position, adding to 627 applications. There were 22% EU and 78% non-EU applicants. The distribution by continents was 60% Asia, 24% Europe, 11% Africa and 5% America. Following a selection procedure, each ESR was recruited under a 36 month contract as research staff in one of TRUSS beneficiaries, which acted as main host. All ESRs are also significantly exposed to working and cultural environments different from their employer, via secondments that vary between 3 and 9 months.

3 WP2 DISSEMINATION AND OUTREACH

WP2 disseminates the novel outputs produced by TRUSS structured PhD research program via presentations at national workshops, world's leading international conferences, publications in peer-reviewed journals of high-impact factor, reports made available free online and outreach activities. So far, TRUSS has published a total of 60 conference papers, 15 journal papers, 21 posters and delivered presentations in 23 countries covering the 5 continents. Two workshops (in UK and Ireland) and two symposia (as part of ESREL 2017 in Slovenia and IALCCE 2018 in Belgium) have been organised to highlight TRUSS progress and achievements.

The website (<http://trussitn.eu>) has 178 pages viewed 95,649 times by 19,127 new users in 33,652 sessions (averaging 2.84 pages and 2 minutes and 56 seconds per session). It contains information for the public/wider community about the project's aims, activities and material available, external links to ESR's blogs, to their publications made available in repositories, and to other websites containing info of interest. TRUSS profiles in Facebook (142 followers and 24,398 people reached at <https://www.facebook.com/trussitn.eu>), Google+ (71 followers at <https://plus.google.com/+TrussITN>), LinkedIn (140 connections at <https://www.linkedin.com/in/trussitn/>), Twitter (<https://twitter.com/TRUSSITN> with 150 followers), YouTube (22 videos in <https://www.youtube.com/c/TrussITN> viewed 6,298 times), SlideShare (1120 views of <https://www.slideshare.net/TRUSSITN/presentations>), ResearchGate (https://www.researchgate.net/profile/Truss_Itn) and fourteen blogs maintained by the ESRs (hosted in web addresses from <http://esr1truss.blogspot.ie/> to <http://esr14truss.blogspot.ie/> with 125 posts and 32,000

views), have been used to bring awareness on the importance of this research to support a community, region or country.

TRUSS has participated in activities in 6 High and Junior Schools (i.e., Science Week), and in 6 research exhibitions and Open Days at Universities to motivate School and University students to pursue an engineering career. Furthermore, TRUSS researchers have been featured in 4 press releases in mainstream newspapers, magazines [2] and television.

4 WP3 STRUCTURED TRAINING

WP3 governs the provision of appropriate structured PhD training modules for the ESRs, to ensure that the quality of structured training meets best practice and that the training needs of the ESRs, as planned in their Project Career Development Plan (PCDP), are being adequately addressed. The TRUSS training programme is structured in two ways: Supervised research towards a doctoral award (Section 4.1), network-wide (Section 4.2) and local (Section 4.3) training activities.

4.1 Supervised research

Each ESR has a project supervisor who guides them in specialist matters, such as the scientific state-of-the-art, key research tools, and dissemination strategies to support publication in the best international journals. In addition, the supervisor liaise with other participants to ensure that the training weeks are delivering modules appropriate to the ESRs under their supervision; these modules are offered either locally or by a University in the network.

4.2 Network-wide training

ESRs have practised their communication skills, and received academic and industrial training and feedback at network-wide meetings held approximately every 6 months. More specifically, TRUSS has run a training week in Nottingham (30/11-04/12/2015), a plenary meeting in Santander (16-17/06/2016), a training week in Barcelona (16-20/01/2017), a plenary meeting and workshop in London (24-25/05/2017), a symposium in Portoroz (18-22/06/2017), a training week (15-19/01/2018), a project management course (11-14/06/2018) and a workshop in Dublin (29-30/01/2018), and final symposium will be held in Ghent (28-31/10/2018). Figure 3 shows the structure of a typical training week delivering intensive, highly focused modules to all ESRs.

	Monday	Tuesday	Wednesday	Thursday	Friday
Morning	Core Module Research Methods (yrs. 1&2) Business Skills (year 3)	Communication Skills	Core Module Research Methods (yrs. 1&2) Business Skills (year 3)	Research Seminars and DSP	Specialist Modules Structural Load and Material Modelling, Monitoring & Testing Methods
Afternoon	Research Methods (yrs. 1&2) Business Skills (year 3)	Technical Visit	Research Methods (yrs. 1&2) Business Skills (year 3)		Innovation Workshop: Case Studies

Figure 3. Typical training week.

Core research modules are concentrated during the first two training weeks as these skills are required to undertake research in subsequent years. They include ‘methods of safety quantification’, ‘reliability analysis’, ‘life cycle assessment’, ‘updating of random variables using on-site information’, ‘material modelling’, ‘load modelling’, ‘overview of fault diagnostic methods’, ‘structural health monitoring’,

vulnerability and risk assessment’, ‘uncertainty quantification and propagation for sensitivity or reliability purpose’, ‘practical reliability engineering’, ‘survival analysis and discrete event simulation applied to reliability’, ‘advanced finite element modelling’, ‘multi-Level MC methods for stochastic analysis and robust optimum design’, ‘reducing uncertainty in structural safety through static NDT’ and ‘reducing uncertainty through the structured expert elicitation’. Communication skills include ‘presentation skills’, ‘How to succeed at interview’ and ‘grant writing – a short guide to survival and success’. Transferable skills such as ‘planning your research’, ‘knowledge management: the path to innovation’, ‘responsible conduct in research and innovation’, ‘working with industry on collaborative research projects’, ‘leadership & people management/managing change’ and ‘career planning for PhD students’ are also delivered. Conversely, core business skills take place in the 3rd training week when results are available and these skills are needed to exploit/communicate them. A list of topics covered are ‘concept to commercialization’, ‘stages of funding. Being investor ready’, ‘entrepreneurship & SME formation’, ‘Intellectual property’, ‘patent searching’, ‘creating organisational structures’, ‘commercialisation and exploitation’ and ‘project management’. The research seminars are interactive sessions that prepare the researchers to present their own work at other national and international events. In the Innovation Workshop, ESRs are given a real case study proposed by industry beneficiaries and they present an oral and written solution to colleagues and experts from industry and academia in an interruptible forum. Within this module the students are introduced to value of technical innovation and problem solving.

4.3 Local training

ESRs receive on-the-job training from the local research group at their host, and at the institution/s where they are seconded. A range of advanced research methods, project management, language courses, transferable skills and communication modules are made available to the ESR locally. By combining local research expertise with appropriate modules in specialist topics, the ESRs acquire all of the requisite skills necessary to conduct the high-level research necessary to achieve their PhD.

5 WP4 BUILDINGS, ENERGY AND MARINE INFRASTRUCTURE

Projects by ESR1 to ESR6 fall within WP4, distinguished by the very aggressive environments that the infrastructure is subjected to (corrosive, radioactive, non-linear structural responses) or relatively high uncertainties regarding materials and modelling. WP4 addresses uncertainties in the response of not-well known materials via lab testing or strength assessment in existing buildings, in the variation of the non-linear dynamic response of sliding structures under water due to differences in the modelling, in the loads and safety of large wind turbine towers and in the remaining life of assets (some operating beyond their original design life) in extreme and harsh marine conditions. The titles of these projects are listed in Table 1.

Table 1. Projects in WP4.

ESR	Title
1	Reliability of concrete structures reinforced with braided FRP
2	Reduction of uncertainty in assessing concrete strength of existing structures
3	Reduction of uncertainty in design of free standing nuclear spent fuel rack
4	Probabilistic optimisation of the design of offshore wind turbine towers
5	A probabilistic framework for fatigue crack management of ship structures
6	Residual life assessment and management of ship unloaders

Through a combination of laboratory work and numerical modelling, ESR1 shows that the geometric design plays a significant role on the reliability of concrete structures reinforced with braided FRP [4-9]. ESR2 uses common non-destructive testing methods to assess concrete strength, and finds large variability and influence of scale effects. Instead, a new approach based on the installation of a screw anchor in the concrete is proposed [4,10-12]. ESR3 identifies seven sources of uncertainty in the response of free standing nuclear spent fuel racks. He provides error estimates via a probabilistic analysis [4,13-16]. ESR4 carries out an analysis of univariate significant wave heights. Kriging models are proposed for analysing the towers of wind turbines [4,17-21]. Fatigue plays a critical role in service life assessment of marine structures. ESR5 show how the interval for the first inspection of ageing marine structures can be extended if crack initiation life is considered [4,22-28]. ESR6 reduces the uncertainty associated to dynamic loads employed in assessment of ship unloaders via numerical models and field measurements [4,29-33].

6 WP5 RAIL AND ROAD INFRASTRUCTURE

The infrastructures covered in WP5 are characterized by a variable traffic load. The objectives of WP5 are to reduce uncertainty, improve structural assessments and management of land transport infrastructure via the development of new monitoring/sensor technologies that will allow more efficient data collection, and new algorithms that will process the data collected from the structure to estimate its safety more accurately than current approaches. Table 2 gives the WP5 project undertaken by each ESR.

Table 2. Projects in WP5.

ESR	Title
7	Bridge condition assessment using rotation measurements
8	Probabilistic modelling of bridge damage based on damage indicators
9	Railway bridge condition monitoring and fault diagnostics
10	Assessment of bridge condition and safety based on measured vibration level
11	Development of optical fibre distributed sensing for SHM of bridges and large scale structures
12	Bridge damage detection using an instrumented vehicle
13	Using truck sensors for road pavement performance investigation
14	Reduction of uncertainty through regularized, automated road infrastructure inspection, using unmanned aerial vehicles

ESR7 tests the sensitivity of rotation to damage when a bridge is traversed by a moving load, both numerically and experimentally [34,35-37]. The effect of localized damage on the global bridge safety is assessed by ESR8 via Bayesian updating [34,38-41]. ESR9 computes displacements using a finite element model to demonstrate the ability of a Bayesian Belief Network to predict the health state of a bridge [34,42-45]. ESR10 shows that vibration intensity in the form of vibrars exhibit considerable damage sensitivity when tested under ambient excitation [34,46-53]. Experiments carried out by ESR11 test the possible spatial resolution, strain accuracy and long-term reliability of measurements performed with optical fibre distributed sensing for structural health monitoring of bridges and large scale structures [34,54-63]. ESR12 investigates the feasibility of employing sensors mounted on an instrumented vehicle to detect damage while traversing a bridge. Numerical simulations show that a vehicle can detect a change in the curvature response when the bridge is damaged in a noise-free environment [34,64-70]. ESR13 is also using truck sensors, but for road pavement performance investigation, when a Big Data approach has concluded that the impact of road conditions on truck fleet fuel economy is significant [4,71-74]. A customized unmanned aerial vehicle has been built by ESR14 for image-based inspection, and tested in a controlled lab situation, where the 3D reconstruction method has shown a millimetre level precision [34,75-77].

7 CONCLUSIONS

The improved reliability resulting from TRUSS is expected to contribute to more efficient designs and maintenance strategies and to the cancellation of costly and unnecessary interventions in existing structures. The individual projects in TRUSS are quite diverse. Nonetheless, the need to overcome uncertainty in material, load and structural performance represents a core thread that ties the projects together. This has led to interactions between researchers, and to generate innovations that forms the basis of their PhD research. With the help of innovative health monitoring, damage detection, structural simulations and tests, use of new materials and probabilistic assessments altogether, TRUSS will have an impact on: (a) economic activities, by facilitating an early exploitation of research results and avoiding unnecessary repair works via optimization of structures in terms of their entire life-cycle; (b) sustainability, by reducing waste materials during construction and rehabilitation works and by utilizing innovative and environment-friendly inspection, maintenance and rehabilitation methodologies; (c) social terms, i.e., by avoiding road closures in the case of bridge repairs or failure that will lead to longer travel times and increase costs in many economic sectors, and (d) education, science and technology, by connecting research and its real application via experiences such as the academia-industry partnerships existing in every individual project.

ACKNOWLEDGMENTS



The TRUSS ITN project is funded by the European Union's Horizon 2020 research and innovation programme under the Marie

REFERENCES

- [1] <https://ec.europa.eu/research/participants/portal4/desktop/en/opportunities/h2020/calls/h2020-msca-itn-2014.html> Accessed 22 April 2018.
- [2] Gonzalez, A. and Perrotta, F. (2018), 'Training the next generation', *Impact Magazine*, 2018(1): 64-66, March.
- [3] Gonzalez, A. (2017), 'Developments in damage assessment by Marie Skłodowska-Curie TRUSS ITN project', *Journal of Physics: Conf. Series*, 842(1):012039.
- [4] González, A., Perrotta, F., Milana, G., Zou, G., Teixeira, R., González Merino, A., Sourav, S.-N. A., Antonopoulou, S., McNally, C., Al-Sabah, S., Costas, L., O'Connor, A., Nogal, M., Banisoleiman, K., Faber, M.H., Parry, T. and Neves, L. (2018), 'Contributions by Marie Skłodowska-Curie TRUSS-ITN towards reducing uncertainty in structural safety of buildings, roads, energy and marine infrastructure', *Proceedings of 7th International Symposium on Uncertainty Modelling and Analysis (ICVRAMISUMA2018)*, Florianópolis, Brazil, April 8-11.
- [5] Antonopoulou, S., McNally, S. and Byrne, G. (2016), 'Developing braided FRP reinforcement for concrete structures', *Proceedings of 4th Symposium on Bridge and Infrastructure Research in Ireland*, National University of Ireland, Galway, Ireland, August 29-30.
- [6] Antonopoulou, S., McNally, C. and Byrne, G. (2016), 'Development of braided basalt FRP rebars for reinforcement of concrete structures', *Proceedings of 8th International Conference on Fibre-Reinforced Polymer (FRP) Composites in Civil Engineering (CICE 2016)*, Hong Kong, China, December 14-16.
- [7] Antonopoulou, S., McNally, S. and Byrne, G. (2017), 'The effect of braiding parameters on the performance of braided FRP composites for concrete reinforcement', *Proceedings of 8th International Conference on Composites Testing and Model Identification (CompTest 2017)*, KU Leuven, Belgium, April 5-7.
- [8] Antonopoulou, S. and McNally, S. (2017), 'Reliability assessment of braided BRFP reinforcement for concrete structures', *Proceedings of 27th European Safety and Reliability Conference (ESREL 2017)*, Portoroz, Slovenia, June 18-22.
- [9] Antonopoulou, S., McNally, S. and Byrne, G. (2018), 'A comparative study on different BRFP rebar design methodologies', *Proceedings of Civil Engineering Research in Ireland CERI 2018*, UCD, Dublin, August 29-30.
- [10] Sourav, S.N.A., Al-Sabah, S. and McNally, C. (2016), 'Strength assessment of in-situ concrete for the evaluation of structural capacity: State of the art', *Proceedings of Civil Engineering Research in Ireland Conference (CERI 2016)*, Galway, Ireland, August 29-30.
- [11] Sourav, S.N.A., Al-Sabah, S. and McNally, C. (2017), 'Post-installed screws for in-situ assessment of mortar strength', *Proceedings of 27th European Safety and Reliability Conference (ESREL 2017)*, Portoroz, Slovenia, June 18-22.
- [12] Sourav, S.N.A., Al-Sabah, S. and McNally, C. (2018), 'Statistical reliability of the screw pullout test in assessing in-situ concrete strength', *Proceedings of Civil Engineering Research in Ireland CERI 2018*, UCD, Dublin, August 29-30.
- [13] Gonzalez Merino, A., Costas, L., and Gonzalez, A. (2016), 'Dynamic analysis of the nonlinear response of high density fuel storage racks', *Proceedings of Civil Engineering Research in Ireland Conference (CERI 2016)*, Galway, Ireland, August 29-30.
- [14] Gonzalez Merino, A., Costas, L. and Gonzalez, A. (2017), 'Parametric analysis of modelling properties governing the seismic response of free-standing spent fuel racks', *Proceedings of 27th European Safety and Reliability Conference (ESREL 2017)*, Portoroz, Slovenia, June 18-22.
- [15] Gonzalez Merino, A., Costas, L. and Gonzalez, A. (2017), 'Uncertainties in seismic design of HDSFS Racks', *Energy Procedia*, September, 127, 310-319.
- [16] Gonzalez Merino, A., Costas, L. and Gonzalez, A. (2018), 'Comparison of numerical and experimental results for a seismic analysis of an underwater free-standing 2-rack structure', *Proceedings of Civil Engineering Research in Ireland CERI 2018*, UCD, Dublin, August 29-30.
- [17] Teixeira, R., O'Connor, A.J. and Nogal, M. (2016), 'Comparative analysis of the probabilistic methods to estimate the probability of failure of offshore wind turbine towers', *Proceedings of Civil Engineering Research in Ireland Conference (CERI 2016)*, Galway, Ireland, August 29-30.
- [18] Teixeira, R., O'Connor, A.J., Nogal, M., Nichols, J. and Spring, M. (2017), 'Structural probabilistic assessment of offshore wind turbine operation fatigue based on Kriging interpolation', *Proceedings of 27th European Safety and Reliability Conference (ESREL 2017)*, Portoroz, Slovenia, June 18-22.
- [19] Teixeira, R., O'Connor, A.J., Nogal, M., Nichols, J. and Krishnan, N. (2017), 'Analysis of the design of experiments of offshore wind turbine fatigue reliability design with Kriging surfaces', in *Proceedings of International Conference on Structural Integrity (ICSI2017)*, Funchal (Portugal), September 4-7, pp. 8.
- [20] Teixeira, R., Nogal, M. and O'Connor, A.J. (2018), 'On the suitability of the generalized Pareto to model extreme waves', *Journal of Hydraulic Research*, March.
- [21] Teixeira, R., O'Connor, A.J. and Nogal, M. (2018), 'Structural Probabilistic analysis using Kriging surrogate models.', *Proceedings of Civil Engineering Research in Ireland CERI 2018*, UCD, Dublin, August 29-30.
- [22] Zou, G., Banisoleiman, K. and González, A. (2016), 'Methodologies for crack initiation in welded joints applied to inspection planning', *International Journal of Civil, Environmental, Structural, Construction and Architectural Engineering*, 10(11), 1406-1413.
- [23] Zou, G., Banisoleiman, K. and González, A. (2017), 'Reliability-based inspection planning in view of both crack initiation and propagation', in *Proceedings of 27th European Safety and Reliability Conference (ESREL 2017)*, Portoroz, Slovenia, June 18-22.
- [24] Zou, G., Banisoleiman, K. and González, A. (2017), 'Development of probabilistic fracture mechanics method for fatigue life prediction based on EIFS concept', *Proceedings of the ASEM 2017 36th International Conference on Ocean, Offshore and Arctic Engineering (OMAE 2017)*, Trondheim, Norway, June 25-30.
- [25] Zou, G., Banisoleiman, K. and González, A. (2017), 'Uncertainty quantification and calibration of a modified fracture mechanics model for reliability-based inspection planning', *Proceedings of the 12th International Conference on Structural Safety & Reliability (ICOSSAR 2017)*, Vienna, Austria, August 6-10.
- [26] Zou, G., Banisoleiman, K. and González, A. (2018), 'A risk-informed decision support tool for holistic management of fatigue design, inspection and maintenance', *Proceedings of the 13rd International Conference on Smart Ship Technology*, London, UK, January 23-24.
- [27] Zou, G., Banisoleiman, K. and González, A. (2018), 'Value of inspection in fatigue management of steel structures', *Proceedings of 2nd International Conference on Sustainable Development and Green Buildings (ICSDGB 2018)*, Xiamen, China, March 1-3.
- [28] Zou, G., Banisoleiman, K. and González, A. (2018), 'On the effectiveness and uncertainty of inspection methods for fatigue crack management', *Proceedings of Civil Engineering Research in Ireland CERI 2018*, UCD, Dublin, August 29-30.
- [29] Milana, G., Banisoleiman, K. and González, A. (2016), 'Sources of structural failure in ship unloaders', *Proceedings of the European Safety and Reliability Conference (ESREL2016)*, Glasgow, UK, September 25-29.
- [30] Milana, G., Banisoleiman, K. and González, A. (2016), 'Fatigue life assessment methods: the case of ship unloaders', *Proceedings of the 1st International Conference on Natural Hazards & Infrastructure (ICONHIC2016)*, Chania, Crete Island, Greece, June 28-30.
- [31] Milana, G., Banisoleiman, K. and González, A. (2017), 'Field characterization of location-specific dynamic amplification factors towards fatigue calculations in ship unloaders', *Proceedings of 27th European Safety and Reliability Conference (ESREL 2017)*, Portoroz, Slovenia, June 18-22.
- [32] Milana, G., Banisoleiman, K. and González, A. (2018), 'Impact of a moving trolley on the dynamic response of a ship unloader boom', *Proceedings of 13th International Conference on Steel, Space and Composite Structures (SS18)*, Perth, Australia, January 31- February 2.
- [33] Milana, G., Banisoleiman, K. and González, A. (2018), 'Reduction of uncertainties associated to the dynamic response of a ship unloader', *Proceedings of Civil Engineering Research in Ireland CERI 2018*, UCD, Dublin, August 29-30.
- [34] González, A., Huseynov, F., Heitner, B., Vagnoli, M., Moughty, J.J., Barrias, A., Martinez, D., Chen, S., O'Brien, E., Laefer, D., Casas, J.R., Remenyte-PreScott, R., Yalamas, T. and Brownjohn, J. (2017), 'Structural health monitoring developments in TRUSS Marie Skłodowska-Curie innovative training network', *Proceedings of 8th International Conference on Structural Health Monitoring of Intelligent Infrastructure (SHMII-8)*, Brisbane, Australia, December 5-8.

- [35] Huseynov, F., Brownjohn, J., O'Brien, E. and Hester, D. (2017). 'Analysis of load test on composite I-girder bridge', *Journal of Civil Structural Health Monitoring*, 7(2), 163–173.
- [36] Xu, Y., Huseynov, F., Brownjohn, J.M.W., O'Brien, E.J. and Hester, D. (2017). 'Tracking deflection in the field using optical system: A case study', *Proceedings of 27th European Safety and Reliability Conference (ESREL 2017)*, Portoroz, Slovenia, June 18-22.
- [37] Huseynov, F., Brownjohn, J., O'Brien, E. and Hester, D. (2018), 'Structural health monitoring of bridges using inclinometers', *Proceedings of Civil Engineering Research in Ireland CERI 2018*, UCD, Dublin, August 29-30.
- [38] Heitner, B., O'Brien, E., Schoefs, F., Decatoire, R., Yalamas, T. and Leahy, C. (2016). 'Evaluation of bridge safety based on Weigh-in-Motion data', *Proceedings of Civil Engineering Research in Ireland Conference (CERI 2016)*, Galway, Ireland, August 29-30.
- [39] Heitner, B., O'Brien, E., Schoefs, F., Yalamas, T., Decatoire, R. and Leahy, C. (2016), 'Probabilistic modelling of bridge safety based on damage indicators', *Procedia Engineering*, 156, 140-147.
- [40] Heitner, B., Yalamas, T., Decatoire, R., O'Brien, E.J. and Schoefs, F. (2017), 'Comparative study on Bayesian updating of bridge safety model', *Proceedings of 27th European Safety and Reliability Conference (ESREL 2017)*, Portoroz, Slovenia, June 18-22.
- [41] Heitner, B., O'Brien, E., Schoefs, F., Yalamas, T. and Causse, G. (2018), 'Finding the influence line for a bridge based on random traffic and field measurements on site', *Proceedings of Civil Engineering Research in Ireland CERI 2018*, UCD, Dublin, August 29-30.
- [42] Vagnoli, M., Remenyte-Priscott, R. and Andrews, J. (2017), 'Railway bridge fault detection using Bayesian belief network', *Proceedings of Stephenson Conference: Research for Railways*, London, United Kingdom, April 25-27.
- [43] Vagnoli, M., Remenyte-Priscott, R. and Andrews, J. (2017), 'A fuzzy-based Bayesian belief network approach for railway bridge condition monitoring and fault detection', *Proceedings of 27th European Safety and Reliability Conference (ESREL 2017)*, Portoroz, Slovenia, June 18-22.
- [44] Vagnoli, M., Remenyte-Priscott, R. and Andrews, J. (2017), 'Railway bridge structural health monitoring and fault detection: State-of-the-art methods and future challenges', *Structural Health Monitoring*, SAGE, August, 1-37.
- [45] Vagnoli, M., Remenyte-Priscott, R. and Andrews, J. (2018), 'A machine learning classifier for condition monitoring and damage detection of bridge infrastructure', *Proceedings of Civil Engineering Research in Ireland CERI 2018*, UCD, Dublin, August 29-30.
- [46] Moughty, J.J., Casas, J.R. and Rodrigues, F. (2016), 'Assessment of vibration intensity as a condition and safety indicator for short-span bridges' *Proceedings of the Fifth International Symposium on Life-Cycle Civil Engineering (IALCCE 2016)*, Delft, The Netherlands, October 16-19.
- [47] Moughty, J.J. and Casas, J.R. (2016). 'Advancements of vibration based damage detection techniques for small to medium span bridges', *Proceedings of Civil Engineering Research in Ireland Conference (CERI 2016)*, Galway, Ireland, August 29-30.
- [48] Moughty, J.J. and Casas, J.R. (2016), 'Vibration based damage detection techniques for small to medium span bridges: A review and case study', *Proceedings of the 8th European Workshop on Structural Health Monitoring (EWSHM 2016)*, Bilbao, Spain, July 5-8.
- [49] Casas, J.R. and Moughty J.J. (2017), 'Bridge damage detection based on vibration data: past and new developments', *Frontiers in Built Environment*, 3(4).
- [50] Moughty, J.J. and Casas, J.R. (2017). 'A state of the art review of modal-based damage detection in bridges: Development, challenges, and solutions', *Applied Sciences*, 7(5), 510.
- [51] Moughty, J.J. and Casas, J.R. (2017), 'Evaluation of the Hilbert Huang transformation of transient signals for bridge condition assessment', *Proceedings of 27th European Safety and Reliability Conference (ESREL 2017)*, Portoroz, Slovenia, June 18-22.
- [52] Moughty J.J. and Casas, J.R. (2017), 'Performance assessment of vibration parameters as damage indicators for bridge structures under ambient excitation', *Procedia Engineering*, 199, 1970-1975.
- [53] Moughty, J. and Casas, J.R. (2018), 'Vibration-based, output-only damage identification of bridge under vehicle induced excitation', *Proceedings of Civil Engineering Research in Ireland CERI 2018*, UCD, Dublin, August 29-30.
- [54] Barrias, A., Casas, J.R., Villalba, S. and Rodriguez, G. (2016), 'Health monitoring of real structures by distributed optical fiber', *Proceedings of the Fifth International Symposium on Life-Cycle Civil Engineering (IALCCE 2016)*, Delft, The Netherlands, October 16-19.
- [55] Rodriguez, G., Casas, J.R., Villalba, S. and Barrias, A. (2016), 'Monitoring of shear cracking in partially prestressed concrete beams by distributed optical fiber sensors' *Proceedings of the 8th International Conference on Bridge Maintenance, Safety and Management (IABMAS 2016)*, Foz do Iguacu, Brazil, June 26-30.
- [56] Barrias, A., Casas, J.R. and Villalba, S. (2016), 'Review of civil engineering applications with distributed optical fiber sensors', *Proceedings of the 8th European Workshop on Structural Health Monitoring (EWSHM 2016)*, Bilbao, Spain, July 5-8.
- [57] Barrias, A., Casas, J.R., and Villalba, S. (2016), 'A review of distributed optical fiber sensors for civil engineering applications', *Sensors*, 16(5), 748.
- [58] Barrias, A., Casas, J.R., Rodriguez, G. and Villalba, S. (2017), 'UPC—BarcelonaTech experience on the use of Rayleigh based distributed optical fiber sensors for SHM of concrete structures', *Proceedings of 27th European Safety and Reliability Conference (ESREL 2017)*, Portoroz, Slovenia, June 18-22.
- [59] Barrias A., Casas J.R. and Villalba S. (2017), 'Application study of embedded Rayleigh based distributed optical fiber sensors in concrete beams', *Procedia Engineering*, 199, 2014-2019.
- [60] Barrias A., Casas J.R. and Villalba S. (2017), 'Performance assessment of embedded distributed optical fiber sensors in reinforced concrete structures', *Proceedings of 39th IABSE Symposium*, Vancouver, BC, Canada, September 19-23, 1461-1468.
- [61] Barrias, A., Rodriguez, G., Casas, J.R., and Villalba, S. (2018), 'Application of distributed optical fiber sensors for the health monitoring of two real structures in Barcelona', *Structure and Infrastructure Engineering*, February.
- [62] Barrias A., Casas J.R. and Villalba S. (2018), 'Fatigue testing of reinforced concrete beams instrumented with distributed optical fiber sensors (DOFS)', *Proceedings of Civil Engineering Research in Ireland CERI 2018*, UCD, Dublin, August 29-30.
- [63] Barrias, A., Casas, J.R., and Villalba, S. (2018), 'Embedded distributed optical fiber sensors in reinforced concrete structures - A case study', *Sensors* 18(4), 980.
- [64] Martínez, D., O'Brien, E.J., Sevillano, E. (2016), 'Damage Detection by Drive-by Monitoring Using the Vertical Displacements of the Bridge' A. Zingoni, A.A. Balkema eds. *Structural Engineering, Mechanics and Computation (SEMC 2016)*, Cape Town, South Africa, September 5-7.
- [65] Martínez, D., O'Brien, E.J., and Sevillano, E. (2016). 'Drive-by bridge damage detection using curvatures in uncertain environments', *Proceedings of Civil Engineering Research in Ireland Conference (CERI 2016)*, Galway, Ireland, August 29-30.
- [66] O'Brien, E. J., Sevillano, E., and Martínez, D. (2016). 'Monitoring the condition of a bridge using a traffic speed deflectometer vehicle travelling at highway speed', *Proceedings of the 3rd International Balkans Conference on Challenges of Civil Engineering*, Tirana, Albania, May 19-21.
- [67] Sevillano, E., O'Brien, E. J., and Martínez, D. (2016). 'Instantaneous curvature in bridge damage detection', *Proceedings of the CSHM-6: Structural health monitoring of new and ageing infrastructure*, Queens University, Belfast, Northern Ireland, United Kingdom, May 26-27.
- [68] O'Brien, E.J., Martínez, D., Malekjafarian, A. and Sevillano, E. (2017), 'Damage detection using curvatures obtained from vehicle measurements', *Journal of Civil Structural Health Monitoring*, 7(3): 333-341.
- [69] Malekjafarian, A., Martínez, D. and O'Brien, E.J. (2017), 'Pavement condition measurement at high velocity using a TSD', *Proceedings of 27th European Safety and Reliability Conference (ESREL 2017)*, Portoroz, Slovenia, June 18-22.
- [70] Martínez, D., O'Brien, E.J., Malekjafarian, A., Mohammed, Y.M. and Uddim, N. (2018), 'Identification of Bridge Stiffness using Drive-by Deflection Measurements', *Proceedings of Civil Engineering Research in Ireland CERI 2018*, UCD, Dublin, August 29-30.
- [71] Perrotta, F., Trupia, L., Parry, T., and Neves, L. (2017), 'Route level analysis of road pavement surface condition and truck fleet fuel consumption', *Proceedings of Pavement Life-Cycle Assessment Symposium 2017*, Urbana-Champaign, Illinois, USA, April 12-13.
- [72] Perrotta, F., Parry, T., and Neves, L. (2017). 'A big data approach to assess the influence of road pavement condition on truck fleet fuel consumption', *Proceedings of TIS 2017: AIIT International Congress on Transport Infrastructure & Systems*, Rome, Italy, April 10-12.
- [73] Perrotta, F., Parry, T., and Neves, L. (2017), 'Using truck sensors for road pavement performance investigation', *Proceedings of 27th*

European Safety and Reliability Conference (ESREL 2017), Portoroz, Slovenia, June 18-22.

- [74] Perrotta, F., Parry, T. and Neves, L.C. (2018), 'A big data approach for investigating the performance of the road infrastructure', *Proceedings of Civil Engineering Research in Ireland CERI 2018*, UCD, Dublin, August 29-30.
- [75] Chen, S., Laefer, D.F. and Mangina, E. (2016), 'State of technology review of civilian UAVs', *Recent Patents on Engineering*, 10(3), 160-174.
- [76] Chen, S., Laefer, D.F., Byrne, J. and Natanzi, A.S. (2017), 'The effect of angles and distance on image-based three-dimensional reconstructions', *Proceedings of 27th European Safety and Reliability Conference (ESREL 2017)*, Portoroz, Slovenia, June 18-22.
- [77] Chen, S., Truong-Hong, L. and Laefer, D. (2018), 'Outlier detection of point clouds generating from low cost UAVs for bridge inspection', *Proceedings of Civil Engineering Research in Ireland CERI 2018*, UCD, Dublin, August 29-30.

A comparative study on different BFRP rebar design methodologies

Sofia Antonopoulou¹, Ciaran McNally¹, Greg Byrne²

¹School of Civil Engineering, University College Dublin, Dublin, Ireland

²Burgmann Packings Ltd, Dublin, Ireland

email: sofia.antonopoulou@ucd.ie, ciaran.mcnally@ucd.ie

ABSTRACT: This study compares the physical properties and tensile behaviour of two different basalt fibre reinforced polymer (BFRP) rebar designs. Both types are developed using basalt fibres and epoxy resin as reinforcement and matrix respectively; composites with a constant cross section of 8 mm diameter are manufactured using a vacuum assisted resin infusion technique. The first configuration consists of eight braided layers at various angles, while the second one combines a unidirectional core with four outer braided layers. The latter hybrid design is introduced to improve the elastic modulus of braided BFRP reinforcement used in concrete structures. Tensile performance of all BFRP rebars produced in UCD laboratory is numerically and experimentally evaluated, and results for both approaches are compared. The effective longitudinal in-plane modulus (E_x^{FRP}) and the fibre volume fractions (ϕ_f) of each sample is calculated using the classical laminate theory and then, tensile tests are performed in accordance to the B2_ACI 440.3R-04 standard to experimentally validate the numerical results. Initial findings indicate that the elastic modulus of BFRP rebar can be enhanced by combining braiding with a unidirectional fibre core while a sufficient tensile strength is obtained, but additional research towards an optimal hybrid design is required.

KEY WORDS: BFRP rebars; Braiding technique; Unidirectional fibres; Tensile behaviour; Characterisation of FRP materials.

1 INTRODUCTION

Degradation of reinforced concrete structures due to corrosion of steel is reported as one of the main causes of structural deficiency that severely affects structural safety of RC elements. Harsh loading conditions and aggressive environmental factors can largely influence the long-term durability of structures in civil engineering applications and eventually lead to undesired repairs, additional costs and shorter service lives. According to IMPACT study, published by NACE International on 2016, a total of about \$2.5 trillion is currently spent worldwide each year; approaches that have been taken so far, like stainless steel, epoxy coating, galvanizing procedures etc., have been found to be insufficient to provide a viable solution in a cost-effective way [1-3].

Advanced composite materials, such as basalt fibre reinforced polymer (BFRP), have the capacity to significantly address this problem. Due to both their high strength-to-weight ratio and their excellent corrosion resistance, these materials have the potential to replace traditional steel in civil engineering applications [4-6]. There are however limitations that prevent their use on a larger scale, and lack of ductility is the most significant. The tensile behavior of FRP rebars is characterized by a linear stress-strain behaviour up to failure, thus a direct substitution between FRP and steel rebars is not feasible [2, 7-9].

The overall properties and durability of FRPs are strongly dependent on the constituent materials, the composite's fibre and void content, the fibre-matrix interface and the orientation of fibres, which is strongly related to the used manufacturing technique. FRP reinforcement for concrete structures has traditionally been manufactured using pultrusion process, a low cost method providing composites with a constant cross

section and a smooth surface. A detailed investigation on available design methodologies for the optimum development of FRP composites, suggests that a braiding technique could provide the required performance benefits through increased ductility and flexibility; it can also enhance the bond between FRP and concrete, which has a direct influence on both the serviceability and the ultimate load-carrying capacity of the structure. Nevertheless, braided composites exhibit complex damage and failure behavior, mainly due to their textile nature related properties, like multiple curved yarn interfaces, resin rich areas and nesting of different layers. As a result, a decrease on stiffness and strength values can be observed compared to unidirectional composites [1, 9-11]. By combining aspects of pultrusion and braiding into a single manufacturing process, a hybrid FRP rebar consisting of both unidirectional and off-axis oriented fibres can be produced. The stress-strain behaviour of the composite can be tailored by careful selection of raw materials and architectural design for the core structure and the braided sleeve respectively. The final part is a composite rebar with high initial tensile strength, contributed mostly by the high modulus unidirectional core followed by a gradual failure process associated with the outer braided sleeve [12-14].

This study presents a combined experimental and analytical approach for the design and development of two different basalt fibre reinforced polymer (BFRP) rebar types, using braiding technique and unidirectional fibre design. Mechanical properties of laboratory manufactured composites are numerically simulated using Classical Laminate Theory (CLT) and tensile tests are then conducted in order to experimentally evaluate the analytical data. Finally, comparisons are made between the two rebar configurations

towards the optimisation of the designing and manufacturing process.

2 MATERIALS, DESIGNS AND MANUFACTURING METHODS

Two different types of basalt fibre reinforced polymer (BFRP) composites for internal concrete reinforcement are developed and mechanically characterised within this study; a fully braided and a hybrid design.

The various raw materials used to develop BFRP rebars are presented in Table 1. Basalt fibres (3 yarns sizes) and epoxy resin are used as reinforcement and matrix respectively. Polyethylene terephthalate (PET) fibres are also used to promote resin flow on samples during impregnation process.

Table 1. Raw material properties.

Product name	Uses	Tensile strength (MPa)	Elastic modulus (GPa)
BASALTEX® - Basalt assembled roving – 300, 600, 2400 tex 13, 17, 19 µm	Fibre reinforcement	2800 – 4800	87 - 89
M183 semi-dull round - PET Monofilament	Impregnation aid	57 – 60	10
Easy Composites - IN2 Epoxy infusion resin/ Slow cure	Resin	65.5 – 73.5	2.95

BFRP preforms in two different configurations are designed and manufactured in Burgmann Packings Ireland, using (i) a pure braiding technique and (ii) a combined approach with a unidirectional fibre core. In particular, the desired rebar configuration consists of a braided or unidirectional core, one or two layers of PET material to promote resin flow, and outer finishing braiding layers to achieve the desired structural geometry. The target is a solid braid of circular cross section with an outer diameter (OD) of 8 mm. In Figure 1, a complete BFRP preform along with resin impregnated rebars are presented, while in Table 2 design details are illustrated.



Figure 1. (a) BFRP rebar preform, (b) Resin impregnated composite rebars.

Table 2. Technical designing details.

BFRP 1 - 8 mm				
Layer	Material	Yarns	OD	Angle
1	300	8	1.6	12
2	300	16	2.7	16
3	600	16	4.0	17
4	PET	32	4.9	12
5	PET	32	5.6	14
6	300	16	6.5	16
7	600	16	7.2	45
8	600	24	7.9	40
BFRP 2 - 8 mm				
Layer	Material	Yarns	OD	Angle
Core	2400	10	4.4	0
1	PET	24	5.3	30
2	600	8	5.8	45
3	600	8	6.5	45
4	600	12	7.2	45
5	600	12	7.8	45

* Note: All values are an average of readings taken at several locations of manufactured samples; OD: Outer diameter (mm); Braid yarns: Basalt (TEX), PET Monofilament; Angle (°).

A vacuum assisted resin infusion method (VARIM) is selected for producing all BFRP specimens. The main reason for that is the minimization of both void content and dry spots in the composite, as well as final rebar products with high fibre content. This method involves placing the preform inside the aluminum mould, which is then completely sealed, and immediately after, epoxy resin is infused using a vacuum. A post-curing procedure is then followed to ensure the composite's quality; the rebar is placed in the oven for 6 hours in 60 °C after 24 hours in room temperature environment. The preforming methods and impregnation procedures were accordingly adjusted in order to reduce defects and optimize the process.

Moreover, a theoretical numerical approach based on CLT was developed to determine the stiffness properties of braided composites, calculating the effective longitudinal in-plane modulus (E_x^{FRP}) and the fibre volume fractions (ϕ_f) of each braided sample [7, 15, 16].

3 MECHANICAL CHARACTERISATION - TENSILE TESTS

The tensile properties of the manufactured BFRP rebars are determined by testing three representative specimens for each configuration in accordance to B2_ACI 440.3R-04/ ASTM D7205 standard. All tests are performed at room temperature with an Instron 500 Universal Testing Machine of 500 kN capacity, by displacement control and constant loading rate of 1 mm/min. Throughout the whole duration of the test, the applied load, displacement and specimen elongation are electronically recorded. More specifically, an Epsilon 3543-100M-100M-ST Axial Extensometer (100 mm gauge length) attached on the mid-length position of the rebar is used to track the specimen's elongation. Notched metallic jaws are used in order to properly align the sample in the testing machine. During each test, specimen should fail in the test

section and slippage should be avoided throughout the length of the anchors. This is the reason for introducing a special anchoring system prepared in UCD laboratory; the initial length, L_s , of each specimen is 950 mm and both ends are embedded into steel tubes with grip length of 300 mm, L_a , using an anchor filler material - a 1:1 mixture by weight of epoxy resin and clean sand - along with 3D printed caps for alignment (Figure 2). Mechanical treatment - surface sanding - of specimen's ends before mounted into the anchorage is performed to promote adhesion of the rebar with the filler material.



Figure 2. Special anchorage system with specimen dimensions and sensor location.

A total of 6 specimens from 2 different rebar configurations, described on Table 2, are mechanically tested within this study. The sample size is statistically acceptable, as the low coefficients of variation (CoV) ensure the consistency of obtained data. For both series of tests, the average value, standard deviation, and coefficient of variation for each property is calculated. Stress-strain curves are generated for each sample from the load and strain measurements recorded from the extensometer. The tensile strength of the specimens is calculated according to the following equation:

$$f_u = F_u/A \quad (1)$$

where f_u is the tensile strength (MPa), F_u is the tensile capacity/ measured load (N) and A is the rebar's cross-sectional area (mm^2).

The tensile modulus of elasticity is taken as the linear regression of the data points from 20 to 50% of the rebar's tensile strength and is given by the following equation:

$$E = (f_1 - f_2)/((\varepsilon_1 - \varepsilon_2)A) \quad (2)$$

where E is the tensile modulus of elasticity (GPa), A is the cross-sectional area (mm^2), f_1 and f_2 are the applied stresses corresponding to about 50% and 20% of the ultimate tensile strength, respectively, and ε_1 and ε_2 are the corresponding strains [17, 18].

4 RESULTS

The results of tensile tests on laboratory manufactured fully braided and hybrid (UN core) BFRP rebars are summarized in Table 3. The critical properties of maximum load and displacement, ultimate tensile strength, strain and elastic modulus per configuration are represented by average values with a sample size of 3. The consistency of results is guaranteed by the relatively low coefficients of variation (CoV) for each measured property, less than 0.1% for all configurations. All specimens failed within the test section area, demonstrating a successful grip system.

Table 3. Test results for the two BFRP composite rebar designs.

Sample no	BFRP 1	BFRP 2
OD (mm)	8	
Fibre Volume Fraction (%)*	51.63	48.96
	Aver./ CoV	
Maximum Load (kN)	17.84/ 0.01	17.38/ 0.03
Ultimate Tensile Strength (MPa)	354.99/ 0.01	345.73/ 0.03
Maximum Displacement (mm)	10.09/ 0.05	10.50/ 0.06
Ultimate Strain (%)	2.59/ 0.06	2.50/ 0.10
Elastic Modulus (GPa)	14.76/ 0.02	14.27/ 0.06

* Note: Numerically calculated using CLT approach

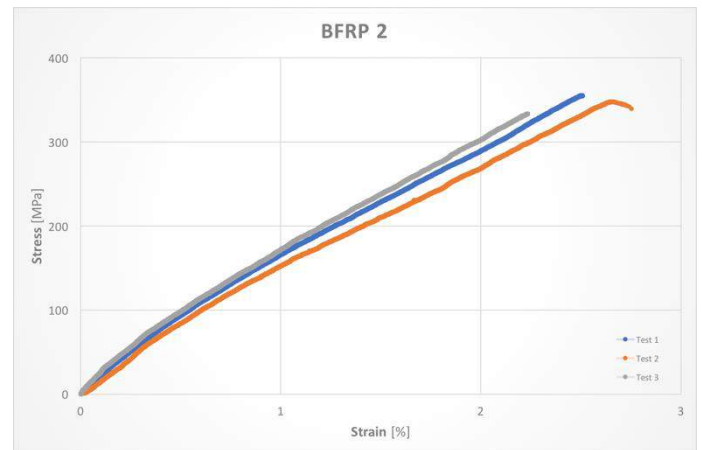
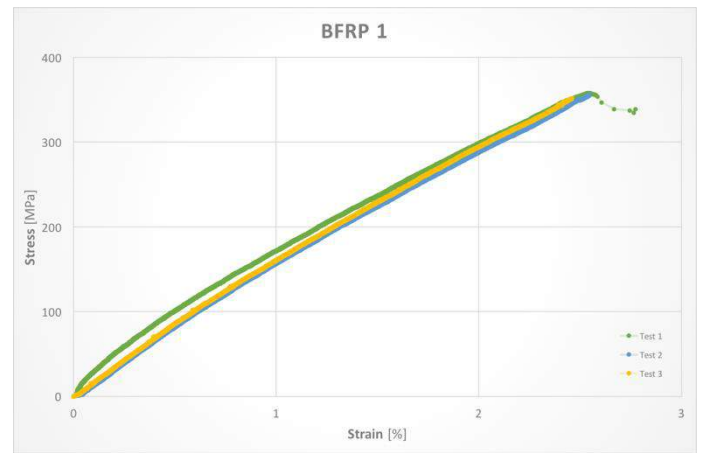


Figure 3. Stress – Strain curves for all manufactured BFRP rebars with an outer diameter of 8mm.

Figure 3 shows the tensile stress-strain curves for all six specimens of different configurations. The tested rebars showed a linear elastic stress–strain relationship up to failure, typical for all FRP products. Comparing the different design approaches, a similar mechanical behaviour is noticed; as the fibre volume fractions are increased from 48.96 % to 57.76 %, the elastic moduli are also increased from 1427 % to 14.76 %. Both samples exhibited a tensile strength comparable to the one of general steel bars (~ 400 MPa) and the maximum value - 354.99 MPa - obtained for the fully braided configuration. In

addition, the tested specimens showed a strain at failure ranging from 2.50% to 2.59%, almost the same as the 2.5% provided by Elgabbas et al. (2015) for pultruded BFRP bars. Brittle fracture types were noticed on all BFRP rebars, as shown in Figure 4.

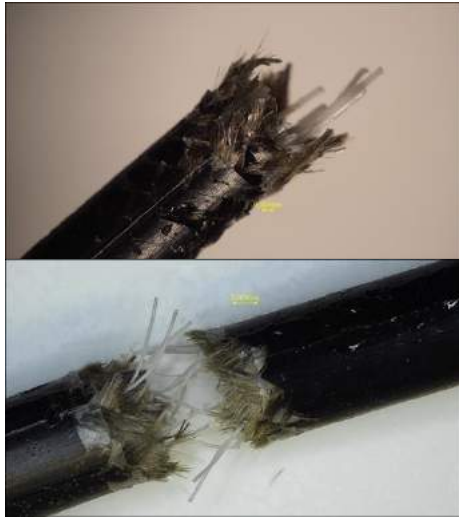


Figure 4. Micrograph of tested BFRP bars - Observed failure modes.

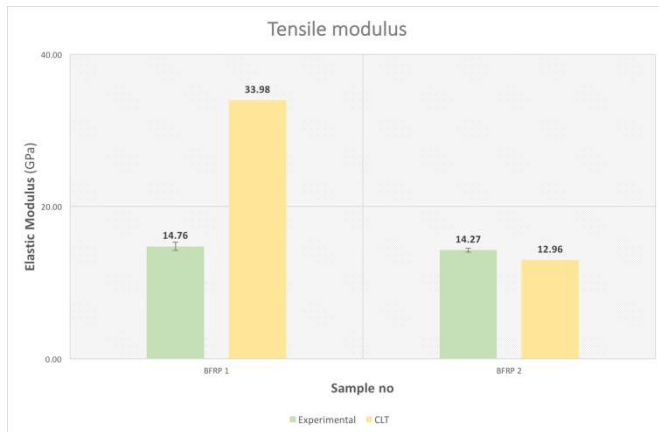


Figure 5. Tensile modulus of elasticity (E_x^{FRP}) for the two different rebar designs - Experimental vs CLT results.

Analytical results gained from Classical Laminate Theory (CLT) calculations [1, 7] have been correlated with average values of 3 test results for each composite rebar design. Figure 5 shows both the experimentally obtained and the numerically calculated tensile modulus of elasticity, E_x^{FRP} , for the two different BFRP rebar configurations. The predicted modulus for the fully braided design – BFRP 1 - is much higher (33.98 GPa) than the test data (14.76 GPa) and overestimate stiffness, whereas the one for the BFRP 2 design - unidirectional core & outer braided layers – is slightly lower (12.96 GPa) than the experimental results (14.27 GPa). CLT method has limitations for use with braided-reinforced composites and is mostly applied to unidirectional fibres designs, where the influence of undulations and orientations of yarns are not taken into account. More specifically, this method relies on the assumption of homogeneous strain and stress distributions in a

uniaxial specimen; it applies symmetric properties to braided composites, that do not actually exist, and does not allow any prediction of their locally varying out-of-plane properties.

5 CONCLUSIONS

This paper focuses on the development and characterisation of BFRP composites for internal concrete reinforcement, using both braiding and hybrid designs. More specifically, the aim of this work is to develop an understanding of the mechanical behaviour of composite rebars and correlate it with design and manufacturing process. Two different BFRP rebar design methodologies are introduced in order to obtain similar stress-strain characteristics of steel and maintain ductility in reinforced concrete structures. Both configurations - circular cross section with an outer diameter of 8 mm - are manufactured using either only braiding technique or a combination of high modulus unidirectional fibre core and an outer multilayer braided sleeve, along with a vacuum assisted resin infusion process. The experiments include tensile testing of all manufactured specimens according to B2_ACI 440.3R-04 and ASTM D7205 standard test methods. In particular, the mechanical response and the stiffness of both braided and hybrid BFRP composites is experimentally evaluated and compared with results from CLT numerical analysis.

The results demonstrate a clear dependency of modulus and strength on both designing parameters, like core architecture, no of layers, angle, yarn size, no of carriers, and fibre volume fraction. The mechanical response is mainly dominated by the fibre architecture, which significantly affects localized properties, crack propagation and load redistribution in the material. The maximum tensile strength obtained, is comparable to the one of steel and both design approaches exhibited similar mechanical behaviour, although hybrid types can reach higher values with improved fibre volume fractions. There are also significant discrepancies between theoretical and experimental values for tensile properties on the fully braided type, mainly due to the anisotropic nature and out-of-plane properties of braided composites. The CLT method was instead able to predict the elastic modulus of the hybrid type to a satisfactory degree.

In general, the results obtained contribute to a further understanding on the various available design approaches for FRP composite rebars and their properties. Additional work towards an optimal FRP rebar design should be conducted, taking advantage of both the design flexibility and the wide availability of manufacturing processes. Moreover, a more detailed investigation on the mechanical properties of FRP composites is essential in order to assess the relation between manufacturing parameters and rebar performance for improved rebar design and thus, to generate more confidence on the use of this innovative material in civil engineering applications.

ACKNOWLEDGMENTS



This project has received funding from the European Union's Horizon 2020 research and innovation programme under the Marie Skłodowska-Curie grant agreement No. 642453.

REFERENCES

- [1] Antonopoulou, S. and McNally, C. (2017), 'Reliability assessment of braided BFRP reinforcement for concrete structures', *Proceedings of 27th European Conference on Safety and Reliability (ESREL2017)*, Portorož, Slovenia.
- [2] Benmokrane, B. and Ali, A.H. (2016), 'Durability of FRP rebars in aggressive environments', *Proceedings of 8th International Conference on Fibre-Reinforced Polymer (FRP) Composites in Civil Engineering (CICE2016)*, Hong Kong, China.
- [3] Koch, G., Varney, J., Thompson, N., Moghissi, O., Gould, M. and Payer, J., *International Measures of Prevention, Application, and Economics of Corrosion Technologies Study*, NACE International Houston, Texas, USA: Gretchen Jacobson, 2016.
- [4] Elgabbas, F., Ahmed, E.A. and Benmokrane, B. (2015), 'Physical and mechanical characteristics of new basalt-FRP bars for reinforcing concrete structures', *Construction and Building Materials*, 95, 623-635.
- [5] Fiore, V., Scalici, T., Di Bella, G. and Valenza A. (2015), 'A review on basalt fibre and its composites', *Composites Part B: Engineering*, 74, 74-94.
- [6] Holloway, L.C. (2010), 'A review of the present and future utilisation of FRP composites in the civil infrastructure with reference to their important in-service properties', *Construction and Building Materials*, 24(12), 2419-2445.
- [7] Antonopoulou, S., McNally, C. and Byrne, G. (2016), 'Development of braided basalt FRP rebars for reinforcement of concrete structures', *Proceedings of 8th International Conference on Fibre-Reinforced Polymer (FRP) Composites in Civil Engineering (CICE2016)*, Hong Kong, China.
- [8] Ibell, T., Darby, A. and Denton, S. (2009), 'Research issues related to the appropriate use of FRP in concrete structures', *Construction and Building Materials*, 23(4), 1521-1528.
- [9] Portnov, G., Bakis, C.E., Lackey, E. and Kulakov, V. (2013), 'FRP Reinforcing bars - designs and methods of manufacture (Review of Patents)', *Mechanics of Composite Materials*, 49(4), 381-400.
- [10] Birkefeld, K., Roder, M. and VonReden, T. (2012), 'Characterization of Biaxial and Triaxial Braids: Fiber Architecture and Mechanical Properties', *Applied Composite Materials*, 19, 259-273.
- [11] Seo, D.W., Park, K.T., You, Y.J. and Lee, S.Y. (2016), 'Experimental Investigation for Tensile Performance of GFRP-Steel Hybridized Rebar', *Advances in Materials Science and Engineering*, 1-12.
- [12] Lam, H., F. Hampton, F.K. Ko, and H.G. Harris (2001), 'Design methodology of a ductile hybrid kevlar-carbon reinforced plastic for concrete structures by the braidtrusion process', *Proceedings of the 13th International Conference on Composite Materials*, Beijing, China.
- [13] Pastore, C.M. and Ko, F. (1999), 'Braided Hybrid Composites for Bridge Repair', National Textile Center Annual Report, Drexel University.
- [14] Ivey, M.A., Carey, J.P., and Ayranci, C. (2016), 'Manufacturing and Characterization of Braidtruded Fiber Reinforced Polymer Rebar', *Polymer Composites*.
- [15] Bank, L. C., *Composites for construction: Structural design with FRP materials*. Hoboken, N.J.: John Wiley & Sons, 2006.
- [16] Valentino, P., Furgiuele, F., Romano, M., Ehrlich, I. and Gebbeken, N. (2013), 'Mechanical characterization of basalt fibre reinforced plastic with different fabric reinforcements – Tensile tests and FE-calculations with representative volume elements (RVEs)'. *Proceedings of Convegno Nazionale IGF XXII*, Italy, 231-240.
- [17] ACI Committee 440, *Guide Test Methods for Fiber-Reinforced Polymers (FRPs) for Reinforcing or Strengthening Concrete Structures*, American Concrete Institute, ACI 440.3R-04, 2004.
- [18] American Society for Testing and Materials, *Standard Test Methods for Tensile Properties of Fiber Reinforced Polymer Matrix Composite Bars*, Conshohocken, USA, ASTM D7205, 2011.

Statistical reliability of the screw pullout test in the assessment of in-situ concrete strength

Md Shah Nur Alam Souav¹, Salam Al-Sabah², Ciaran McNally¹

¹Department of Civil Engineering, UCD, Belfield, Dublin, Ireland

²Arup, Dublin, Ireland

email: shah-nur-alam.sourav@ucdconnect.ie, Salam.Al-Sabah@arup.com, ciaran.mcnally@ucd.ie

ABSTRACT: The assessment of concrete compressive strength is an essential element in assessing the load carrying capacity of structural members in an existing structure. The reliability of non-destructive tests (NDTs) results for assessing concrete strength is always a questionable issue. This is mainly due to the uncertainty associated with the strength predictions based on the NDT measurements. This paper studies the Post-installed Screw Pullout (PSP) test as a potential method for assessing in-situ concrete strength. The objective of this paper is to study the reliability of the assessment using PSP test by analysing the effects of several influencing factors: presence of coarse aggregates, types and size of coarse aggregates, and the amount of coarse and fine aggregates. Analyses of results are presented to evaluate the repeatability and reliability of the PSP test with respect to test standard deviation, coefficient of variation and RMSE. The repeatability of the screw pullout test has been compared with the other NDTs available in literature.

KEY WORDS: compressive strength, in-situ concrete, non-destructive tests, Post-installed Screw Pullout test, reliability, uncertainty, TRUSS.

1 INTRODUCTION

Assessing the compressive strength of concrete is an essential component in assessing the load carrying capacity of structural members in an existing structure. Direct measurement of the compressive strength of in-situ concrete can be obtained by testing of standard cores collected from concrete that is under investigation. In-place or non-destructive test (NDT) methods can offer useful information about the material condition that will assist the assessment process. NDTs, either completely non-destructive or partially destructive, are a useful approach with the benefits of low cost, fast application, portability, no or limited damage on the surface and sometimes instant results on site. Currently, there are no in-place tests that provide direct measurements of compressive strength of concrete in an existing structure [1], [2]. NDTs are indirect approaches and are affected by several factors resulting in the uncertainty of the test results. These factors cannot be quantified and in most cases, are uncontrollable in practice. As such, the use of NDTs suffers from a main drawback that it is difficult to ascertain the level of accuracy and confidence in the strength estimates of concrete. NDTs are commonly used in conjunction with cores to reduce the amount of coring required to estimate the compressive strength throughout the structure. Considerable care should be taken to establish valid estimates of compressive strength based on these indirect tests.

The quality of concrete strength assessment is limited due to the sources of uncertainty arising at various levels and caused by the testing method itself, interference of the environment, intrinsic material variability, human error, and data interpretation [2]. The interpretation of NDT test results is a challenging task for users of NDT methods. Currently, no general rule can be applied to relate NDT test results to the

compressive strength of concrete. Use of empirical relationships developed for the concrete under investigation is a common practice. Empirical relationships developed for a particular concrete are only valid for that concrete within a certain degree of confidence; extension of this relationship to any other concrete provides uncertainty in the assessment and leads to erroneous assessment of concrete strength.

Currently several NDT techniques are available to assess the concrete strength [3]. Each of the NDTs has its own advantages and limitations. Post-installed Screw Pullout (PSP) test [4] is one of the most recent development in the field of concrete strength assessment. The method is partially destructive in nature. In this method, a standard concrete screw is installed in a hole that is drilled into the concrete and the screw is subsequently pulled out of the concrete. In the PSP test, the loading arrangement is such that a concrete cone failure does not occur, rather the failure occurs by complete pullout of the screw involving crushing of the concrete present between the threads of the screw. This paper aims to study the PSP test to better understand the reliability, variability and applicability in the assessment of concrete strength. The paper focuses on the response of the PSP test towards various parameters in order to understand the limitation of the test method. Different parameters include presence of coarse aggregate, types and sizes of the coarse aggregates, the amount of coarse and fine aggregates in concrete. The results are compared with two popular NDTs, rebound hammer (RH) and ultrasonic pulse velocity (UPV) test.

2 POST-INSTALLED SCREW PULLOUT (PSP) TEST

The PSP test involves drilling a hole in the concrete. A commercially available screw, HUS3-H8, a product of Hilti [5] having the outer thread diameter of 10.40 mm and inner

stem diameter of 7.7 mm, is installed in the 9 mm diameter hole. The screw is installed using an impact torque wrench having a maximum torque of 450 Nm. The screw is then pulled from the concrete, ensuring the type of failure known as the complete pullout failure in concrete (Figure 1a), and avoiding a concrete cone failure (Figure 1b). Complete pullout failure ensures that the pullout load is associated with local crushing of the concrete underneath the threads. The peak load obtained during the pullout is then correlated with the compressive strength of concrete. The theoretical consideration of the PSP test and details of the test configuration and preliminary test result can be found in [4].



Figure 1a. Complete pullout failure.



Figure 1b. Concrete cone failure.

A commercial pullout tester can be used for in-situ assessment. This offers a low cost method for carrying out the PSP test in comparison to core testing and some other available NDTs. The PSP test is quite easy to perform and simple as the test takes only 10-15 minutes. The damage in concrete associated with the test process due to the drilling of hole is minimal and has practically no effect on the structural capacity of the concrete members. An advantage of the test method is that the test provides a measurement of the direct interaction of the screw with the concrete. Figure 2 illustrates the PSP test set-up in the laboratory, whereas Figure 3 shows screws with the crushed materials in between the threads collected after the PSP test.



Figure 2. Experimental test set-up of PSP test.



Figure 3. Crushed materials in between the threads after PSP test.

3 TEST PROGRAMME

In order to investigate the repeatability of PSP test and the effect of several influencing factors on the reliability of the test results in the assessment, different batches of concrete and mortar were designed. Mortar and concrete samples were prepared using different types of aggregates in different amounts. Concrete cube samples of 150 mm dimension are used for conducting the PSP test; these were correlated against 100 mm cube samples that are used for determining compressive strength of concrete. Each set of data includes 4 PSP tests and 3 compressive strength tests.

In total, 73 different mixes concrete and mortar were prepared in the laboratory, leading to 292 PSP test with 219 compressive strength tests. Samples were tested at different ages; 7, 14, 28 and 100 days to ensure different strength levels of concrete. This allowed to investigate the main purpose of the PSP test, i.e., investigation of the relationship of compressive strength and obtained peak load from the PSP test. Three types of coarse aggregates were used to prepare the concrete mixes: locally available limestone, crushed brick chips, and pumice as a lightweight aggregate. Different combination of cement content, water-cement ratio, and coarse aggregate content were used by offsetting the quantity of the fine aggregate content. Locally available normal sand and crushed fines were used as fine aggregates. Fine aggregates consisting of 2/3 normal sand and 1/3 crushed rock fines. Maximum aggregate size in limestone and brick chips is 20 mm, whereas in lightweight aggregate is 14 mm.

Alongside the PSP test, rebound hammer (RH) and ultrasonic pulse velocity (UPV) test were also carried out on the corresponding 150 mm concrete cube samples during the investigation process. RH and UPV test were chosen due to the popularity of these two test methods in the field of in-situ concrete strength assessment, and were carried out on the same samples before the PSP test. Two sets of RH and UPV test results were obtained per mix. RH test and UPV tests were carried out following the EN 12504-2 [6] and EN 12504-4 [7] respectively.

4 RESULTS AND DISCUSSION

The PSP test measures the peak load during the pullout of the screw from the concrete sample following the complete pullout failure in the concrete. The typical load displacement curve for a PSP test (Figure 4) shows that almost all curves follow similar pattern in which stiffness varies from strong to weak, with the initial stiffness being almost linear. The peak load occurs following the softening behaviour of the curve indicating the maximum resistance of the material between the threads against the pullout force. The curve then follows a negative slope and the shearing of the remaining portion of materials under the threads along the outer edge of the screw threads continues forming a shear band. A complete shearing surface is formed along the outer edge of the threads as the screw moves a distance nearly equals to the pitch of the threads. The remaining acting force resisting the movement of the screw is a result of the possible small mechanical interlock between the threads and the damaged materials, and friction. These forces remain almost constant for the following screw movement.

The results of the PSP test were investigated in two ways; first, the PSP test was investigated for its repeatability to assess the inherent scatter of the results associated with the test method and second, its ability to predict the compressive strength of concrete. Statistical analyses were performed to determine the influencing factors affecting the test results. All the analyses were conducted with a 95% confidence level unless otherwise specified.

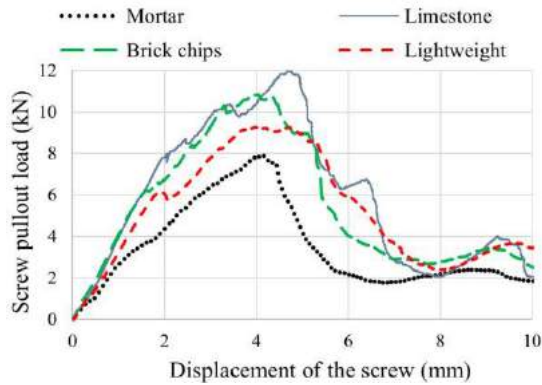


Figure 4. Typical load-displacement curve in PSP test.

4.1 Repeatability of the PSP test

As per the definition of ISO 3534-1 [8], the repeatability is the precision under the conditions where the independent test results are obtained with the same method on identical test items in the same laboratory by the same operator using the same equipment within short intervals of time. ACI 228.1R-03 [9] reports repeatability as the within-test variation to show the inherent scatter associated with a particular test method. Repeatability analysis techniques mostly concentrate on the use of coefficient of variation (CoV) for taking into account the variability of different material characteristics, rather than the standard deviation. CoV as the parameter of repeatability contributes to the better understanding of the margin of variability and dispersion of the test data. For this reason, it is important to know how the different influencing factors affects the CoV i.e. variability of the test results. It is to be mentioned here that for the sake of this study, none of the obtained data was regarded as outliers and omitted from the dataset.

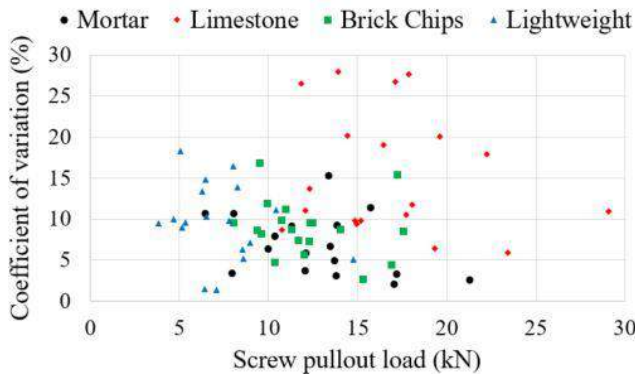


Figure 5. With-in test coefficient of variation as a function of average screw pullout load.

Figure 5 shows the with-in test CoV of PSP test as percentage as a function of average screw pullout load. The figure

illustrates the degree of scatter in the PSP test results. Mortar and concrete having lightweight and brick chips aggregate resulted in lower values (mean values are around 7%, 9% and 9% respectively) in comparison to concrete with limestone (mean value of around 16%), depicting the higher consistency of the PSP test in mortar and concrete with softer aggregate. Concrete with limestone aggregate shows higher variability attributing the pronounced influence of the harder aggregate on the PSP test.

An analysis of variance (ANOVA) was performed on the obtained CoV to determine if coarse aggregate type had an impact on the scatter of the peak load values of PSP test. ANOVA analysis showed that concrete with limestone resulted in significant difference in the CoV, unlike the mortar and concrete with softer aggregate. As indicated by the ANOVA analysis, no significant difference can be observed in the CoV of peak load in the case of mortar, and concrete with brick chips and lightweight aggregate.

Apart from the effect of aggregate type on the PSP test results, effect of different combination of the components of the concrete for different mixes was also investigated using the ANOVA analyses. No significant difference of the CoV of peak load was obtained based on the different mix designs of mortar and concrete, the differences exist only due to chance variation, as concluded from the ANOVA analyses. CoV was also found to be independent of the strength of the mortar and concrete.

4.2 Strength relationships

To investigate the effect of the various parameters on the peak load of the PSP test, a regression analysis was performed. Selected parameters were compressive strength, water-cement (w/c) ratio, cement content, coarse aggregate (CA) content, total aggregate (TA) content, fine aggregate content (FA) with respect to total aggregate, coarse aggregate (CA) density, particle size in the aggregate in terms of D10, D50 and D90, and age. Results of the regression analysis with correlation coefficient are provided in Table 1. P-value is also shown inside the bracket indicating the significance level of the correlation coefficient. For simplicity, a linear regression has been assumed for the analysis.

Table 1. Correlation coefficient for each parameters.

	Concrete and mortar	Only concrete
Peak load	1	1
Concrete strength	0.852 (0.00)	0.865 (0.000)
w/c ratio	-0.223 (0.029)	-0.171 (0.104)
Cement content	0.253 (0.015)	0.136 (0.158)
CA content	-0.080 (0.250)	-0.151 (0.133)
TA content	-0.073 (0.271)	-0.016 (0.454)
FA content	0.081 (0.247)	0.186 (0.084)
CA density	Not included	0.734 (0.000)
D10	0.186 (0.057)	0.429 (0.000)
D50	0.089 (0.227)	0.305 (0.011)
D90	0.171 (0.074)	0.556 (0.00)
Age	0.525 (0.000)	0.494 ((0.000)

From Table 1, the effect of compressive strength on the peak load can be clearly demonstrated. When mortar is taken into consideration with all the concrete, no other parameters except concrete strength and age has significant influence on the peak load. When mortar was excluded from the datasets, coarse aggregate density along with age and particle size of D10, D50, and D90 influenced the peak load. The effect of particle size on the peak load is due to the fact that lightweight aggregate contained maximum particle size of 14 mm and also produced lower concrete strength in comparison to concrete with limestone and brick chips. This was confirmed by carrying out regression analyses on the datasets of concrete with limestone and brick chip, where the particle size does not show any significant level of correlation with peak load.

All the obtained test results of PSP and compressive strength tests are presented in Figure 6, showing that there is clear trend of increase in pullout load of PSP test with the increase of compressive strength of concrete, f_c' . The effect of aggregate type on the PSP test can be clearly demonstrated from Figure 4 and Figure 6. Different types of aggregate resulted in different peak load depending on the elastic modulus and strength of aggregates used in concrete. Concretes containing limestone aggregates shows higher screw pullout load than mortar and the concretes of similar compressive strength containing brick chips and lightweight aggregates.

Figure 6 also includes the simple best-fit linear relationships between the compressive strength and screw pullout load for mortar and concrete. No attempts were made to force the correlation lines to pass through the origin. It is evident that concrete with limestone resulted in a higher value of screw pullout load and lightweight concrete had lowest value, while concrete with brick chips aggregates resulted in between the two. Good correlations were observed for mortar and concrete with lightweight aggregate having an R-squared value of 0.90 and 0.87 respectively. Concrete with limestone and brick chip aggregate resulted in R-squared values of 0.80 and 0.83 respectively. All the relationships follow a similar slope, except that of mortar. When all the datasets were combined, an R-squared value of 0.73 was obtained. R-squared value of 0.75 was found with the datasets of all concrete only, except the mortar.

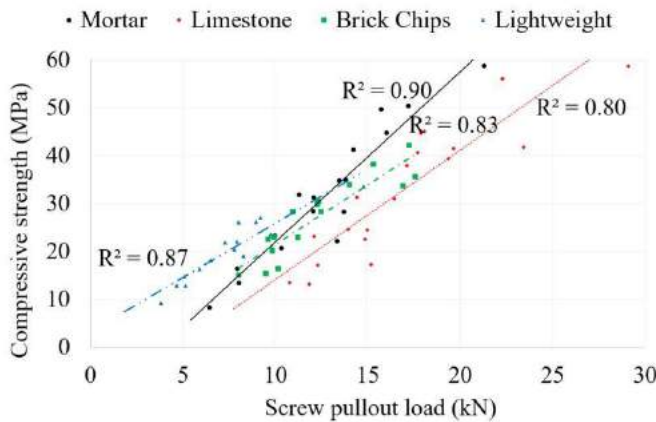


Figure 6. Relationship between f_c' and screw pullout load of PSP test for all mixes of concrete and mortar.

Table 2 shows the strength relationship of the PSP test for the best fit lines and the lines passing through the origin in case of different concrete and mortar separately, and including all the datasets together. The R-squared value does not change significantly in any case. To determine if the best fit line and the line through the origin produce statistically significant results, a paired t-test was performed. Each case, providing the p-value of greater than 0.05, confirms that there is no significant difference whether the relationship is taken as the best fit line or the line passing through the origin, though the best fit line produces a higher reliability in the strength assessment.

Table 2. Strength relationship of PSP test.

	Best fit line		Through origin	
	Equation	R-sq	Equation	R-sq
Mortar	$f_c' = 3.5629 * PL - 13.7$	0.90	$f_c' = 2.5669 * PL$	0.82
Limestone	$f_c' = 2.7057 * PL - 12.946$	0.80	$f_c' = 1.989 * PL$	0.74
Brick chips	$f_c' = 2.7173 * PL - 7.8183$	0.83	$f_c' = 2.1048 * PL$	0.82
Lightweight	$f_c' = 2.3023 * PL - 2.6442$	0.86	$f_c' = 2.6276 * PL$	0.84
All	$f_c' = 2.1486 * PL + 0.7825$	0.73	$f_c' = 2.2037 * PL$	0.73
All except mortar	$f_c' = 1.9292 * PL + 2.3302$	0.75	$f_c' = 2.0906 * PL$	0.74

The strength relationships for RH and UPV test were shown in Figure 7 and Figure 8. Again, No attempts were made to force the correlation lines to pass through the origin. In the case of the RH test, the obtained rebound value was found to be less in concrete with limestone than the concrete with lightweight or brick chip aggregates for the same of compressive strength of concrete. This result was found to be consistent with the results found in the literature [10]. A good strength correlation (R-squared value of 0.88) was obtained for concrete limestone, while concrete with brick chip and lightweight aggregate resulted R-squared value of around 0.70. When all the datasets are combined, an R-squared value of 0.74 is obtained.

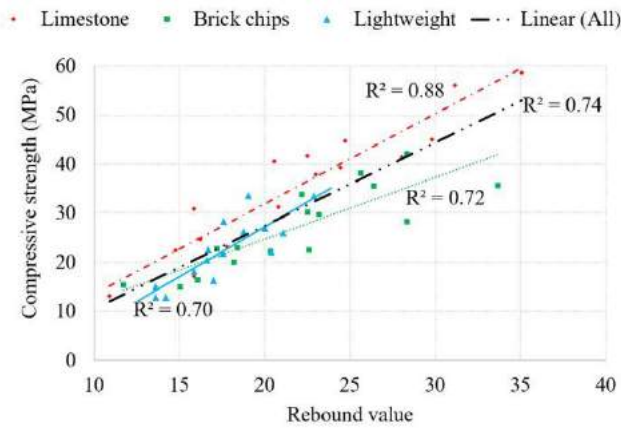


Figure 7. Relationship between f_c' and rebound value.

Figure 8 shows the relationship of UPV value with the compressive strength. A clear distinction of the UPV value based on the aggregate type can be observed for the same level of compressive strength as UPV value mostly depends on the density of the concrete, mostly contributed from the aggregate particles. Concrete with brick chips and limestone separately resulted high R-squared values (more than 0.90 in both cases), whereas lightweight concrete resulted in R-squared value of only 0.45. When all the datasets are combined, an R-squared value of 0.53 is obtained. The use of RH and UPV testing has not been proven to be successful in the assessment of compressive strength of concrete in practice due to uncontrolled factors on site [11], even though in many cases, RH and UPV resulted in good correlations with compressive strength in the laboratory [12].

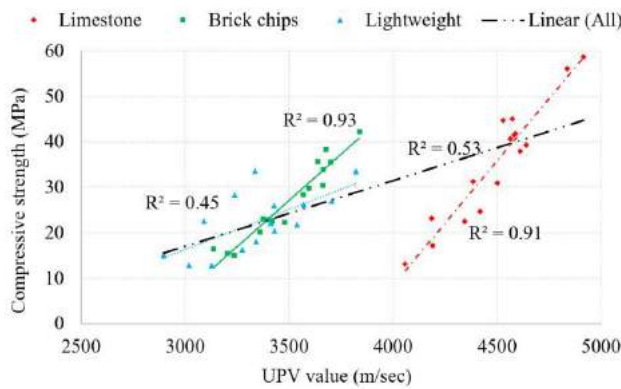


Figure 8. Relationship between f_c' and UPV value.

Table 3 presents the statistical reliability of the PSP test in the assessment of the compressive strength. The R-squared values of mortar and concrete with lightweight aggregate are high (0.90 and 0.87 respectively), compared to reasonable value for concrete with brick chips (0.83), and the lowest value was obtained for concrete with limestone (0.80). Mortar and concrete with brick chips, and lightweight aggregates resulted in low values of mean residual strength and RMSE compared with the concrete with limestone. Absolute mean residuals between measured concrete strength and strength estimated from the best fit line as a measure of error were found to be less than 5 MPa in all cases when separate strength relationship were used. When a single relationship for

the all datasets was used, the error was found to be 5.26 MPa. When the mortar was excluded from the dataset, the error reduced to 4.70 MPa. The range of error can be considered reasonably good for the empirical relationship used in the this study. Figure 9 illustrates the residuals using the obtained linear regression models with respect to predicted compressive strength.

Table 3. Statistical reliability of the PSP test.

Aggregates	R-sq	Mean Residual (MPa)	RMSE (MPa)
Mortar (No aggregate)	0.90	3.24	4.47
Limestone	0.80	4.98	6.29
Brick chips	0.83	3.40	3.33
Lightweight	0.87	1.90	2.28
All	0.73	5.26	6.83
All except mortar	0.75	4.70	6.13

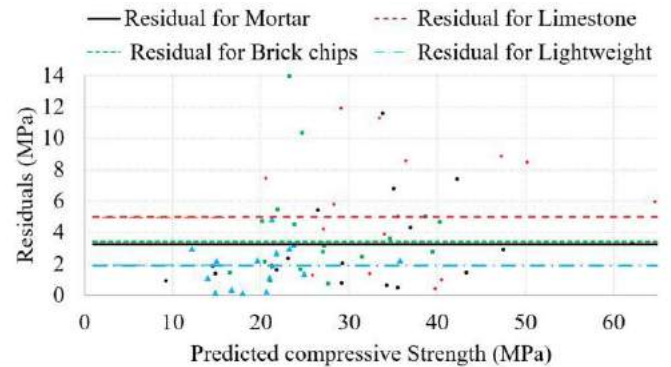


Figure 9. Obtained residuals versus predicted compressive strength for PSP test.

5 CONCLUSIONS

The paper investigated a newly developed non-destructive test, the post-installed screw pullout test (PSP test), for the assessment of in-situ concrete strength. The PSP test was developed to improve the reliability of strength assessment in a cost effective way. In the PSP test, as the screw is pulled out of the concrete to obtain a complete pullout failure, the concrete under the threads crushes. The peak load at failure provides an indication of the compressive strength of the concrete. The purpose of the paper was to investigate the statistical variability and reliability of the PSP test due to the influence of different parameters for the assessment of compressive strength of concrete. The following conclusions can be drawn from the presented results:

- The repeatability of the PSP test in terms of CoV is highly affected by the aggregate characteristics. The harder the aggregate particle (i.e. limestone) in the concrete, higher the coefficient of variation of the PSP test.
- The CoV of the PSP test is found to be independent of the strength of the mortar and concrete.
- The PSP test is not affected by the change in the mix proportion of the constituents of the concrete.

- The strength relationship obtained for each type of concrete when considered separately resulted in minimum R-squared values of 0.80. When all the datasets were taken into consideration, an R-squared value of 0.73 was obtained.
- Mean residual as a measure of error was found to be around 5 MPa for the concrete with limestone whereas mortar and concrete with other aggregates resulted in mean residuals of around 3 MPa.
- Strength relationships of RH and UPV test were compared with that of PSP test, where strength relationships of RH test and PSP test were comparable to each other. When compared with UPV test, the PSP test showed high reliability.
- The type of coarse aggregate influences the peak load obtained in the PSP test. Compared to the RH test, the PSP test is not affected by the surface conditions, such as texture, moisture, surface irregularities, and carbonation.

The study presented in this paper shows that the PSP test can be used as a viable method in the field of the assessment of compressive strength of in-situ concrete. The PSP test shows the potential to be reliable and reasonably accurate, especially in case of concrete with softer aggregate, yet cost effective compared to core testing and some other NDTs. This will ultimately contribute to the reduction of the uncertainty in the assessment of compressive strength of in-situ concrete. The future study will consider the on-site applicability, reliability and consistency of the PSP test for the assessment of compressive strength of in-situ concrete.

ACKNOWLEDGMENTS



This project has received funding from the European Union's Horizon 2020 research and innovation programme under the Marie Skłodowska-Curie grant agreement No. 642453.

REFERENCES

- [1] V. M. Malhotra and Carino N. J., Eds, *Handbook on Non Destructive Testing of Concrete*, CRC Press, Boca Raton, USA, second edition, 2004.
- [2] J. H. Bungey, S. G. Millard, and M. G. Grantham, Eds, *Testing of Concrete in Structures*, Taylor and Francis, Abingdon, England, Fourth edition, 2006.
- [3] M. S. N. A. Sourav, S. Al-Sabah, and C. McNally (2016), 'Strength assessment of in-situ concrete for the evaluation of structural capacity : State of the art', *Proceedings of Civil Engineering Research in Ireland Conference*, National University of Ireland Galway, 599-604..
- [4] M. S. N. A. Sourav, S. Al-sabah, and C. McNally (2018), 'Use of post-installed screws in the compressive strength assessment of in-situ concrete,' *Preceeding of The Sixth International Symposium on Life-Cycle Civil Engineering (IALCCE 2018)*, Ghent, Belgium, In press.
- [5] Hilti Ireland, Hilti: Anchor Fastening Technology Manual, Available at <https://www.hilti.ie/>. [Accessed: 15-Feb-2018].
- [6] National Standards Authority of Ireland, *I.S. EN 12504-2: Testing concrete in structures - Part 2: Non-destructive testing - Determination of rebound number*.
- [7] National Standards Authority of Ireland, *I.S. EN 12504-4, Testing Concrete-Part 4: Determination of Ultrasonic Pulse Velocity*.
- [8] International Organisation of Standardisation, *ISO 5725-1: Accuracy (trueness and precision) of measurement methods and results - Part 1: General principles and definitions*.
- [9] American Concrete Institute, *ACI 228.1R-03: In-Place Methods to Estimate Concrete Strength*, 2003.
- [10] H. Rong, C. Qian, L. Gao, J. Han, and C. Wang (2011), 'The testing strength curves of lightweight aggregate concrete by rebound method and ultrasonic-rebound combined method', *Journal Wuhan University*

- of Technology, Materials Science Edition*, 26(5), 1010–1017.
- [11] D. Breyse (2012), 'Nondestructive evaluation of concrete strength: An historical review and a new perspective by combining NDT methods', *Construction and Building Materials*, 33, 139–163.
 - [12] J. H. Bungey, S. G. Millard, and M. G. Grantham, Eds, 'Partially destructive strength tests,' in *Testing of Concrete in Structures*, Taylor and Francis, Abingdon, England, Fourth edition, 2006, 82–119.

Vibration tests of an underwater free-standing 2-rack system

Alberto Gonzalez Merino^{1,2}, Luis Costas², Arturo Gonzalez²

¹ Department of analysis and design, Equipos Nucleares, Avda. Juan Carlos I, 8 Maliaño, 39600, Spain

² School of Civil Engineering, University College Belfield, Dublin 4, Ireland
email: gonzalez.alberto@ensa.es, costas@ensa.es, arturo.gonzalez@ucd.ie

ABSTRACT: Nuclear power plants are responsible for the spent fuel management. Closely spaced racks submerged in a pool are generally used to store and to cool the nuclear fuel. A free-standing design allows to isolate the rack base from the pool floor and therefore to reduce the impact of seismic loads. However, the seismic response of free-standing racks is difficult to predict accurately using theoretical models given the uncertainties associated with inertial forces, geometrical nonlinearities and fluid-structure interactions. An ad-hoc analysis methodology has been developed to overcome these difficulties in a cost-effective way, but some dispersion of results still remains. In order to validate the analysis methodology, experimental tests are carried out on a scaled 2-rack mock-up equipped with fake fuel assemblies. The two rack units are submerged in free-standing conditions inside a rigid pool tank and subjected to accelerations on a unidirectional shaking table. A hydraulic jack induces a given acceleration time-history while a set of sensors and gauges monitor the transient response of the system. Accelerometers track the acceleration of the pool and units. Load cells measure the impact forces on the rack supports as well as the fluid forces at the centre of the rack faces. Video cameras record the transient displacements and rotations. Results provide evidence of a water-coupling effect leading to an in-phase motion of the units.

KEY WORDS: Vibration tests; Free-standing; Rack; Water coupling.

1 RACK SEISMIC RESPONSE

Racks are metallic structures formed by a rigid pedestal and an array of rectangular parallelepiped storage cells. Rack units rest submerged in free-standing conditions spaced by only a few centimeters on the bottom of the spent fuel pool. The clearance space is essentially limited by the possible collision between units during an earthquake event. Seismic accelerations are actually transmitted from the pool to the rack units through friction on supports and compression of the water volume. Hence, each base-isolated rack undergoes a complex 3D motion relative to the pool including sliding, rocking, twisting and turning. Moreover, fuel assemblies are free to rattle inside their storage cell hitting the cell walls and affecting the motion of the units. It is anticipated that both motions involve inertial and viscous forces as well as fluid-structure interactions.

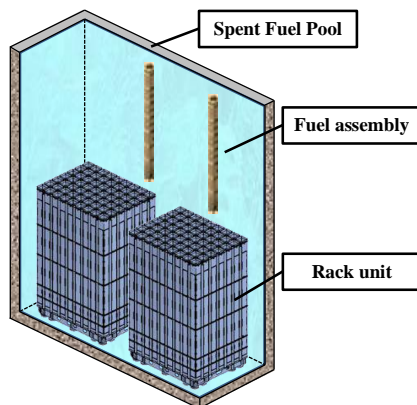


Figure 1. Spent fuel pool equipped with 2 rack units.

The rack seismic response is highly sensitive to variables related to geometry, load, excitation, friction, damping, etc. An accurate estimation of this response is essential to achieve a safe pool layout and a reliable structural design. The United States Nuclear Regulatory Commission has issued overall design requirements and licensing acceptance criteria for their performance [1-3]. However, the rack seismic response is difficult to predict given the uncertainties associated with inertial forces, geometrical nonlinearities and fluid-structure interactions. An ad-hoc analysis methodology has been developed to overcome these difficulties in a cost-effective way, but some dispersion of results still remains. This uncertainty not only comes from the input data, but also from the assumed modeling properties and the user-defined solution controls [4].

In order to validate the modeling and analysis procedures, vibration tests are carried out on a scaled 2-rack mock-up equipped with fake fuel dummies. Transient rack accelerations and displacements, impact forces and hydrodynamic pressures are recorded. The experimental response and numerical simulations will be compared to provide insight on the error of the analysis methodology.

2 PHYSICAL MODEL TESTS

2.1 Scaled 2-rack mock-up

A vibration tests campaign is carried out by a Spanish joint collaboration between Instituto de Hidraulica de Cantabria and Equipos Nucleares S.A. [5]. It enlarges the previous experimental studies on isolated racks [6-13] and places focus on the interactions between more than one unit. Hence, a functional scaled 2-racks model is tested on a unidirectional

vibration table for different initial configurations. Both units are allowed to move on their own. Figure 2 shows the physical model including the vibration table, the pool tank and the mockups of the rack units and fuel assemblies. The vibration table is equipped with a hydraulic jack able to apply a unidirectional excitation shaking at the required frequency and amplitude. For practical reasons, a reduction scaling factor needs to be applied to the physical model in order to reduce its size. Then, all geometric dimensions are multiplied by 1/3. In addition, time is compressed ($1/\sqrt{3}$) and masses lightened by the factor $1/3^2$. Such a similarity law respects both accelerations and densities and avoids problems related to scaling gravitational effects and water properties. The rest of physical dimensions defining the model can be derived from these three fundamental similarities.

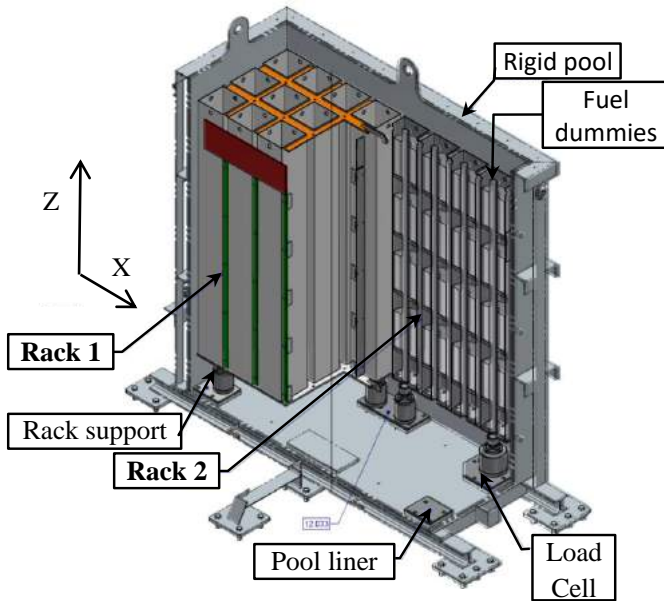


Figure 2. Rack and fuel mockups inside the pool tank.

It is noted that only the lower part of the real pool is modelled. According to the Housner approach [14], racks are submerged in the impulsive region where the water volume moves in unison with the tank, far enough from the influence of the convective component. Hence, the pool must be covered to avoid head losses related to free surface sloshing. The cover does not pressurize the volume but it leaves a 35 cm sheet of water over the rack units. Such a water thickness is considered sufficient to simulate the 3D flow disturbances caused by the bending of streamlines around the rack edges. Computational Fluid Dynamics (CFD) analysis confirms the limited influence of surface sloshing even for reduced pool dimensions [15].

The physical model is designed to represent the real pool conditions. Pool walls and supports are heavily reinforced to increase their rigidity and avoid resonance with the racks motion during the shakings. The ensemble table-pool is therefore considered as a rigid body. The mock-ups of the racks aim to preserve the natural frequencies of the original structures. Each rack mockup adds up to 4x3 cells containing 12 fuel dummies. The base-isolation is achieved by pad supports sliding over the metallic liner of the pool floor. Friction coefficient is obtained from experimental test of the

contacting plates in an inclined angle. Table 1 gives the most representative variables.

Variables	Units	Value	Comments
Seismic accelerogram	m/s ²	Fig.4	Measured A1
Rack submerged mass	kg	500	Weighed
Fuel submerged mass	kg	1900	Weighed
Horizontal eigen-frequency	Hz	16	Hammer impact test
Vertical eigen-frequency	Hz	90	FE analysis
Rack-Pool friction coefficient	-	0.25	Measured
Fuel-Cell gap space	mm	6.40	Measured
Fuel beam inertia	m ⁴	8.25E-8	Measured

2.2 Data acquisition system

Experimental data is collected by multiple sensors placed at different locations all over the pool. Figure 3 represents a section along the symmetric XY plane to illustrate their location.

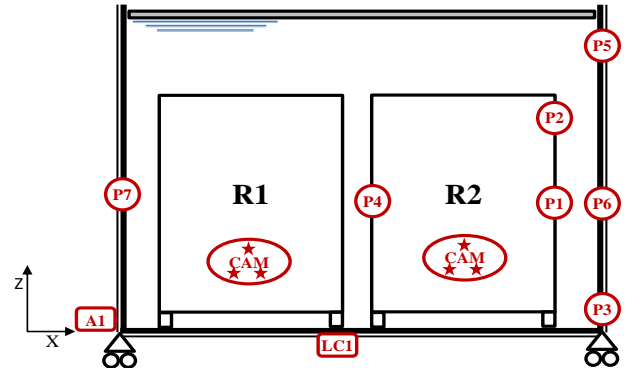


Figure 3. Pool section view with the location of the sensors.

The following instrumentation is available:

- An accelerometer (A1) is boarded on the vibration table to track the acceleration time-history of the shaking table in x direction,
- A load cell (LC1) is placed at the contact between the rack support and the pool floor. It measures the vertical reaction along the test,
- Pressure sensors (P1-P7) record the hydrodynamic pressures at different locations on the rack sides as well as on the pool walls,
- Several video cameras (CAM) attached to the vibration table film the motion of respective targets through transparent windows on the pool walls. They return the 3D relative displacements and rotations of the rack units.

2.3 Seismic loading acceleration

The physical model is vibrated in the x-direction with a synthetic earthquake derived from a real design response spectra. The inverse Power Spectra Density method allows the combination of waves of different amplitude and frequency. Figure 4 shows the resulting accelerogram as measured by the

accelerometer A1. The applied acceleration time-history lasts for 10 seconds with peaks up to $\pm 8 \text{ m/s}^2$ reaching velocities up to 0.7 m/s . A low excitation starting interval (0-2 seconds) is followed by high excitation shakings (2-8 seconds) which progressively blow out during the last 2 seconds.

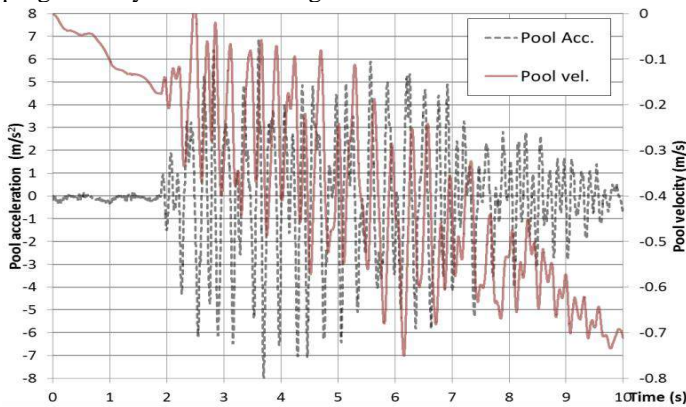


Figure 4. Acceleration and velocity time histories of the pool.

3 HAMMER IMPACT TESTS

The Eigen-frequencies of the scaled mock-ups tested on the vibration table are measured through hammer impact testing (Fig. 5). Tests are conducted with the mock-up installed free-standing on the pool tank in order to take the real supporting conditions into account.



Figure 5. Hammer tests on the rack mock-up

These natural frequencies characterize the dynamic response of the units. They result from intrinsic physical properties such as the rack mass, the flexibility of the storage cells and the stiffness of the support contacts. The frequency spectrum resulting for the empty mock-up is provided in Figure 6. Several impacts of different magnitude are performed returning peak values around 16 Hz . It indicates the frequency of the first mode of vibration in the horizontal direction. Secondary peaks around 50 and 60 Hz are considered to be related to the vertical support conditions.

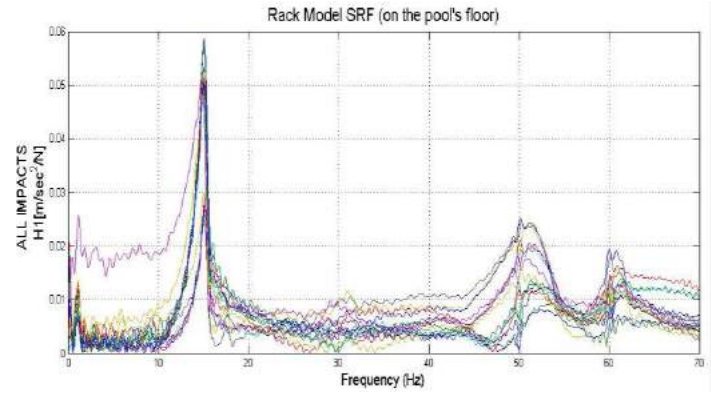


Figure 6. Frequency spectrum of the empty rack mock-up.

4 EXPERIMENTAL VIBRATION TESTS

4.1 Rack response

Figure 7 shows the sliding displacement of the racks over the pool floor in relation to the pool acceleration time-history. Slidings are measured as the difference between pool and racks displacements along the x axis. No collisions are observed so the vibration test is accepted. The peaks of the sliding cycles are in phase with those of the pool shakings which indicates the pool accelerometer clearly governs the rack motion.

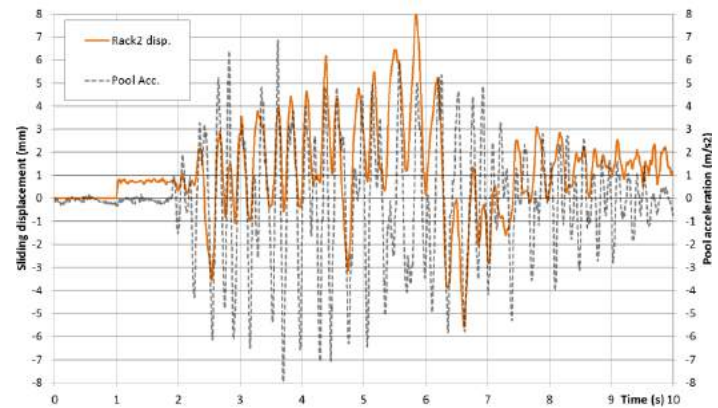


Figure 7. Relationship between the acceleration-time history and the sliding displacement of Rack2.

It is noted that the larger sliding cycles occur during the interval of maximal accelerations (between $t=2\text{s}$ and $t=8\text{s}$). In addition, Iwasaki concludes that although free-standing racks have no defined frequency response to seismic motion, their sliding response increases with the period of the acceleration excitation [16]. Both facts indicate that the governing factor of the slidings is the velocity reached by the units. All in all, the amplitude and frequency of the seismic acceleration time-history determine the energy of the excitation; large accelerations throughout long cycles give the rack units time to gain velocity. From the displacements point of view, it corresponds to high frequency and large amplitude pool displacements.

With regard to the rocking response, it is observed that rack supports tend to uplift or pierce the pool liner alternatively during the rack body oscillations. Figure 8 highlights that the reaction forces on support also share the frequency of the accelerogram. However, a short delay in the response is sometimes observed corresponding to the time needed to stop and change the direction of the rack sliding motion.

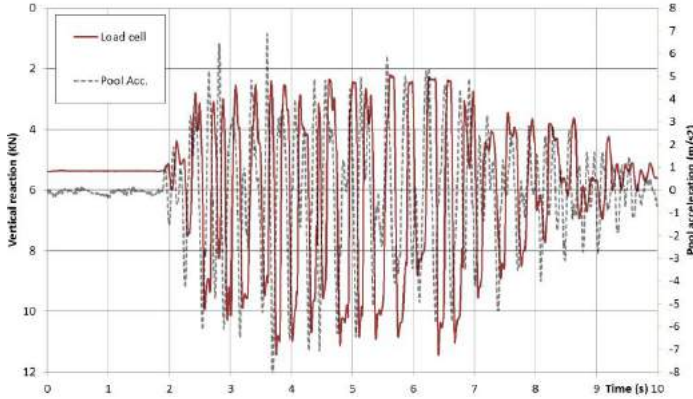


Figure 8. Relationship between the acceleration-time history and the reaction forces on support.

The initial reaction represents the underwater self-weight supported by each of the 4 feet. This value is more than doubled during the seism as a consequence of the inertial effects and the fuel rattling inside their storage cell. It starts at 5.88kN (i.e. the underwater self-weight) and reach 11.32kN at its peak ($t=3.8s$). On the other hand, it is worth noting that the support foot never lift-ups during the test. The reaction force never goes under 2kN.

4.2 Hydrodynamic forces and water coupling effect

The motion of pool and racks are connected through the water volume enclosed in-between. Any relative acceleration of the submerged structures creates local compressions or decompressions in the water volume that can only be relieved by flowing through the clearance spaces. Hence, the degree of water coupling is subjected to the drag coefficient of the rack body and to the pool layout. Large rack faces and the presence of outer plates boost the hydrodynamic resistance arising higher pressures. Narrow water gaps create flow bottlenecks blocking the evacuation and increasing the confinement.

The resulting pressure field tends to couple the whole system by opposing relative acceleration. Together with the friction forces, it transmits the seismic accelerations from the pool walls to the rack faces. Figure 9 plots the water pressure at PS1 against the accelerogram. The pressure peaks and the acceleration peaks are aligned in synchrony. However, an out-of-phase component appears during the high excitation as a consequence of the rack sliding relative acceleration.

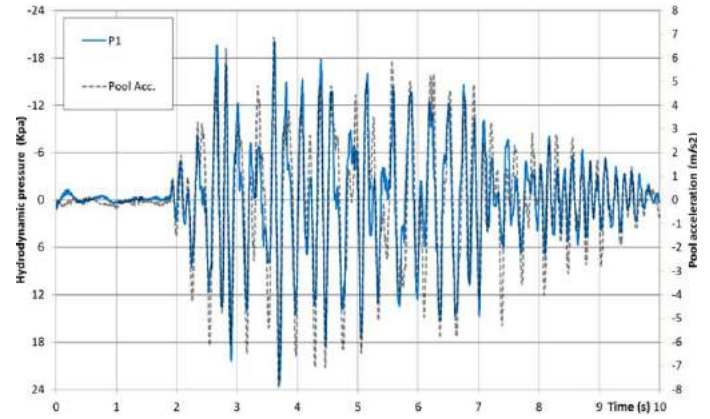


Figure 9. Relationship between the acceleration-time history and the hydrodynamic pressures.

However, the water action is not uniform. Rack faces act as blunt bodies blocking the pressure field with a high angle of attack. Streamlines have to bend around the edges looking for a way out through the clearance spaces to relief the pressure. This internal recirculation flow lowers down the pressure on the boundaries. The last is noticed by pressure sensors during the vibration test. Figure 10 provides pressure readings at the center and top of the rack face with differences on the pressure peaks of up to 25%. This pressure fall is larger on the top edge as streamlines finds an easy exit with less confinement. This observation is in agreement with the experimental tests carried out by Iwasaki [17].

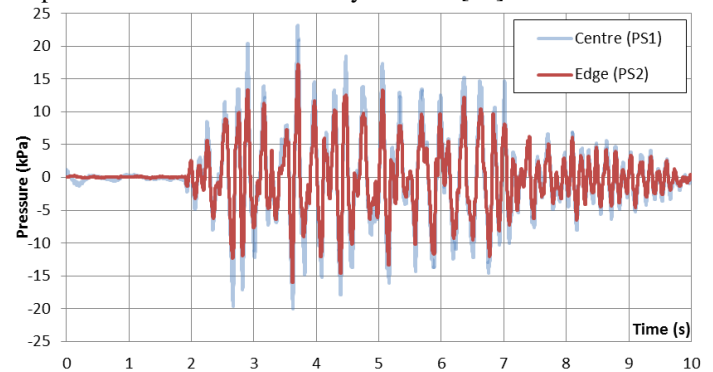


Figure 10. Boundary effects on the water pressure distribution along the rack body face.

4.3 Coupling between rack units

The 2 rack units move nearly in phase and with similar amplitudes. Figure 11 plots both sliding displacements over the pool floor. It highlights how their separation progressively cumulates along time from its initial gap ($t=0$) to 8 mm at the end of the earthquake ($t=10$).

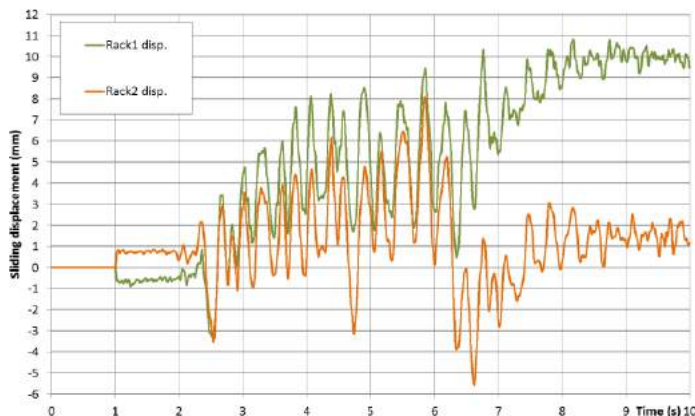


Figure 11. Sliding displacements of both rack units.

This coupling is closely related to the water action pressure field within the pool. Figure 12 compares the internal pressure in-between rack units to the external pressure between rack and pool. Water pressure is clearly larger at the outskirts of the pool. A factor 5 is noticed between both. It confirms the small alteration of the water gaps in-between racks and therefore a nearly in-phase motion.

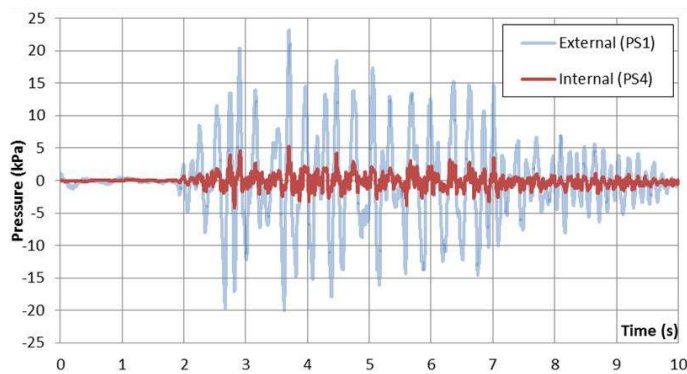


Figure 12. Comparison of internal vs. external pressures.

CONCLUSIONS

This paper describes the vibration tests campaign conducted on a reduced scale 2-rack model. It provides evidence of the water coupling effect and the in-phase motion of the free-standing units. Both units slide over the pool liner following the pool shakings but their separation slightly evolves. Such an in-phase motion can also be noted from the analysis of the hydrodynamic pressures. Internal pressures between units are a fraction of the external pressures raised between racks and pool walls.

In addition, hydrodynamic pressures are recorded at different points of the rack faces. Pressure falls near the edges as a consequence of the loss of confinement of the streamlines. A 25% difference on the pressure peaks is observed between the center of the rack face and the top edge. It adds an overturning moment that impacts the rack rocking and spinning motion.

ACKNOWLEDGMENTS



This research has received funding from the European Union's Horizon 2020 research and innovation programme under the Marie Skłodowska-Curie grant agreement No. 642453 (<http://trussitn.eu>). Physical tests are part of the ANSTER research project funded by the Spanish Ministry of Economy, Industry and Competitiveness 'Retos colaboracion 2014'.

REFERENCES

- [1] U.S. Nuclear Regulatory Commission, *OT position for review and acceptance of spent fuel storage and handling applications*. Amended by NRC letter in 1979, 1978.
- [2] U.S. Nuclear Regulatory Commission, *Standard Review Plan for the review of safety analysis reports for nuclear power plants. Chapter 3—Design of structures, components, equipment and systems*. NUREG-0800, formerly issued as NUREG-75/087, 1981.
- [3] DeGrassi G., *Review of the technical basis and verification of current analysis methods used to predict seismic response of spent fuel storage racks*, NUREG/CR-5912, BNL-NUREG-52335, 1992.
- [4] Gonzalez, A., Costas, L., Gonzalez, A. (2017), 'Sources of uncertainty in the seismic design of submerged free-standing racks', *Energy Procedia*, 127, 310-319.
- [5] Gobierno de España, IHcantabria, ENSA, *ANSTER - Almacenamiento Nuclear Seguro Ante TERremotos*, 2015. <http://anster.ihcantabria.es/>
- [6] Fujita, K., Tanaka, M., Nakamura, M. and Tsujikura Y. (1988), 'Study of the seismic isolated spent fuel storage rack', *Proceedings of 9th World conference on earthquake engineering*, Tokyo-Kyoto (Japan).
- [7] Fujita, K., Tanaka, M., Nakamura, M. and Tsujikura Y. (1990), 'Seismic testing of the base-isolated PWR spent-fuel storage rack', *JSME international Journal, Series III*, 33(3).
- [8] Moudrik R, Queval J.C, Gantenbein F., Champomier F. and Trollat C. (1995), 'Test and calculations on a scale one spent fuel storage rack', *Proceedings of conference on structural mechanics in reactor technology (SMIRT-13)*, Porto Alegre (Brazil).
- [9] Queval J.C, Sollogoub P., Champomier F. and Vallat S. (1999), 'Seismic behaviour of spent fuel storage racks', *Proceedings of conference on structural mechanics in reactor technology (SMIRT-15)*, Seoul (Korea).
- [10] Iwasaki A., Nekomoto Y., Morita H., Taniguchi K., Okuno D., Matsuoka T. and Chigusa N. (2012), 'Experimental study on free standing rack loading full fuel assembly', *Proceedings of ASME Pressure Vessels and piping conference PVP2012-78458*, Toronto (Canada).
- [11] Kaneko S. and Shirai H. (2015), 'Construction of dynamic model for free standing spent fuel rack under seismic excitation', *Proceedings of pressure Vessels and piping conference PVP2015-45069*, Boston (USA).
- [12] Sakamoto K., Kan R., Takai A. and Kaneko S. (2017), 'Construction of dynamic model of planar and rocking motion for free standing spent fuel rack', *Proceedings of ASME pressure vessels and Piping Conference PVP2017-65172*, Hawaii (USA).
- [13] Liu Y., Lu D. Liu H., Huang Y. (2018), 'The shaking table experiments on sliding and overturning of CAP1400 spent fuel storage rack with the effect of FSI', *Annals of Nuclear energy*, 112, 277-288.
- [14] Housner G.W. (1963), 'The dynamic behaviour of water tanks', *Bulletin of the seismological society of America*, 53(2), 381-387.
- [15] Takaki Y., Katsuhiko T., Kishimoto J., Iwasaki A., Nekomoto Y., Kuga T. and Kameyama M. (2017), 'Seismic design of free standing racks in Japanese nuclear power plants', *ASME Pressure Vessels and piping conference PVP2017-65740*, Hawaii (USA).
- [16] Iwasaki A., Nekomoto Y., Morita H., Kishimoto Y., Taniguchi K. and Takaki Y. (2016), 'Development of free-standing rack seismic evaluation', *Mitsubishi Heavy Industries Technical Review*, 53(2), 103-10.
- [17] Iwasaki A., Nekomoto Y., Morita H., Taniguchi K., Okuno D., Matsuoka T. and Chigusa N. (2012), 'Experimental parameter study on free standing rack', *Proceedings of ASME Pressure Vessels and piping conference PVP2012-78451*, Toronto (Canada).

Application of Gaussian process regression for structural analysis

Rui Teixeira¹, Alan O'Connor¹, Maria Nogal¹

¹Department of Civil, Structural and Environmental Engineering, Trinity College Dublin, College Green, Dublin 2
email: rteixeir@tcd.ie, oconnoaj@tcd.ie, nogalm@tcd.ie

ABSTRACT: The current paper discusses the applicability of Gaussian process regressions, also known as Kriging models, in the context of structural and reliability analysis. Due to their flexibility these models appear in the field of structural analysis in many forms. Applications to approximate limit state functions, replace the computational expensive codes that solves the dynamic of complex systems, or replicate stochastic fields can be identified. Due to this fact, a discussion on the different parameters that depend on the implementation procedure chose to use these model is presented in the current paper. Design of experiments, polynomial approximation, correlation function, hyperparameters convergence and estimation function are the main global variables analysed. When implementing a Gaussian regression or Kriging model, the user is faced with the choice of these before any further progress. The discussion presented complements previous works on the implementation of such models in the sense that it focus on the structural analysis application and on how these parameters influence the accuracy. It is shown that depending on the approximation, significant advantage can be taken from understanding these major variables. Different examples are presented to support the understanding of the problem and the main conclusions on the applicability of the Gaussian regression models as surrogates for structural analysis are drawn.

KEY WORDS: CERI 2018; TRUSS; Uncertainty; Surrogate modelling; Probabilistic analysis

1 INTRODUCTION

The growing trend of interest in probabilistic assessments combined with the growing trend in complexity of physical systems has been demanding the development of innovative techniques to enable their comprehensive understanding.

For complex systems, the applicability of surrogate models has shown the highest potential to enable accurate probabilistic assessments. These can behave as black-box functions that replace computationally expensive codes or data sets. When these systems are inherently stochastic and affected by noise, the usage of surrogate models demands a careful approach. Fomented by TRUSS's goal of quantifying uncertainty the current paper discusses the application of a type of surrogate models, Gaussian process regression, also known as Kriging models.

The Gaussian process regression emerged recently as powerful tools for reliability and probabilistic analysis due to their capability of interpolating a function and at same time considering some degree of uncertainty in the interpolation.

Several examples of applications of these models for structural applications can be identified [1-8]. Most of these focus on the usage of these models in a reliability context, where their function is to approximate a limit state function.

[9] implemented a design process using a Kriging model in the specific context of wind turbine analysis,. The authors conduct a multi-level optimization where the surrogate model is introduced to replace the evaluator of design variables that links these with the performance function.

[10] also applies the Gaussian regressions as surrogates to replace the original time consuming and complicated simulation code. As a result, optimization is enabled as the Kriging predicts the response of the system with minimal effort.

[11] analyses the probability of failure of an offshore wind turbine (OWT) by using the Kriging to predict the extreme loads on the system. [12] uses the Kriging to predict fatigue design reliability. The Kriging is used to create a fatigue surface that predicts the long term fatigue life. [13] extends the main findings presented in [12], and introduces a noise component in the design of experiments (DoE) used to create the Kriging surrogate. Additionally, the authors present a new active criteria developed for practical Kriging applications that depends on an external distribution of input parameters. [14] presents a different approach to fatigue and uses the Kriging surrogate models to interpolate intervals of confidence. The concept is then applied in the analysis of a structural component in order to predict the intervals of confidence in long term cumulative structural fatigue damage.

The purpose of the current paper is to discuss the applicability of the Kriging models in the context of structural and reliability analysis. In particular it was seen that the Kriging surrogate model appear in different contexts when applied to physical systems. Its interest for reliability applications has been growing steadily in recent years. Different variables can affect the accuracy of the surrogate approximation, many of which are imposed by the user. It is of interest to frame the applicability of the different approaches that use these models and discuss the assumptions that need to be done during the implementation phase in order to facilitate further exploitation of Kriging models in both, the field of structural analysis as well as in other fields of engineering.

To achieve the proposed goal Section 2 introduces the theory behind these type of models, Section 3 discusses their applicability and the different parameters and variables that are included in the analysis with Kriging, or Gaussian

regression, models. A comparative analysis is developed for an implementation scenario. Finally, the main conclusions of the discussion are drawn in section 4.

2 GAUSSIAN PROCESS REGRESSION FORMULATION

Kriging models can be implemented as “black-box” models that interpolate a data set with the assumption that the interpolator follows a Gaussian stochastic process.

These approximate a true function $g(x)$, $x \in \mathbb{R}^d$ with an approximate model $G(x)$ that considers Gaussian uncertainty in the approximation. d is the dimension of the x space.

Being $\mathbf{X} = [x_1, x_2, \dots, x_k]$ a vector of realisations of x with respective true evaluations $\mathbf{Y} = [g(x_1), g(x_2), \dots, g(x_k)]$, $G(x)$, the Kriging approximation, is defined as,

$$G(x) = f(\boldsymbol{\beta}; x) + Z(x)$$

$$f(\boldsymbol{\beta}; x) = \beta_1 f_1(x) + \dots + \beta_p f_p(x)$$

$f(\boldsymbol{\beta}; x)$ is a deterministic regression model with p ($p \in \mathbb{N}^+$) basis function that depend on the order of the regression and that are to be defined based on the \mathbf{X} sample.

$Z(x)$ is a Gaussian stochastic process with mean equal to 0 and covariance matrix,

$$\mathbf{C}(x_i, x_j) = \sigma^2 R(x_i, x_j; \boldsymbol{\theta}), \text{ with } i, j = 1, 2, 3 \dots k$$

\mathbf{C} defines the correlation generic \mathbf{X} points using; the constant process variance σ^2 and a correlation function $R(x_i, x_j; \boldsymbol{\theta})$ that depends on the points and on a set of $\boldsymbol{\theta}$ hyperparameters. It is common to find application that use the so-called separable correlation function [15],

$$R(x_i, x_j; \boldsymbol{\theta}) = \prod_{i=1}^d R(h_i; \theta_i), \boldsymbol{\theta} \in \mathbb{R}^d$$

Alternative formulations for the correlation function can be found in [16, 17]. $R(h_i; \theta_i)$ depends on $h = [h_1, \dots, h_d]$ that has an incremental form and a set of $\boldsymbol{\theta}$ hyperparameters. $R(x_i, x_j; \boldsymbol{\theta})$ interpolates the between the regression model prediction and the true limit state realisations.

Using the equations above it can be seen that the fitted surface $G(x)$ depends on three main parameters: σ^2 , $\boldsymbol{\theta}$ and $\boldsymbol{\beta}$.

For a set of given support points \mathbf{Y} the problem of prediction can be solved through a generalised least squares formulation. $\boldsymbol{\beta}$ and σ^2 are then defined as a function of the $\boldsymbol{\theta}$ hyperparameters,

$$\boldsymbol{\beta} = \hat{\boldsymbol{\beta}}(\boldsymbol{\theta}) = (\mathbf{F}^T \mathbf{C}^{-1} \mathbf{F})^{-1} \mathbf{F}^T \mathbf{C}^{-1} \mathbf{Y}$$

$$\sigma^2 = \hat{\sigma}^2 = \frac{1}{k} (\mathbf{Y} - \mathbf{F} \hat{\boldsymbol{\beta}}(\boldsymbol{\theta}))^T \mathbf{C}^{-1} (\mathbf{Y} - \mathbf{F} \hat{\boldsymbol{\beta}}(\boldsymbol{\theta}))$$

where \mathbf{F} is the $k \times p$ regression matrix that has rows equal to the evaluation of the p regression functions at \mathbf{X} . The problem of finding $\boldsymbol{\theta}$ can be solved by a maximum likelihood formulation.

As a result a prediction for $g(x)$ in a generic point in space u is given by an expected value μ_G and a variance σ_G ,

$$\mu_G(u) = f(u)^T \boldsymbol{\beta} + \mathbf{c}(u)^T \mathbf{C}^{-1} (\mathbf{Y} - \mathbf{F} \boldsymbol{\beta})$$

$$\sigma_G^2(u) = \sigma^2 \left(1 + D(u)^T (\mathbf{F}^T \mathbf{C}^{-1} \mathbf{F})^{-1} D(u) - \mathbf{c}(u)^T \mathbf{C}^{-1} \mathbf{c}(u) \right)$$

$$D(u) = \mathbf{F}^T \mathbf{C}^{-1} \mathbf{c}(u) - f(u)$$

$\mathbf{c}(u) = c(u, x_i), i = 1, 2, \dots, k$ is a vector that defines the correlation of u with the known points of \mathbf{X} . \mathbf{F} is the matrix of $f_p(x)$ functions of the polynomial approximation.

One important characteristic of the Kriging interpolator is that \mathbf{Y} predictions have a variance component of value 0, meaning the \mathbf{Y} is exactly predicted when u takes any value of \mathbf{X} .

It is known that in most cases this does not represent the real behaviour of \mathbf{Y} and frequently $g(\mathbf{X})$ will have some noisy or probabilistic component ε .

$$\mathbf{Y} = \mathbf{Y}_e + \varepsilon$$

In such cases \mathbf{Y} is better described by an expected value \mathbf{Y}_e and a noise component ε . To account for this effect a slight modification of the $\mathbf{C}(x_i, x_j)$ is introduced,

$$\mathbf{C}(x_i, x_j) = \mathbf{C}(x_i, x_j) + \delta \boldsymbol{\tau}^2$$

where $\boldsymbol{\tau}^2$ is the vector of variance of \mathbf{Y} , the support points used to estimate $G(x)$. δ is the identity matrix of size $k \times k$. Figure 1 presents an example of a Kriging model containing a noise component (I) and the same model disregarding it (II).

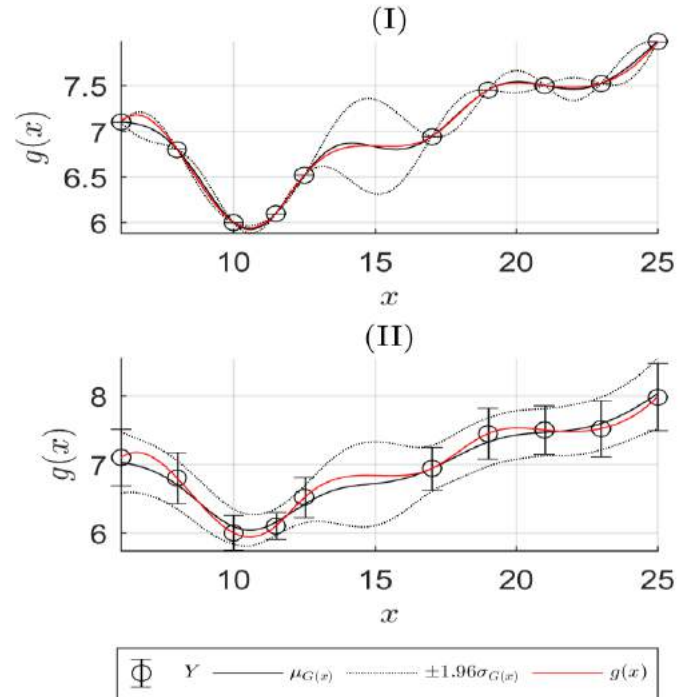


Figure 1. Example of Kriging considering non-noisy \mathbf{Y} (I) and noisy \mathbf{Y} (II) for the same \mathbf{X} .

If the goal is to approximate accurately $g(x)$ then the normal interpolator is of interest. In such scenario the Y prediction is assumed to be perfectly known and there is no need to introduce further complexity in the model.

However this is not always the case, it was seen in Section 1 that the Kriging is used many times to approximate the response of computationally expensive models. If the model response is deterministic then $G(x)$ can be used to interpolate it. Frequently this is not common, and as computational models grow in complexity, the complexity of the models' response also increases. Considering the uncertainty in the code or its inherent stochasticity is of interest, and as a result, it is also of interest to consider the approach that uses the noise component. The alternative that consider the local variance component is commonly known as the noisy.

3 ANALYSIS OF COMPLEX SYSTEMS USING GAUSSIAN REGRESSION MODELS

The Gaussian regression formulation highlights the flexibility of these models.

On one side they can be applied to approximate a function where the main goal is to have a deterministic prediction with some degree of uncertainty (e.g. similar case to a simple polynomial approximation). As alternative these models can be applied to replicate full probabilistic fields by using the local statistical distributions to interpolate further predictions in regions of x where no information is available. The result is not only the interpolation of the curve, but instead of the whole probabilistic field.

The most frequent application of the kriging in the context of structural and reliability analysis is in the replacement of computationally expensive dynamic coupled codes used to model physical systems. Approximation of the limit state function is also widely identified.

When the application involves approaching the computationally expensive code, attention needs to be given to the different parameters of the Gaussian regression model. These may be used to better approximate the true response function. In the particular case where a full probabilistic field is to be predicted, the usage of these models is complex. While it is generally simple to approach the mean function of the probabilistic field, the same does not happen for the variance, as it will be seen in Section 3.6.

3.1 Design of Experiments

Figure 2 presents an example of the Kriging approximation with two different designs of experiments.

The term Design of Experiments (DoE) refers to the points X and respective Y . Naturally, the DoE is the most relevant variable in the definition of the Kriging model. Due to this, extensive research has been developed on how to define and infill the DoE [13, 18-21]. The usage of Latin Hypercube sampling schemes to set the initial design, and further improvement the Kriging using an active search is common.

It can be seen in Figure 2 that if the DoE is not well represented inaccurate predictions may occur. In the left region of Figure 2 there is no DoE point. The result is an inaccurate prediction of any point in that region, as it can be

identified in the cross-validation curve (corresponds to the smaller value $\mu_{g(x)}$ point).

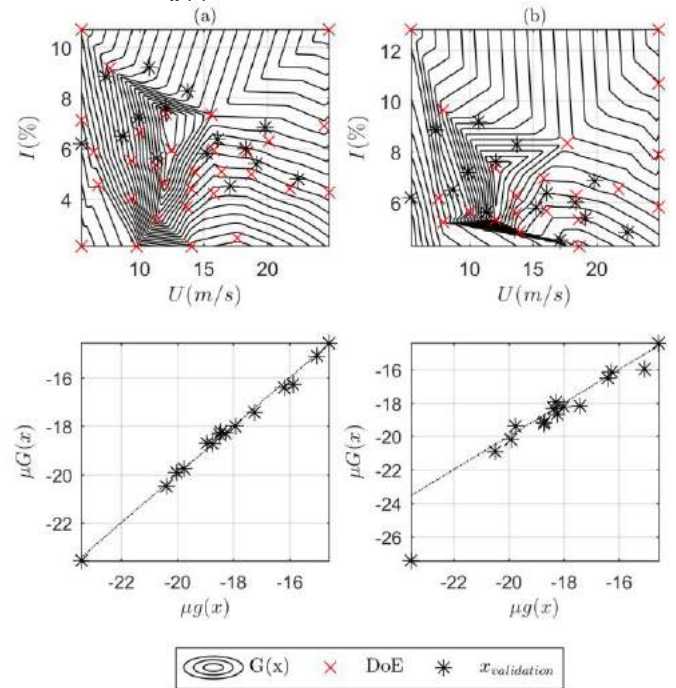


Figure 2. Example of cross validation of the same function using two distinct DoEs.

Most of the Kriging implementation effort should be addressed to investigate on the best solution to define X . [13] showed that a comprehensive understanding on the definition of X with a Gaussian regression model can reduce the effort to implement a physical process by 80%. Furthermore, the authors support the need for a full understanding of the problem *a priori* to the Kriging implementation.

An efficient definition of the DoE for accurate results is increasingly relevant as d increases. [7] refers that the Gaussian regression models hold well for very high d . However, even if these models are accurate in high dimensional space, the definition of the DoE is particularly concerning due to the curse of dimensionality.

3.2 Polynomial approximation

The deterministic component of the Kriging uses a polynomial approximation. The effects of this polynomial approximation in the accuracy of the results is limited. [7] studied the influence of the order of the polynomial function in a problem of reliability concluding that it is negligible.

It is of interest to infer that the statistical component of the Kriging is so dominant that, even when a constant basis function is used, the regression predictions at X are still Y if the noise component is not considered.

The influence of the polynomial approximation commonly depends on how much is known about the surface. For small or medium X sizes, the influence of the polynomial approximation is already negligible.

The points in Figure 3 were computed using a subset of the DoE in Figure 1. If a very high polynomial approximation is used, the unique Gaussian uncertainty properties of the

regression may be lost, and the surrogate will behave as a polynomial approximation.

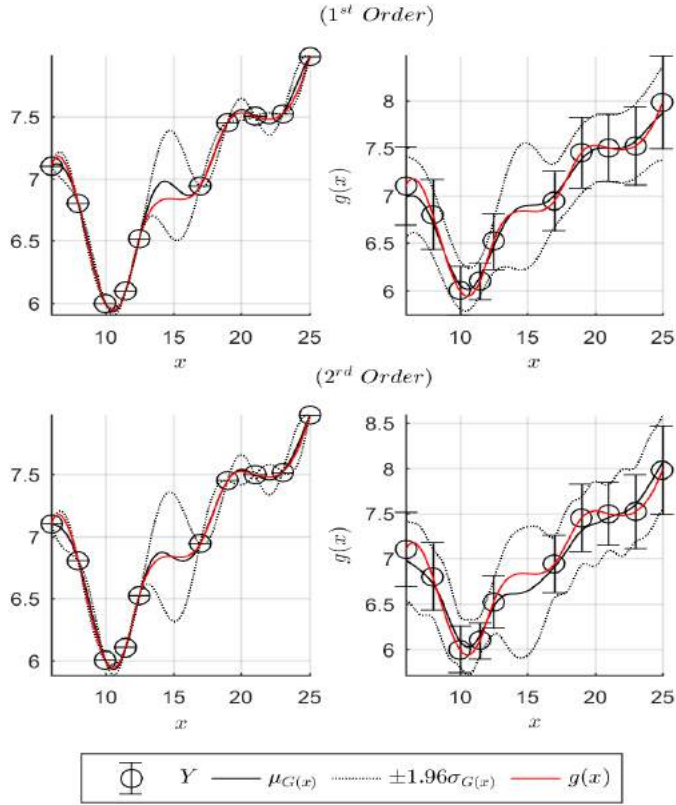


Figure 3. Influence of the polynomial approximation in the Kriging approximation.

3.3 Correlation functions

It was shown in Section 2 that several correlation functions are available for the Kriging approximation. Common types of correlation function are the *separable* and *isotropic*.

$$R_{sep}(x_i^I, x_i^{II}, \theta) = \prod_{i=1}^d R_{sep}(x_i^I, x_i^{II}, \theta_i)$$

$$R_{sep}(x_i^I, x_i^{II}, \theta) = R(h), \quad h = \sqrt{\sum_i^d \left(\frac{x_i^I - x_i^{II}}{\theta_i} \right)^2}$$

For structural and reliability purposes the *separable* form is most widely applied. Both the correlation function types use a difference to relate two generic points x_i^I and x_i^{II} . Then the correlation formulation imposes that, e.g. by the form of a negative exponential or a maxima comparison, as the distance increase between points they are progressively less correlated.

The correlation function in combination with the θ , discussed in the following subsection, has a significant weight on the definition of a prediction due to its direct influence on the covariance Matrix. However, if the remaining variables

are fixed and only the correlation function is changed its effect is negligible, Figure 4.

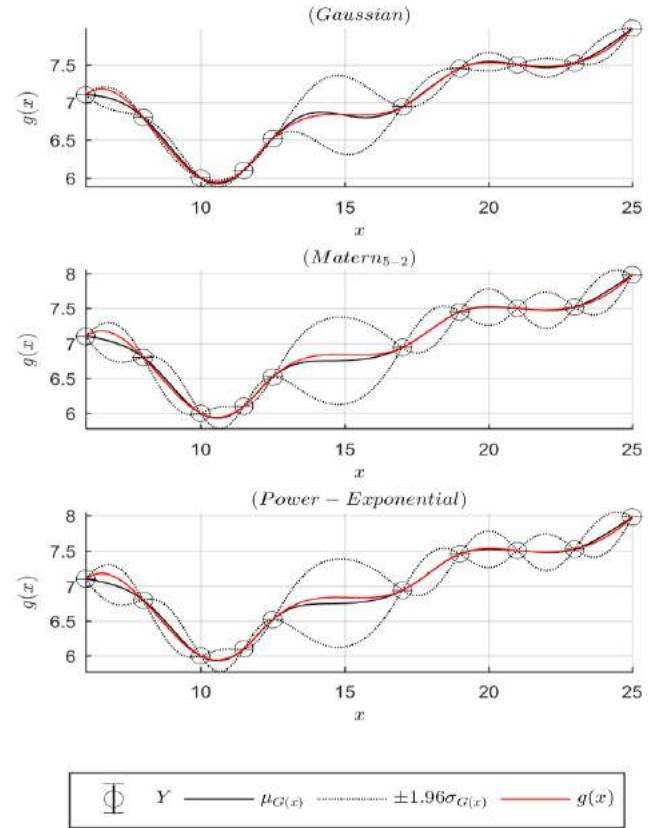


Figure 4. Approximation of $G(x)$ for a pre-specified X using different correlation functions.

The effect of the correlation function is more significant when analyzed from the point of view of how θ defines its shape. θ is very relevant in the definition of the Kriging, and apart from the DoE, is the most influential variable and the one that can be more significantly further exploited to optimize the Gaussian regression or Kriging usage.

3.4 Hyperparameters θ

It was seen before that the problem of the Kriging approximation can be reduced to a problem of maximum likelihood estimation dependent on the Kriging hyperparameters θ . These are very influent components of the model approximation. The hyperparameters appear in the correlation functions as well as on the estimation of the local $\mu_{G(x)}$ and $\sigma_{G(x)}$. As a result they can have influence on the relative weight of the correlation function on the d dimensions.

Figure 5 presents the influence of the value of the θ hyperparameters in both $\mu_{G(x)}$ and $\sigma_{G(x)}$ for $d = 2$ dimensions associated with the U and I , wind speed and turbulence intensity respectively.

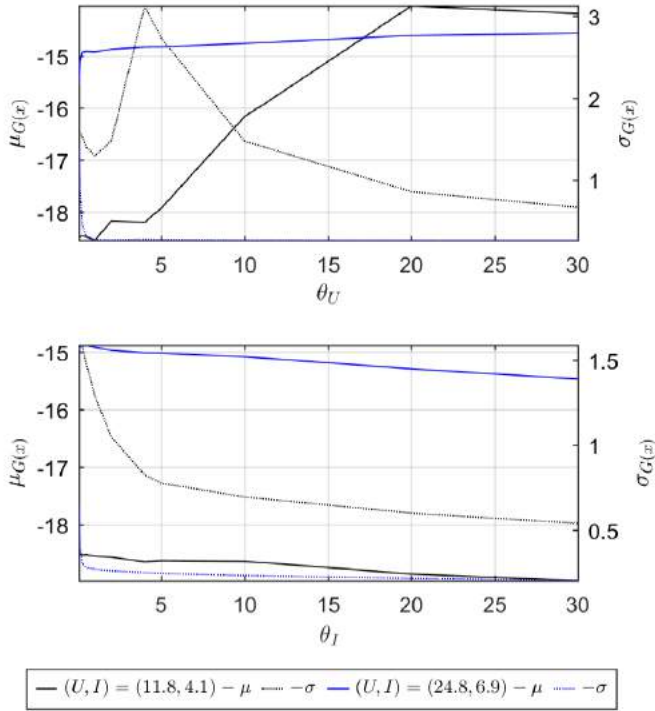


Figure 5. Influence of the θ hyperparameters on the first and second moment of the $G(x)$.

In Figure 5 it can be identified that a change in the θ_i values can result in a significant change in the $G(x)$ approximation. When implementing a surrogate formulation with a Kriging model, intervals for the convergence of θ are required.

The trends in the increase and decrease are not linear, but in the particular case where one is monotonic, e.g. θ_I for the case of μ and σ , the remaining hyperparameters can be used to calibrate the model.

It is relevant then to exploit the influence of these parameters in the results. Attention should be given to the fact that for $i = 1, \dots, d$ the Kriging parameters are calculated simultaneously and through an optimization process. After an initial solution, an alternative to specific application can be to use a series of cross-validation points to search θ for the best approximation. It is a fact that this introduces additional computational time, and requires a careful approach to not fit the Kriging very accurately for small regions of x leaving the approximation in other areas of x inaccurate. This is of most interest when using a surrogate of the stochastic response which needs to mimic a function, instead of deliberately converging for a certain function $g(x)$.

Even though that not exactly the same approach the estimation alternative Leave-One-Out (*LOO*) to set the Kriging model includes subsets of cross-validation in order to calculate θ .

3.5 Estimation method

Different estimation methods are available to define $G(x)$, being the most popular the Maximum likelihood (*ML*)

estimator. [16] presents an extensive discussion on some of the alternative methods to estimate θ . Other common methodology, which will be used for comparison in the non-noisy case, is the *LOO* estimation technique.

It is frequently assumed that the estimation method has limited influence on the results. This is related to the fact that the estimation method is related to the hyperparameters definition and as such, its influence is directly related with the influence of changing these length scales. The hyperparameters have a major role in the model.

3.6 Comparison case study

Simple comparative results to compare the discussed variable were computed in order to have a simultaneous comparison of the variables discussed. In order to analyse their influence a comparative indicator η is defined as:

$$\eta = \frac{1}{n} \sum_i^x \left| \frac{G(x) - g(x)}{g(x)} \right|$$

the averaged difference between $G(x)$ and $g(x)$ when $x = x_{cross}$, being x_{cross} a series of cross validation points. 25 points were used to compute the cross validation in the example described. The need to define this indicator is related to the difficulty of comparing the influence of the different variables discussed. Table 1 shows comparative results for the variables discussed in the structural fatigue analysis of an OWT tower component.

Table 1 – Cross-Validation comparative results for an OWT tower component. DoE used is presented in Figure 2-(a).

	no τ^2	with τ^2	
	η_μ	η_μ	η_σ
DoE			
$k = 11$	0.029	0.033	>1
$k = 21$	0.016	0.031	>1
$k = 31$	0.017	0.013	0.49
Polynomial Function			
Constant	0.023	0.023	0.94
1 st	0.020	0.014	0.67
2 nd	0.017	0.013	0.49
3 rd	0.025	0.022	0.34
4 th	0.041	0.025	0.89
Correlation Function			
Matérn3-2	0.014	0.014	0.48
Matérn5-2	0.015	0.014	0.47
Gaussian	0.017	0.013	0.49
Exponential	0.018	0.014	0.91
Hyperparameters θ			
$\theta_{1,2} = 0.01$	0.067	0.064	>1
$\theta_{1,2} = 0.5$	0.040	0.041	>1
$\theta_{1,2} = 1$	0.022	0.022	>1
$\theta_{1,2} = 2$	0.033	0.016	0.89
$\theta_{1,2} = 10$	>1	0.045	0.56
$\theta_{1,2} = 100$	>1	0.069	0.69
Estimation Method			
ML	0.017	-	-
LOO	0.018	-	-

To compare the influence of the DoE, a DoE with 11, 21 and 31 points were computed. The remaining results were computed using $k = 31$. The reference case considered also a 2th order polynomial function and a Gaussian correlation function and *MLE* estimation in between [0.5 2] for the case without τ^2 and [0.5 0.5, 2, 10] when τ^2 was considered. To highlight that this *screening* is limited in the sense that only a partial number of conclusions can be drawn from its simplified approach.

It can be seen that apart from the DoE, θ has the most significant influence in all the cases. In most implementation the default boundaries will avoid inaccurate predictions due to these. However, emphasis should be given to these parameters during implementation. Relevant improvements can be attained by searching the θ space without additional effort on improving the DoE. It is also important to understand these parameters as length scales that will weigh the Gaussian regression on its different d dimensions. Different weights in the search space (by using wider intervals or higher absolute values) may be of interest to achieve accurate results.

In most cases the polynomial function has limited influence in the accuracy, this was identified previously in [7]. However when the model intends to approximate τ^2 , this is not the case. For such scenario the polynomial approximation has determinant influence in the results.

Within the most widely applied correlation functions, Gaussian and Matérn_{5/2}, little influence in the accuracy of the approximation can be identified. As expected there is also limited variation in the results by effect of the estimation techniques. The same occurs for the estimation, due to the reasons previously highlighted.

4 CONCLUSIONS

The present paper discussed the different variables that influence the usage of Gaussian process regressions, or Kriging models, as tools for structural analysis on both reliability, as well computational efficiency applications.

These models, due to their inherent probabilistic behaviour, are of interest to structural, in particular reliability, applications where uncertainty is a concern. Quantifying uncertainty and uncertainty analysis has been growing steadily in the engineering field, justifying the demand for such models.

Five main generic global parameters that influence the modelling with these type of surrogates were discussed as means of improving their implementation: Design of Experiments, Polynomial approximation, Correlation function, Hyperparameters and Estimation method. Discussion showed that each of these has different influence on the accuracy of the Kriging approximation. Individually, better accuracy can be achieved by a better definition of the Design of Experiments and Hyperparameters. The effect of the remaining variables is reduced, very specific, or is to some degree correlated with the definition of the first two. Correlated effects of these variables was not studied and should be addressed in future studies. Further studies should also focus on constant process variance.

Future works should consider the extension of the presented initial comparison in order to generate a reference comprehensive guide on how to apply these powerful models for structural analysis. Nonetheless, it is highlighted that a deep knowledge of the problem in hands is required for a useful implementation.

ACKNOWLEDGMENTS



This project has received funding from the European Union Horizon 2020 research and innovation programme under the Marie Skłodowska-Curie grant agreement No. 642453.

REFERENCES

- [1] Romero, V.J., Swiler, L.P. and Giunta, A.A. (2004), 'Construction of response surfaces based on progressive-lattice-sampling experimental designs with application to uncertainty propagation', *Structural Safety*, 26(2), 201-219.
- [2] Kaymaz, I. (2005), 'Application of kriging method to structural reliability problems', *Structural Safety*, 27(2), 133-151.
- [3] Li, H., Wang, Q.X. and Lam, K.Y. (2004), 'Development of a novel meshless local kriging (lokriking) method for structural dynamic analysis', *Computer Methods in Applied Mechanics and Engineering*, 193(23-26), 2599-2619.
- [4] Bichon, B.J., Eldred, M.S., Swiler, L.P., Mahadevan, S. and McFarland, J.M. (2008), 'Efficient global reliability analysis for nonlinear implicit performance functions', *AIAA journal*, 46(10), 2459-2468.
- [5] Echard, B., Gayton, N. and Lemaire, M. (2011), 'Ak-mcs: an active learning reliability method combining kriging and monte carlo simulation', *Structural Safety*, 33(2), 145-154.
- [6] Echard, B., Gayton, N., Lemaire, M., and Relun, N. (2013), 'A combined importance sampling and kriging reliability method for small failure probabilities with time-demanding numerical models', *Reliability Engineering & System Safety*, 111, 232-240.
- [7] Gaspar, B., Teixeira, A.P., and Guedes Soares, C. (2014), 'Assessment of the efficiency of kriging surrogate models for structural reliability analysis', *Probabilistic Engineering Mechanics*, 37, 24-34.
- [8] Zhang, L., Lu, Z., and Wang, P. (2015), 'Efficient structural reliability analysis method based on advanced kriging model', *Applied Mathematical Modelling*, 39(2), 781-793.
- [9] Maki, K., Sbragio, R., and Vlahopoulos, N. (2012), 'System design of a wind turbine using a multi-level optimization approach', *Renewable Energy*, 43, 101-110.
- [10] Yang, H., Zhu, Y., Lu, Q. and Zhang, J. (2015), 'Dynamic reliability based design optimization of the tripod sub-structure of offshore wind turbines', *Renewable Energy*, 78, 16-25.
- [11] Morató, A., Sriramula, S. and Krishnan, N. (2016), 'Reliability analysis of offshore wind turbine support structures using Kriging models', *Proceedings of ESREL Conference*, Glasgow, September.
- [12] Teixeira, R., O'Connor, A., Nogal, M., Nichols, J. and Spring, M. (2017), 'Structural probabilistic assessment of offshore wind turbine operation fatigue based on kriging interpolation', *Proceedings ESREL Conference*, Portoroz, Slovenia, June.
- [13] Teixeira, R., O'Connor, A., Nogal, M., Nichols, J. and Dumas, A., 'Fatigue analysis of Offshore wind turbines using Kriging models'. [Under review]
- [14] Teixeira, R., O'Connor, A. and Nogal, M. (2018), 'Interpolation of confidence intervals for fatigue design using a surrogate model', *Proceedings IFED Conference*.
- [15] Roustant, O., Ginsbourger, Y. and Deville, D. (2012), 'Dicekriging, diceoptim: Two R packages for the analysis of computer experiments by kriging-based metamodeling and optimization', *Journal of Statistical Software*.
- [16] Rasmussen, C. ., Gaussian processes in machine learning. In *Advanced lectures on machine learning*, 63-71. Springer, 2004.
- [17] Marelli, S., and Sudret, B. (2014), 'Uqlab: A framework for uncertainty in matlab', *Proceedings 2nd Int. Conf. on Vulnerability, Risk Analysis and Management (ICVRAM)*, 2554-2563.
- [18] Jones, D.R., Schonlau, M., and Welch, W.J. (1998), 'Efficient global optimization of expensive black-box', *Journal of Global optimization*, 13(4), 455-492.

- [19] Huang, D., Allen, T. T., Notz, W. I. and Zeng, N. (2006), 'Global optimization of stochastic black-box systems via sequential kriging meta-models', *Journal of global optimization*, 34(3), 441-466.
- [20] Liu, J., Han, Z. H. and Song, W. P. (2012), 'Comparison of infill sampling criteria in kriging-based aerodynamic optimization', *Proceedings of 28th Congress of the International Council of the Aeronautical Sciences*, 23-28).
- [21] Picheny, V., Wagner, T. and Ginsbourger, D. (2013), 'A benchmark of kriging-based infill criteria for noisy optimization', *Structural and Multidisciplinary Optimization*, 48(3), 607-626.

On the effectiveness and uncertainty of inspection methods for fatigue crack management

Guang Zou^{1,2}, Kian Banisoleiman¹, Arturo González²

¹Global Technology Centre, Lloyd's Register, SO16 7QF, Southampton, UK

²School of Civil Engineering, University College Dublin, Belfield, Dublin, Ireland
email: guang.zou@lr.org, kian.banisoleiman@lr.org, arturo.gonzalez@ucd.ie

ABSTRACT: Non-destructive testing (NDT) methods have been widely used for damage examination and structural maintenance, e.g. detecting and repairing fatigue cracks. In-service inspections help to increase fatigue reliability by providing new information for updating structural failure probability and making decisions on repair. However, these benefits are often compromised by uncertainties associated with inspection methods. Sometimes existing cracks may not be identified, and positive inspection indication may not exist. It is of great interest to consider the influence of inspection uncertainty in maintenance optimization because the benefits and costs of maintenance are affected by inspection decisions (inspection times and methods) which are subjected to inspection uncertainty. However, the influence of inspection uncertainty on maintenance optimization has not been explicitly and adequately covered in the literature. In this paper, the problem has been investigated by probabilistic modelling of the qualities of inspection methods via probability of detection (PoD) functions. A new PoD function has been proposed to characterize the inspection quality when inspection uncertainty is not considered. Optimum inspection decisions are derived with the objective of maximizing lifetime reliability index under two scenarios (considering and not considering inspection uncertainty). The effectiveness of a planned inspection is defined based on the max reliability indexes under the two scenarios. It is shown that the max lifetime reliability index generally decreases when inspection uncertainty is considered. However, inspection uncertainty may have little influence on the lifetime reliability index depending on the planned inspection time. The effectiveness of a planned inspection increases with the decrease of the mean detectable crack size.

KEY WORDS: Structural integrity management; Risk-based inspection; Maintenance optimization; Inspection uncertainty.

1 INTRODUCTION

In-service inspections and maintenance are important means to validate and recover operational safety of infrastructures, assets and vehicles. The need for in-service maintenance comes from inherent variabilities in environmental loads, modelling uncertainties, human errors in design and fabrication, discrepancies between as-built conditions and design, changes of operational modes, and others hazards that cannot be foreseen at the design stage. Although some of these factors can be considered in design via conservative safety factors, direct and indirect costs of conservative design usually outweigh its benefits. To reduce costs of conservative design, it is justified to adopt appropriate design factors and develop an in-service inspection programme that will validate operational safety and identify potential damages developed in service [1].

Cracks are very common damages in welded structures that need to be inspected periodically and repaired if detected to ensure integrity of structures. Cracks are usually caused by cyclic fatigue loading under which cracks develop and grow until fracture occurs. Crack propagation in fatigue-critical components can cause sudden rupture of the whole structural system, which represents a significant risk to safe operation and in the event of occurrence will have serious consequences, not only financially, but also environmentally and socially.

Fatigue inspection and maintenance decision-making is typically challenged by limited budgets for operational safety management and uncertain information about crack damage

states in terms of location, occurrence time, extent, geometry, growth rate, etc., which are difficult to predict accurately due to sources of uncertainties in material properties, loads, modelling, etc. While inspection and maintenance can help to increase operational safety and reduce risks, these benefits can be compromised by the uncertainties. The extent of risk mitigation is subjected to maintenance decisions such as inspection times, inspection method, repair criteria, repair methods, etc, which are further subjected to the uncertainties. The expected life cycle costs (LCC, the sum of expected costs of inspection, repair and failure) are also subjected to the uncertainties, as both the crack growth and inspection results are probabilistic at the inspection planning stage (i.e. at the beginning of service). Hence, maintenance decision-making models, which can consider various sources of uncertainties in a rational and consistent way, have the potential to reduce LCC while keeping acceptable risk level.

This paper addresses maintenance optimization by probabilistic modelling of crack growth and inspection quality. The quality of an inspection method is characterized by the detectable crack size a_d . Focus is placed upon the uncertainty associated with inspection quality. Inspection uncertainty leads to probabilistic inspection result, which makes maintenance decision-making difficult, together with probabilistic crack damage states. Reliability-based maintenance optimization approaches, with and without consideration on inspection uncertainty have been developed taking into account corresponding PoD functions. The effects of inspection uncertainty on lifetime fatigue reliability have

been presented, and based on this, a method to evaluate the effectiveness of a planned inspection have been proposed.

2 PROBABILISTIC CRACK GROWTH

Fracture mechanics (FM) approach is employed for fatigue analysis. Fatigue failure is explained as the process of crack initiation, and crack growth until final fracture. The reason for this choice, i.e. as opposed to S-N approach, is obvious. Herein the damages that need to be inspected and controlled are fatigue cracks. A FM approach is suitable for crack growth prediction from an initial crack size a_0 to the final critical crack size a_c , while the objective of a S-N approach is to obtain a prediction on the overall fatigue life with a relatively high confidence level.

For welded structure, there are inevitable inclusions or initial flaws/cracks in materials introduced during the welding process, which decrease fatigue performance and shorten fatigue life. Due to the existence of initial flaws, it is often thought that the crack initiation stage is negligible compared with the crack growth stage. The relationship between crack growth rate and the stress intensity factor is given by Paris law, formulated by Equation (1) and (2).

$$\frac{da}{dN} = C \Delta K^m, \quad \Delta K_{th} \leq \Delta K \leq K_{mat} \quad (1)$$

$$\Delta K = \Delta \sigma Y(a) \sqrt{\pi a} \quad (2)$$

where a is crack size; N is number of cycles; da/dN is crack growth rate; C and m are material parameters; ΔK is stress intensity factor range; K_{mat} is material fracture toughness; ΔK_{th} is threshold value for the stress intensity factor range; $Y(a)$ is geometry function; and $\Delta \sigma$ is stress range.

If failure is defined by the crack depth reaching a critical size a_c , then the crack growth life can be obtained by integration of Equation (1) from an initial crack size a_0 to a_c .

As an illustrative example, herein a typical stiffened plate of a ship structure is investigated (Figure 1). Stiffeners are the most common structural components in ship structures employed to increase stability of plates of shells. However, crack initiation and growth along stiffeners is highly likely to occur during lifetime due to the very large number of stiffeners in a ship. The integrity of the plate thus needs to be validated and recovered by periodical inspections and maintenance. The required service life T_R for the ship is typically 20 years. The frequency of wave loading is about 0.16Hz, which is equal to approximately $N_0 = 5 \times 10^6$ cycles per year.

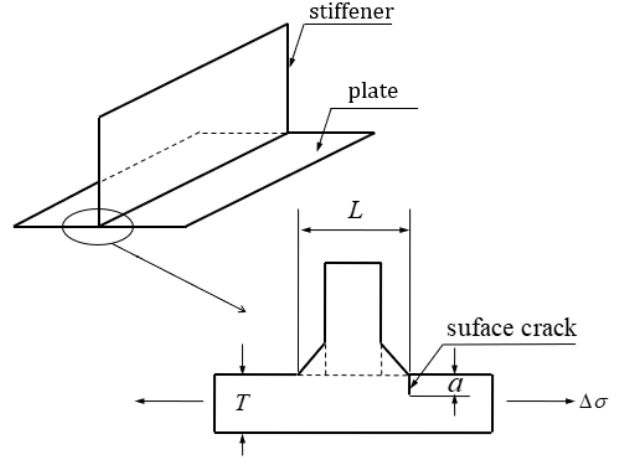


Figure 1. A welded detail in a stiffened plate in ship structure

Fatigue resistance of the welded detail is given by a S-N curve as Equation (3).

$$\begin{aligned} N_F \Delta \sigma^{m_1} &= \bar{a}_1 & N_F &\leq 10^7 \\ N_F \Delta \sigma^{m_2} &= \bar{a}_2 & N_F &\geq 10^7 \end{aligned} \quad (3)$$

where m_1 and m_2 are the fatigue strength exponents, and \bar{a}_1 and \bar{a}_2 are the fatigue strength coefficients. The parameters for the S-N curve can be found in rules of ship classification societies. A fatigue design factor (FDF) of 8 has been applied to welded structural detail, which requires that the maximal allowable equivalent stress range is $\Delta \sigma_e = 17.28$ MPa. The plate thickness is $T = 25$ mm. The parameters are summarized in Table 1.

Table 1. Design parameters for the welded detail.

Parameter	Unit	Value
T_R	Year	20
N_0	Cycle	5×10^6
$\log_{10} \bar{a}_1$	[N, mm]	11.855
$\log_{10} \bar{a}_2$	[N, mm]	15.091
T	mm	25
$\Delta \sigma_e$	MPa	17.28
m_1	-	3
m_2	-	5

The crack growth prediction is subjected to several sources of uncertainty. It is believed that the accuracy of using Paris law for crack growth prediction mainly depend on accuracy of input parameters: initial crack size a_0 , material parameter C and stress range $\Delta \sigma$. Figure 2 provides a schematic representation of probabilistic crack growth. In this paper, the initial crack size a_0 and the crack growth rate C are modelled as variables. Uncertainties associated with calculation of stress range $\Delta \sigma$ are modelled as an additional variable B . The mean value and standard deviation (SD) for all variables are listed in Table 2.

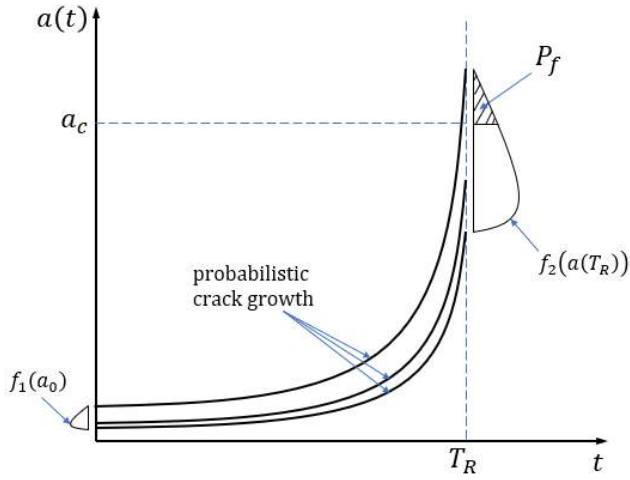


Figure 2. Schematic representation of probabilistic crack growth and failure probability (f_1 is probability density function of a_0 ; f_2 is probability density function of crack size at the end of service life $a(T_R)$; P_f is failure probability within the required service life T_R).

Table 2. Variables for reliability analysis (a_d is detectable crack size of an inspection introduced in Section 4).

Variable	Distribution	Unit	Mean	SD
a_0	Exponential	mm	0.50	0.50
$\log_{10} C$	Normal	[N, mm]	-12.74	0.11
B	Normal	-	1.00	0.30
a_d	Exponential	mm	$E(a_d)$	$E(a_d)$

3 MAINTENANCE STRATEGY

The adopted maintenance strategy is such that cracks detected by inspections will be repaired immediately, which is widely applied in engineering maintenance [2-4]. The repair method used in this paper is fixed, and out of the decision-making process. It is assumed that after repair, crack size returns to its initial distribution. The latter is also widely adopted in the literature [3, 5, 6]. This is a relatively reasonable assumption, as it considers imperfect effect of repairing, i.e. there is still a failure probability associated with the repaired structure within the required service life. The decisions that need to be made include inspection methods and times in the lifetime, which affect lifetime fatigue reliability and expected LCC. Optimum inspection decisions are subjected to uncertain crack sizes and uncertain inspection results. Under the aforementioned maintenance strategy, there can be two possible inspection results: ‘detection’ and ‘no detection’. Therefore, at a planned inspection time, to be optimized, there can be three scenarios:

- S1: Failure has already occurred
- S2: The structural detail has survived, and an inspection is carried out. Cracks are detected and repaired.
- S3: The structural detail has survived, and an inspection is carried out. There is no detection and thus no further action

Figure 3 shows the decision tree analysis for one maintenance intervention. The small round circles in the figure are chance nodes. By decision tree analysis, the occurrence probability of each branch at the nodes can be

calculated as well as the lifetime failure probability associated with each scenario.

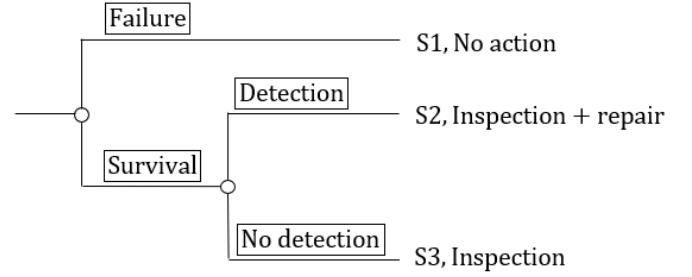


Figure 3. Decision tree analysis for one maintenance intervention.

4 INSPECTION UNCERTAINTY

For maintenance, inspection actions are carried out to provide additional information on crack damage states, in addition to initial crack growth prediction with Paris law, both of which form basis for repair decision. As for fatigue crack detection, commonly adopted inspection methods are (close) visual inspection and NDT methods, e.g. liquid penetrant, ultrasonic, magnetic particle, and acoustic emission inspection methods.

Crack detection by NDT methods is inherently probabilistic, as there are many factors that can influence inspection results. Sometimes existing cracks cannot be identified. Conversely, a positive indication may be false due to the absence of a crack. It is also often found that an existing crack can be detected by one inspector but can be missed by other inspectors. NDT results depend on the reliability of the specific instrument-human system. Generally, the following factors can influence the chance of crack detection:

- Crack characteristics (sizes, shape, location, etc.);
- The reliability of instrumentation
- The environment where inspection is carried out;
- Inspection procedure;
- Human factors associated with inspector.

To utilize information provided by inspection results, reliability of the instrument-human system and confidence level on inspection results must be adequately demonstrated in terms of the level of accuracy that inspection results can represent the true crack characteristics. The reliability of an inspection method is often characterized by a PoD curve. PoD is defined as the probability that a given crack of a fixed size can be detected by a given inspection method.

PoD curves for inspection methods is traditionally obtained by inspection experiments on structural details of a range of crack sizes. Based on inspection results, an appropriate function is assumed for the PoD curve, and parameters of the function are estimated by statistical methods. Confidence range on the PoD can also be specified based on estimated parameters. The experimental approach is typically very expensive and time-consuming as there are so many factors that can affect the probability of detection. Nowadays, simulation approaches are also developed to obtain PoD curves [7-9]. In this paper, the exponential PoD function given by Equation (4) is employed.

$$PoD(a) = F(a) = 1 - \exp(-a/E(a_d)) \quad (4)$$

where $E(a_d)$ is the mean detectable crack size.

Using this function, uncertainties associated with inspection quality are taken into account by modelling the detectable crack size a_d of an inspection method as a variable. The PoD function is actually the cumulative density function (CDF) of the variable a_d .

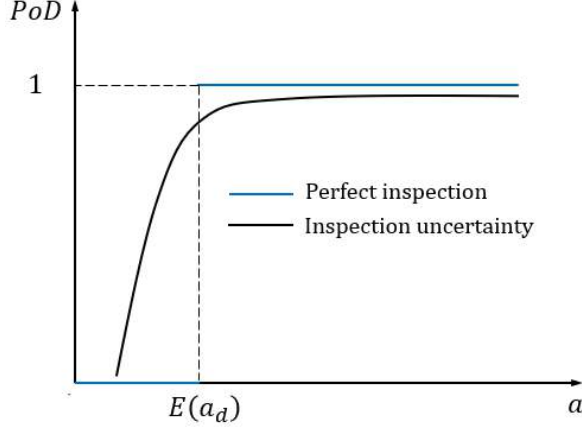


Figure 4. Probability of detection (PoD) curves ('Inspection uncertainty' & 'Perfect inspection' mean inspection uncertainty is considered and not considered respectively).

To investigate the influence of inspection uncertainty on optimum maintenance decisions, comparative studies are carried out while considering and neglecting inspection uncertainty respectively in maintenance optimization. Two different kinds of PoD functions are applied, as shown schematically in Figure 4. The first one is the above exponential PoD function, which provides means to consider inspection uncertainty by predicting a specific detection probability for any given crack size. The other PoD function is defined as below.

$$PoD(a) = \begin{cases} 0 & a < E(a_d) \\ 1 & a \geq E(a_d) \end{cases} \quad (5)$$

Equation (5) assumes that cracks equal to or larger than $E(a_d)$ will be detected with a probability of 1, which means perfect detectability for those cracks. Equation (5) also implies that the detectable crack size a_d of an inspection method is a constant value $E(a_d)$.

5 FATIGUE RELIABILITY

5.1 Initial reliability

Herein failure of the structural detail is defined as occurrence of through-thickness crack, i.e. the critical crack size is equal to plate thickness (Equation (6)).

$$a_c = T \quad (6)$$

The limit state function is given by Equation (7).

$$M(t) = a_c - a(t) \quad (7)$$

where $M(t) < 0$ signifies fracture failure. The critical crack size a_c is set to be equal to the plate thickness T , as failure is

defined as occurrence of through-thickness crack. Failure probability P_f and reliability index β are given by Equation (8) and (9) respectively.

$$P_f(t) = P(M(t) < 0) \quad (8)$$

$$\beta(t) = -\Phi^{-1}(P_f(t)) \quad (9)$$

where Φ is cumulative distribution function of standard normal distribution.

Based on Equation (7), the initial failure probability and reliability index without maintenance at each service year can be calculated by reliability methods. In this paper, Monte Carlo simulation has been adopted, and the decline of reliability index with service year is shown by Figure 5. It can be seen that the reliability index at the end of required service life (lifetime reliability index) is $\beta_0 = 1.050$. The reliability is low, and thus in-service inspection and maintenance actions are needed.

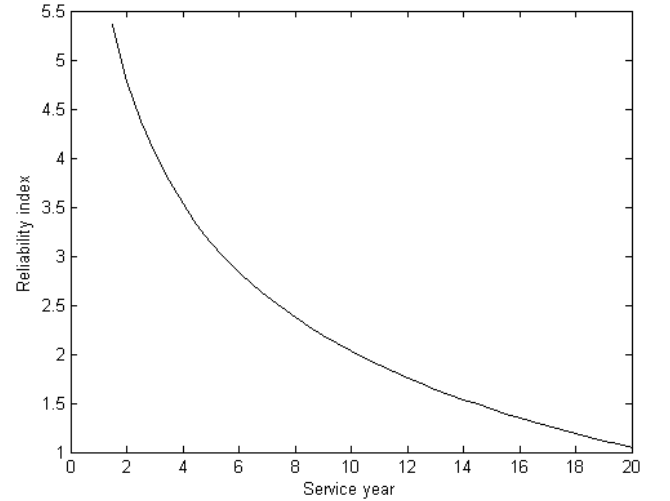


Figure 5. Decline of reliability index with service year.

5.2 Reliability with planned maintenance

Planned maintenance helps to increase lifetime fatigue reliability. Based on the decision tree analysis of Figure 3, if cracks were detected, they are repaired in time, and lifetime failure probability will decrease. If the inspection result was no detection, lifetime failure probability will also decrease taking the additional information of no detection into account. Based on Figure 3, lifetime failure probability with one planned maintenance intervention can be calculated by Equation (10).

$$P'_f(t_i) = \sum_{s=1}^3 P_s \cdot P_{f|s} \quad (10)$$

where t_i is the planned inspection time, P_s is the probability of scenario s occurs, and $P_{f|s}$ is the failure probability conditional that scenario s occurs.

Equation (11) gives the updated lifetime reliability index.

$$\beta'(t_i) = -\Phi^{-1}(P'_f(t_i)) \quad (11)$$

6 EFFETIVENESS OF IMPERFECT INSPECTION

Three inspection methods have been applied to investigate the effect of inspection quality: magnetic particle inspection (MPI), close visual inspection (CVI), and visual inspection (VI). The mean detectable crack size $E(a_d)$ for the inspection methods is based on Madsen et al. [5] and Dong and Frangopol [7]. With each inspection method, two PoD functions as described in Section 4 have been adopted, and the max reliability indexes corresponding to the PoD functions have been derived. Equation (12) defines the effectiveness of a planned inspection.

$$\eta = \beta'_{iu,max} / \beta'_{pi,max} \quad (12)$$

where $\beta'_{iu,max}$ is the max lifetime reliability under the scenario ‘inspection uncertainty’, i.e. inspection uncertainty is considered by using Equation (4); $\beta'_{pi,max}$ is the max lifetime reliability under the scenario ‘perfect inspection’, i.e. inspection uncertainty is not considered, and Equation (5) is used.

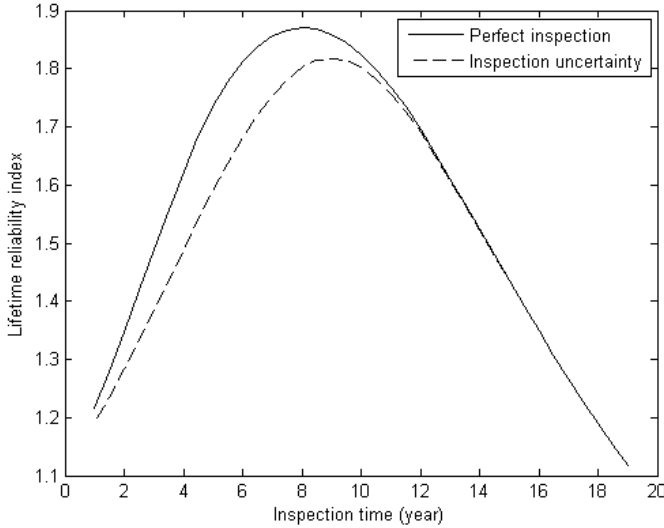


Figure 6. Lifetime reliability index against inspection time (MPI).

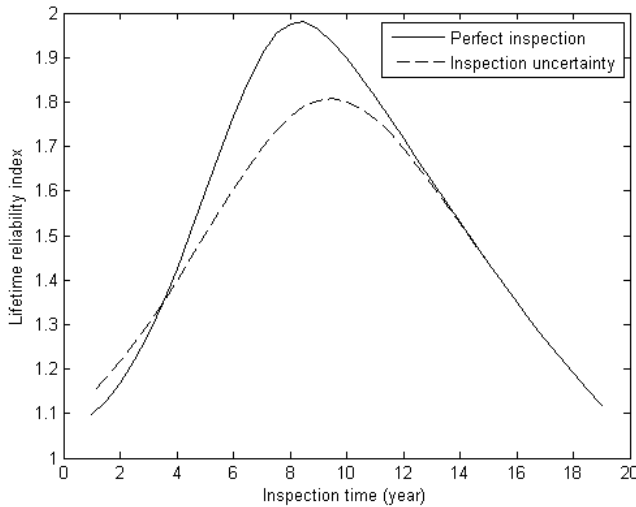


Figure 7. Lifetime reliability index against inspection time (CVI).

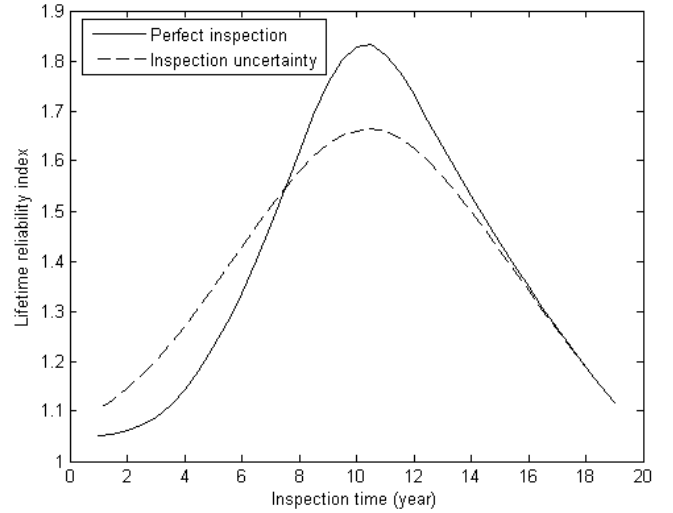


Figure 8. Lifetime reliability index against inspection time (CI).

Table 3. Effectiveness of a planned inspection.

Method	$E(a_d)$	$\beta'_{pi,max}$	$\beta'_{iu,max}$	η
MPI	0.89mm	1.871	1.818	0.972
CVI	2.00mm	1.979	1.807	0.913
VI	4.35mm	1.832	1.664	0.908

Figure 6-8 give lifetime reliability index against planned inspection time for the three inspection methods under investigation. Table 3 summarizes the results. Based on the figures and table, it is concluded that the max lifetime reliability index generally decreases when inspection uncertainty is considered for all the three inspection methods. However, if an inspection is scheduled at the late stage of service life, inspection uncertainty has little influence on the lifetime reliability index. The lifetime reliability index can be higher when inspection uncertainty is considered than neglected, if CVI or VI is adopted, and an inspection is scheduled at the early stage of service life. The effectiveness of a planned inspection increases with the decrease of $E(a_d)$. When considering inspection uncertainty, the effectiveness of a planned inspection adopting MPI is higher than adopting CVI and VI.

7 CONCLUSIONS

Maintenance optimization is important, for engineering structures with a substantial number of fatigue-prone details and locations, in terms of increasing operational reliability and decreasing maintenance costs. The main challenge for maintenance decision-making is uncertain damage states in service life. In this regard, in-service inspections are assigned to gather information on damage states. However, there is an unavoidable uncertainty associated with an inspection method, which may affect maintenance optimization.

The influence of inspection uncertainty on reliability-based maintenance optimization has been studied by explicitly modelling the uncertainties associated with crack growth rate, initial crack size, stress calculation, and inspection quality. The inspection quality of an inspection method is

characterized by the detectable crack size. A new PoD function has been proposed for perfect inspection quality, i.e. without a consideration on inspection uncertainty. The PoD function serves as a comparison to the PoD function that models the inspection quality as a variable. The effectiveness of a planned inspection has been defined base on the max lifetime reliability index while considering and neglecting inspection uncertainty.

It has been shown that the max lifetime reliability index generally decreases when inspection uncertainty is considered. However, inspection uncertainty may have little influence on the lifetime reliability index depending on the planned inspection time. The effectiveness of a planned inspection increases with the decrease of the mean detectable crack size.

ACKNOWLEDGMENTS



The authors would like to express their gratitude to the European Union's Horizon 2020 research and innovation programme for their funding toward this project under the Marie Skłodowska-Curie grant agreement No. 642453 (<http://trussitn.eu>).

REFERENCES

- [1] Moan, T. (2011), 'Life-cycle assessment of marine civil engineering structures', *Structure and Infrastructure Engineering*, 7(1-2), 11-32.
- [2] Kim, S., Soliman, M., and Frangopol, D.M. (2013), 'Generalized Probabilistic Framework for Optimum Inspection and Maintenance Planning', *Journal of Structural Engineering*, 139(3), 435-447.
- [3] Soliman, M., Frangopol, D. M., and Mondoro, A. (2016.), 'A probabilistic approach for optimizing inspection, monitoring, and maintenance actions against fatigue of critical ship details', *Structural Safety*, 60, 91-101.
- [4] Valdebenito, M. A. and Schuëller, G. I. (2010), 'Design of maintenance schedules for fatigue-prone metallic components using reliability-based optimization', *Computer Methods in Applied Mechanics and Engineering*, 199(33), 2305-2318.
- [5] Madsen, Torhaug, H., R., and Cramer, E. (1991), 'Probability-based cost benefit analysis of fatigue design, inspection and maintenance', *Proceedings of marine structural inspection, maintenance and monitoring symposium*, 18-19.
- [6] Zou, G., Banisoleiman, K., and González, A. (2018), 'Value of inspection in steel structural integrity management', *IOP Conference Series: Earth and Environmental Science*, 146(1), 012080.
- [7] Wall, M., Wedgwood, F., and Burch, S. (1998), 'Modelling of NDT reliability (POD) and applying corrections for human factors', *Proceedings of the 7th European Conference on NDT*, Copenhagen, Denmark.
- [8] Wall, M., Burch, S., and Lilley, J. (2009), 'Review of models and simulators for NDT reliability (POD)', *Insight-Non-Destructive Testing and Condition Monitoring*, 51(11), 612-619.
- [9] Volker, A., Dijkstra, Terpstra, F., Heerings, S., H., and Lont, M. (2004), 'Modeling of NDE reliability: Development of a POD generator', *Proceedings of the 16th World Conference on Nondestructive Testing*.
- [10] Dong, Y. and Frangopol, D. M. (2016), 'Incorporation of risk and updating in inspection of fatigue-sensitive details of ship structures', *International Journal of Fatigue*, 82, 676-688.

Reduction of uncertainties associated to the dynamic response of a ship unloader

Giulia Milana^{1,2}, Kian Banisoleiman¹, Arturo González²

¹Lloyd's Register, Global Technology Centre, Southampton, UK

²School of Civil Engineering, University College Dublin (UCD), Dublin, Ireland

email: giulia.milana@lr.org, giulia.milana@ucdconnect.ie, kian.banisoleiman@lr.org, arturo.gonzalez@ucd.ie

ABSTRACT: Here, the TRUSS (Training in Reducing Uncertainty in Structural Safety) ITN (Innovative Training Network) Horizon 2020 project (<http://trussitn.eu>, 2015-19) demonstrates how the accuracy of residual life assessment predictions can be improved by achieving a good agreement between measured and predicted dynamic responses of a crane structure. Existing records of measured strain data are often missing information such as the weight of the payload, the hoisting speed and acceleration that are relevant for structural assessment purposes. This paper aims to reduce uncertainties associated with the recorded data in an aged grab ship unloader by comparing measured and non-linear transient finite element analyses results for a loading/unloading cycle. The speed pattern is determined from a best match to the measured record. The moving load consisting of 'trolley + grab + payload' is modelled with parameters that are derived from minimizing differences between measured and simulated responses. The determination of these loading parameters is central to accurately assess the remaining life of ship unloaders.

KEY WORDS: Ship unloader; Dynamics; Uncertainties; Reconciled model.

1 INTRODUCTION

Ship unloader quay side cranes are a fundamental link in the maritime freight/cargo transport system, allowing ports to comply with rising trade demand. This is only possible by ensuring full operational reliability of these cranes that will minimize unscheduled maintenance and maximising safety. The quay side operating environment and variations in load duty cycles, specifically at the times of increased trade, is contributory to fatigue damage and deterioration of capacity of these cranes. Thus, when not adequately maintained, this could potentially lead to unexpected and costly downtime. In this application the weight of the cargo is 52% of the weight of the lifting boom, therefore, an understanding of the operational behaviour of these cranes in terms of loading, capacity and structural response dependency to lifting, moving, positioning and releasing cargos (as held in a grab or a container) is needed to address fatigue damage evaluation and hence improve maintenance planning, cost and safety. In practice, retrospective relevant information to achieve an accurate understanding of the operational behaviour (for fatigue damage evaluation) may be missing. This paper presents an example of such a case and presents a method of reducing uncertainty and better understanding of the loading duty cycle.

1.1 The structure

Figure 1 shows the subject ship unloader, highlighting the structural members more relevant to this study. In fact, focusing on the structural response due to loading/unloading cycle, the lifting boom is considered to be the most representative structural element [1]. Therefore, an equivalent model of the boom was used to carry out the transient dynamic analysis. Since, the interaction between the lifting boom and the waterside ties (outer and inner ties in Figure 1)

strongly influences the overall behavior, it is important to take this interaction into account when building the model.

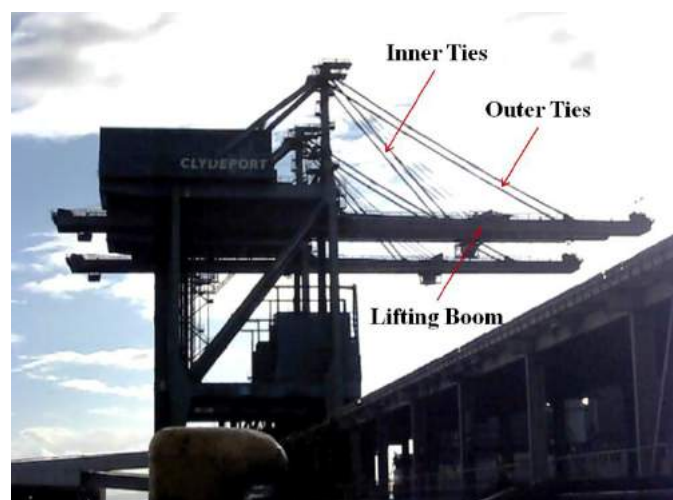


Figure 1. Location of boom and ties in a ship unloader.

The structure analyzed, was a 34 years old grab ship unloader, based in Scotland, used for unloading coal. The coal is carried by a grab attached to the main trolley, which is travelling backwards and forwards along the boom. Its maximum travel range extends from 18 m landside to 48 m waterside, from the front leg. However, the trolley could be covering a reduced travel range, which varies depending on the vessel unloaded [2].

In 2012, a monitoring system, consisting in 48 channels of strain, was installed on the structure to record the data while unloading operations on different vessels. The transducers were installed at 16 locations: one on each waterside and

landside tie, leg and lateral tie; one on each side of the rear and lifting boom. Among them, the one corresponding to the south side of the lifting boom (Fig. 6) is here analyzed in detail. Figure 2 shows the vertical bending stress at this location, obtained from the variation in strains recorded for one sample of the data (10-minute acquisition binary file). It is worth noting that the transducer, from which these measurements were obtained, was installed at approximately 27 m waterside from the front leg. The stresses corresponding to not-in-operation conditions (from 240s to 340s in Figure 2), were subtracted from those obtained while the unloader was in operation, unloading a vessel. The latter allows removing the effect of strain due to environmental effects such as temperature from the total measured strain due to both environmental effects and loading.

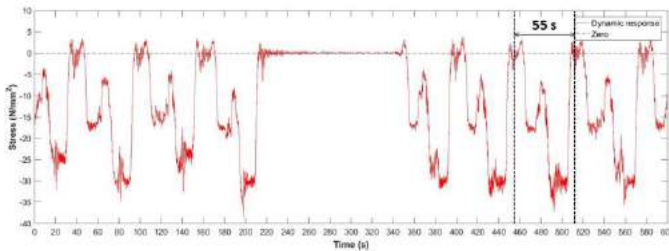


Figure 2. Vertical bending stress in the lifting boom while unloading a vessel (10 minute recorded data).

In this case, information recorded regarding location, speed and actual weight of the trolley payload over the monitoring period was not available. As can be seen from Figure 2, each loading cycle took approximately 55 s. One of these load cycles has been analysed in detail, in the following sections, to estimate the missing information from the recorded data.

2 THEORETICAL MODEL

The missing information associated with the operation of the ship unloader can be estimated through a comparison between the recorded data and the results obtained from a transient dynamic analysis, which couple a simplified model of the lifting boom (Section 2.1) and one of the moving system: trolley + grab + payload (Section 2.2) as exemplified below.

2.1 Equivalent model of the boom

A simplified model of the lifting boom is used to analyze the transient dynamic response resulting from one loading/unloading cycle. Given that the waterside ties (outer and inner ties in Figure 1) strongly influences the response of the boom, their interaction is taken into account via the addition of equivalent spring and mass elements at the connection points following Zrníc et al. [1]. Figure 3 shows the 2D Finite Element (FE) model of the lifting boom used for the calculations. The pinned end of the model represents the location at which the lifting boom is pinned joint to the rear boom (1.35 m waterside from the front leg). The total length of the model between the pinned support and the free end is 51 m. The model is discretized into 34 beam elements and has a total of 105 Degrees of Freedom (DOFs). The inner and outer cables are connected to the boom at 19.5 m and 42 m respectively from the pinned support. The section of the boom

has an area of 0.074718 m² and inertia of 0.028232 m⁴. A lumped mass M_1 and a spring k_1 are located at DOF no. 41 and a lumped mass M_2 and a spring k_2 are located at DOF no. 86. The vertical springs model the stiffness of the upper substructure, and the two lumped masses take into account the weight due to the waterside ties and other components not explicitly modelled. The FE model is built using MATLAB [3].

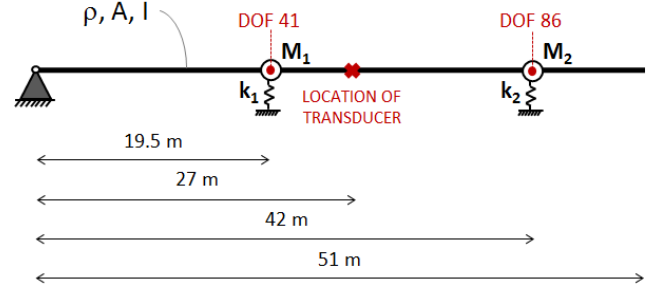


Figure 3. Equivalent 2D model of the lifting boom.

2.2 Model of the moving system

Due to the impact of the trolley-boom interaction on the dynamic response of the structure, different ways of modelling the moving system were preliminarily examined [4]. Here, the moving load is composed by two masses (m_T and m_P) connected by a linear spring (k_S) (Fig. 4). An illustrative stiffness of 10⁶ N/m was assumed for the spring connecting the two masses, to model a sufficiently elastic connection [5].

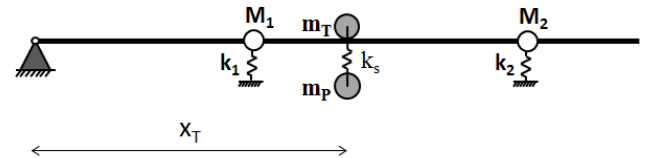


Figure 4. Model of the moving load and hoisting location x_T .

3 RECONCILED MODEL

The parameters, characterizing the equivalent model of the boom, were defined through a comparison with a 3D model of the structure, built in ANSYS APDL [6]. Thus the 2D MATLAB model was reconciled in terms of vertical bending stresses and deflections, through static analyses, and for its natural frequencies and mode shapes, through modal analyses.

3.1 3D ANSYS Model & 2D MATLAB Model

Figure 5 shows the three-dimensional FE model, used to reconcile the 2D MATLAB model. The primary structural members were modelled using beam elements; while the influence of the secondary members (i.e. the lift, the machinery room etc.), not explicitly modelled, was taken into account by introducing additional point masses and adjusting the material density of the primary members.

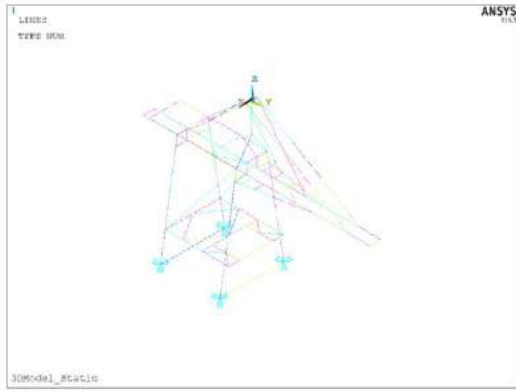


Figure 5. 3D ANSYS model of the ship unloader.

A modal test was conducted on the real structure, and two frequencies of the upper substructure only obtained carrying out an Operational Modal Analysis (OMA). The identified modes had frequencies of 0.78 Hz and 0.91 Hz, respectively. Even though the modal analysis carried out on the 3D model interested the whole structure, the two modes from the OMA were predicted by the FE model with an error of 5%. In fact, the frequencies for the two modes considered were 0.74 Hz and 0.86 Hz. The modes shape of the latter mode is shown in Figure 6, together with that provided by OMA.

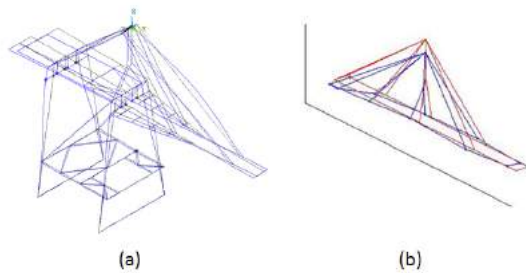


Figure 6. Mode shape for the upper substructures: (a) 3D model in ANSYS and (b) from OMA.

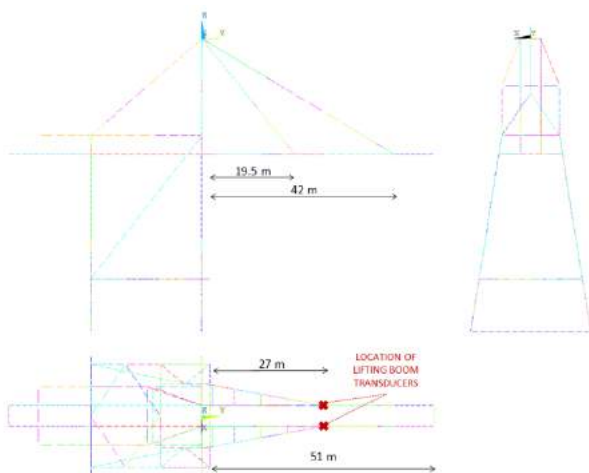


Figure 7. Side, front and top view of the 3D model, with measurements related to the lifting boom and location of the transducers on it.

Figure 7 gives side, front and top view of the 3D model, and shows the measures characterizing the 2D Model (Fig. 3). In addition the location of the transducers (shown by the two red marks) is the location at which all the results will be obtained in the following sections.

3.2 Static analysis

The remaining parameters of the equivalent model of the boom (ρ , M_1 , M_2 , k_1 , k_2) were evaluated in order to reduce the scatter between the static results from the 3D model and those from the 2D one. The static analyses were carried out considering both the case with and without gravity. In addition, different load scenarios were considered, applying one point load at the time, at different locations along the boom. Two load scenarios are presented here: force applied at vertical degree of freedom DOF 41 and DOF 86 corresponding to locations at the springs (Fig. 3).

3.2.1 Stiffness of the springs

The two spring stiffnesses (k_1 and k_2) were evaluated by carrying out a comparison in terms of vertical bending stress, considering the scenario with gravity off. In fact, the data obtained from the monitoring system provides the variation in strain (i.e. stress) due to the application of loads. This information excludes residual stress due to the dead-load.

An iterative process led to $k_1 = 46889939.89 \text{ N/m}$ and $k_2 = 31004369.51 \text{ N/m}$. Having evaluated the relationship between the two stiffnesses (k_1 and k_2), in order to obtain the desired stress trend, their values have been proportionally increased until matching the maximum values of the bending stresses.

Figure 8 shows the bending stresses for both models, for the two load scenarios, introducing the aforementioned stiffnesses. It is easy to notice the correlation between the stresses obtained from the 3D model (solid lines) and those from the 2D one (dashed lines).

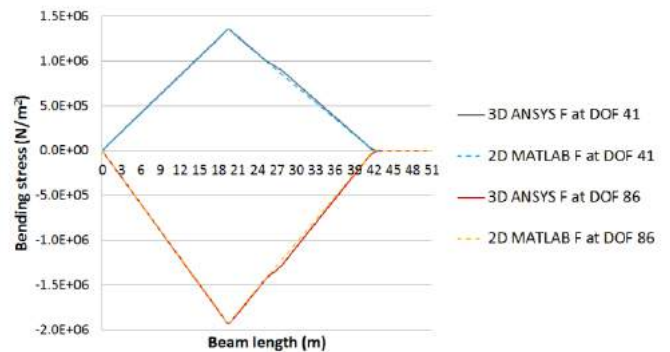


Figure 8. Static vertical bending stresses for 3D and 2D models, for the two load cases without dead-load.

3.2.2 Density and lumped masses

Conversely, the values of the material density, to be assigned to the beam, and of the two lumped masses (M_1 and M_2) were evaluated based on a comparison in terms of deflections. The same load cases were considered, but this time including the dead-load (gravity on). Minimizing the

scatter between the displacements from the 3D model and those from the 2D one, led to $\rho = 15713.27 \text{ kg/m}^3$, $M_1 = 83423.56 \text{ kg}$ and $M_2 = 122844.78 \text{ kg}$.

The small discrepancy in deflections, between 2D and 3D models can be seen in Figure 9.

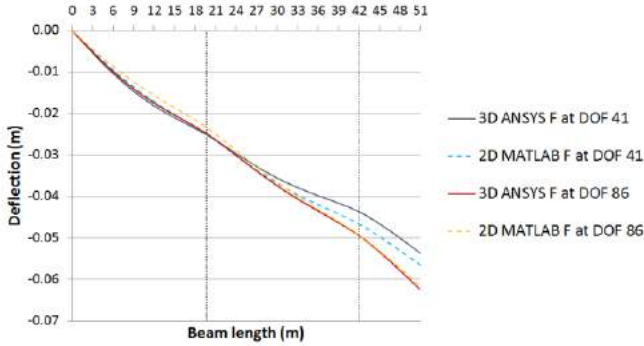


Figure 9. Static deflections for 3D and 2D models, for the two load cases with dead-load.

As can be noticed from the graph (Fig. 9), the scatter increases with increasing distance of the observation point from the location at which the load was applied (showed by the two dashed lines in Figure 9). Highest accuracy was achieved location at which the load was applied. Since the maximum displacement always occurs at the right hand side (free end) of the beam, the 2D model was consistently more conservative in terms of displacements, even when the force was applied at other locations on the beam.

3.3 Dynamic analysis

3.3.1 Natural frequencies and mode shapes

Once all the parameters for the 2D model were evaluated, an additional verification was conducted in terms of natural frequencies and modal shapes. Figure 10 shows the modal shapes for the first three modes, obtained using the 3D model. In order to carry out an effective comparison, additional constraints were introduced in the 3D model, to restrict the modes in the third dimension (not modelled in the 2D model); furthermore, the modes considered were only those affecting the lifting boom.



Figure 10. First three modal shapes for the 3D model in ANSYS.

Figure 11 shows the mode shapes, for the first three modes, of the simplified 2D model. It can be seen that there is good correspondence between the two models.

In addition, close agreement in the values of the natural frequencies for the first three modes, presented in Table 1, corroborate the correlation between the two models.

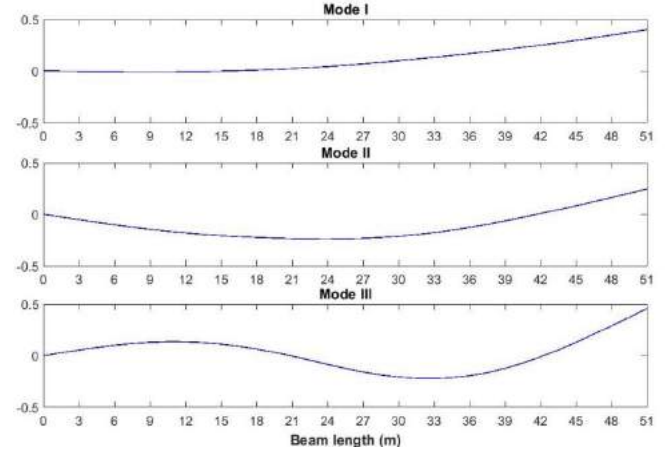


Figure 811. First three modal shapes for the 2D model in MATLAB.

Table 1. Comparison in terms of natural frequencies between the 3D and 2D models.

MODE	NATURAL FREQUENCIES		Error (%)
	3D ANSYS Model	2D MATLAB Model	
I	2.32	2.33	0.43
II	3.44	3.39	1.45
III	6.30	6.30	0

Thus, the parameters defined for the simplified two-dimensional model were considered fitting and the MATLAB model able to provide a satisfying prediction of the real behavior of the structure, even though in a simplified form.

4 FITTING

The dynamic response of a ship unloader due to loading/unloading cycles is influenced by a number of factors, such as the weight, travelling and hoisting speeds and acceleration/deceleration of the payload. Carrying out a non-linear transient dynamic analysis using the 2D model allowed fitting the resultant stresses with the measured one, with the aim to estimate the most significant factors affecting the stress variations. The response was obtained by applying Wilson Theta step-by-step integration method [7]. A Rayleigh damping, as shown by Equation 1, was evaluated.

$$C = \eta M + \delta K \quad (1)$$

Assuming a damping ratio ξ for the two frequencies (ω_i and ω_j) equal to 0.75%, the values of η and δ are evaluated from Equation 2 [8].

$$\delta = \frac{2\xi}{\omega_i + \omega_j} \quad \text{and} \quad \eta = \frac{2\xi \omega_i \omega_j}{\omega_i + \omega_j} \quad (2)$$

The weights of the main trolley and of the empty grab are $m_T = 8000 \text{ kg}$ and $m_g = 10500 \text{ kg}$, respectively.

4.1 Dynamic response from the monitoring system

Focusing on one single cycle extrapolated from the response shown in Figure 2, the recorded stress values were analysed to determine the missing information. Figure 12 shows, both the dynamic vibratory and the mean response of stress for a single loading cycle, obtained by filtering the recorded data. The latter was obtained applying an 8th order Chebyshev Type I low-pass filter, with a cut-off frequency of 0.4 Hz.

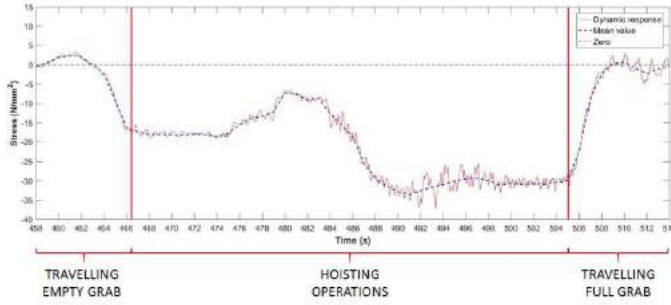


Figure 12. Measured dynamic stress, at transducer location (27 m), of the lifting boom due to a single unloading cycle.

As shown here, three main operating phases have been identified:

- Traveling empty grab (horizontal motion only; the main trolley, carrying the empty grab, is moving from above the hopper to the hoisting location,)
- Hoisting operation (vertical motion only; the empty grab is lowered, it is filled with coal and finally lifted), see section 4.1.2 and Figure 15 for more information on hoisting operation.
- Travelling full grab (horizontal motion only; the main trolley, carrying the filled grab, is moving from the lifting boom towards the hopper, where the coal is dropped)

In the following sections, each phase is illustrated more in detail.

4.1.1 Travelling empty grab

The 2D model, built in MATLAB, resembles part of the travelling range of the main trolley, specifically the section extending waterside from the front leg [4]. Thus, it was assumed that once the trolley reached the pinned connection of the boom, its speed stabilized at a constant value, before starting braking and arriving to a stop at the hoisting location (Fig. 13).

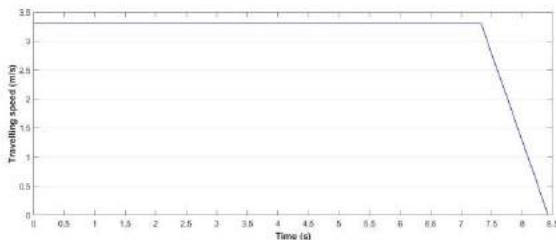


Figure 9. Travelling speed profile assumed for the 'Travelling empty grab' phase.

Since it was noticed that the change in deceleration did not entail a significant change in the response, the two main

variables to be defined were the travelling speed (v_T) and the distance (measured from the left hand side of the beam), at which the trolley stops at (x_T) (Fig. 4). The former was evaluated by taking into account the time period (5.0 s) until the bending stress crossed the zero line. It was observed, from previous static analysis, that there was a sign inversion in the bending stresses when the load was applied at a distance of 16.5 m or more from the joined end. Hence, a travelling speed of (16.5 m/5.0 s) 3.3 m/s was derived. A realistic deceleration of 3m/s^2 was assumed. Carrying out static analysis for different load locations, a trend line between the location of the load (x in Eq. 4) and the maximum stress at the location where the transducer is installed (y in Eq. 4) was extrapolated.

$$y = -0.0954 x^2 + 2.129 x - 7.8911 \quad (4)$$

Introducing, in Equation 4, the maximum filtered mean response, for the 'Travelling empty grab' phase, the hoisting location was estimated: $x_T = 26 \text{ m}$.

4.1.2 Hoisting operation: profile force

During hoisting operation, it was assumed that the main trolley was stationary at $x_T = 26 \text{ m}$. Figure 14, upper and lower, shows the speed and force profiles respectively. Since in real operation condition there is an overlap between the travelling and the hoisting phases, it was assumed that the speed at which the grab is lowered (lifted) reached a constant value when the hoisting operation phase, considered here, starts (finishes). It can be seen, that three stages were identified:

- Grab down (the empty grab is lowered until it is grounded)
- Filling grab (the grab is filled with coal)
- Grab up (the filled grab is lifted)

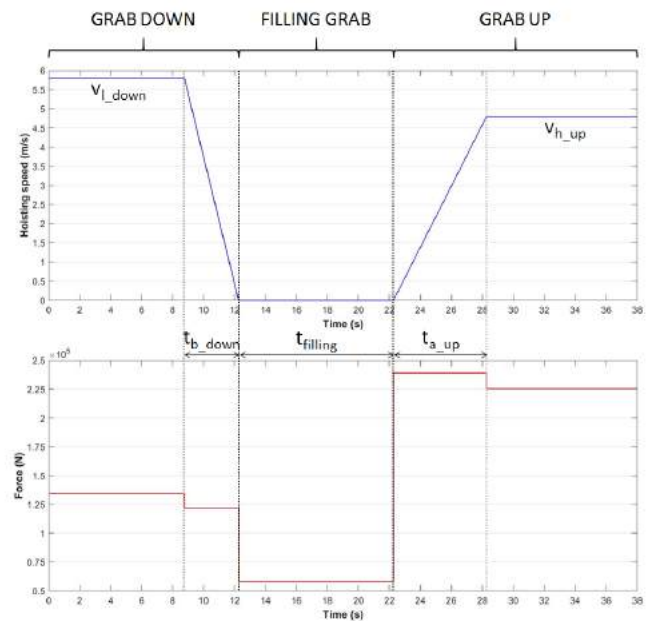


Figure 10. Hoisting speed and force profile respectively, for the 'Hoisting operation' phase.

Considering a range of lift of 61 m, as specified by the available information, the hoisting speed profile shown in

Figure 15 was assumed. The six identified variables were then: lowering speed of the empty grab (v_{l_down}); breaking time to go from constant to zero lowering speed (t_{b_down}); time required for filling the grab with coal ($t_{filling}$); acceleration time to go from zero to constant hoisting speed (t_{a_up}); hoisting speed of the filled grab (v_{h_up}) and mass of the payload (m_p). The latter is the most relevant for future applications; in fact, it was the most influencing variable on the stress range from those listed above (in this paragraph). This stress range is used for the fatigue life assessment procedure as described in the British Standards document [9].

Looking at the times at which the recorded dynamic response encounters steps (Fig. 12), the aforementioned parameters, apart from m_p , can be determined. Once all the above variables had been obtained, the value of the payload mass (m_p) was determined by matching the maximum achievable bending stress. The values are: $v_{l_down} = 5.8 \text{ m/s}$, $t_{b_down} = 3.5 \text{ s}$, $t_{filling} = 10 \text{ s}$, $t_{a_up} = 6 \text{ s}$, $v_{h_up} = 4.8 \text{ m/s}$ and $m_p = 12 \text{ 500 kg}$.

4.1.3 Travelling full grab

The values of the speed and deceleration/acceleration, estimated for the initial phase with empty grab, were assumed to be the same also for the case with filled grab. In fact, looking at real ship unloaders in operation it appears that the travelling system is acting in the same way when carrying full or empty grab. As shown in Figure 15, the speed pattern for this last phase is reversed compare to the case with empty grab.

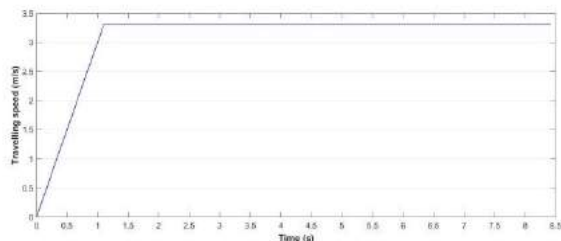


Figure 11. Travelling speed profile assumed for the 'Travelling full grab' phase.

4.1.4 Full cycle

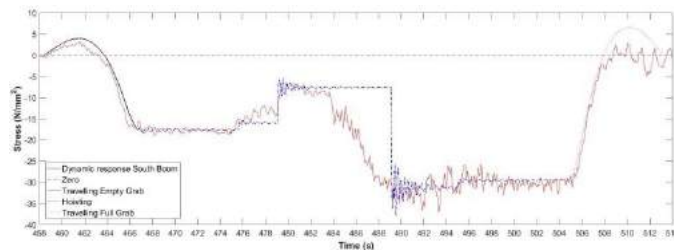


Figure 12. Comparison, in terms of vertical bending stresses, between the dynamic recorded response and that obtained by carrying out transient dynamic analyses in the 2D model.

Even though, in real unloading operation these phases overlap each other, the assumption of a clear separation among them was done here. It provides simple scenarios, to enable matching the main features of the response, as shown in Figure 16. The match over the hoisting operation is the one

mostly affected by neglecting the overlapping; nevertheless, the model is able to predict the maximum variation in stresses.

5 CONCLUSIONS

The data recorded from a monitoring system installed on a ship unloader has been analyzed. Main focus was given to the lifting boom, considered the most representative structural elements in terms of dynamic response. For the latter, a simplified finite element model was built and used to carrying out transient analysis. Once reconciled with the 3D model of the same structure, it has then been shown that fitting the response obtained from the 2D model with the recorded response of the actual structure it is possible to define some variables, often not recorded while the data is captured automatically. Among these the main parameters, influencing significantly the structural response, turned out to be the hoisting location (x_T) and the payload mass (m_p). An accurate estimation of these parameters, and a range of value they can assume, would allow a more reliable assessment of the loading cycles for the structure. In fact, employing a more accurate value of the payload cycles when carrying out the static analyses for fatigue assessment [10], would allow a more accurate estimation of the stress ranges, also at the locations where the transducers are not installed, and consequently a more reliable assessment of the residual life of these structures for integrity assessment.

ACKNOWLEDGMENTS



This project has received funding from the European Union's Horizon 2020 research and innovation programme under the Marie Skłodowska-Curie grant agreement No. 642453

(<http://trussitn.eu>).

REFERENCES

- [1] Znic, N.D., Hoffmann, K. and Bosnjak, S.M. (2009), 'Modelling of dynamic interaction between structure and trolley for mega container cranes' *Mathematical and Computer Modelling of Dynamical Systems*, Taylor & Francis, 15, 295-311.
- [2] Milana, G., Banisoleiman, K. and Gonzalez, A. (2017), 'Field characterization of location-specific dynamic amplification factors towards fatigue calculations in ship unloaders', *Proceedings of 27th European Safety and Reliability Conference (ESREL2017)*, Portoroz, Slovenia.
- [3] MATLAB Release 2016a, *The MathWorks, Inc.*, Natick, Massachusetts, United States.
- [4] Milana, G., Banisoleiman, K. and Gonzalez, A. (2018), 'Impact of a moving trolley on the dynamic response of a ship unloader boom', *Proceedings of 13th International Conference on Steel, Space and Composite Structures, (SS18)*, Perth, Australia.
- [5] Znic, N. D., Gasic, V. M. and Bosnjak, S.M. (2015), 'Dynamic responses of a gantry crane system due to a moving body considered as moving oscillator', *Archives of Civil and Mechanical Engineering*, Elsevier, 15, 243-250.
- [6] ANSYS® Mechanical APDL, Release 14.0.
- [7] Tedesco, J.W., McDougal, W.G. and Ross, C.A., *Structural dynamics: theory and applications*, Pearson, first edition, 1998.
- [8] Wilson, E. L., *Static and Dynamic Analysis of Structures*, Berkeley, fourth edition, 2004.
- [9] British Standards Document 7608, *Code of practice for fatigue design and assessment of steel structures*, 1993.
- [10] Federation Europeenne de la Manutention (FEM) 1.001. *Rules for the Design of Hoisting Appliances*, third edition, 1987.

Nothing on the road axle detection system using direct strain measurements – A case study

F. Huseynov^{1,2}, E.J. OBrien², J.M.W. Brownjohn³, D. Hester⁴, K. Faulkner³

¹Full Scale Dynamics LTD, Kay Building North Park Road, Exeter EX4 4QF, UK

²School of Civil Engineering, University College Dublin, Richview Newstead Block B, Belfield, Dublin 4, Ireland

³Vibration Engineering Section, College of Engineering, Mathematics and Physical Sciences, University of Exeter, North Park Road, Exeter EX4 4QF, UK

⁴School of Natural and Built Environment, Queen's University Belfast, Stranmillis Road, Belfast, Northern Ireland, UK

Email: f.huseynov@fullscaledynamics.com, eugene.obrien@ucd.ie; j.brownjohn@exeter.ac.uk; d.hester@qub.ac.uk; kf312@exeter.ac.uk

ABSTRACT: This paper proposes a new axle detection methodology using direct strain measurements. Initially, numerical analyses are carried out on a 1-D simply supported bridge structure to investigate the strain response of a bridge to a 2-axle moving vehicle. The strain response obtained from the numerical model is further studied and a new axle detection strategy, based on the second derivative of strain with respect to time, is proposed. Having developed the theoretical concept, field testing is carried out on a single span simply supported railway bridge to validate the proposed methodology and test its robustness of on a full-scale bridge.

KEY WORDS: TRUSS, Axle detection; Bridge; Weigh-In-Motion; Strain; Field testing; Railway.

1 INTRODUCTION

Bridges, connecting communities and serving as regional lifelines, are vital components of transport infrastructure. They are designed to maintain their functionality for 75 to 100 years of services life [1, 2]. In most developed countries, the majority of bridges are nearing the end of their designed service lives [3], while the weights and frequencies of freight transport vehicles are increasing. Further, many bridges are being kept in service much longer than they were originally designed for. Therefore, bridge owners are particularly interested in accurate methods of assessing vehicle weight and verifying load carrying capacity of their ageing structures.

Current bridge evaluation specifications are built on available design standards, which contain a certain degree of uncertainty that leads to conservative results. One of the main sources of such uncertainty is associated with traffic loading. Standards cover a wide range of loading conditions whereas every site presents a unique situation and has its own characteristics and requirements. Therefore, to keep aging bridge structures in operation and prevent disruption to traffic, it is desirable to obtain site-specific traffic loading information and evaluate bridge safety accordingly. This can be achieved by installing a Bridge Weigh-In-Motion (B-WIM) system.

A B-WIM system, first proposed by Moses [4], uses the response of a bridge to a traversing vehicle to predict its axle weights. B-WIM consists of a system of sensors, axle detectors and a data acquisition unit. An axle detection system, which identifies the presence of vehicle axles, is used to find the speed and axle spacings and is an indispensable part of the B-WIM system, directly affecting the accuracy of weight predictions.

Early axle detection instrumentation utilised in B-WIM systems included tape switches or pneumatic tubes which were placed on the road surface and may require lane closures for installation. The condition of such systems deteriorates rapidly over time when they are exposed to heavy traffic.

To overcome the complications of lane closures and durability issues inherent in the traditional axle detection systems, a Free of Axle Detection (FAD) approach was proposed in the WAVE project. This utilises strain sensors installed on the bridge, instead of having instrumentation on the road surface [5]. Typically, strain sensors are installed on the soffit of a slab structure under each lane and measure a local strain response of a bridge due to a passage of an axle over the sensor location. However, the FAD approach imposes certain restrictions on the loading conditions and the type of selected deck structure. The method fails to identify the presence of axles if the load is directly applied on the main girders (beams) of a beam-and-slab bridge [6]. FAD is more suitable for short span bridges, short integral bridges with thin slabs, bridges with secondary transverse beams or orthotropic steel deck structures.

To overcome the existing shortfall, some researchers developed efficient post-processing techniques to increase the accuracy of FAD sensors. In [7–9] authors used wavelet transformation techniques to identify closely spaced axles from the FAD signals. The results show that wavelet techniques can improve the accuracy of axle identification for a tandem and tridem group which FAD method fails to identify from direct measurements. Other authors have also developed contactless axle detection methodologies using vision-based system [10, 11].

This paper presents a new axle detection methodology which is based on the second derivative of strain with respect to time. Initially, numerical analyses are carried out on a 1-D bridge model, loaded with two moving loads, to develop the theoretical basis of the proposed axle detection system. Having seen that in theory it is possible to identify the axle locations using the proposed methodology, field testing was conducted on a single span simply supported railway bridge to validate the concept and test the robustness of the proposed methodology on a full-scale bridge. Section 2 develops the theoretical basis of the proposed axle detection system, Section 3 provides specific details of the field testing

conducted on a real bridge and Section 4 presents the results obtained from the experimental study.

2 THEORETICAL BASIS

This section develops the theoretical basis of the proposed axle detection concept. Initially, numerical analyses are carried out on a 1-D simply supported bridge structure to obtain a strain response of the bridge model due to a moving 2 axle vehicle. The hypothetical structure is modelled as a 5.1 m long simply supported steel bridge. The Elastic Modulus and Second Moment of Area are assigned as 210 GPa and $1.23 \times 10^9 \text{ mm}^4$, respectively. The axle weights of the moving vehicle is taken as 3.5 tonnes, spaced at 2.6 m apart. The vehicle travels over the bridge at a speed of 4 m/s. Approach spans, 4 m long, are located at the entrance and exit of the bridge. A hypothetical sensor is placed at 1.1 m from the left-hand support location to 'record' the strain response of the bridge due to the moving vehicle loading. Figure 1 shows a sketch of the 1-D bridge model, axle configuration of the moving vehicle and the location of the strain sensor.

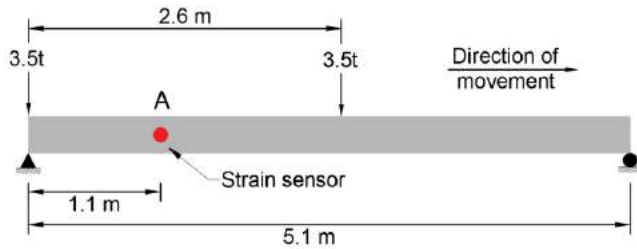


Figure 1. Sketch of the 1-D simply supported bridge model.

Figure 2(a) presents the strain time history obtained from the numerical model due to the two-axle moving vehicle loading. The black curve shows the total response of the structure while the red and blue dashed curves represent the contributions of the individual axles.

The proposed axle detection concept is based on the second derivative of the strain time history signal with respect to time. The strain time history function due to the moving multi-axle loading is a first order conditional polynomial. The first derivative of the first order conditional polynomial with respect to time becomes discontinuous at the points where axles arrive or depart from the bridge or pass the sensor location. The red plot in Figure 2 (b) depicts the corresponding results obtained from the first derivative of the strain time history. Discontinuous functions are not differentiable at locations where there is a lack of continuity so the first derivative of the strain signal with respect to time is taken as continuous. The dashed blue lines in Figure 2(b) represent the corrections to re-establish the continuity of the signal.

Having observed the discontinuity feature in the first derivative of the strain response with respect to time, it is proposed in this study that the second derivative of the strain signal with respect to time, will smooth out the constant part of the function. At locations where the first derivative of the function would normally become discontinuous, this will result in peaks that will identify axle locations.

The corresponding results obtained by differentiating the strain signal twice, is presented in Figure 2(c). There are four

positive and two negative peaks observed in this plot. The positive peaks correspond to the time when an axle enters or exits the bridge whereas negative peaks occur when each axle passes the sensor location. Since the hypothetical sensor is placed on the left-hand side of the bridge, the magnitude of peaks when an axle arrives on the bridge is greater than the magnitude when it leaves the structure.

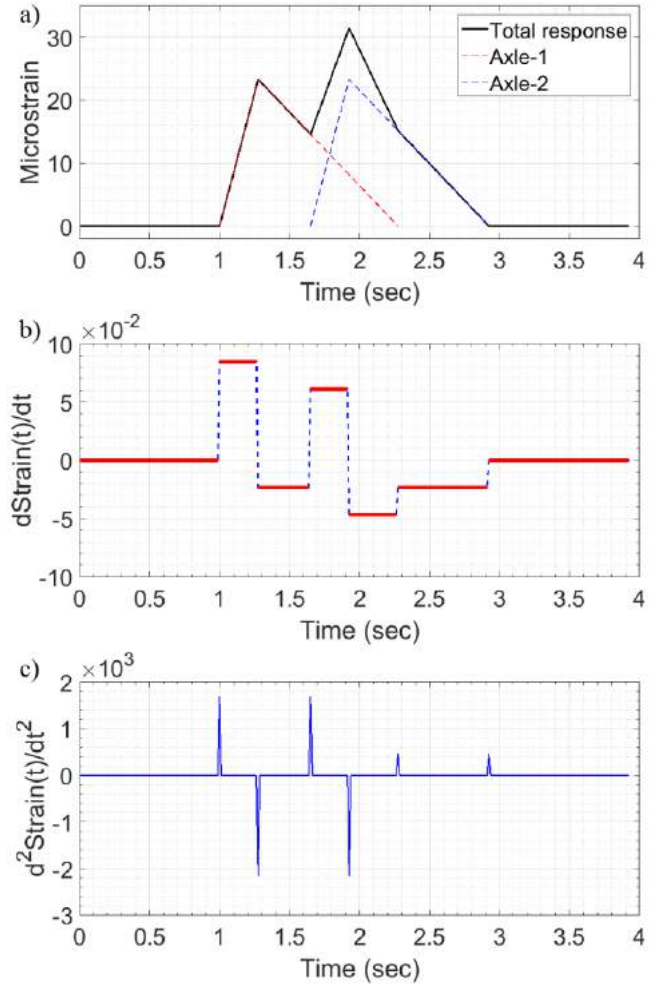


Figure 2. (a) Moment time history obtained at hypothetical sensor location. (b) First derivative of moment with respect to time. (c) Second derivative of moment with respect to time.

3 FIELD TESTING

Having seen that in theory the second derivative of the strain signal can identify the axle locations along the length of a bridge structure, a field test is conducted on a single span simply supported steel railway bridge in an effort to validate the feasibility of the proposed axle detection system. Section 3.1 describes the test structure and Section 3.2 discusses the instrumentation used on the structure and gives specific details about the field testing.

3.1 Test Structure

The test structure is a single span simply supported steel railway bridge located in South West England, UK. The bridge is 5.1 m long and consists of two main girders made of $356 \times 406 \times 235$ UKC beams, placed 1505 mm apart. The main girders are connected with secondary beams made of

254×254×73 UKC beams and are designed only to prevent lateral buckling as they do not carry any load directly from train loading. Therefore, the loads from trains are equally distributed between girders transversely.

The connection between the bridge deck and abutments consists of laminated elastomeric bearings designed to allow free span movement in the bridge longitudinal direction. The bridge is located approximately 50 m away from a train station and carries a single track which rests on top of the main girders. Figure 3 shows the bridge plan view drawings and a photograph of the test site.

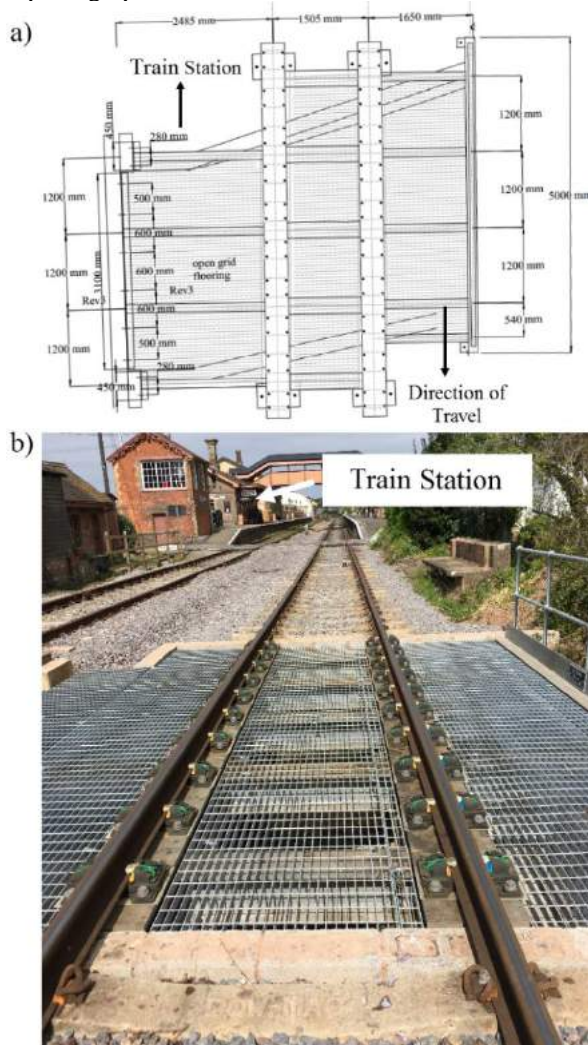


Figure 3. (a) Plan view of the test structure. (b) Photograph of the test site (in foreground).

3.2 Instrumentation and testing

The test structure is instrumented with a strain transducer at 1.1 m from the support location on the train station side of the bridge to record strains under train loading. The strain sensors used during the field testing was developed by a company named Bridge Diagnostics, Inc. (BDI). These are reusable Wheatstone full bridge resistive sensors encased in rugged transducer packages that are mounted on the structure with bolted tabs. The length of the strain transducer is 76 mm. Figure 4 (a) shows the location of the test point and Figure 4 (b) shows a photograph of the strain sensor installed on the bridge.

The strain transducer is connected into an STS4 4-node data acquisition system using wired connection which is wirelessly linked to an STS4-BS-C base station to transfer stored data to a laptop. The data is recorded at a 1000 Hz sampling rate. Based on the gain, excitation and full-scale range of the sensor and software settings, 0.3 micro-strain resolution is determined for the measurement readings.

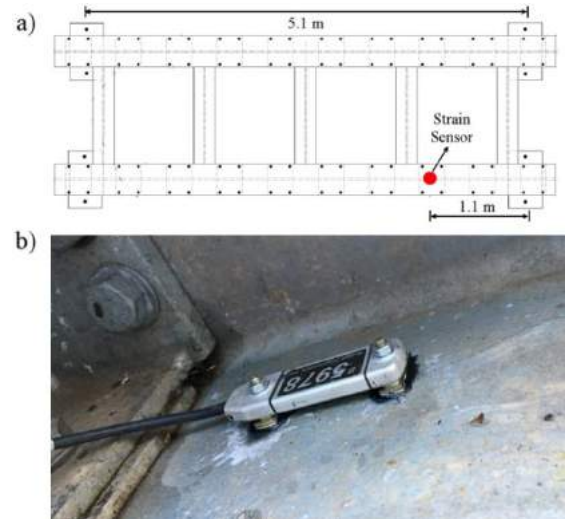


Figure 4. (a) Sketch of the test structure depicting sensor location. (b) Strain transducer installed on the bridge.

The strain data was recorded while a British Class 115 Diesel Multiple Units (DMU) type train crossed the bridge. The train consists of three sets: Two Driving Motor Brake Second (DMBS) cars which are located at the front and rear and a Trailer Composite with Lavatory (TCL) type carriage located in the centre. Each set consists of 2 bogies and each bogie has 2 axles spaced at 2.6 m, adding up to 12 axles in total for the full set of cars. Figure 5 shows a sketch of the DMBS and TCL cars and the British Class 115 type train crossing the test structure

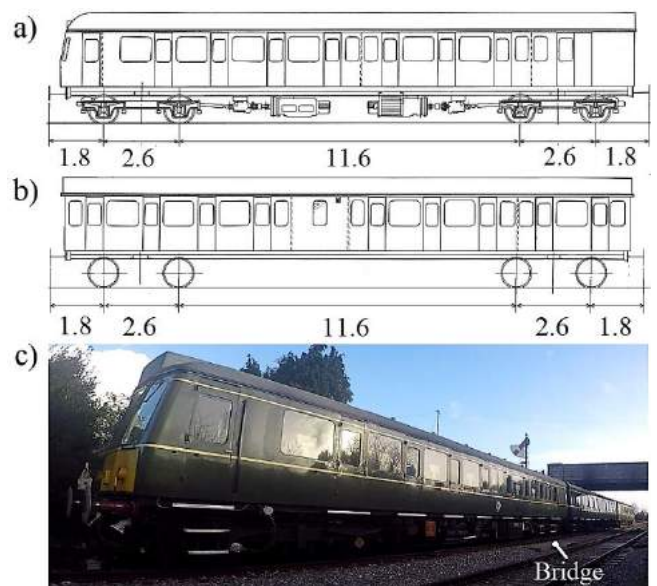


Figure 5. (a) Sketch of the DMBS car. (b) Sketch of the TCL car (c) British Class 115 train crossing the test structure.

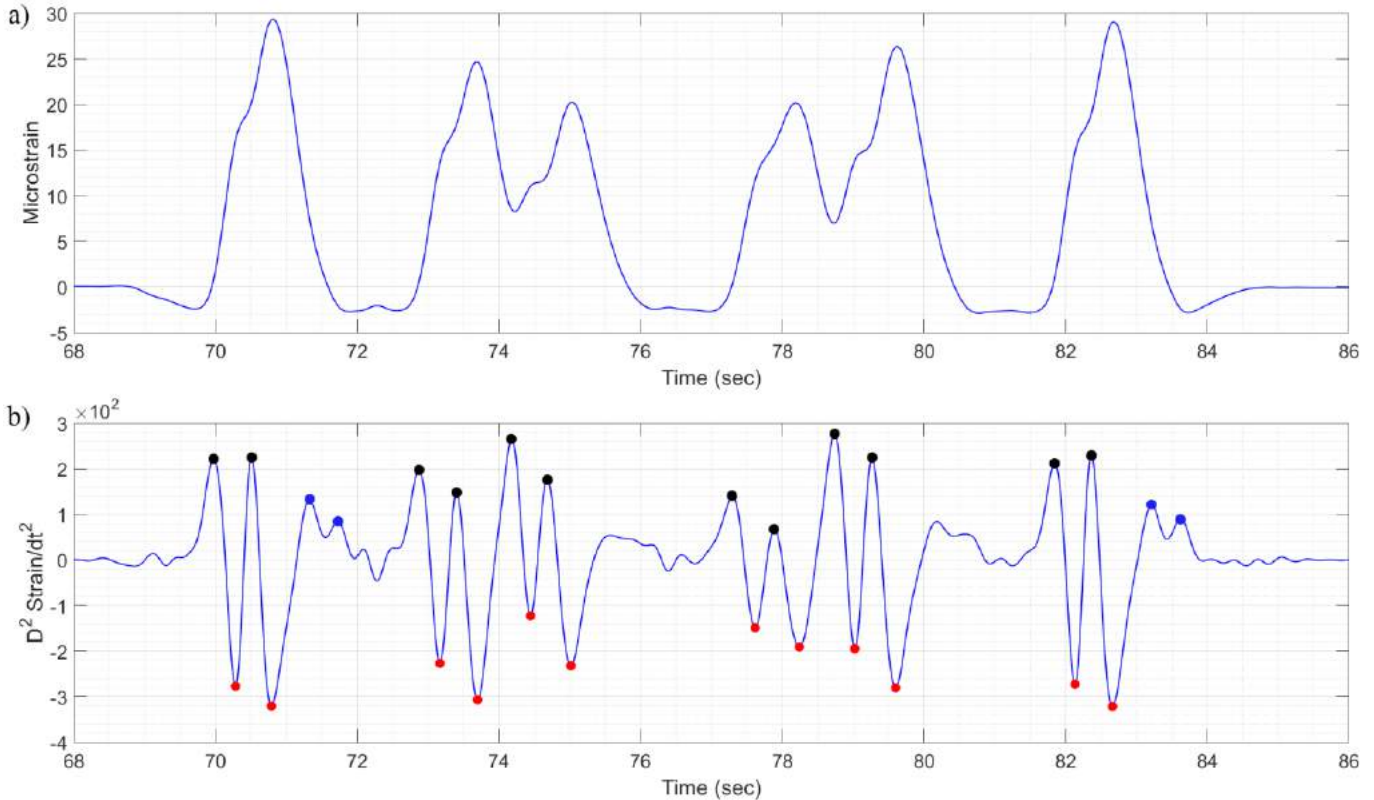


Figure 6. (a) Strain time history recorded under train loading (b) Second derivative of strain measurements with respect to time.

4 RESULTS AND DISCUSSION

The strain time history obtained in response to the British Class 115 type train loading is presented in Figure 6(a). There are 6 peaks in the strain signal which correspond to the passage of the 6 bogies across the length of the test structure. The strain signal obtained under train loading is differentiated twice in an effort to identify the presence of axles and the corresponding results are presented in Figure 6(b). As described in the previous sections, positive peaks show the time when an axle enters or leaves the bridge whereas negative peaks correspond with times when an axle passes the sensor location. First looking at the negative peaks, there are twelve in total which identifies the time instants when axles are at the sensor locations.

Among the positive peaks, the ones with higher amplitude show the time instants when axles enter the bridge. There are 12 peaks identified in Figure 6(b) which are marked with solid black circle markers. The remained positive peaks (blue solid circle markers in Figure 6(b)) correspond with time instants when an axle leaves the bridge structure. Since the magnitudes of negative peaks when axles are leaving the structure are much less than the corresponding peaks when axles enter the bridge, for some axles, such as axles 3-10, it is not possible to accurately identify the time when they are leaving the structure.

5 CONCLUSIONS

This paper investigates the potential of identifying the presence of axles using the second derivative of measured strain with respect to time. Initially, numerical analyses are

carried out on a 1-D simply supported bridge model to develop the theoretical basis of the proposed method. Having seen that in theory it is possible to identify the presence of axles using the second derivative of the strain signal obtained under a traversing vehicle, a field test is conducted on a single span simply supported railway bridge in an effort to validate the proposed methodology. The following conclusions can be drawn from this study:

- The second derivative of strain results in positive and negative peaks where positive peaks show the times when axles enter or leave the bridge and negative peaks correspond to times when an axle passes the sensor location.
- The results obtained from the field testing confirms that the proposed methodology can successfully identify the presence of axles when they enter the bridge and pass the sensor location. However, since the sensor is installed closer to the support location at the entrance side of the bridge, the proposed methodology failed to accurately identify the times when axles left the structure.

ACKNOWLEDGMENTS



This research project has received funding from the European Union's Horizon 2020 research and innovation programme under the Marie Skłodowska-Curie grant agreement No. 642453.

REFERENCES

- [1] American Association of State Highway and Transportation Officials. *AASHTO LRFD Bridge Design Specifications*, 6th ed, 2012.
- [2] Eurocode BS EN 1990:2002 - *Basis of Structural Design*, 2002.

- [3] Žnidarič A, Pakrashi V, O'Brien E, et al. (2011), 'A review of road structure data in six European countries', *Proc Inst Civ Eng - Urban Des Plan*, 164, 225-232.
- [4] Moses F. (1979), 'Weigh-in-Motion system using instrumented bridges', *Transp Eng J ASCE*, 105, 233-249.
- [5] O'Brien, E.J., Znidaric, A., Baumgärtner, W., González, A. and McNulty P. *Weighing-in-motion of axles and vehicles for Europe (WAVE). Report of work package 1.2: bridge WIM systems (B-WIM)*, 2001.
- [6] Lydon, M., Taylor, S.E., Robinson, D., et al. (2016), 'Recent developments in bridge weigh in motion (B-WIM)', *J Civ Struct Heal Monit*, 6, 69–81.
- [7] Dunne, D., O'Brien, E.J., Basu, B., et al. (2005), 'Bridge WIM systems with Nothing On the Road (NOR)', *Proceedings of the 4th international WIM conference*, Taipei, Taiwan, 109-117.
- [8] Chatterjee, P., OBrien, E., Li, Y., et al. (2006), 'Wavelet domain analysis for identification of vehicle axles from bridge measurements', *Comput Struct*, 84, 1792–1801.
- [9] Yu, Y., Cai, C. and Deng, L. (2017), 'Vehicle axle identification using wavelet analysis of bridge global responses', *J Vib Control*, 23, 2830–2840.
- [10] Caprani, C.C., O'Brien, E.J. and Blacoe S. (2013), 'Vision systems for analysis of congested traffic', IABSE Symposium Report, May, 99(12), 1329-1336(8).
- [11] Ojio, T., Carey, C.H., OBrien, E.J., Doherty, C. and Taylor, S.E. (2016), 'Contactless Bridge Weigh-in-Motion', *ASCE Journal of Bridge Engineering* 21(7): 04016032.

Finding the influence line for a bridge based on random traffic and field measurements on site

Eugene J. OBrien¹, Franck Schoefs², **Barbara Heitner**^{1,3}, Guillaume Causse³, Thierry Yalamas³

¹School of Civil Engineering, University College Dublin, Dublin, Ireland

²Research Institute of Civil Engineering and Mechanics, Université de Nantes, Nantes, France

³Phimeca Engineering, Cournon-d'Auvergne, France

email: eugene.obrien@ucd.ie, franck.schoefs@univ-nantes.fr, heitner@phimeca.com, cause@phimeca.com, yalamas@phimeca.com

ABSTRACT: The influence line of a structure reflects its structural behaviour as well as any possible damage present on the bridge. An iterative algorithm is presented in this paper in order to obtain the shape of the influence line of a bridge together with the load distribution of trucks passing overhead. One great advantage of this approach is that sensor calibration with pre-weighed trucks can be avoided. The only initial information needed are the measurement data and a preliminary estimate of influence line based on engineering judgement. An illustrative example is shown, where strain data have been collected on a reinforced concrete culvert. Apart from the efficiency of the proposed algorithm, the influence of the temperature on the results is also shown.

KEY WORDS: Bridge reliability; Influence line; Health monitoring; SHM; BHM.

1 INTRODUCTION

Influence lines of bridges can provide key information on the structural behaviour. In some studies influence lines have been used directly in damage identification of bridges [1]. In addition, the influence line of the bridge is the basis of Bridge Weigh-in-Motion (B-WIM) system, where the aim is to obtain the weight of trucks passing over the bridge. An extensive literature exists on B-WIM algorithms that all utilize the approximate influence line of the structure [2,3].

It is important to properly approximate the true influence line of the structure. A widely accepted way to find influence line is using the finite element model, although different new and more reliable methods have been reported in the literature [4-6].

In this paper an algorithm is presented, which combines Quilligan's method [6] to calculate the influence line and Moses' method [2] to calculate the axle weights of the passing vehicles in parallel. The method's robustness is tested using mid-span strain data on a reinforced concrete culvert recorded during ambient traffic conditions. In addition it is shown that using a statistically relevant volume of trucks, the effect of temperature on the behaviour of the structure can be investigated. This suggests not only that the effect of temperature on the stiffness of the structure has to be accounted for but also that the method can be used to detect damage.

2 THEORY

2.1 Moses' method

The algorithm that Moses introduced in [2] is used to calculate the axle weights of a truck given the corresponding measured response and influence line ordinates. The main principle of the algorithm is to minimise the least square error between the measured response (x_m) and the theoretical bridge response (x_{th}) that can be calculated as follows:

$$x_{th}(t) = \sum_{i=1}^N Q_i \times IL_i(t) \quad (1)$$

where t is the number of scans of the influence line and so of the response (being time or distance), N is the number of axles of the vehicle, Q_i is the i th axle weight and IL_i is the vector of the influence line ordinates corresponding to the i th axle. The non-zero influence line ordinates are identical for each axle; however they are shifted depending on the location of each axle. Then the least square error can be expressed as follows:

$$\varphi = \sum_{t=1}^K (x_m(t) - x_{th}(t))^2 \quad (2)$$

The algorithm searches for the Q vector by setting the partial derivatives of φ to zero. Solving this equation in matrix form, the following equation can be obtained:

$$\{Q\} = \frac{[IL]^T \{x_m(t)\}}{[IL]^T [IL]} \quad (3)$$

This equation is the basis of B-WIM calculations and is the first part of the combined iterative method introduced in this paper.

2.2 Quilligan's method

Quilligan [6] defined the matrix equation to calculate, based on the same principles as Moses' algorithm, the influence line ordinates given the measured response and the axle weights of a passing calibration vehicle. He proposed the solution in a matrix form that can be used independently from the number of axles of the vehicle. This solution of the influence line ordinates can be expressed as follows:

$$\{IL\}_{K-C_N,1} = [Q]_{K-C_N,K-C_N}^{-1} \{M\}_{K-C_N,1} \quad (4)$$

where $[Q]$ is a symmetric matrix dependent on the axle weights, $\{M\}$ is a vector dependent on the axle weights and the measured response, K is the total number of scans of the response signal and C is a vector containing the cumulative sums of the axle spacings expressed in scan numbers (starting from $C_1 = 0$). Hence, C_N is the total number of scans

corresponding to the wheelbase of the vehicle. The elements of $[Q]$ are:

- Diagonal elements:
Sum of squares of axle weights

$$q_{i,i} = \sum_i^N Q_i^2 \quad (5)$$

- Off-diagonal elements:
0 except for

$$q_{i,i+(C_j-C_i)} = Q_i Q_j \quad (6)$$

where $i + (C_j - C_i) < N - C_N$

The M vector can be expressed as follows:

$$\{M\}_{K-C_N,1} = \begin{cases} Q_1 M_1 + Q_2 M_{1+C_2} + \dots + Q_N M_{1+C_N} \\ \vdots \\ Q_1 M_{K-C_N} + Q_2 M_{K-C_N+C_2} + \dots + Q_N M_K \end{cases} \quad (7)$$

2.3 Combined iterative method

In order to obtain the influence line of the structure using Quilligan's algorithm, it is necessary to know the load distribution of the vehicle, i.e. both the axle spacings and the axle weights. The axle spacings can be obtained with signal processing methods. However to know the axle weights the truck has to be pre-weighted.

The method presented herein overcomes this limitation by introducing an iterative procedure starting from a general preliminary influence line based on engineering judgement. In practice this means two things: the length of the influence line has to be estimated as well as its shape. Using this preliminary influence line, that may have a shape of a triangle for example for a single span structure, Moses' algorithm can be applied to calculate the axle weight distribution. Then with the help of these values Quilligan's method can be used to calculate the influence line ordinates. These two steps are repeated iteratively until convergence is reached. Convergence can be considered established when the calculated axle weights of two consecutive steps of iteration are sufficiently close. In general, convergence can be reached rather quickly for simple structures.

With the proposed iterative approach, it is possible to obtain the shape of the influence line as well as the relative load distribution of the trucks based solely on measurement data. In order to verify the method and to see if the results are reliable, different tests have been conducted. However one straightforward test is to evaluate the fit between the measured and the calculated, theoretical signal by computing the coefficient of determination, i.e. the r^2 value.

3 CASE STUDY ON A CULVERT

3.1 Bridge and sensor data

The data available for this study has been collected from a highway bridge in Slovenia, near Ljubljana (see Figure 1). It is a reinforced concrete culvert with 2 lanes in each direction. The length of the bridge is 6.5 metres, while its total width of the structure is 32.3 metres. The strain sensors, used to weigh

the trucks, are located in the midspan along the width of the bridge (see Figure 2). One of the slow lanes is the focus of this paper; consequently only single truck crossing events are considered.



Figure 1. View of the case study bridge.



Figure 2. View of the strain sensors attached to the bottom of the slab of the case study bridge.

The response signals are post-processed to filter out the dynamic effects and to obtain the number of axles and the axle spacings of the crossing vehicles. The signals are also zeroed in order to eliminate the effect of thermal expansion/contraction on the strain history. An example of the post-processed signals can be seen on Figure 3. The four sensors under the studied lane are considered only. However they are not calibrated, so all the signals contain raw data in Volts. The summed up signal can be seen in the figure too. This is the signal that is used in the further analysis. Summing up various signals can help to reduce the influence of the trucks transversal position and the pavement roughness.

It can be seen in Figure 2 that at some points (in the middle of each lane) additional strain sensors are placed in the quarter points of the structure. These sensors are used to calculate the speed of the crossing vehicles.

Apart from strain sensors, temperature sensors are also installed on the structure. A daily temperature cycle for temperature of the pavement, the bottom of the slab and the middle of the slab can be seen in Figure 4. The temperature in the middle of the slab has much smaller amplitudes than the others and a shift can also be seen, as expected, i.e. the slab takes time to respond to changes in ambient temperature. As this slab temperature influences most directly the behaviour of the structure, it is referred to as the temperature from now on.

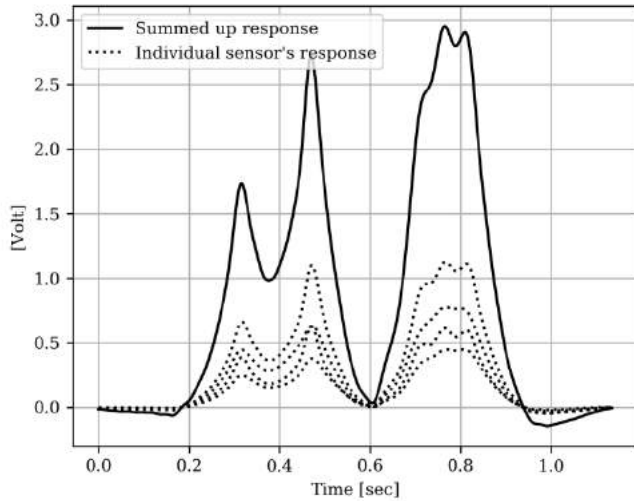


Figure 3. Measured signals during a slow lane single truck crossing event.

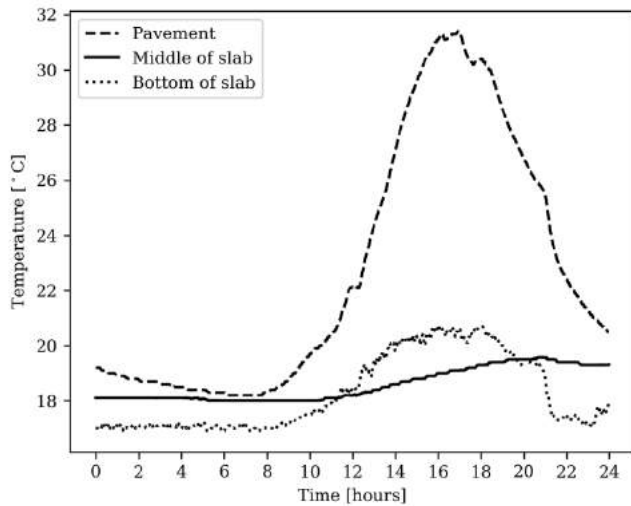


Figure 4. One daily cycle of temperature.

3.2 Applying the iterative method

The iterative method presented in the previous section has been applied on the strain measurement data of the culvert. Due to the effect of the culvert-soil interaction it has been decided to include in the influence line some metres before and after the bridge itself. The preliminary shape of the influence line was defined as a triangle along the bridge with two ‘zero-tail’ zones before and after the bridge (it is marked with dashed line on Figure 6). The total length of the influence line is set to 17 metres.

One drawback of the method is that convergence cannot always be reached. An example for this case can be seen on Figure 5 (note increase of the order of magnitude of the ordinates compared to the ones reported in Figure 6). For this reason a specific stopping criterion has to be defined, i.e. in case the difference between the calculated axle weights of two consecutive steps are not decreasing, the algorithm quits the iteration. However even in this case the shape of the influence line and the load distribution results do not have to be directly discarded but further analysed and carefully treated. Non-

convergence happens mostly because multiple vehicles are present on the bridge, perhaps passing in the opposite direction, introducing extra ‘noise’ in the measured signal. In Figure 6 a well converged case is presented together with the preliminary influence line (dashed line). In this case the influence line shape and the load distribution can be extracted and used without further doubt.

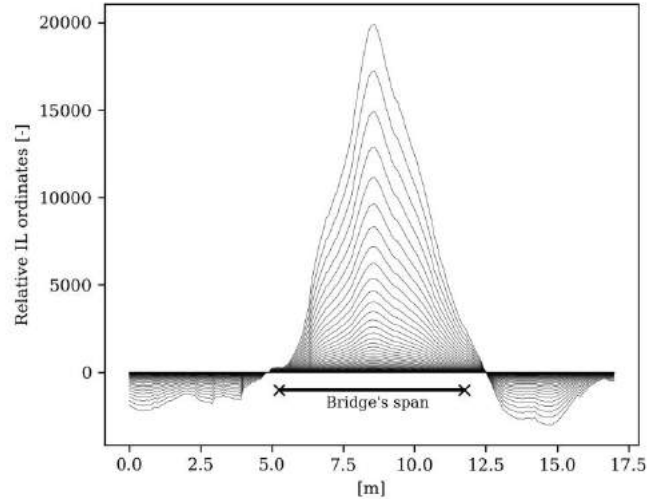


Figure 5. Iterative steps to find the shape of the influence line – convergence cannot be reached.

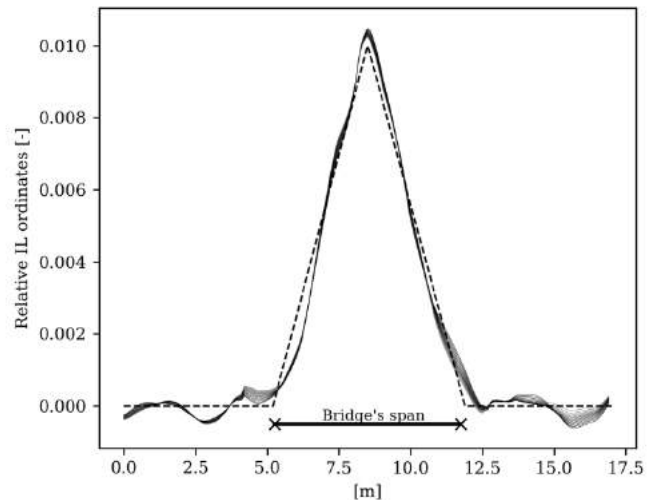


Figure 6. Iterative steps to find the shape of the influence line – convergence is reached.

The calculated ‘theoretical’ signal using the obtained influence line and load distribution can be compared to the measured signal. Computing r^2 values of the two signals (the closer to 1, the better) is one way to quantify the quality of the method. In Figure 7 the results of an example truck are shown. The dashed line marks the measured signal while the continuous line marks the calculated one. The five thin continuous lines mark the individual responses of the five axles of the truck. The r^2 value in this case is 0.998, reflecting the very good fit.

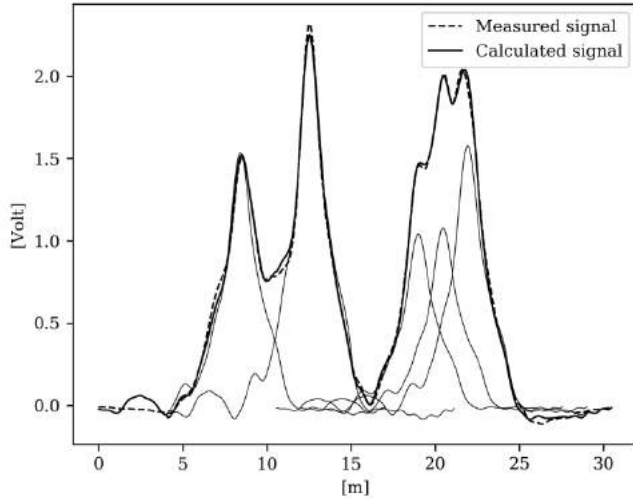


Figure 7. Comparing the calculated truck response (the individual axle responses are marked with thin lines) and the measured response.

3.3 Effect of temperature

The database of the signals is split into several parts depending on the temperature. Each subpart then corresponds to a narrow temperature band of 2°C. The iterative method is applied to the trucks' signals of each subset. The original sample size has been 10000 trucks for each temperature range. However all the cases with convergence problems are filtered out. The resulting final sample size and the average r^2 values depending on the temperature range, can be found in Conclusions

The iterative method presented in this paper allows the influence line shape of a structure to be obtained as well as the load distribution of the passing vehicles. Through an illustrative example it is shown that although there are some limitations and difficulties in the method, it provides encouraging preliminary results.

Temperature change can affect the stiffness of different parts of the bridge (and soil) and so it may influence the structural response. For this reason, a study on temperature effect has been conducted to show that this effect exists and can be tackled with the developed method.

The iterative method's greatest advantage is that pre-weighting trucks can be avoided. Thus, it has high potential for both B-WIM and damage detection of bridges. Future research is planned on exploring better the limitations and robustness of the method and to define more in detail the areas of possible application.

Table 1. The mean calculated relative Gross Vehicle Weight (GVW) of a general population and of a population of 5-axle trucks only are presented in Figure 8. As the average GVW of a population of trucks is not expected to vary with the temperature, it can be concluded that the observed variation is due to the variation of the structural behaviour that is sensitive to the temperature change. It can be also seen that focusing on 5-axle trucks only results in a smoother curve, i.e. more robust relationship between calculated GVW and temperature.

4 CONCLUSIONS

The iterative method presented in this paper allows the influence line shape of a structure to be obtained as well as the load distribution of the passing vehicles. Through an illustrative example it is shown that although there are some limitations and difficulties in the method, it provides encouraging preliminary results.

Temperature change can affect the stiffness of different parts of the bridge (and soil) and so it may influence the structural response. For this reason, a study on temperature effect has been conducted to show that this effect exists and can be tackled with the developed method.

The iterative method's greatest advantage is that pre-weighting trucks can be avoided. Thus, it has high potential for both B-WIM and damage detection of bridges. Future research is planned on exploring better the limitations and robustness of the method and to define more in detail the areas of possible application.

Table 1. Sample size and average r^2 value for each temperature range considered.

Temperature range [°C]	Sample size	r^2 values
0-2	7945	0.9984
2-4	7937	0.9983
4-6	8131	0.9984
6-8	8057	0.9984
8-10	7904	0.9983
10-12	7891	0.9984
12-14	7902	0.9983
14-16	7843	0.9983
16-18	8060	0.9983
18-20	8072	0.9982
20-22	8050	0.9983
22-24	8097	0.9983
24-26	8034	0.9981
26-28	8138	0.9982
28-30	8165	0.9980

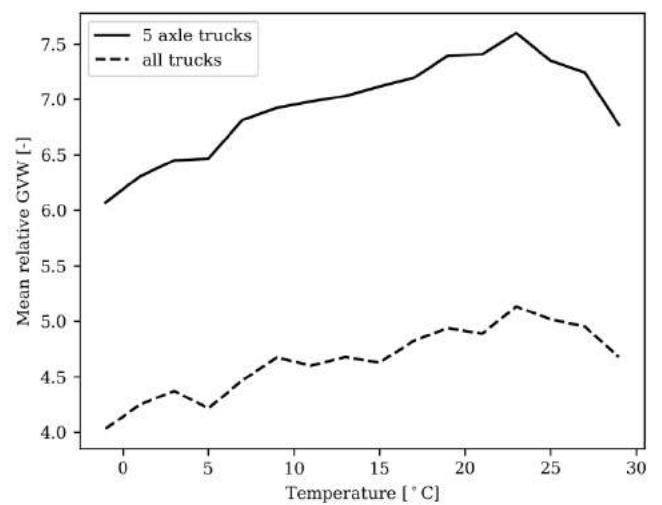


Figure 8. Mean relative GVW plotted against temperature for a population of general trucks and of 5-axle trucks.

ACKNOWLEDGMENTS



This work was supported under the TRUSS project. TRUSS is funded by the European Union's Horizon 2020 research and innovation programme under Marie Skłodowska-Curie agreement No. 642453.

Measurement data were made available courtesy of the BridgeMon project from the Research for the Benefit of SMEs (Small and Medium size Enterprises) scheme of the 7th Framework Programme of the European Commission.

REFERENCES

- [1] Cantero, D., Karoumi R. and González A. (2015), 'The Virtual Axle concept for detection of localised damage using Bridge Weigh-in-Motion data', *Engineering Structures*, 89, 26–36.
- [2] Moses F. (1979), 'Weigh-in-motion system using instrumented bridges', *Transportation Engineering Journal of ASCE*, 105(3), 233–49.
- [3] Ojio, T., Carey, C.H., O'Brien, E.J., Doherty, C. and Taylor, S.E. (2016), 'Contactless Bridge Weigh-in-Motion', *ASCE Journal of Bridge Engineering* 21(7): 04016032.
- [4] Wang, N-B., He, L-X., Ren, W-X. and Huang, T.L. (2017) 'Extraction of influence line through a fitting method from a bridge dynamic response induced by a passing vehicle', *Engineering Structures*, 151, 648–664.
- [5] Frøseth, G.T. , Rønnquist, A., Cantero, D. and Øiseth, O. (2017), 'Influence line extraction by deconvolution in the frequency domain', *Computers and Structures*, 189, 21–30.
- [6] O'Brien, E.J., Quilligan, M. and Karoumi, R. (2006), 'Calculating an influence line from direct measurements', *Bridge Engineering, Proceedings of the Institution of Civil Engineers*, 159(1), 31–34.

A machine learning classifier for condition monitoring and damage detection of bridge infrastructure

Matteo Vagnoli¹, Rasa Remenyte-Prescott¹, John Andrews¹, Chul-Woo Kim²

¹Resilience Engineering Research Group, the University of Nottingham, Science Road, University Park, NG7 2RD, Nottingham, United Kingdom

²Dept. of Civil and Earth Resources Eng., Graduate School of Eng., Kyoto University, Kyoto 615-8540, Japan
email: Matteo.Vagnoli@nottingham.ac.uk, R.Remenyte-Prescott@nottingham.ac.uk, John.Andrews@nottingham.ac.uk, kim.chulwoo.5u@kyoto-u.ac.jp

ABSTRACT: Structural Health Monitoring (SHM) techniques are able to monitor the behaviour of critical infrastructure over time, by improving the safety and reliability of the asset. A large amount of data is generated by SHM methods continuously. Therefore, machine learning methods can be developed in order to transform the available data into valuable information for decision makers, by pointing out vulnerabilities of the critical infrastructure. In this paper, a machine learning classifier for condition monitoring and damage detection of bridges is proposed by adopting a Neuro-Fuzzy algorithm. The method allows to assess the health state of the infrastructure automatically, accurately and rapidly, every time when a new measurement of the bridge behaviour is available. The method is validated and tested by monitoring the behaviour of an in-field steel truss bridge, which is subjected to a progressive damage process.

KEY WORDS: Machine learning; Neuro-fuzzy neural network; Empirical Mode Decomposition (EMD).

1 INTRODUCTION

Bridges are continuously deteriorating due to aging, traffic load, and environmental effects such as wind, storm and changing temperatures. Time-consuming and expensive visual inspection techniques are widely adopted to assess the health state of bridges, at fixed time intervals, ranging from one to six years [1]. Furthermore, visual inspections are based on expert knowledge, and consequently the outcomes can be significantly variable, due to subjectivity of the assessor [2]. Structural Health Monitoring (SHM) methods can overcome the limitations of visual inspections, by relying on the analysis of the bridge static and dynamic responses with the aim of assessing the bridge health state accurately, remotely and continuously [3]. In addition, maintenance costs increase dramatically when the degradation of the bridge is left unaddressed, since visual inspections might only identify the degradation years after its starting date.

SHM methods can improve the reliability of the whole transportation network by providing rapid and robust information to decision makers regarding the health state of the bridge, by identifying unexpected behaviour of the bridge [4]. For these reasons, SHM methods have been widely studied in the last decades, by developing model-based and data-driven methods. Model-based SHM methods, such as Finite Element Model (FEM) updating methods, have demonstrated to accurately assess the health state of bridges [5]. However, a complex and time-consuming process is required to develop a reliable and accurate FEM of the bridge, i.e. an FEM that is able to represent the behaviour of a real structure with good accuracy. As a consequence, continuous condition monitoring of the bridge might not be achieved. Conversely, data-driven methods, such as Artificial Neural Networks (ANNs) [6], Principal Component Analysis (PCA) [7], supervised and unsupervised clustering techniques [8], and vibration-based analysis [9] show promising results for continuous condition monitoring of bridges. However, the

performance of data-driven methods strongly depends on the quality and quantity of available data.

In this paper, we present a machine learning method to monitor the health state of bridges, by identifying and diagnosing damages of the bridge infrastructure. The method relies on a first-step that aims to extract statistical and frequency-based features from the raw data of bridge behaviour, followed by a second-step that aims to assess the trend over time of the computed features. Finally, a Neuro-Fuzzy algorithm, which is able to classify the behaviour of the bridge based on its similarity with the behaviour of a training dataset, is adopted to assess the bridge health state. The method allows to evaluate the health state of the bridge automatically, accurately and rapidly, every time when a new measurement of the bridge behaviour is available.

The main novelty of our work lies in the extraction of the trend of the statistical and frequency-based features, which allow to assess the health state of the bridge, without requiring a time-consuming and complex process to achieve good and robust results. Indeed, the trend of the features is obtained by assessing the residuals of the Empirical Mode Composition (EMD) of each feature [10]. In the SHM framework, the EMD is generally adopted to identify structural changes by analysing dynamic behaviour of the infrastructure directly, i.e. the dynamic behaviour of the bridge is used as an input to the EMD process [11; 12]. Such application has shown good results when an FEM was analysed [11], however, misclassifications and false alarms were observed when a real in-field bridge was monitored [12]. In this paper, we adopt the EMD to extract the trend of the features of the bridge behaviour. In fact, several studies have demonstrated that the EMD trend of the features can provide valuable information with respect to the level of degradation of a system [10; 13].

The proposed method is tested by monitoring the behaviour of an in-field steel truss bridge, which is subjected to a progressive damage under a moving vehicle excitation [14].

The remaining of the paper is organized as follows: Section 2 describes the proposed data-driven method; Section 3 shows the results of the proposed method in monitoring the steel truss bridge; Section 4 presents the conclusion and future work.

2 THE PROPOSED MACHINE LEARNING SHM METHOD

The proposed data-driven method is described in this section, by providing a step-by-step description of the method. The aim of the method is to monitor the health state of the steel truss bridge continuously, by assessing the health state of the bridge every time when new evidence of the bridge behaviour is made available by the sensors that are installed on the bridge. In this way, unexpected behaviour of the bridge, which can be caused by degradation mechanisms, can be detected as soon as the behaviour of the bridge is affected. Furthermore, the proposed method is able to diagnose the cause of unexpected behaviour of the bridge, and consequently diagnose damage of the bridge. Decision-makers can take informed decisions by relying on the rapid and valuable information provided by the proposed method.

In what follows, an overview of the method is presented. Each step of the analysis is then described by applying the method to the real steel truss bridge.

2.1 Overview of the method

The proposed condition monitoring and damage detection methodology is depicted in Figure 1. The dynamic behavioural response of the bridge is recorded by accelerometers that are installed on the bridge infrastructure [14]. Every time when a new set of raw bridge behaviour is provided by the sensors, due to the fact that a vehicle runs over the bridge, the dynamic response of the bridge is divided into three time windows: *a*) an equilibrium position of the bridge, when no vehicles are travelling over the bridge, and the bridge response is influenced only by environmental factors, such as wind; *b*) a forced response of the bridge, when a vehicle is passing over the bridge; *c*) a free vibration response of the bridge, when the vehicle leaves the bridge, which continues to vibrate due to the influence of the vehicle, until a new equilibrium is reached. A feature extraction process is then developed, with the aim of reducing the dimensionality of the raw bridge behaviour. In fact, sensors provide thousands of values of the bridge behaviour at each time second, whereas features can extract relevant information regarding the bridge health state, by merging together the thousands sensor values into a lumped assessment [15]. Statistical features (such as mean value, standard deviation, kurtosis, root mean square, etc.) and frequency-domain features (such as peaks and amplitudes of the Fast Fourier Transform (FFT)) are assessed at each τ time step in order to extract information from the bridge behaviour (Figure 2). The obtained features are usually noisy, i.e. features show high level of oscillations, and as a consequence the trend of each feature can be obtained by assessing the residuals of the EMD of each feature assessment [10]. In fact, the EMD trend can provide information with respect to the level of degradation of the bridge. The trend of the features is finally used as input to a Neuro-Fuzzy classifier, which has been trained adequately in order to assess the health state of the bridge. Therefore, the

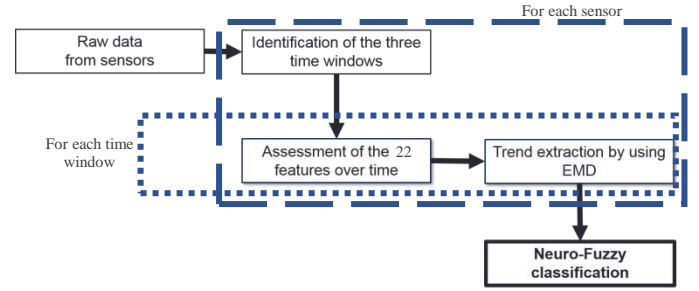


Figure 1. Flowchart of the proposed methodology

health state of the bridge is evaluated every time when new evidence of the bridge dynamic behaviour is available, by extracting its features and classifying the bridge health state based on the trend of its features.

3 STEEL TRUSS BRIDGE CONDITION MONITORING AND DAMAGE DETECTION

In this case study, the method is applied to an in-field steel truss bridge, which was subjected to progressive damage tests with a moving vehicle excitation [14]. The acceleration data of the bridge are provided by sensors installed on the bridge infrastructure, and used as the input to the proposed methodology. In what follows, the bridge is presented, and the steps of the proposed methodology discussed with the aim of assessing the health state of the bridge.

3.1 The steel truss bridge

A simply-supported steel Warren truss bridge is considered in this paper. The length of the bridge is 59.2m, with 3.6m width and 8m of maximum height, as shown in Figure 3 [14]. The bridge was demolished in 2012. However, progressive damage tests were carried out while the bridge was closed to the public in order to develop a dataset of bridge behaviour under changing health states of the bridge, and consequently develop SHM strategies based on real in-field structures. The dynamic behaviour of the bridge was collected by 8 accelerometers, denoted as A_i ($i = 1, 2, \dots, 8$) circles in Figure 3, whose sample rates was equal to 200 Hz.

Three different health state classes of the bridge were analysed by damaging progressively the bridge infrastructure (Figure 3): *i*) intact bridge scenarios, with no damage of the bridge infrastructure (class 1); *ii*) a complete cut of the mid-span vertical member (DMG1, class 2); *iii*) a complete cut of the vertical member at 5/8th span (DMG2, class 3).

1. Mean	12. Median
2. Standard deviation	13. Norm
3. Peak value	14. Integral
4. Minimum value	15. Amplitude of first harmonic (FFT)
5. Skewness	16. Amplitude of second harmonic (FFT)
6. Kurtosis	17. Amplitude of third harmonic (FFT)
7. Root Mean Square (RMS)	18. Amplitude of fourth harmonic (FFT)
8. Interquartile distance	19. Peak of first harmonic (FFT)
9. 5 th percentile	20. Peak of second harmonic (FFT)
10. 95 th percentile	21. Peak of third harmonic (FFT)
11. Covariance	22. Peak of fourth harmonic (FFT)

Figure 2. List of extracted features.

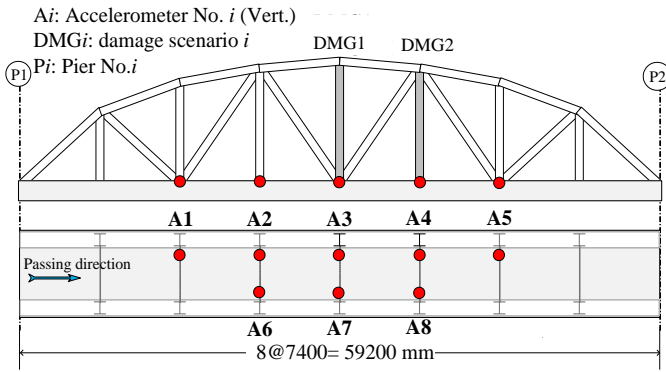


Figure 3. Steel truss bridge and sensors locations.

For each class, the vehicle used for the experiment was a two-axle vehicle, with a total weight of about 21kN. The vehicle was driven across the bridge three times for each scenario at a speed ranging from 36 to 41 km/hr to induce excitation.

Figure 4 shows a sample time-history of the bridge acceleration response, and the definition of the three time windows, which are represented by dotted vertical lines. Finally, it is worth mentioning that during the progressive damage tests, all traffic except the load vehicle was prohibited.

3.2 Feature extraction

The bridge behaviour gathered from the 8 sensors consists of 1600 data points for each second (8 sensors, with a sampling rate of 200 Hz), and as a consequence large data storage capacity and high computation power are required to efficiently store and analyse such amount of data. Conversely, the dimension of the bridge behaviour data can be reduced into more valuable information, with respect to the bridge health state, by extracting informative features from the raw acceleration data. Therefore, the 22 features in Figure 2 are extracted from the raw bridge acceleration every τ seconds, by reducing the dimensionality of the data from $1600 \cdot \tau$ to 176 (22 features \cdot 8 sensors), i.e. every τ seconds the 22 features are evaluated for each sensor and stored in order to monitor the evolution of the bridge condition over time. In this case study, τ is equal to 2 seconds, and consequently 2600 values are lumped into 176 values, which are assessed every 2 seconds. The features are extracted from both time domain and frequency domain by using an FFT approach. In this way, both the statistical and frequency-based behaviour of the

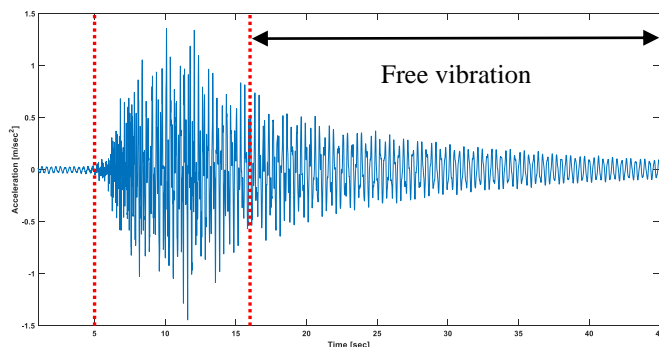


Figure 4. Vehicle induced bridge acceleration and time windows example.

bridge are evaluated in order to assess the health state of the bridge. In fact, statistical features are adopted to monitor the health state of complex systems, such as aircraft engines [16], whereas changes of the bridge frequency-based behaviour are widely adopted as bridge damage parameters [14]. In what follows, the analysis of the free vibration responses of the bridge (as shown in Figure 4) is presented, in order to avoid any potential noise of the passing vehicles on the results. This assumption is suggested by the structural analysis of the steel truss bridge [14].

Without loss of generality, Figure 5 shows 8 of the 22 features that are evaluated for the free vibration window (c)) of the bridge acceleration recorded by sensor 3. It should be noted that the features are noisy, by presenting a high level of oscillations, and thus a robust and reliable assessment of the bridge condition can be threatened by such oscillations. For this reason, a further step of data processing is introduced by using the EMD, in order to retrieve the trend of the feature, and as a consequence, assess the health state of the bridge in a robust and reliable way.

3.3 Feature trend smoothing

The trend of the features is assessed by decomposing the feature pattern, such as shown in Figure 5, which shows high oscillations, into multiple signals of equal duration, known as Intrinsic Mode Functions (IMFs) through the application of the EMD process [17]. The EMD is a data-driven decomposition method that is able to decompose a signal into multiple simple harmonics of various frequencies, i.e. multiple IMFs with different frequencies. The EMD process can be applied to any oscillatory and non-stationary time series as follows:

1. Identify all maxima and minima of the feature pattern to be decomposed.
2. Connect peaks using a polynomial spline fitting to enhance interpolation.
3. Assess the mean value of both maxima and minima spline envelope.
4. Subtract the mean of the envelope from the original feature pattern.
5. Perform steps 1 to 4 until a zero-mean of the envelope is obtained. The resulting time-series is the first IMF.
6. Perform steps 1 to 5 to the obtained IMFs until a monotonic function remains or until a predetermined threshold is reached. This final time-series is known as residuals and represent the trend of the decomposed feature pattern.

The EMD process allows to decompose the noisy pattern of the feature of Figure 5, into a set of IMFs and a function that represents the trend of the feature pattern over time.

The IMF satisfy the following two criteria: *i*) the number of extrema and number of zero crossings is either equal or differ at most by one; *ii*) the mean value of the spline envelopes is equal to zero.

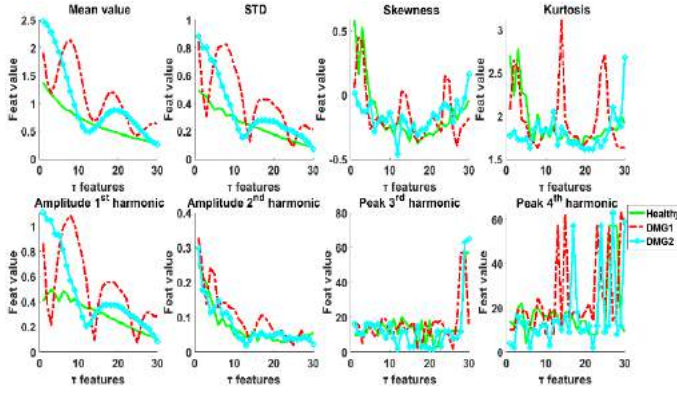


Figure 5. Example of features extraction for sensor 3

The residuals of the EMD for the 8 features of Figure 5 are shown in Figure 6. It is worth noting the difference between the pattern of the features (Figure 5) and their trend (Figure 6): the trend of the features allows to point out different bridge behaviour, i.e. each health state of the bridge is represented by a different trend clearly. On the contrary, the assessment of both statistical and frequency-domain features does not allow to point out different bridge health states in a clear manner. For example, the patterns of the third and fourth harmonic peaks of the FFT, which represent each class of the bridge health state, are overlapped in Figure 5, and thus it is difficult to identify the health state of the bridge correctly by analysing such features. Conversely, the trends of the same features in Figure 6 are well separated, and as a consequence, the health state of the bridge can be identified robustly by relying on the analysis of such trend.

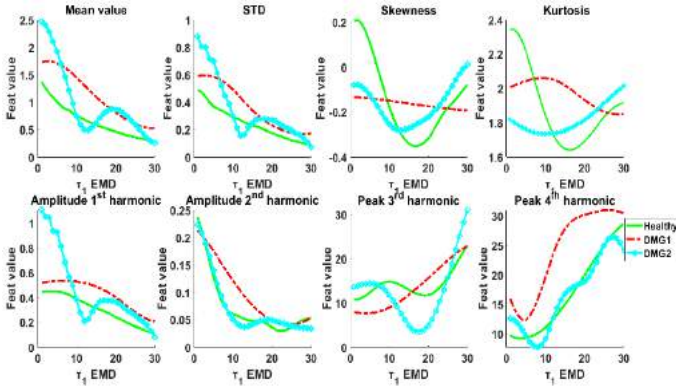


Figure 6. Trend of the 8 features presented in Figure 5.

In what follows, a machine learning method, which relies on a Neuro-Fuzzy classifier, is introduced with the aim of assessing the health state of the bridge every time when the new evidence of the bridge behaviour is available, by using the trend of the features as input to the Neuro-Fuzzy classifier.

3.4 The Neuro-Fuzzy classifier for automatic assessment of the bridge health state

Machine learning methods are able to classify the behaviour of a system by evaluating the similarity between system behaviours. In fact, a machine learning method is usually trained by using a database of system behaviour under different health states. In this way, when the unknown

behaviour of the system is made available by the sensors, the machine learning method allows to assess the health state of the system, by assigning the unknown behaviour to the most similar class, i.e. the class that contains the most similar behaviour.

In this paper, we adopt a Neuro-Fuzzy classifier, which allows to merge fuzzy classification techniques with the learning capabilities of a Neural Network. The detail description of the Neuro-Fuzzy classifier is out of the scope of this paper, and an interested reader can find more information in [18]. Hereafter, the main steps of the Neuro-Fuzzy classifier are presented.

The method requires a database of historical behaviour of the bridge for the different health states of the bridge (healthy-class 1, DMG1-class 2 and DMG3-class 3, in this case study) in order to carry out the training process. Indeed, the method aims to recognize and classify the different health states of the bridge, during the continuous monitoring of unknown bridge behaviour. With this aim, the accelerations of the steel truss bridge are divided in two groups randomly, in order to firstly train the Neuro-Fuzzy classifier, and then to test its performance in identifying the health state of the bridge correctly. The two sets of data are processed in the same way: *i*) the feature extraction process is carried out (Section 3.2); *ii*) the trend of the features is assessed (Section 3.3); *iii*) the trend of the features is used as input to the Neuro-Fuzzy classifier, during both the training and testing phases.

It should be noted that a feature selection process is performed during the training phase of the machine learning method, in order to increase the number of correct classifications (known as accuracy) of the Neuro-Fuzzy method. In fact, some of the 22 features can be redundant or non-informative, and as a consequence they can decrease the accuracy of the proposed method. In fact, these features increase the number of the Neuro-Fuzzy inputs, without providing valuable information about the different health states of the bridge. Therefore, an optimization algorithm (a Differential Evolution algorithm [19]) is used in order to iteratively select a combination of feature trends (e.g. the 8 features shown in Figures 5 and 6), and assess the accuracy of the Neuro-Fuzzy classifier by using only the selected combination of features as input to the machine learning method. The optimization method ends when the accuracy of the Neuro-Fuzzy method is maximized with respect to the considered training dataset. The optimal features selected in this case study are shown in bold in Figure 2.

The Neuro-Fuzzy classifier is developed as follows:

- 1) the trend of the features for each health state class of the bridge is used as input to the Neuro-Fuzzy classifier.
- 2) a k-means clustering method is applied to the trend data of each class with the aim of defining fuzzy rules. This means that the trend data of each health state class of the bridge are separated into different clusters in order to describe the relation between data belonging to the same class. For example, a fuzzy rule can be defined as follows: if the data x_1 of the considered trend belongs to cluster 1, and the data x_2 belongs to cluster 2, then the trend belongs to class 1.

- 3) the weight of each rule and each cluster is assessed by evaluating the size of each cluster.
- 4) a Gaussian probability density function is defined for each rule and each cluster. Therefore, a membership function is introduced, by using the centre of each cluster as mean value of the Gaussian distribution, whereas the standard deviation of the membership function is equal to the standard deviation of the data that belong to each cluster of each class.
- 5) a fuzzification process is developed by assessing the membership value of each data of each trend to each Gaussian probability distribution.
- 6) a defuzzification and normalization process is finally carried out in order to assign each value of each trend to a class, i.e. each data of each trend is assigned to the class with the higher membership value.
- 7) the accuracy of the process is assessed, by counting the number of correct classifications, i.e. the number of trend values that have been assigned to the correct class.
- 8) if the accuracy is lower than a threshold (95% in this case study), the steps 4 to 7 are repeated iteratively, by modifying the mean value and standard deviation of the Gaussian probability distributions slightly with respect to a set of pre-defined parameters [18].

When the training process of the Neuro-Fuzzy classifier is complete, the method can be used to monitor the health state of the bridge, with the aim of identifying and diagnosing unexpected behaviour of the bridge. In what follows, the Neuro-Fuzzy classifier is applied to monitor the health state of the steel truss bridge.

3.5 Application of the Neuro-Fuzzy classifier to the steel truss bridge

The health state of the steel truss bridge is monitored by measuring the acceleration of the bridge every time when a vehicle is passing over the bridge. When new evidence of the bridge acceleration is provided by the 8 sensors that are installed on the bridge, the 22 features of Figure 2 are extracted and the trend of the features is evaluated, by applying the EMD to the features pattern. The trend of the features is then used as input to the Neuro-Fuzzy classifier. The machine learning classifier is trained with trends representing each health state class of the bridge, and thus the Neuro-Fuzzy method is able to assess the health state of the bridge by classifying an unknown measurement of the bridge behaviour based on its similarity with the training trends of each class.

The Neuro-Fuzzy classifier provides the probability that each trend belongs to a health state class. For example, Figure 7 shows the results of the classification of two unknown acceleration measurements of the bridge (a healthy scenario and a damaged scenario of the bridge): Figure 7(a) shows that proposed method is able to recognize a healthy state of the bridge, i.e. the behaviour of the healthy bridge is classified as healthy (class 1) with a probability of 80%, whilst Figure 7(b) shows that damaged health states of the bridge are detected by

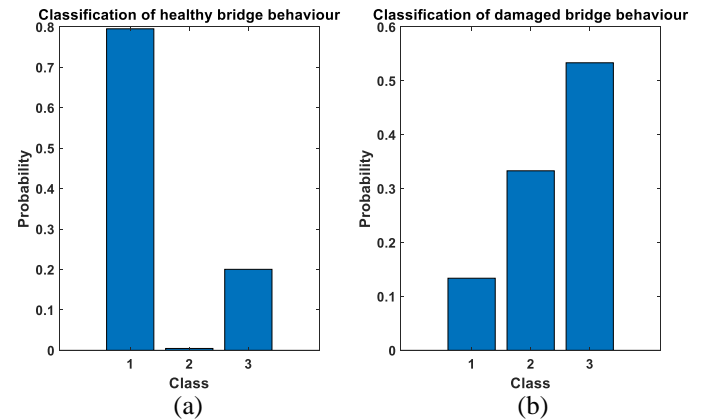


Figure 7. Classification of unknown bridge behaviour.

the Neuro-Fuzzy method (classes 2 and 3). At the same time, the Neuro-Fuzzy method is able to diagnose the nature of the damage of the bridge, by providing a probability for each class. For example, Figure 7(b) shows that the health state of the bridge is damaged, and the nature of the damage is class 3 (i.e. DMG1 in Figure 3).

In this case study, the performance of the Neuro-Fuzzy classifier is verified by assessing the health state of the bridge during 6 unknown scenarios, i.e. 6 acceleration measurements are analysed in order to assess the health state of the bridge. The 6 scenarios are composed of 2 healthy scenarios, and 4 damaged scenarios, 2 for each damaged class *ii*) and *iii*). The proposed method is able to correctly identify the nature of all 6 scenarios, whereas the diagnosing process of the damage scenarios is successful in 3 out of 4 scenarios.

The proposed method requires a database of bridge behaviour during different health state scenarios of the bridge, in order to recognize unknown health state of the bridge. Although, a low amount of the data can be a limitation for the accuracy of machine learning methods, the Neuro-Fuzzy classifier has demonstrated good performance also with small dataset. However, the performance of the proposed method can be improved by increasing the size of the training dataset, in order to take account of the variability of the bridge behaviour due to the effect of different environmental condition.

4 CONCLUSIONS

In this paper, a machine learning classifier has been proposed in order to monitor and assess the health state of a bridge continuously, every time when new evidence of the bridge behaviour is provided by the measurement system that is installed on the bridge. The proposed method relies on a three-step data-driven process: *i*) assessment of 22 statistical and frequency-based features, in order to extract valuable information from the acceleration of the bridge and by reducing the dimensionality of the acceleration data; *ii*) assessment of the trend of the feature over time, in order to reduce the noise of the features pattern, and thus provide a robust and reliable assessment of the bridge health state; *iii*) automatic assessment of the health state of the bridge by using the trend of the features as input to a Neuro-Fuzzy classifier, which has been previously trained, and by detecting and diagnosing bridge damage scenarios.

The proposed method has been applied to an in-field steel truss bridge, which was subjected to progressive damage tests under moving vehicle excitation. The method has demonstrated to be able to classify the health state of the bridge correctly, by detecting and diagnosing selected damage scenarios of the bridge.

The performance of the proposed method can be improved by increasing the size of the training dataset and introducing a pre-processing of the acceleration data, with the aim of cleansing the data from the noise that is unavoidably present when a real bridge infrastructure is monitored.

Although the proposed method showed good performance in monitoring and assessing the health state of the bridge, further developments of the method are required in order to improve both the accuracy and the robustness of the proposed method. With this aim, a larger dataset of bridge behaviour is required for the training process, in order to take account of the variability of the bridge behaviour due to different environmental condition. Indeed, the dynamic behaviour of the bridge depends on both the nature of the external bridge excitations, such as different vehicles that run over the bridge at different speeds, and the environmental weather condition, e.g. a variation of the ambient temperature leads to a strong variation of the bridge behaviour without modifying its health state. Therefore, a more complete training dataset, which contains the variability of the bridge behaviour due to the change of environmental condition, can lead to a more accurate and robust analysis of the bridge health state.

ACKNOWLEDGMENTS



This project has received funding from the European Union's Horizon 2020 research and innovation programme under the Marie Skłodowska-Curie grant agreement No. 642453.

REFERENCES

- [1] Moughty, J.J. and Casas, J.R., (2017), 'A state of the art review of modal-based damage detection in bridges: Development, challenges, and solutions', *Applied Sciences* (Switzerland), 7(5), art. no. 510.
- [2] Stajano, F., Hoult, N., Wassell, I., Bennett, P., Middleton, C. and Soga, K. (2010), 'Smart bridges, smart tunnels: Transforming wireless sensor networks from research prototypes into robust engineering infrastructure', *Ad Hoc Networks*, 8(8), 872-888.
- [3] Huseynov, F., Brownjohn, J.M.W., O'Brien, E.J. and Hester, D. (2017), 'Analysis of load test on composite I-girder bridge', *Journal of Civil Structural Health Monitoring*, 7(2), 163-173.
- [4] Vagnoli, M., Remenyte-Priscott, R. and Andrews, J., (2017), 'Railway bridge structural health monitoring and fault detection: State-of-the-art methods and future challenges', *Structural Health Monitoring*, doi: 10.1177/1475921717721137.
- [5] Sanayei, M., Khaloo, A., Gul, M. and Necati Catbas, F., (2015), 'Automated finite element model updating of a scale bridge model using measured static and modal test data', *Engineering Structures*, 102, 66-79.
- [6] Hakim, S.J.S. and Abdul Razak, H. (2013), 'Structural damage detection of steel bridge girder using artificial neural networks and finite element models', *Steel and Composite Structures*, 14(4), 367-377.
- [7] Cavadas, F., Smith, I.F.C. and Figueiras, J., (2013), 'Damage detection using data-driven methods applied to moving-load responses', *Mechanical Systems and Signal Processing*, 39(1-2), 409-425.
- [8] Alves, V., Cury, A. and Cremona, C. (2016), 'On the use of symbolic vibration data for robust structural health monitoring', *Proceedings of the Institution of Civil Engineers: Structures and Buildings*, 169(9), 715-723.
- [9] Moughty, J.J. and Casas, J.R., (2017), 'Performance assessment of vibration parameters as damage indicators for bridge structures under ambient excitation', *Procedia Engineering*, 199, 1970-1975.
- [10] Mosallam, A., Medjaher, K. and Zerhouni, N., (2014), 'Time series trending for condition assessment and prognostics', *Journal of Manufacturing Technology Management*, 25(4), 550-567.
- [11] Han, J., Zheng, P. and Wang, H. (2014), 'Structural modal parameter identification and damage diagnosis based on Hilbert Huang transform', *Earthq. Eng. & Eng. Vib.*, 13(1), 101-111.
- [12] Moughty, J. and Casas, J. (2017), 'Evaluation of the Hilbert Huang transformation of transient signals for bridge condition assessment', *European Safety and Reliability Conference. Safety and Reliability: Theory and Applications*, Portoroz: CRC Press, 2741-2749.
- [13] Sekkal, M.C., Berrached, N., Medjaher, K. and Varnier, C. (2017), 'Skeleton of a generic approach for the generation of health indicators of physical systems', *Colloquium in Information Science and Technology, CIST*, art. no. 7804960, 621-626.
- [14] Chang, K.-C. and Kim, C.-W. (2016), 'Modal-parameter identification and vibration-based damage detection of a damaged steel truss bridge', *Engineering Structures*, 122, 156-173.
- [15] Chalouli, M., Berrached, N.-E. and Denai, M. (2017), 'Intelligent Health Monitoring of Machine Bearings Based on Feature Extraction', *Journal of Failure Analysis and Prevention*, 17(5), 1053-1066.
- [16] Lei, Y., Li, N., Guo, L., Li, N., Yan, T. and Lin, J., (2018), 'Machinery health prognostics: A systematic review from data acquisition to RUL prediction', *Mechanical Systems and Signal Processing*, 104, 799-834.
- [17] Huang, N.E. and Wu, Z. (2008), 'A review on Hilbert-Huang transform: method and its applications to geophysical studies', *Rev. Geophys.*, 46, 1-23.
- [18] Cetisli, B. (2010), 'Development of an adaptive neuro-fuzzy classifier using linguistic hedges: Part 1', *Expert Systems with Applications*, 37(8), 6093-6101.
- [19] Di Maio, F., Vagnoli, M. and Zio, E. (2015), 'Risk-based clustering for near misses identification in integrated deterministic and probabilistic safety analysis', *Science and Technology of Nuclear Installations*, doi:10.1155/2015/693891.

Vibration-based, output-only damage identification of bridge under vehicle induced excitation

John James Moughty¹, Joan Ramon Casas¹

¹Department of Civil and Environmental Engineering, Technical University of Catalonia (BarcelonaTech), Campus Nord, Calle Jordi Girona, 1-3, 08034, Catalonia, Spain

email: john.james.moughty@upc.edu, joan.ramon.casas@upc.edu

ABSTRACT: Many traditional methods of damage identification in bridge structures implement numerical models and/or modal parameters as a means of condition assessment. While such techniques can often be effective, they may also succumb to their own intrinsic constraints, such as shortcoming in numerical model calibration to dynamic behaviour and environmental sensitivity of modal parameters. Furthermore, the degree of vibration signal non-stationarity that may be induced due to vehicle excitation can limit the applicability of some common signal processing techniques, such as Fourier transforms. The current study investigates vibration-based approaches to damage identification that circumvent some of these issues. Vibration data obtained from a real bridge structure subjected to a progressive damage test under vehicle induced excitation is used as a test subject. Novel vibration parameters obtained from the raw signals are assessed for their damage detection, localisation and quantification capabilities. Additionally, advanced Empirical Mode Decomposition (EMD) and the Hilbert-Huang Transformation (HHT) is applied to the non-stationary signals for the purpose of damage identification. The investigation shows that damage detection, localisation and quantification is achievable from the vehicle induced vibration signals using the proposed empirical techniques.

KEY WORDS: Damage identification, SHM, TRUSS ITN.

1 INTRODUCTION

Structural damage and degradation of bridges is a dangerous and costly occurrence. It is vital that bridge owners conduct necessary visual inspections and structural integrity testing on a regular basis, although this is somewhat impractical due to the quantity of bridges in the network. Instead of directly inspecting all bridges, sensors can be employed to indirectly infer the presence of damage using theoretical relationships, such as that of modal frequency and bending stiffness. Many modal parameters have been proposed for this reason, some of which are discussed in Moughty & Casas, (2017), however, using modal parameters as damage sensitive features can have some drawbacks and their performance may suffer from their sensitivity to environmental and operational conditions. Additionally, the non-stationarity of some vibration signals creates a problem when using standard modal techniques that employ Fourier-based transforms, as linear stationarity is assumed to accurately obtain each frequency's relative power.

The present paper explores alternative approaches to this problem by detailing a number of vibration-based, output-only damage sensitive parameters that have been designed to be applicable to vehicle induced excitation vibration responses.

2 VIBRATION BASED DAMAGE SENSITIVE FEATURES

This section provides a description of a number of damage sensitive features applied herein to short non-stationary vibration signals for the purposes of damage identification.

2.1 Cumulative Absolute Displacement (CAD)

CAD is summation of displacement over a discrete duration. As the subject of present study involves short duration vibration signals, an accurate approximation of transient

displacement can be obtained from the acceleration signal using integration and band-pass filtering to avoid drift. It is, however, necessary to ensure that the bridge is close to static behavior at $t=0$ sec in the neutral axis position to avoid errors.

$$CAD = \int_0^t |x(t)| dt \quad (1)$$

2.2 Vibration Decay Parameters

A feature of short vibration signals resulting from an impulse force or vehicle passage is the subsequent decay of the signal. A common method of assessing damage from changes in the decay of a signal is to obtain modal damping values; however, depending on the methodology employed, modal damping values may come with significant standard deviations, which reduce damage sensitivity.

$$y(t) = y_0 e^{at} \quad (2)$$

where: Decay Intercept = y_0
Decay Constant = a

An alternative option is to fit an exponential decay function to the free vibration of the signal, which can characterize the structure's energy dissipation into discrete quantifiable parameter values. Equation 2 provides the exponential decay function applied to the vibration signals herein. Its components $\{y_0\}$ and $\{a\}$ represent the Exponential Decay Intercept (EDI) and Exponential Decay Constant (EDC), respectively. These two parameters can be utilized for the purposes of damage identification. Figure 1 provides a graphical example of the exponential decay function plotted alongside their respective vibration signals for an undamaged and damage response.

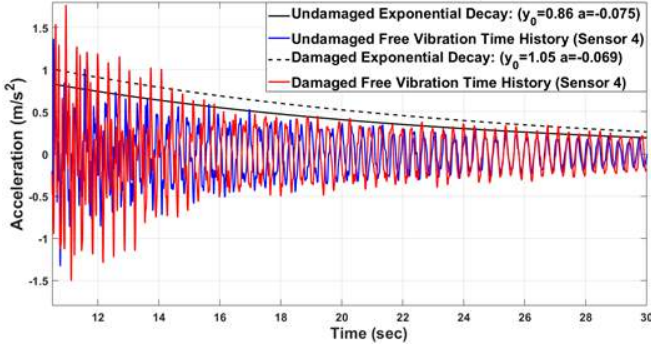


Figure 1. Example of exponential decay functions for an undamaged and damaged vibration response.

2.3 Instantaneous Vibration Intensity (IVI)

IVI is a damage sensitive feature designed for use on non-stationary data. IVI is the product of two Hilbert-Huang Transform (HHT) (Huang et al., 1998) parameters; instantaneous amplitude and instantaneous frequency, commonly presented together in a Hilbert-Huang Spectrum. However, this representation is not easily quantifiable. A more objective representation of instantaneous amplitude and frequency can be obtained via IVI, whose calculation is summarized in following explanatory paragraphs. For a more in-depth explanation, see Moughty & Casas (2018).

The first step is to decompose the raw non-stationary vibration signals into Intrinsic Mode Functions (IMFs) using Empirical Mode Decomposition (EMD). The present study utilizes an advanced method of EMD called Improved Complete Ensemble Empirical Mode Decomposition with Adaptive Noise (ICEEMDAN) (Colominas, et al., 2014).

The IMFs $\{c_i(\tau)\}$ obtained from the EMD process are input into the Hilbert Transform (Equation 3).

$$H[c_i(t)] = \frac{1}{\pi} \int_{-\infty}^{\infty} \frac{c_i(\tau)}{t - \tau} d\tau \quad (3)$$

The resulting Hilbert Transform $H[c_i(t)]$ is grouped with $\{c_i(\tau)\}$ to form an analytic signal $z(t)$ (Equation 4) whose constituents $a_i(t)$ and $\theta_i(t)$ are the instantaneous amplitudes and instantaneous phases, respectively (Equation 5 & Equation 6). Instantaneous frequencies $\{\omega_i(t)\}$ of each IMF are determined by differentiating the instantaneous phase function (Equation 7). Finally, the desired vibration parameter IVI is obtained by combining the instantaneous amplitudes and frequencies, as per Equation 8.

$$z(t) = c_i(t) + jH[c_i(t)] = a_i(t)e^{j\theta_i(t)} \quad (4)$$

$$a_i(t) = \sqrt{c_i^2(t) + H^2[c_i(t)]} \quad (5)$$

$$\theta_i(t) = \arctan\left(\frac{H[c_i(t)]}{c_i(t)}\right) \quad (6)$$

$$\omega_i(t) = \frac{d\theta_i(t)}{dt} \quad (7)$$

$$IVI_i(t) = a_i^2(t) / \omega_i(t) \quad (8)$$

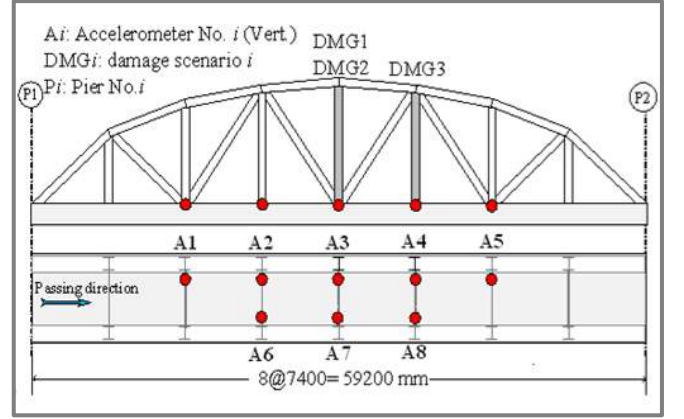


Figure 2. Sketch of test structure with damage locations highlighted in grey & sensor locations in red.

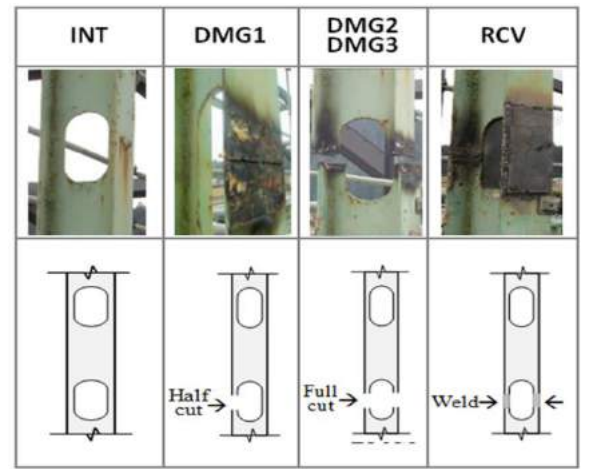


Figure 3. Pictures and sketches of bridge damage scenarios.

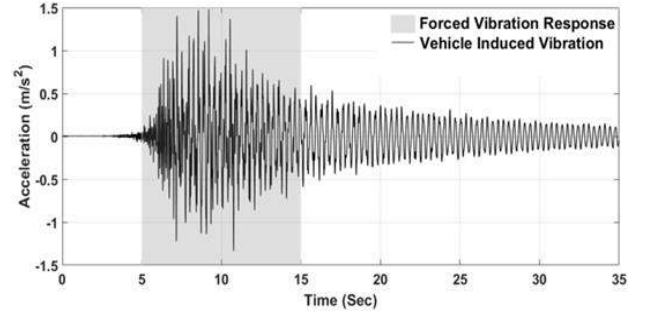


Figure 4. Example of vehicle induced vibration response with period of forced vibration shaded.

3 CASE STUDY SUBJECT

The test data utilized herein is obtained from a progressive damage test conducted on a steel truss bridge that was subjected to vehicle excitation (Kim et al., 2013). The bridge is a simply-supported steel truss bridge with a 59.2m span, 3.6m width and a peak height of 8m. Dynamic vibration response was recorded from 8 uniaxial accelerometers at a sample rate of 200Hz, positioned as per Figure 2.

The damage actions entail the severing of vertical truss members at locations presented in Figure 2. The progression of the damage states are described in Table 1 and shown in Figure 3. The damage actions start with the partial intersection of the vertical member at mid-span (DMG1), before its full

intersection was completed for DMG2. After which, the severed member was reconnected (RCV) via a welded flange. Finally, the vertical member at the 5/8th span location was completed severed for damage action DMG3.

Table 1. Description of damage actions

Damage State	Damage Actions
Undamaged	No action
DMG1	Half cut in vertical member at mid-span
DMG2	Full cut in vertical member at mid-span
RCV	Mid-span member reconnected
DMG3	Full cut in vertical member at 5/8th span

For each damage scenario, a 21kN double-axle vehicle was driven across the bridge 3 times at approximately 40km/h. A sample time-history of acceleration response is presented in Figure 4 with the period of forced vibration shaded in grey. The forced vibration response is short in duration and highly non-stationary and is therefore unsuitable for Fourier-based transformation techniques. In the present study, the period of forced vibration is assessed using the proposed HHT based damage sensitive feature IVI.

4 RESULTS

Results obtained for the assessed vibration-based, output-only damage sensitive features of *CAD*, *EDC*, *EDI* & *IVI* are presented in this section. The assessment of potential damage in the present study is conducted on sensors 1-5, as per Figure 2, for damage scenarios DMG2, RCV & DMG3, as per Figure 3. The reduction in sensors and damage scenarios assessed is to conserve space while retaining sufficient scope of investigation. Additionally, only the first vehicle passage for each assessed damage scenario is presented for the same purposes.

CAD: Figure 5 presents the CAD values obtained at all 8 sensor locations (as per Figure 2.) for the condition states of; Undamaged, DMG2, RCV & DMG3. All values are normalized to the largest undamaged value. It is clear that DMG3 yields a significant change in CAD at Sensor 4, which is the location of damage. In Figure 8, the percentage variation from baseline for sensors 1-5 for DMG2, RCV & DMG3 is given, which shows clear damage at sensors 3 & 4 for damage states DMG2 & DMG3, respectively. Both sensors are located at the point of damage, indicating a successful damage identification assessment. Furthermore, the RCV condition state is close to baseline, which correctly indicates no damage present.

EDI: Figure 6 presents the EDI values obtained at all 8 sensor locations for the condition states of; Undamaged, DMG2, RCV & DMG3. Again, it is clear that DMG3 yields a significant change in EDI at Sensor 4, which is the location of damage. In Figure 9, the percentage variation from baseline for sensors 1-5 for DMG2, RCV & DMG3 is given, which shows clear damage at sensors 3 & 4 for damage states DMG2 & DMG3, respectively. Both sensors are located at the point of damage, indicating a successful damage identification

assessment and also that the RCV condition state is close to baseline, correctly indicating no damage present.

EDC: Figure 7 presents the EDC values obtained at all 8 sensor locations for the condition states of; Undamaged, DMG2, RCV & DMG3. Again, it is clear that DMG3 yields a significant change in EDC at the damage location of Sensor 4, however it fails to identify damage at Sensor for condition state DMG2. This is shown in Figure 10, where the percentage variation from baseline for sensors 1-5 for DMG2, RCV & DMG3 is given.

IVI: Figure 11 to Figure 15 present the IVI's obtained for Sensors 1-5, respectively. In each case, the "(a)" subfigure presents the IVIs resulting from the condition states of Undamaged and DMG2. The damage location for DMG2 is at Sensor3, where a vertical member is severed. The evidence shows a slightly greater difference between the two sets of IVI at this location (Figure 13 (a)) when compared against the other 4 Sensor locations, although it is difficult to discern.

For the RCV condition, which entails the repair of the severed vertical member from DMG2 via a welded flange, results are presented in the "(b)" sub-figures of Figure 11 to Figure 15. For all sensors, the IVIs obtained for the RCV condition seem to have reduced from the Undamaged condition IVIs, which may indicate some variability in the vehicle passage loading. However, the RCV IVIs obtained at Sensor3 (Figure 13(b)) portray a greater reduction from the original undamaged state, which may indicate that the welded flange provides an enhance stiffness to the structure than its original condition.

For the DMG3 damage scenario, which entails the severing of a vertical member at Sensor 4, results are presented in the "(c)" subfigures of Figure 11 to Figure 15. From the evidence of these results it is very clear that Sensor 4 shows a greater difference between the two sets of IVI than other locations, who all demonstrate very similar responses of IVI. Note that in this case the reference condition state is that of the RCV damage scenario instead of the Undamaged state, as the severing of the vertical member for DMG3 occurred after the RCV repair work, therefore the use of the original undamaged condition as a reference state for DMG3 would produce variations in IVI for both RCV and DMG3.

To quantifiably assess the results of IVI presented in Figures 11-15, a damage indicator function called Cumulative Difference Ratio (CDR) is used. CDR is presented in Equation 9, where $\sum_{i=1}^n (IVI_{Dam_i})$ and $\sum_{i=1}^n (IVI_{UD_i})$ are the cumulatively summed values of IVI across time for the damaged state and undamaged state, respectively.

Figure 16 presents the IVI variation per sensor per damage scenario using CDR as the damage indicator function. It can be seen that the IVI successfully identifies the damage actions and their locations for DMG2 and DMG3, while also seeming to indicate an enhanced performance for the condition state of RCV, which may signify that the welded flange strengthened the bridge slightly from its original condition.

$$CDR(\%) = \frac{\sum_{i=1}^n (IVI_{Dam_i}) - \sum_{i=1}^n (IVI_{UD_i})}{\sum_{i=1}^n (IVI_{UD_i})} \times 100 \quad (9)$$

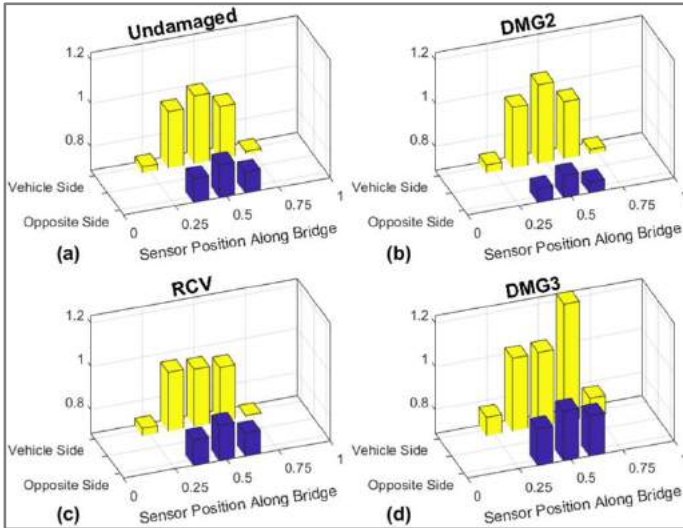


Figure 5. Normalized CAD values per sensor for damage scenarios; (a) Undamaged, (b) DMG2, (c) RCV & (d) DMG3.

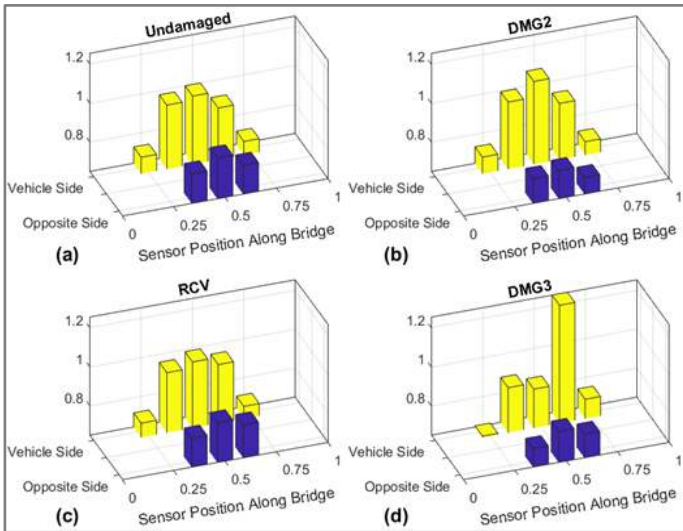


Figure 6. Normalized EDI values per sensor for damage scenarios; (a) Undamaged, (b) DMG2, (c) RCV & (d) DMG3.

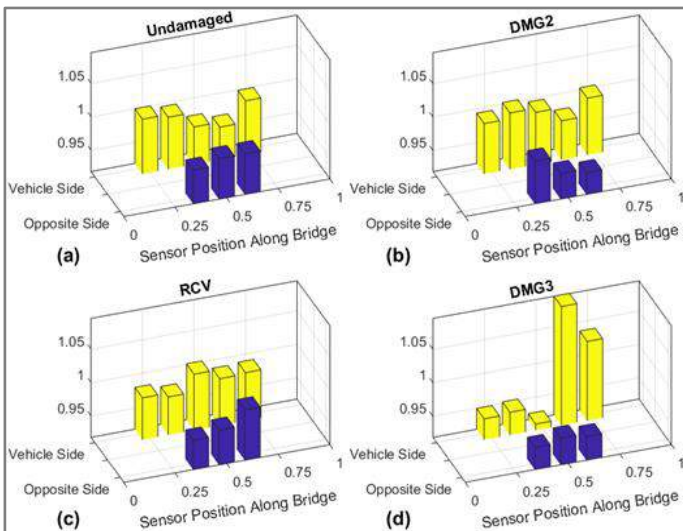


Figure 7. Normalized EDC values per sensor for damage scenarios; (a) Undamaged, (b) DMG2, (c) RCV & (d) DMG3.

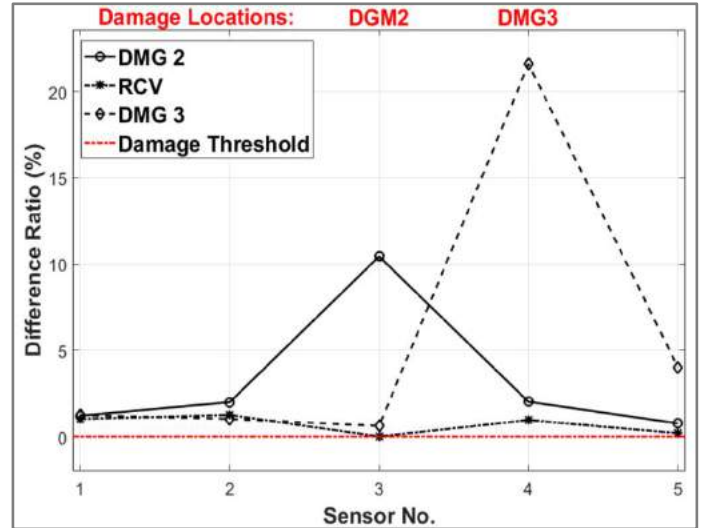


Figure 8. CAD percentage variation from baseline at sensors 1-5 for damage scenarios; DGM2, RCV & DMG3.

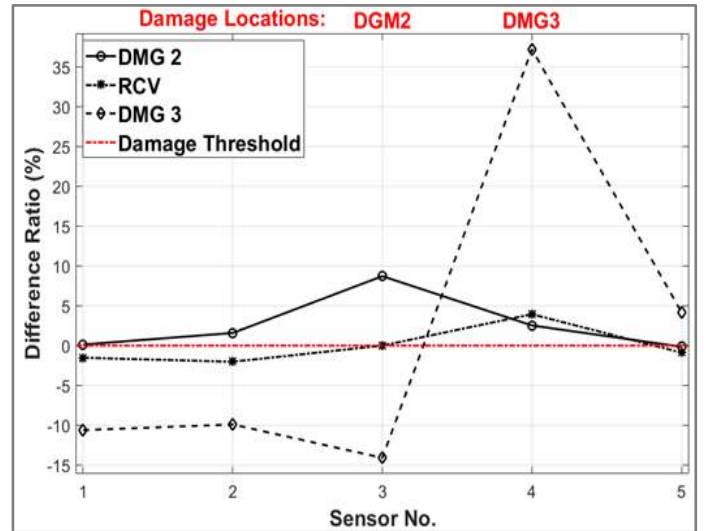


Figure 9. EDI percentage variation from baseline at sensors 1-5 for damage scenarios; DGM2, RCV & DMG3.

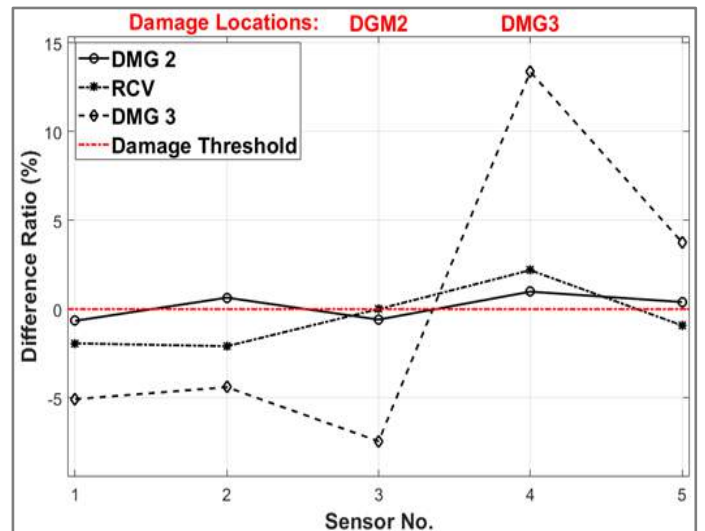


Figure 10. EDC percentage variation from baseline at sensors 1-5 for damage scenarios; DGM2, RCV & DMG3.

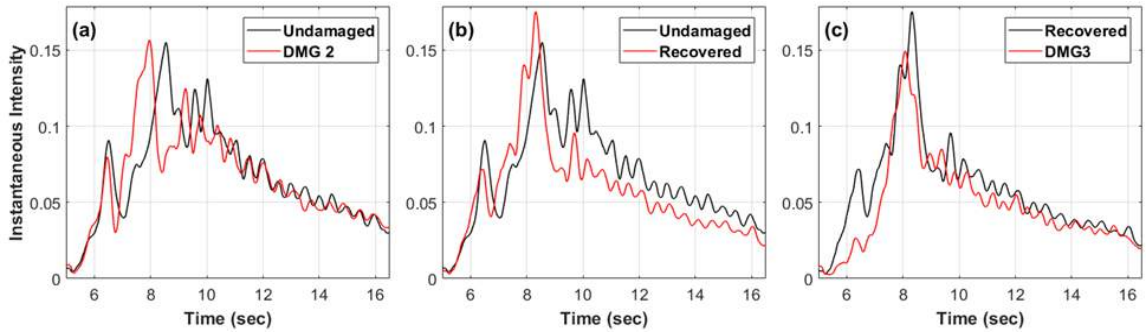


Figure 11. Sensor 1 –IVI responses for damage conditions: (a) DMG2, (b) RCV & (c) DMG3.

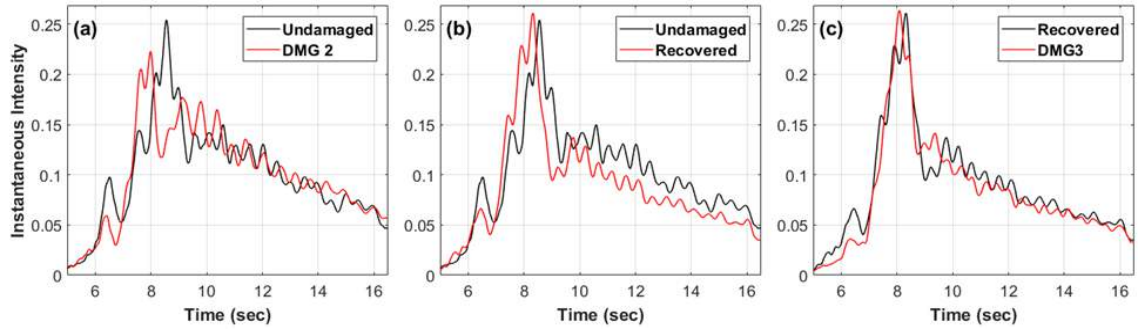


Figure 12. Sensor 2 –IVI responses for damage conditions: (a) DMG2, (b) RCV & (c) DMG3.

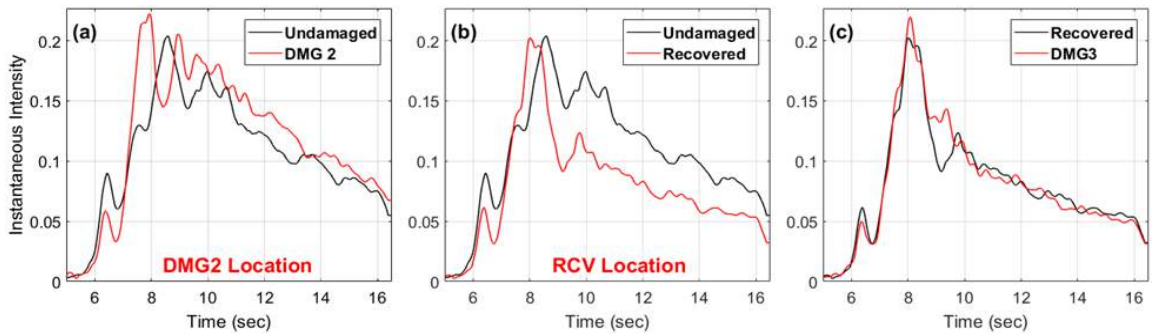


Figure 13. Sensor 3 –IVI responses for damage conditions: (a) DMG2, (b) RCV & (c) DMG3.

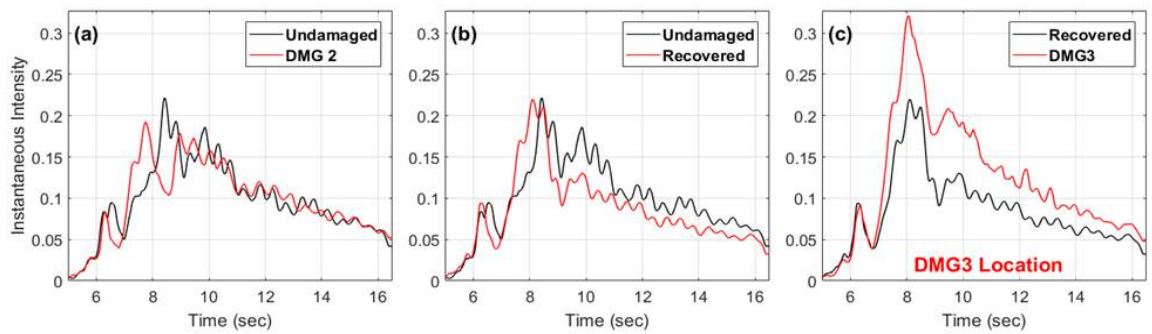


Figure 14. Sensor 4 –IVI responses for damage conditions: (a) DMG2, (b) RCV & (c) DMG3.

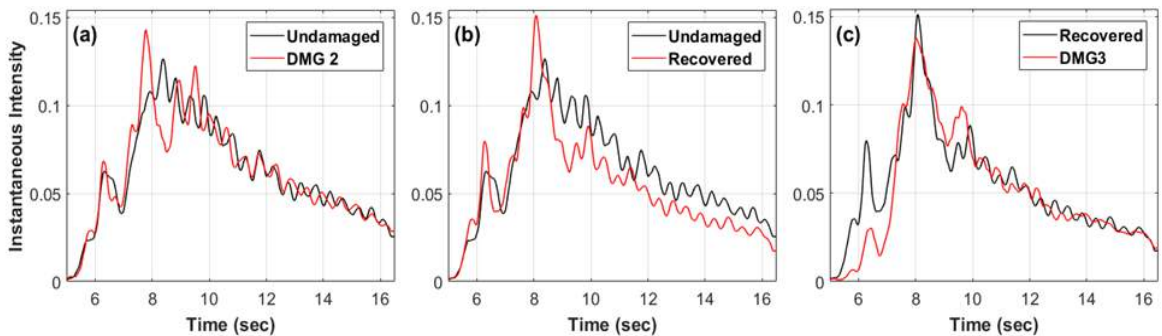


Figure 15. Sensor 5 –IVI responses for damage conditions: (a) DMG2, (b) RCV & (c) DMG3.

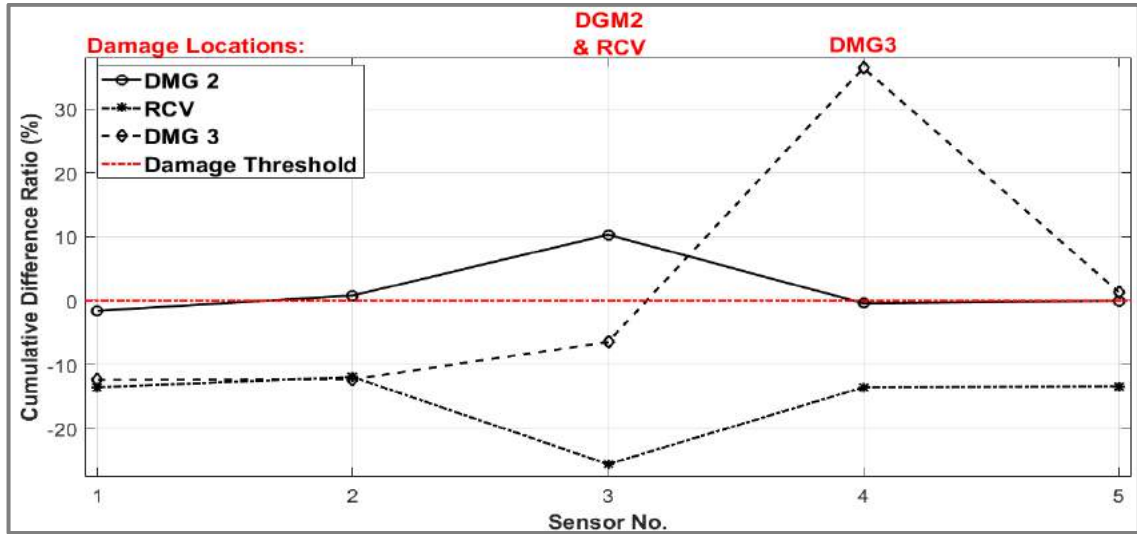


Figure 16. IVI percentage variation at each sensor for damage conditions DGM2, RCV & DMG3 using the Cumulative Difference Ratio damage indicator.

5 DISCUSSION & CONCLUSIONS

The study presented within assessed a number of vibration-based, output-only damage sensitive features specifically developed for damage identification from vehicle induced excitation responses. The parameters assessed were CAD, EDI, EDC & IVI.

To evaluate the damage identification capability of the vibration parameters assessed under vehicle induced excitation, the percentage variation observed at the damage location for condition states; DMG2, RCV & DMG3 are given in Table 2 and are compared against the modal frequency changes for the same damage scenarios in Table 3, as per Kim et al. (2014). From the comparison, all of the vibration parameters assessed appear to outperform the modal frequency changes in this regard.

Further investigation of the exponential decay parameters and IVI is to be completed by the authors to advance damage quantification and to consider the load variability of each vehicle passage.

Table 2. Vibration parameter variation at damage locations

Vibration Parameter	DMG2	RCV	DMG3
CAD	+10.2%	-0.1%	+22.2%
EDI	+8.9%	+0.1%	+36.1%
EDC	-0.4%	0.0%	+13.8%
IVI	+10.31%	-25.56%	+36.40%

Table 3. Modal frequency variation (Kim et al., 2014)

Mode	DMG2	RCV	DMG3
1 st B. Mode	-2.67%	-0.13%	+0.31%
2 nd B. Mode	+0.20%	-0.25%	-5.67%
3 rd B. Mode	-0.21%	-0.87%	-9.05%
4 th B. Mode	+0.22%	-0.72%	-6.87%
5 th B. Mode	+0.58%	+0.19%	-0.16%

ACKNOWLEDGMENTS



This project (<http://trussitn.eu>) has received funding from the EU's Horizon 2020 research and innovation programme under the Marie Skłodowska-Curie grant agreement No. 642453.

The authors would like to thank Prof. Chul-Woo Kim of the Department of Civil and Earth Resources Engineering, Kyoto University, Kyoto, Japan for the generous sharing of the bridge data assessed within the present study.

REFERENCES

- [1] Colominas, M.A., Scholthauer, G. and Torres, M.E. (2014), 'Improved complete ensemble EMD: A suitable tool for bio-medical signal processing', *Biomed. Signal Process. Control*, 14, 19–29.
- [2] Huang, N. E., Z. Shen, S. R. Long, M. C. Wu, H. H. Shih, Q. Zheng, et al. (1998), 'The empirical mode decomposition and the Hilbert spectrum for nonlinear and non-stationary time series analysis', *Proc. R. Soc. London, Ser. A*, 454, 903–993.
- [3] Kim, C.W., Kitauchi, S. and Sugiura, K. (2013), 'Damage detection of a steel bridge through on-site moving vehicle experiments', *Proceedings of the Second Conference on Smart Monitoring, Assessment and Rehabilitation of Civil Structures (SMAR2013)*, Istanbul, Turkey, Sept. 9-11.
- [4] Kim, C.W., Chang, K.C., Kitauchi, S., McGetrick, P.J., Hashimoto, K. and Sugiura K. (2014), 'Changes in modal parameters of a steel truss bridge due to artificial damage', *Proceedings of the 11th Inter. Con. on Structural Safety & Reliability, ICOSSAR, N.Y.*, 3725-3732.
- [5] Moughty, J.J. and Casas, J.R. (2017), 'A state of the art review of modal-based damage detection in bridges: development, challenges, and solutions', *Applied Sciences*, 7(5), 510.
- [6] Moughty, J.J. and Casas, J.R. (2018), 'Damage Identification of Bridge Structures using the Hilbert-Huang Transform', *Proceedings of 6th International Symposium on Life-Cycle Civil Eng. (IALCCE 2018)*, Ghent, Belgium, Oct. 28-31.

Fatigue testing of reinforced concrete beam instrumented with distributed optical fiber sensors (DOFS)

António Barrias¹, Joan R. Casas¹, Sergi Villalba²

¹Department of Civil and Environmental Engineering, Technical University of Catalonia, c/ Jordi Girona 1-3, 08034 Barcelona, Spain

²Department of Engineering and Construction Projects, Technical University of Catalonia, c/ Colom 11, Ed. TR5, 08022 Terrassa (Barcelona), Spain

email: antonio.jose.de.sousa@upc.edu, joan.ramon.casas@upc.edu, sergi.villalba@upc.edu

ABSTRACT: The use of fiber optic sensors on civil engineering structural health monitoring (SHM) applications have become quite popular for the past two decades. Within this type of sensors however, the study and use of Optical Backscatter Reflectometry (OBR) based Distributed Optical Fiber Sensors (DOFS) is relatively new. In this way, there is still some uncertainty that would allow the use of this technology in a more systematic and standardized way. Some of this uncertainty is related with the long-term reliability behavior of these sensors when applied on the monitoring of a structure under a large number of load cycles. In this way, the authors conducted a laboratory experiment where a reinforced concrete beam was instrumented with a DOFS that was adhered in a way to allow the measuring of strain on four different longitudinal segments on its bottom surface. A fatigue test was then conducted on this element where the inputted load range was the one expected on a standard highway bridge between its self-weight and the additional traffic load. Furthermore, each longitudinal segment of the DOFS was adhered to the concrete using a different adhesive in order to assess the optimal one in these conditions. The obtained data is then compared with strain gauges that are also instrumented on the concrete beam.

KEY WORDS: distributed optical fiber sensors, structural health monitoring, fatigue testing, concrete, bridges monitoring

1 INTRODUCTION

All civil engineering infrastructures are subjected to degradation due to the insuppressible passage of time and as well as a great number of various external adverse actions, which compromises their structural integrity, and consequently the safety of its users. As of 2016, in the United States alone, 39% of the bridges in the National Bridge Inventory were built over more than 50 years ago and 9,1% of the total number of bridges were deemed structurally deficient. As a result, an average of 188 million trips were performed daily across these structurally deficient bridges and the most recent estimate projects the backlog of rehabilitation projects for these infrastructures at \$123 billion [1].

Therefore, it is of enormous importance the development and subsequent application of measures that extend and improve the lifetime period of civil engineering infrastructures, optimizing its use without hindering the safety of the users. Moreover, it is easily understandable how this enhances the economic competitiveness and environmental sustainability of the regions where these infrastructures are located. It is in this context that the field of Structural Health Monitoring (SHM) has been greatly studied and advanced for the past few decades. Nonetheless, unfortunately, SHM has not yet been practiced in a large scale and in a regular manner in civil engineering structures. One of the reasons being that there is still a deficit of reliable and affordable generic monitoring solutions [2].

The most common SHM implementations have been based until now on traditional electric based strain sensors, accelerometers, and inclinometers among others which present different challenges when applied in real world conditions [3]. On the other hand, optical fiber sensors (OFS)

when compared with the conventionally used electrical sensors provide the enhanced advantages of being immune to electromagnetic interference, withstanding wide range of temperature variations, chemically inert and also being small and lightweight which facilitates its handling and transport [4]. It is in this way that these type of sensors have become one of the most popular research topics looking to its use in SHM practices. Furthermore, this technology has been mostly applied through the use of Fiber Bragg Grating (FBG) sensors [5], which are point sensors.

However, for a great number of applications, more notoriously in the case of large-scale infrastructures, the number of point sensors that is necessary in order to be able to obtain a complete and global strain information monitoring, can become impractically high. Besides, for the specific case of concrete structures, where beforehand, it is practically impossible to know with certainty the exact location of possible crack formations, these point sensors present serious limitations. Also in practical terms, a large number of sensors also present the difficulty of requiring an associated large number of connecting cables making all the monitoring system more complex. It is in this way that distributed optical fiber sensors (DOFS) provides a unique advantage allowing the strain and temperature monitoring of virtually every cross-section of the element where it is attached to, requiring the use of just up to one single sensor and with it, one connecting cable.

2 DISTRIBUTED OPTICAL FIBER SENSORS

Due to the novelty of this technology, the use of DOFS in civil engineering infrastructures SHM is still a relatively recent practice. These sensors share the same advantages of

the other OFS but as mentioned before present the unique advantage of enabling the monitoring over greater lengths extents of the infrastructure and with a very small distance between each measuring points.

These sensors can be bonded or embedded to the structure to be monitored and when temperature or strain variations occur, these changes are going to be transmitted from the material to the sensor, which then generates a deviation of the scattered signal which is being reflected within the fiber cable core. This is the phenomenon behind the distributed optical fiber sensing as defined by the interaction between the emitted light and the physical optical medium. There are three different scattering processes that occur, which are the Raman, Brillouin and Rayleigh scattering [6].

The Brillouin scattering based sensors have been the most studied and practiced within the DOFS systems in civil engineering applications. This is because this scattering technique allows the monitoring over a great lengths, which can get up to several kilometres. Nonetheless, it has an inherent relatively low spatial resolution of just about 1 m, which is not ideal for the monitoring of crack formations and general damage detections among different other applications.

On the other hand, optical frequency domain reflectometry (OFDR) systems, which uses Rayleigh scattering, provide a spatial resolution that can be as high as one millimetre which makes it, in this way, suitable for damage detection and location. This technology is however currently limited to a length of 70 m although this is expected to be greatly enhanced in the near future.

In this study, the authors use the ODiSI A model from LUNA technologies, Figure 1, which is an optical backscattered reflectometry (OBR) system based on the aforementioned Rayleigh OFDR. This technology is presented in greater detail in the following publications [6], [7].

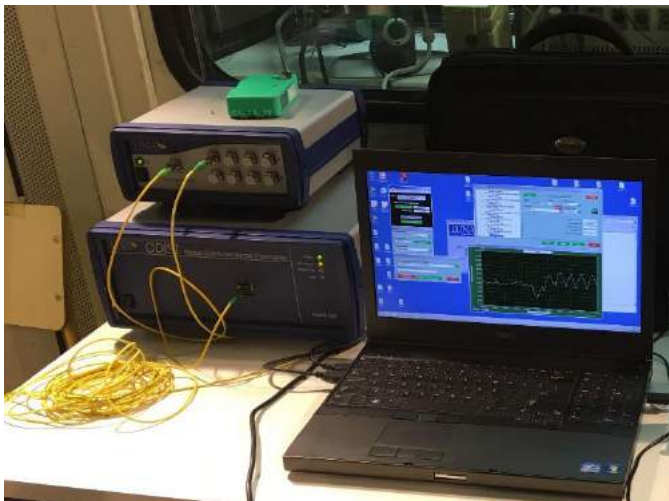


Figure 1. DOFS system used in this experimental campaign.

3 FATIGUE TESTING MOTIVATION

Despite past successful and promising applications where distributed optical fiber sensing technology was used [8]–[10], due to its relatively novelty there are still several uncertainties regarding its use on civil engineering infrastructures. One of these uncertainties, for example, is related with the

performance of these sensors when monitoring real world applications which is translated into long term monitoring periods regarding the stability and reliability of the measurements.

The current available literature regarding the fatigue performance of Rayleigh based OFDR DOFS is extremely scarce. To the authors' knowledge, only two publications were made with this topic.

The first is an engineering note from the manufacturers of the system used in this same experiment, Luna Innovations Incorporated, [11] describes an experiment where polyimide coated distributed DOFS were instrumented to fiberglass coupons and subjected to a $\pm 2000 \mu\epsilon$ and $\pm 4000 \mu\epsilon$ cyclic loads. In this case, it was verified a superior performance of the distributed optical fiber sensors when compared with the also instrumented resistive gauges since the applied DOFS survived the fatigue tests and demonstrated consistency in their strain measurements through the end of the test. On the other hand, the resistive gauges displayed cumulative zero-shift in microstrain from an early period of the fatigue test, which just increased in magnitude throughout the test cycle.

More recently, Wong et al, 2016 described the study of the use of a similar Rayleigh based OFDR distributed sensors to monitor fatigue in a flush step lap joint composite structure used in aerospace engineering [12]. Here it was reported that it was possible to monitor the fatigue induced damage propagation until failure using the mentioned DOFS system. The distributed sensor was also able to follow the crack propagation generated along the adhesion of the stepped lap joint due to the fatigue loading.

Along these lines, the authors decided to assess the performance of these DOFS under a great number of cyclic loads but which were representative of real world conditions, i.e. similar to what is expected to be observed in real and common bridge structures. This is inserted in the scope of the authors' current research, which is related to the use of this type of distributed sensing on the SHM of bridges and other large-scale concrete structures. In this way, an experimental campaign was devised in where a reinforced concrete specimen was instrumented with DOFS and loaded with a high number of cycles. The test setup is described in the next section.

4 EXPERIMENTAL TEST SETUP

In order to assess the performance of the DOFS for the monitoring of reinforced concrete elements subjected to a high number of load cycles, a reinforced concrete beam was used. This beam was characterized by having 600 mm length and a square cross-section of 150 mm width by 150 mm height. This element also had two longitudinal $\phi 12$ rebars and four $\phi 6$ stirrups of S500 grade steel. A scheme of the tested beam is pictured in Figure 2.

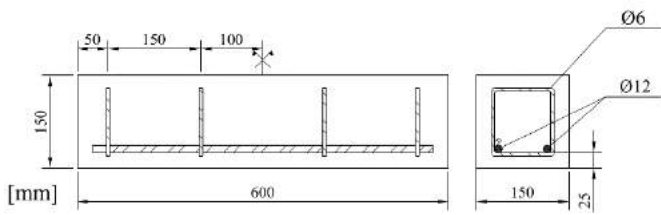


Figure 2. Beam definition scheme (Dimensions in mm).

A 5.2 m long polyimide DOFS was externally bonded to the beam specimen forming a pattern consisting on three horizontal segments in the lateral front face of the beam and four equal horizontal segments in the bottom surface as depicted in Figure 3. Nonetheless, for the purposes of this document, only the results from the four segments adhered to the bottom surface are analysed and presented.

As an additional point of interest in the study, different types of adhesives were used to bond the DOFS to the concrete in order to assess its fatigue performance and deliberate on the optimal one for future applications. In this way, a cyanoacrylate, epoxy, polyester and neutral cure silicone adhesives were used as depicted in Figure 3 and 4.

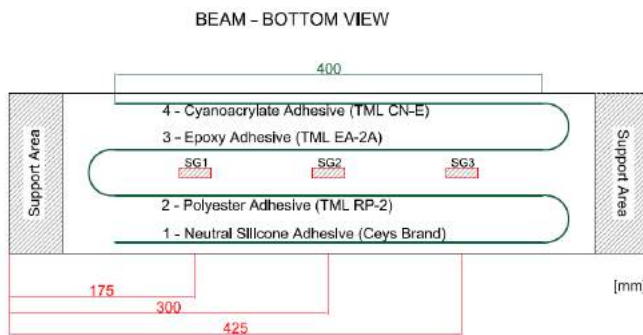


Figure 3. Instrumented sensors at the tested concrete beam.



Figure 4. Photograph of the bottom surface of one of the tested specimens.

Furthermore, three 30 mm length electrical strain gauges from Tokyo Sokki Kenkyujo Co., Ltd were adhered to the bottom surface of the concrete beam among the already mentioned DOFS in order to allow the comparison of the results from both set sensors. The specimen was loaded in a three-point bend test and in this way, the measurements obtained by each segment of the DOFS could be directly compared between them and the three strain gauges, Figure 5.

Additionally, at the time of the production of the concrete for the tested beam specimen, additional cylindrical samples were formed. Afterwards, these samples were tested close to

the date of the test on the beam in order to obtain the mechanical properties of this material. Subsequently, the mean compressive strength (f_{cm}), the mean tensile strength (f_{ctm}) and the mean Young modulus of the concrete (E_c) were obtained as shown in Table 1. With this, the expected maximum tensile strain (ϵ_{ct}) was also obtained.

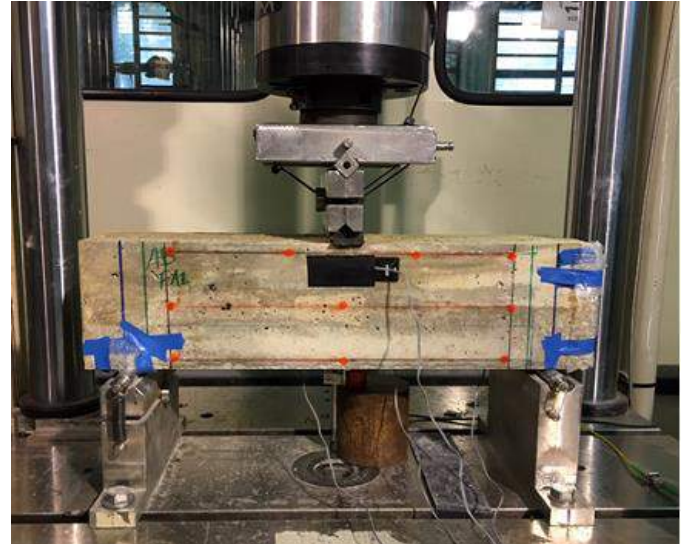


Figure 5. Load arrangement on tested reinforced concrete beam.

Table 1. Concrete material properties

Properties	f_{cm} [MPa]	f_{ctm} [MPa]	E_c [MPa]	ϵ_{ct} [$\mu\epsilon$]
Concrete	48.027	3.944	37886.64	104.1

As mentioned before, the idea was to introduce in the specimen a stress range that would replicate the stress range due to vehicular loads in a standard and common reinforced concrete bridge. Therefore, the two load stages considered for the input of the load cycles were as follows: the lower stress level corresponding to the sole actuation of the self-weight and the higher stress level to the combination of self-weight plus additional traffic. This additional traffic is represented as a four-axle truck with a force of 120 kN by axle and multiplied by a dynamic factor of 1.3, as described in Fatigue Load Model 3 of EN 1991-2 [13].

The stress increments were applied with a frequency of 4 cycles per second up to a 2 million cycles. The applied load level was not expected to generate strain higher than the beam's concrete ϵ_{ct} and thus not expected to induce cracking as seen on Table 2.

Moreover, due to the long and extensive duration of the test, it was deliberated to record the DOFS data being measured every 50 thousand cycles during 5 minutes (1200 cycles). Moreover, these sensors were configured to record measurements every 5 seconds and with a spatial resolution of 1 cm.

Table 2. Load scenarios considered on the load cycles input

	Load combination	Maximum bending moment [kN.m]	σ [MPa]	Equivalent load to apply to beam specimen [kN]	Expected strain [$\mu\epsilon$]
Load Cycle Level [inf]	self-weight	3712.9	2.612	11.75	68.9
Load Cycle Level [sup]	self-weight + additional traffic	4336.3	3.050	13.73	80.5

5 DISCUSSION OF RESULTS

Following the conduction of the three-point load test, the measured data was processed and analysed. It is important to mention that although the data from the DOFS was measured with a sampling acquisition frequency of 0.2 Hz, the data from the strain gauges and from the load actuator was measured with a sampling acquisition frequency of 1 Hz and then decimated and synchronized in order to timely match to the DOFS data.

Furthermore, it is also important to mention that during the conduction of the test there was an electrical power shut-off that occurred at the 180664 cycles mark- Since DOFS measurements were being conducted every 50 thousand cycles, this episode was not recorded live by this set of sensors. After this, the test resumed from this step and continued smoothly until the end.

In this way, Figure 6 depicts the measured data by the DOFS segments adhered to the bottom surface of the concrete over the number of performed load cycles. It is possible to observe how all the adhered segments measure the strain distribution along the beam bottom length over the applied number of load cycles. In this comparison step, it is also noticeable how the silicone bonded segment presents a general smoother spatial measurements when compared with the remaining used adhesives, especially comparing with the cyanoacrylate bonded segment which presents some irregularities and even a small peak close to its midpoint.

In Figure 7, the measured data by the DOFS bonded segments at their midpoints is compared to the data measured by the strain gauge at the same location (SG2). The first and most immediate observation is the difference between all the DOFS bonded segments and SG2. It is observed how all the segments except the cyanoacrylate bonded one start with a measured strain below of what was expected as described in Table 2.

Here it is also observable how after the beginning of the load process there is an increase of the DOFS measured strain until the 150×10^3 cycles mark followed by a small and sudden decrease which the authors believe to be related with the aforementioned electrical power shut-off that occurred at the 180664 cycles mark. Afterwards, a relative stabilization is achieved around the 400×10^3 cycles until the end of the test. This stabilization is considerably more noticeable in the silicone and polyester bonded segments when compared with the remaining two.

Comparing with the values obtained by SG2, it is visible that its initial measured strain is also below of what was expected followed by an increase until $72.61 \mu\epsilon$ at 100×10^3 cycles. This increase is however smaller than the one verified by the DOFS. Then, SG2's readings depicts the same sudden drop around the 200×10^3 followed by a stabilization around

$67 \mu\epsilon$ at the 250×10^3 cycles mark. In this way, it is seen how the greater and longer increase verified by the DOFS sensors beyond the 100×10^3 cycles mark, when compared with the data measured by SG2 is never recovered and is the main issue behind the difference between these two set of sensors throughout the test.

In Figure 8, the readings of each DOFS segment at the beginning and end of the applied load cycles is represented, together with the corresponding measurements of the strain gauges. Here it is even more noticeable how although the DOFS measurements match very well the ones acquired by the strain gauges at the beginning of the load cycles, at the end of these, the two set of sensors present distinct readings. In fact, the average strain increment observed for the DOFS over the fatigue load test was of $29.6 \mu\epsilon$ whereas the SG2 measured an increment of just $9.7 \mu\epsilon$.

It is important to mention that after the conclusion of the test and therefore for an applied load of 0 kN the DOFS measurements present residual readings. These values when subtracted to the measurements at the end of the cycles have the same magnitude of the readings at its beginning. These results were not initially expected and further analysis is currently being performed in order to obtain more assertive conclusions about these findings.

6 CONCLUSIONS

In this document, the performance of DOFS when instrumented on reinforced concrete structures under fatigue testing was performed. A 5.2 m polyimide DOFS was instrumented on a reinforced concrete beam, which was submitted to 2 million load cycles, under a three-point load configuration. The applied load amplitude was representative of what would be expected on a common concrete bridge. As an additional point of interest, four different types of bonding adhesives were used for the implementation of the DOFS to the beam.

It was observed, how the used adhesives influenced the DOFS readings as each bonded segment presented different levels of magnitude for the strain readings during the entire loading process. Furthermore, apart from the differences in values it was seen how the silicone and polyester bonded segments presented a more defined stabilization of its measurements compared with their cyanoacrylate and epoxy counterparts. This stabilization is more in accordance to what was verified by the strain gauge measurements although the order of the measured values of this sensor were distinct of all DOFS segments readings.

These are the initial findings of the performance of the DOFS technology under a high number of load cycles and further analysis is necessary for a more resolute outcome.

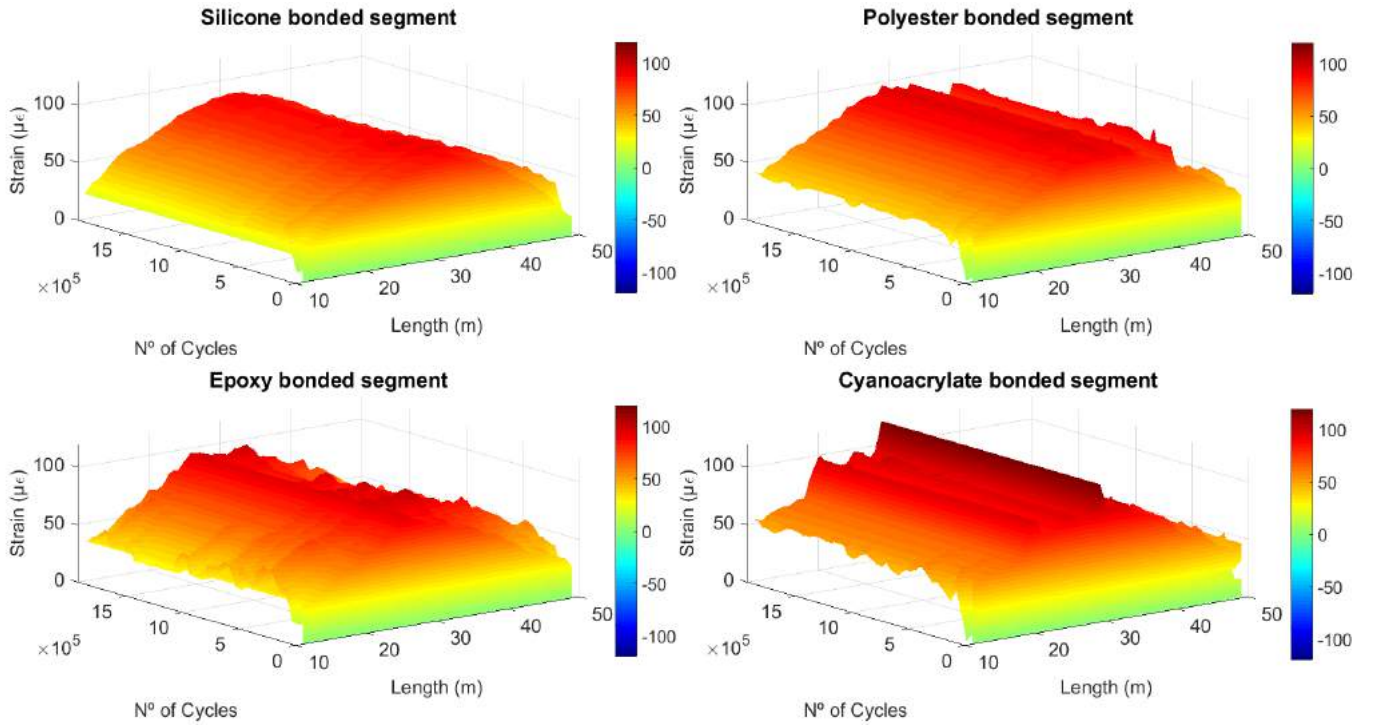


Figure 6. Strain obtained over the four segments on the bottom surface of the tested reinforced concrete beam.

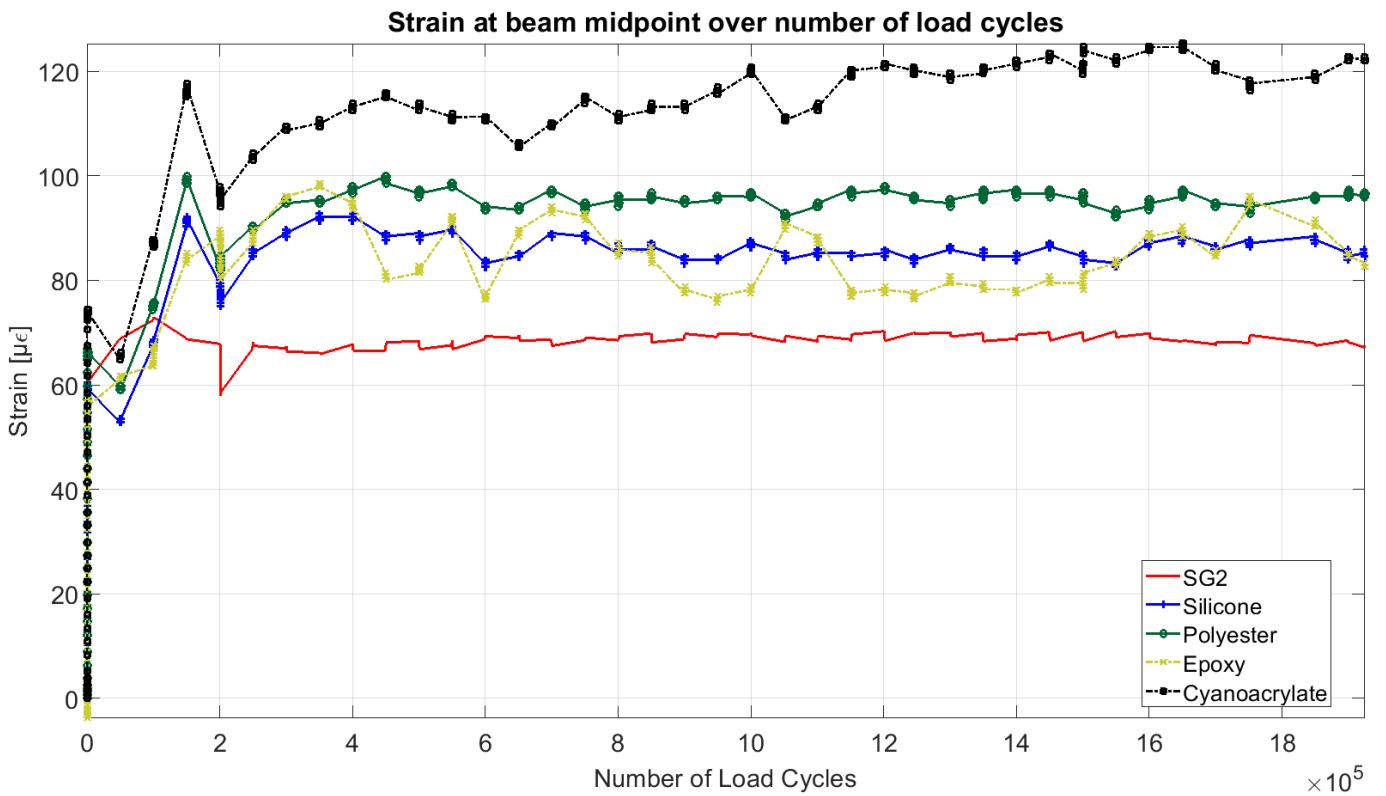


Figure 7. Comparison of measured strain at DOFS segments midpoints and strain gauge 2.

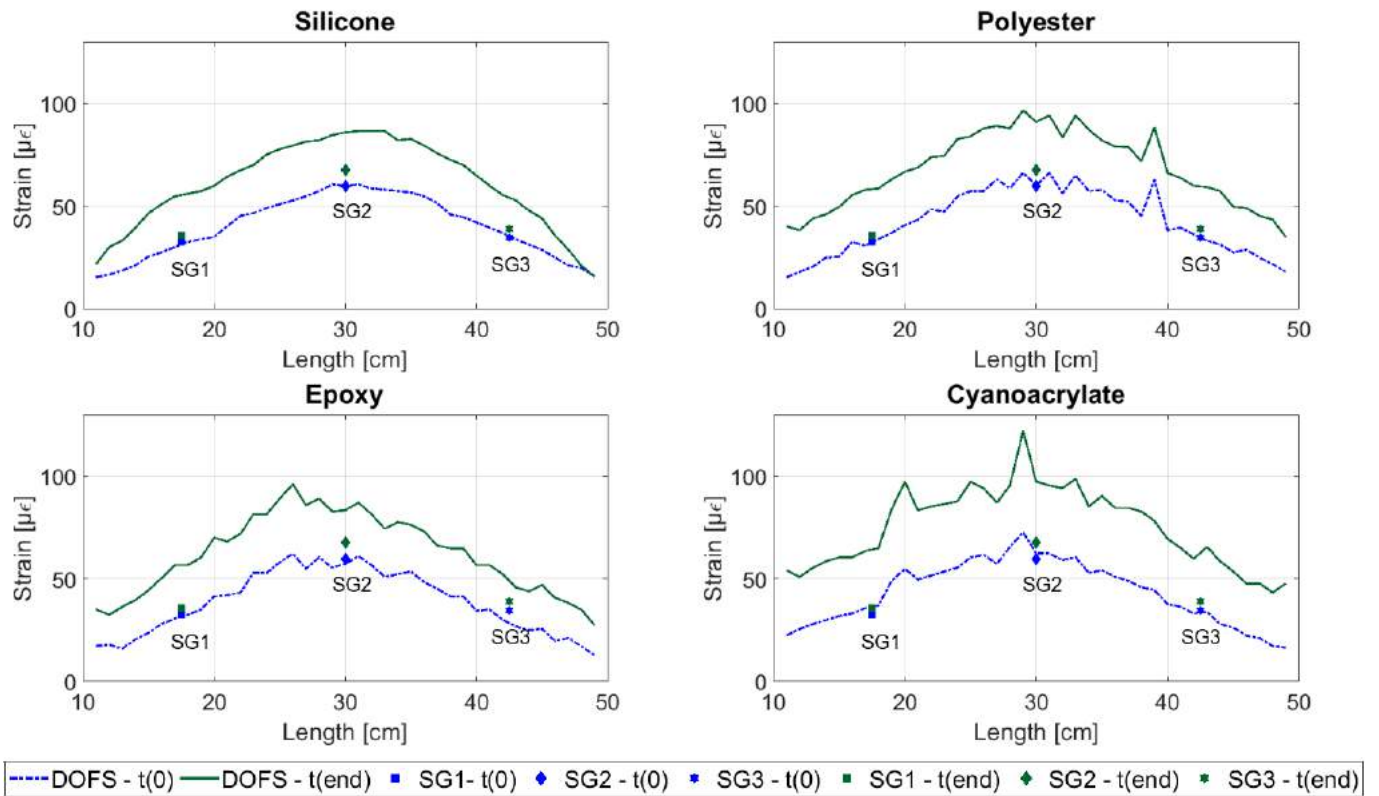


Figure 8. Measured strains by the DOFS and strain gauges at the beginning and end of the applied load cycles.

ACKNOWLEDGMENTS



The authors want to acknowledge the financial support provided from the European Union's Horizon 2020 research and innovation programme under the Marie Skłodowska-Curie grant agreement No. 642453.

REFERENCES

[1] American Society of Civil Engineers, *Infrastructure Report Card ASCE*, 2017.

[2] Glisic, B., Hubbell, D., Sigurdardottir, D.H. and Yao, Y. (2013), 'Damage detection and characterization using long-gauge and distributed fiber optic sensors', *Opt. Eng.*, 52, 87101.

[3] Kudva, J.N., Marantidis, C., Gentry, J.D. and Blazic, E. (1993), 'Smart structures concepts for aircraft structural health monitoring', *1993 North American Conference on Smart Structures and Materials*, 964-971.

[4] Casas, J.R. and Cruz, P.J.S. (2003), 'Fiber Optic Sensors for Bridge Monitoring', *J. Bridg. Eng.*, 8(6), 362-373.

[5] Ferdinand, P. (2014), 'The Evolution of Optical Fiber Sensors Technologies During the 35 Last Years and Their Applications in Structure Health Monitoring', *EWSHM-7th Eur. Work. Struct. Heal. Monit.*

[6] Barrias, A., Casas, J.R. and Villalba, S. (2016), 'A review of distributed optical fiber sensors for civil engineering applications', *Sensors*, May, 16(5), 748.

[7] Rodriguez, G., Casas, J.R., and Villalba, S. (2015), 'SHM by DOFS in civil engineering: a review', *Struct. Monit. Maint.*, Dec, 2(4), 357-382.

[8] Villalba, S. and Casas, J.R. (2012), 'Application of optical fiber distributed sensing to health monitoring of concrete structures', *Mech. Syst. Signal Process.*, 39(1), 441-451.

[9] Rodriguez, G., Casas, J.R. and Villalba, S. (2015), 'Cracking assessment in concrete structures by distributed optical fibre', *Smart Mater. Struct.*, 24(3), 35005.

[10] Barrias, A., Rodriguez, G., Casas, J.R. and Villalba, S. (2018), 'Application of distributed optical fiber sensors for the health monitoring of two real structures in Barcelona', *Struct. Infrastruct. Eng.*

[11] Rahim, N.A.A. et al., *Superior fatigue characteristics of fiber optic strain sensors*, LUNA, 2013.

[12] Wong, L., Chowdhury, N., Wang, J., Chiu, W.K. and Kodikara, J. (2016), 'Fatigue damage monitoring of a composite step lap joint using distributed optical fibre sensors', *Materials (Basel)*, 9(5), 374.

[13] CEN (European Committee For Standardization), *EN 1991-2*, 2002.

Sensitivity of SHM sensors to bridge stiffness

Daniel Martinez¹, Eugene J. OBrien¹, Abdollah Malekjafarian¹, Yahya M. Mohammed², Nasim Uddin²

¹ School of Civil Engineering, University College Dublin, Dublin 4, Ireland

² Department of Civil, Construction and Environmental Engineering, University of Alabama, Birmingham, USA
emails: daniel.martinezotero@ucd.ie, eugene.obrien@ucd.ie, abdollah.malekjafarian@ucd.ie, yahya1@uab.edu, nuddin@uab.edu

ABSTRACT: Bridges play an important role in transport infrastructure and it is necessary to frequently monitor them. Current vibration-based bridge monitoring methods in which bridges are instrumented using several sensors are sometimes not sensitive enough. For this reason, an assessment of sensitivity of sensors to damage is necessary. In this paper a sensitivity analysis to bridge flexural stiffness (EI) is performed. A discussion between the use of strain or deflections is provided. A relation between deflection and stiffness can be set by theorem of virtual work, expressing the problem as a matrix product. Sensitivity is obtained by deriving the deflection respect to the reciprocal of the stiffness at every analysed location of the bridge. It is found that a good match between the deflection and the bridge stiffness profile can be obtained using noise-free measurements. The accuracy of sensors is evaluated numerically in presence of damage and measurement noise. Field measurements in the United States are also described to identify the potential issues in real conditions.

KEY WORDS: Sensitivity; Accuracy; SHM; Bridge; Sensors; Displacement transducers.

1 INTRODUCTION

Sensor-based monitoring (or direct instrumentation) is gaining in importance compared to visual inspection strategies in bridge assessment. The main advantage of the former over the latter is that measured parameters are expected to be more accurate [1]. However, sensor measurements can be polluted by inaccuracies related to environmental noise [2]. These inaccuracies can be a great drawback in bridge damage detection.

The main objective of Structural Health Monitoring (SHM) is to identify damage in an engineering structure [3]. In this paper, bridges are considered. Ideally, the objective is to obtain the flexural stiffness (EI) throughout the bridge, but in most situations this is not possible. Damage detection can be categorised in four different classes [4]:

1. Damage identification on the bridge,
2. Damage location,
3. Damage assessment (location and quantification) and
4. Structure safety for a damage situation.

Inaccuracies can cause the misidentification of damage at some of these levels.

Bridge assessment can be performed using strain measured with a strain gauge. Strain is the deformation of a solid due to load and an elongation or a contraction results. Bridge assessment usually involve using strains or deflection [5]. Displacement transducers [6] are considered and deflection measurements are used in this paper. Deflection is related to flexural stiffness throughout the bridge by the theorem of virtual work. This formula can be expressed as a matrix product and all deflections can be calculated if all stiffnesses are known. Using this relationship, derivatives of the deflection respect to the reciprocal of the stiffness are used here to determine how sensitive deflection is to bridge damage.

A sensitivity analysis is performed in this paper. Sensitivities in a healthy bridge, a damaged bridge and under noisy conditions are considered. A static finite element model

of two point loads traversing a simply supported bridge is adopted. A damage scenario including loss of stiffness is considered. Noise is added to the simulated deflection measurement and sensitivity is analysed. Three different loading locations are considered as well as an envelope of 26 different loading cases.

2 RELATION OF DEFLECTION TO STIFFNESS

The theorem of virtual work is a central concept in structural engineering. From this equation, the displacement at any point can be obtained [7]. This Unit Load Theorem formulation (Eq. 1) establishes the relation between deflections, bending moments and flexural stiffnesses:

$$u = \int_0^L \frac{MM_u}{EI} dx \quad (1)$$

where u is the bridge deflection at an instant of time, M is the bending moment of the bridge caused by the vehicle's loads, M_u is the bending moment caused by a unit load at the analysed location, EI is the flexural stiffness and L is the length of the bridge. This equation can be discretized and transformed into a vector product as shown in Eq. 2:

$$u = P \cdot J \quad (2)$$

where P represents the vector obtained by the element-by-element product of both bending moments in Eq. 1 and J is a vector of the reciprocals of the flexural stiffness components. In matrix form, Eq. 2 can be written as:

$$u = \{P\}_{1 \times n} \times \{J\}_{n \times 1} \quad (3)$$

where P is a row vector with n elements and J is a column vector with the same number of elements. n is defined by the number of locations analysed on the bridge (elements of the finite element model). This means that if deflection is

calculated at t different instants in time, Eq. 3 can be reformulated as a matrix product:

$$\{u\}_{t \times 1} = [P]_{t \times n} \times \{J\}_{n \times 1} \quad (4)$$

P is a matrix of bending moment products. It has to be adapted depending on the load distribution and the location where deflection is measured.

Measured deflections are affected by several sources of inaccuracy. White noise is considered in this example to calculate the sensitivity of deflection to stiffness. The introduced noise is formulated as a function of the maximum measured deflection [8]:

$$u_{noise} = u_{real} + N_{level} \times N_{noise} \times u_{max} \quad (5)$$

where u_{noise} is the noisy deflection signal, u_{real} is the theoretical real deflection, u_{max} is the maximum theoretical deflection, N_{level} is the noise level as a percentage and N_{noise} is a normal distribution with zero mean and a unit standard deviation.

Sensitivity can be defined as uncertainty in the output relative to the input [9]. Sensitivity can be calculated using the partial derivatives of the output with respect to the input [10]. The reciprocal of the stiffness at every location (input) contributes to the deflection calculation (output), so partial derivatives are needed for each of the measurement locations for sensitivity calculation [10]. This can be presented as in Equation 6.

$$S(i, j) = \frac{\partial u_i}{\partial J_j} \quad (6)$$

where $S(i, j)$ is the sensitivity of the deflection respect to the reciprocal of the flexural stiffness and J_j is the reciprocal of the flexural stiffness at element j .

3 NUMERICAL MODEL

A finite element beam model of a vehicle traversing a bridge is used in this paper. Two point loads separated by a distance Δx are considered to simulate the characteristics of a two axle vehicle. No vehicle-bridge dynamic interaction is considered in the model. The main features are represented in Figure 1.

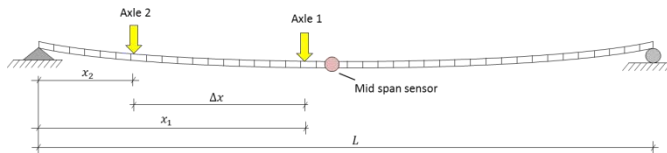


Figure 1. Beam model with two loads.

The loads and the properties of the Euler-Bernoulli beam elements used in this paper are defined in Table 1. A white noise level with $N_{level} = 5\%$ is considered. A single damage location is considered in this paper. A 40% loss of flexural stiffness is simulated. The exact damage location is shown in Figure 2.

Table 1. Point load values and geometrical and mechanical properties of the bridge

Properties	Notation	Value
Point load axle 1	P_1	80 kN
Point load axle 2	P_2	80 kN
Distance between loads	Δx	6 m
Number of elements	n	200
Length	L	20 m
Young's modulus	E	35×10^9 N/m ²
2 nd moment of area	I	1.26 m ⁴



Figure 2. Single damage location for sensitivity analysis.

The sensitivity analysis is performed, considering three different load locations. Figure 3 shows these locations. Location (a) shows a situation in which only the first axle of the vehicle is on the bridge whilst in location (b) first axle is over the mid-span sensor. Location (c) considers a situation in which both the loads have passed mid-span.

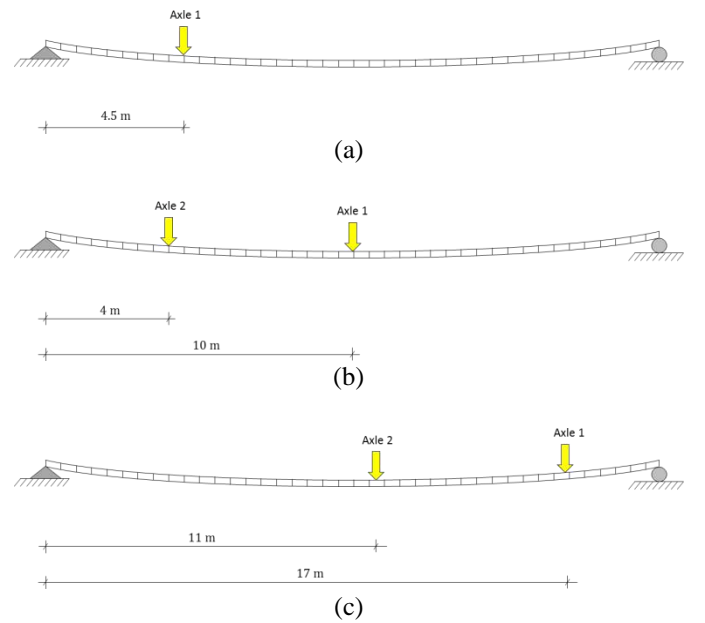


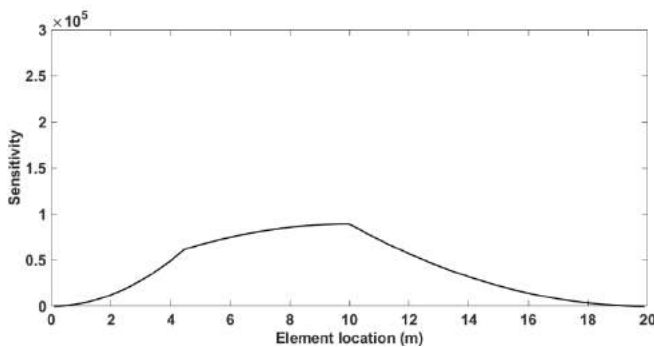
Figure 3. Load cases for sensitivity analysis when (a) 1st axle is at 4.5 m, (b) 1st axle is at mid-span and (c) 1st axle is at 17 m.

4 RESULTS AND DISCUSSION

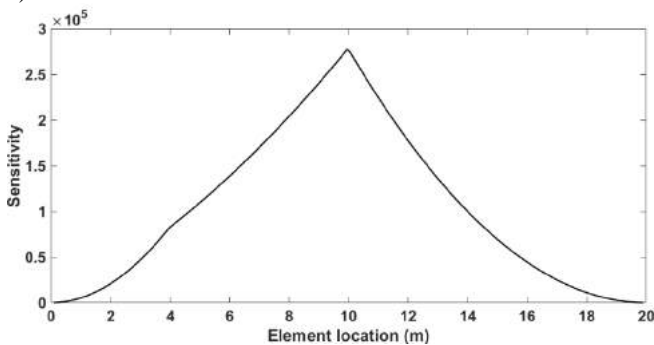
Sensitivities are calculated in this section. Figure 4 illustrates the sensitivities of the deflection signal with respect to the reciprocals of the flexural stiffness (J) at each element location. A value is obtained for every derivative with respect to J_n (see Eq. 6). A continuous plot is created using these values. The sensitivity in Figure 4a has a discontinuity in slope at 4.5 m from the left support, i.e., at the axle location.

The mid-span peak corresponds to the position of the sensor in the simply supported bridge. The greatest sensitivity to flexural stiffness is for the parts of the beam between these points. This trend also occurs in Figures 4b and 4c.

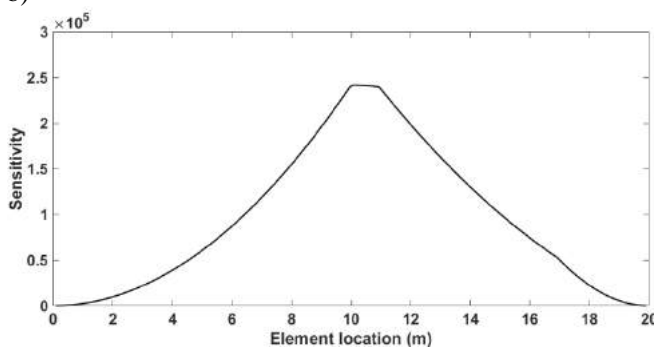
In all cases considered, the peak of the graph is at the sensor location. However, the total load on the bridge and the positions of these loads can influence the sensitivity. The sensitivity of Figure 4a is lower than the sensitivities in Figures 4b and 4c as only one load is located on the bridge and the moments are therefore less. In comparison, the magnitudes of the sensitivities in Figures 4b and 4c are similar. The differences between the former and the latter are caused by the differences in load positions.



a)



b)



c)

Figure 4. Sensitivities obtained from deflection measurements at load case a), b) and c) in Figure 3.

Even if the potential damage is not sensitive for a particular vehicle location, it may be sensitive for other locations. Consequently, an envelope of sensitivities is plotted in Figure 5. Equally spaced loading situations at every metre are considered, totalling 26 cases. The sensitivity envelope is roughly triangular, demonstrating that sensitivity is greatest at the sensor location at the centre of the bridge and reduces

approximately linearly from there. It follows that the sensitivity to damage near the bridge supports is quite low.

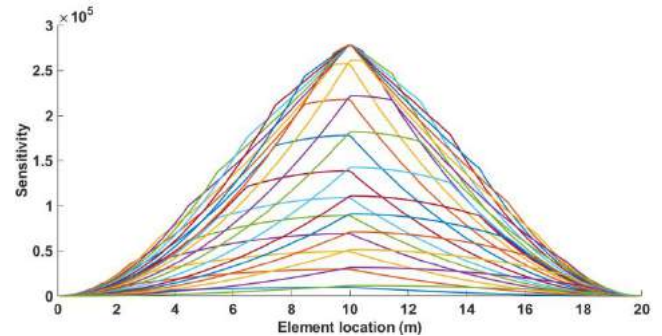


Figure 5. Envelope of the sensitivities.

5 REAL MEASUREMENTS IN DRY CREEK BRIDGE

A test has been taken in Dry Creek Bridge in Alabama, Georgia. The bridge is composed by three simply supported spans and two lanes. Measurements were taken only at the first of the three spans. Five displacements transducers were installed along the cross section of the mid span at five different locations separated by a constant distance. A three axle experimental truck is used to traverse the bridge. One of the lanes is closed for the vehicle to cross the bridge whilst in the other second lane random traffic crosses the bridge. Simplified bridge and vehicle characteristics are displayed in Table 2.

Table 2. Vehicle and bridge mechanical properties

Properties	Notation	Value
Axle load 1	W_1	66.7 kN
Axle load 2	W_2	48 kN
Axle load 3	W_3	46 kN
Distance between Axle 1 and Axle 2	d_{1-2}	4.6 m
Distance between Axle 1 and Axle 3	d_{1-3}	6 m
Vehicle's speed	c	10.12 m/s
Sampling frequency	f_s	200 Hz
Length	L_b	21.34 m
Width	A	10.68 m

Using measured deflections, sensitivity of deflection to an assumed stiffness is analysed. Considering that the bridge has a constant flexural stiffness of $57.7 \times 10^9 \text{ Nm}^2$, a deflection comparison between the real measurements and deflection theoretically obtained is performed. It is assumed that the measured deflection is the average of the three sensors closer to the lane that the truck is traversing. Figure 6 shows that theoretical results are far from the measured deflections as there are many sources of inaccuracy not considered in the model. It can be taken into consideration dynamics, road profile, or noise in displacement transducers.

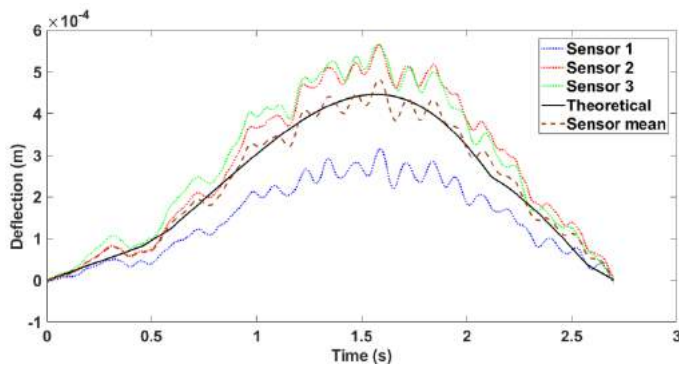


Figure 6. Comparison between theoretical deflection assuming a healthy bridge and the real measurements.

6 CONCLUSIONS

The paper analyses the sensitivity of deflection to bridge flexural stiffness. Sensitivity of deflection to stiffness is dependent on the load and the position of the load that traverses the bridge. Sensitivity is not affected by damage or noise. Unfortunately, measured deflections are very different from the simulated measurements. For this reason, a further analysis is necessary to adapt flexural stiffness to deflections in real conditions. Measurements taken from several vehicles crossing a bridge can improve the accuracy of the bridge deflection.

ACKNOWLEDGEMENTS



The authors acknowledge the support for the work reported in this paper from the European Union's Horizon 2020 Research and Innovation Programme under the Marie Skłodowska-Curie grant agreement No. 642453.

REFERENCES

- [1] OBrien, E.J., Martinez, D., Malekjafarian, A. and Sevillano, E. (2017), 'Damage detection using curvatures obtained from vehicle measurements', *Journal of Civil Structural Health Monitoring*, 7(3), 333-341.
- [2] Peeters, B. and De Roeck, G. (2001), 'One-year monitoring of the Z 24-Bridge: environmental effects versus damage events', *Earthquake engineering & Structural Dynamics*, 30(2), 149-171.
- [3] Ciang, C.C., Lee, J.-R. and Bang, H.-J. (2008), 'Structural health monitoring for a wind turbine system: a review of damage detection methods', *Measurement Science and Technology*, 19(12), 122001.
- [4] Rytter, A. (1993), *Vibration based inspection of civil engineering structures*, PhD Thesis, Dept. of Building Technology and Structural Engineering, Aalborg University, Aalborg, Denmark.
- [5] Lanata, F. and Del Grosso, A. (2006), 'Damage detection and localization for continuous static monitoring of structures using a proper orthogonal decomposition of signals', *Smart materials and structures*, 15(6), 1811.
- [6] Rodrigues, C., Félix, C. and Figueiras, J. (2011), 'Fiber-optic-based displacement transducer to measure bridge deflections', *Structural Health Monitoring*, 10(2), 147-156.
- [7] Salari, M.R., Spacone, E., Shing, P.B. and Frangopol, D.M. (1998), 'Nonlinear analysis of composite beams with deformable shear connectors', *Journal of Structural Engineering*, 124(10), 1148-1158.
- [8] Martinez, D., OBrien, E.J. and Sevillano, E. (2016), 'Drive-by bridge damage detection using curvatures in uncertain environments', *Civil Engineering Research in Ireland Conference (CERI2016)*, Galway, Ireland, August.
- [9] Saltelli, A., Tarantola, S., Campolongo, F. and Ratto, M., *Sensitivity analysis in practice: a guide to assessing scientific models*, 2004.
- [10] Ustinov, E.A., *Sensitivity analysis: Differential calculus of models, Sensitivity Analysis in Remote Sensing*, 3-10, Springer, 2015.

A big data approach for investigating the performance of road infrastructure

Federico Perrotta¹, Tony Parry¹, Luis C. Neves¹, Mohammad Mesgarpour², Emma Benbow³, Helen Viner³

¹Faculty of Engineering, University of Nottingham, University Park, Nottingham, NG7 2RD, England

²Microlise Ltd, Farrington Way, Eastwood, Nottingham, NG16 3AG, England

³TRL Ltd, Crowthorne House, Nine Mile Ride, Wokingham, RG40 3GA, England

e-mail: federico.perrotta@nottingham.ac.uk, tony.parry@nottingham.ac.uk, luis.neves@nottingham.ac.uk

ABSTRACT: “Using truck sensors for road pavement performance investigation” is a research project within TRUSS, an innovative training network funded from the EU under the Horizon 2020 programme. The project aims at assessing the impact of the condition of the road pavement unevenness and macrotexture, on the fuel consumption of trucks to reduce uncertainty in the framework of life-cycle assessment of road pavements. In the past, several studies claimed that a road pavement in poor condition can affect the fuel consumption of road vehicles. However, these conclusions are based just on tests performed on a selection of road segments using a few vehicles and this may not be representative of real conditions. That leaves uncertainty in the topic and it does not allow road managers to review the current road maintenance strategies that could otherwise help in reducing costs and greenhouse gas emissions from the road transport industry. The project investigated an alternative approach that considers large quantities of data from standard sensors installed on trucks combined with information in the database of road agencies that includes measurements of the conditions of the road network. In particular, using advanced regression techniques, a fuel consumption model that can take into consideration these effects has been developed. The paper presents a summary of the findings of the project, it highlights implications for road asset management and the road maintenance strategies and discusses advantages and limitations of the approach used, pointing out possible improvements and future work.

KEY WORDS: Fuel consumption; Road performance evaluation; Big data analysis; TRUSS ITN.

1 INTRODUCTION

In the past several studies focused on assessing the impact of road surface unevenness and macrotexture on vehicle fuel economy (Beuving *et al.*, 2004). This could be of particular interest for governmental authorities and road managers since, if a certain amount of fuel is consumed due to the poor condition of the road surface, maintenance would represent an opportunity for road agencies to reduce costs and the emissions of pollutants from road vehicles significantly.

Recent studies, for example, stated that road unevenness and macrotexture can affect up to 5% of fuel consumption (Beuving *et al.*, 2004; Chatti and Zaabar, 2012). That could mean that road maintenance may allow the United States to reduce costs by \$400 billion and the United Kingdom by £1 billion (with current fuel prices). This, at global level, implies huge possible reduction of costs and emissions from the road transport industry. An opportunity that cannot be neglected.

However, currently road maintenance policies do not account for the extra costs and environmental impact that the poor state of the road infrastructure can generate (Beuving *et al.*, 2004; Chatti and Zaabar, 2012; EP, 2014). This is mainly due to the fact that different studies show different results and because study data are not considered reliable. In the past, researchers collected data by testing a few vehicles driven at a constant speed or performing coast-down measurements on selected and short road segments. Therefore, what still remains unclear is: are those experimental data really representative of real driving conditions at network level?

Because of this uncertainty road maintenance strategies cannot be currently justified and road managers do not account for the direct and indirect costs that the condition of

the road surface can generate for society when making decisions towards road maintenance.

“Using truck sensors for road pavement performance investigation” is a project funded by the European Union under the Horizon 2020 programme within the TRUSS ITN framework (visit www.trussitn.eu for more information). The main aim of the project is to assess the impact of road surface characteristics, such as unevenness and macrotexture, on vehicle fuel economy.

Large quantities of data from trucks driving all across the UK are analyzed in the project and used to model the excess fuel consumption affected by the condition of the road surface. A ‘Big Data’ approach is undertaken combining advanced statistics and machine learning techniques to point out complex correlations across the data and in particular between fuel consumption of the considered vehicles and road surface properties (Perrotta, Parry and Neves, 2017c, 2017b). This represents the main difference with previous studies and testing the feasibility of this innovative approach represents one of the main contributions of the study.

A new fuel consumption model has been developed based on data that comes directly from vehicles driving across the UK. This allows the model to be continuously updated and representative of real driving conditions. This gives to road managers a new method to test the performance of the road infrastructure in terms of vehicle fuel economy in almost real time. That will help engineers in justifying a review of the current road maintenance policies and drivers in selecting the most eco-friendly route between two locations making the road transport industry more efficient.

The paper summarizes results of the project, highlighting implications for road asset managers and discussing advantages and disadvantages of the developed method and possible future developments.

2 DATA

Data about the performance of trucks come anonymized from the database of Microlise Ltd. Microlise is a company that offers fleet management services to its clients by collecting, storing and analyzing data from any vehicle type but mostly from trucks. In fact, in accordance to SAE J1939 (SAE International, 2016) modern trucks are equipped with many sensors that constantly monitor the performance of this vehicle type.

The data include characteristics of the vehicle itself (e.g. type of truck, number of wheels, manufacturer, etc.), vehicle speed, engine parameters (e.g. used torque and revolutions), GPS location and fuel consumption to the nearest 0.001 liter among other parameters and is collected every minute or mile (that is ~1609 m). By analyzing these data, Microlise helps its clients (e.g. big chains of supermarkets, multinational delivery companies, truck manufacturers, etc.) in optimizing the operational costs of their vehicle fleets. That can be in regards to fuel consumption, maintenance of vehicles, training of drivers, optimization of delivery time, etc.

On the other hand, road agencies periodically collect data to analyze the performance of their infrastructure and to inform their decisions towards maintenance of road pavements. These data include road geometry (e.g. gradient, crossfall, radius of curvature, etc.), materials used to build (or rehabilitate) road pavements, measurements of road unevenness and macrotexture, skid-resistance, etc.

These data combined represent an opportunity to model fuel consumption with the possibility of modelling the excess of fuel spent because of the conditions of the road surface. This in the past has been done using experimental data and fuel consumption has been modelled using a physical/mechanistic approach (e.g. Emma Benbow, Brittain, & Viner, 2013; Chatti & Zaabar, 2012). A new challenge for future work would be to model fuel consumption and the excess of fuel spent based on data from vehicles driving under real driving conditions and in situations representative of the whole network.

Previous studies on the topic typically used measurements of IRI (International Roughness Index) for road unevenness and MPD (Mean Profile Depth) for macrotexture. However, in UK, road unevenness is measured as Longitudinal Profile Variance (LPV) at 3, 10 and 30 meters wavelength and macrotexture is measured as Sensor Measured Texture Depth (SMTD). Benbow, Nesnas, & Wright (2006) and Viner et al. (2006) established that these unevenness and texture parameters are closely related.

Measurements are taken at high frequency by a diagnostic vehicle thanks to the lasers and standard sensors installed on it (Highways Agency, 2008). The data is stored in the Highways Agency Pavement Management System (HAPMS) and can be accessed through authorization of Highways England, the strategic road agency in England.

3 METHODOLOGY

This section describes the techniques and methods used in the project to analyse data and construct the fuel consumption model. First this section introduces the methodology applied to clean the data and enrich information from the truck fleet management system with data from the HAPMS.

Then, it focuses on variable selection and on the techniques used for assessing the significance of correlation between road surface characteristics and truck fleet fuel consumption. Finally, techniques used to build the developed model and make estimates of the effect of the road surface conditions on the amount of fuel spent by the considered fleet of trucks are described.

R ver. 3.4.1 (CRAN, 2017) is the main software used for analyzing the data, with 'glmnet' (Friedman et al., 2017), 'caret' (Kuhn, 2017), 'e1071' (Meyer et al., 2017), 'randomForest' (Liaw et al., 2017), and 'neuralnet' (Fritsch, et al., 2016) as main packages used within the project.

3.1 Data mining

As this project represents an initial study which aims at testing the feasibility of a 'Big Data' approach for assessing the impact of road surface characteristics on vehicle fuel consumption, a few assumptions have been made in order to simplify the data analysis and reduce the effect of nonlinearity on the fuel consumption of the considered fleet of trucks. For this reason, only data from heavy trucks driving at constant speed (+/- 2.5 km/h) and collected on motorways (at relatively high speed, ~70-100 km/h) have been analysed. These filters reduce the amount of data available from more than a million rows to a few thousands, which still represent a significant amount of data rarely examined in the literature before.

3.2 Variable selection

In regression analysis one of the most delicate and controversial phases for modelling is the selection of predictors. In fact, identifying causation and distinguishing that from correlation is not an easy task and may require time and multiple tests. For this reason and because linear regression was initially used to model fuel consumption in a first phase of the project, statistics like the Pearson's correlation coefficient, the Akaike Information Criterion (AIC) (Akaike, 1974), and analysis of p-values and the adjusted-R² were used to select the best predictors that increase accuracy and reliability of the developed model.

Although these statistics can be used when dealing with linear regression, recent studies showed that these do not always work well, especially when the data comes in large quantities, from different sources and may hide highly non-linear correlations (Lew, 2013; Baker, 2016).

For this reason, alternative statistics and mathematical methods have been used and tested in combination. in order to obtain more accurate and reliable results.

In particular, methods such as:

- the Lasso (least absolute shrinkage selection operator) (Tibshirani, 1996), a method similar to linear regression that performs variable selection through regularization with the aim of enhancing interpretability and accuracy of the developed models (James, et al. 2013);

- Principal Components Analysis (Pearson, 1901; Hotelling, 1933), a statistical method based on orthogonal transformation commonly used in regression analysis for dimensionality reduction and feature selection (Song, et al. 2010),
- Random Forests (Breiman, 2001), a machine learning method based on the theory of decisions trees (Breiman, et al. 1984) commonly used to solve complex classification or regression problems and that is able to perform variable selection;
- and, Boruta Algorithm (Kursa and Rudnicki, 2010), an evolution of the random forests method specifically designed for variable selection.

have been used to identify the predictors that give the highest correlation with fuel consumption, that increase accuracy and reliability of the developed model, avoiding overfitting.

3.3 Modelling

In the first phase of the study various attempts at fitting a linear regression to the data have been performed (Perrotta et al., 2017; Perrotta, Parry and Neves, 2017c, 2017a) with variables that have been selected by analyzing the Pearson's correlation coefficients, p-values, adjusted-R², AIC and Lasso. Selection of the best predictors to use in the developed models results from an analysis and comparison of all of these statistics listed and causation identified based on the findings of experimental studies (e.g. Emma Benbow et al., 2013; Chatti & Zaabar, 2012).

In the second phase of the project, due to the high quantity and variety of data available application of machine learning has been tested for modelling the fuel consumption of the considered fleet of trucks and performance compared to the linear regression model developed in the first phase. In fact, using machine learning algorithms allows non-linear correlations, avoiding overfitting and issues related to the multicollinearity of predictors. That allows for example, to consider the effect of different wavelengths of unevenness on fuel consumption that may vary in different situations (e.g. different vehicle speed).

For instance, in this second phase of the project, three different models have been developed using different machine learning techniques (Perrotta, Parry and Neves, 2017b, 2018). A Support Vector Regression (SVR) (Gunn, 1998), a Random Forest (RF) (Breiman, 2001) and a back-propagation Artificial Neural Network (ANN) (Goh, 1995) models have been developed. The methods have been chosen as it was found in the literature that these have already been used for modelling the fuel consumption of road vehicles successfully (e.g. Laxhammer & Gascón-Vallbona, 2015; Xu & Zhao, 2010; Zeng et al., 2015). However for different tasks it is not possible to know a priori which method works best and performance may vary based on the accuracy and quantity of the data available. For this reason, all three methods have been tested and performance compared in terms of root-mean squared error (RMSE), mean absolute error (MAE), R² and calculation time.

Due to the way machine learning algorithms work they need to be trained and fed with data before they can give accurate and reliable estimates (James et al., 2013; Ng, 2018). Usually the higher the amount of data fed for training and the higher

the performance of the developed machine learning model (Ng, 2018). However, sometimes performance of the model can depend on how the data is split and generate overfitting (James et al., 2013; Ng, 2018). Crossvalidation (James et al., 2013) is used in order to avoid that.

In the project ten-fold crossvalidation was used in order to develop the SVR, RF and ANN models. This consists in repeating the training process ten times with different subsets of data in order to test the variability of results for different training sets. Constant performance of the model among the ten trials prove that results do not depend on how the data is split and that bias is spread homogeneously across the data.

Initially, a 4 ± 2.5 % set is extracted from the data. That is used to test the performance of the developed models. This is chosen as containing records from trucks that are not included in the rest of the data (96 ± 2.5 %). Similarly, 25% of the remaining data is used for validation and 75% for training. The fact that training, validation and test sets do not contain data from the same trucks allows to test the ability of the developed models to generalize patterns and correlations through the data, avoiding overfitting.

One of the major criticisms in Engineering in regards to the use of machine learning models such as SVR, RF and ANN is the fact that these work as black-boxes and have low interpretability in comparison to linear regression or physical based models. For this reason, a parametric analysis has been conducted in order to 'open' the black box and see how SVR, RF, and ANN approximate the correlation between predictors and fuel consumption. This consists of using SVR, RF and ANN to predict the fuel consumption of trucks for fifty different values of each of the considered variables. The values are chosen to be evenly distributed within the 5th and 95th percentiles of the distribution of the considered predictor. While the value of one predictor changes all others are set to their average.

4 RESULTS

In the first phase of the study, a multiple linear regression model has been developed using data from different truck fleet systems. This was to try to understand the type of information available and explore opportunities within the data.

For example, in one of these initial studies 1420 records from 260 trucks, driving at constant speed on the M18, a motorway in UK, have been analyzed. The data were used to develop a linear model of fuel consumption with measurements of unevenness and macrotexture among the predictors.

In particular, the model presented in (Perrotta, Parry and Neves, 2017c) has equation:

$$FC = 62.42 + 0.00024 \text{ GVW} + 14.84 \text{ g\%} - 0.57 \text{ s} + 0.26 \text{ LPV10} + 0.87 \text{ SMTD} \quad (1)$$

where *FC* is fuel consumption (in l/100km), *GVW* the gross vehicle weight (in kg), *g%* the road gradient (in %), *s* the vehicle speed (in km/h), *LPV10* unevenness as longitudinal profile variance at 10 m wavelength (in mm²), and *SMTD* macrotexture sensor measured texture depth (in mm), see Figure 1.

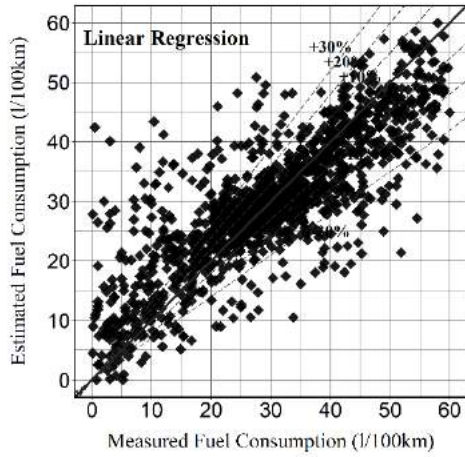


Figure 1. Fit of the linear model. Adapted from (Perrotta, Parry and Neves, 2017c).

Performance of the model in terms of RMSE, MAE and R^2 are summarized in Table 1:

Table 1. Summary of performance of the model presented in (Perrotta, Parry and Neves, 2017c).

RMSE	MAE	R^2
7.80	5.55	0.68

For the considered fleet of trucks the model estimates that 3% of fuel consumption is affected by LPV10 (unevenness) and 5% by the SMTD (macrotexture) of the road surface. As predictors, the model contains only 5 of the 45 variables available. These have been chosen based on the AIC and adjusted- R^2 statistics. Similar results have been obtained previously with other samples of data (Perrotta *et al.*, 2017; Perrotta, Parry and Neves, 2017a).

In the second phase of the study, application of machine learning to fuel consumption modelling of the considered fleet of trucks have been performed.

In this study (Perrotta, Parry and Neves, 2017b), 14,281 records from 1110 articulated trucks driving along the whole M18 and part of the M1 (probably the most important motorway in UK and part of the strategic road network in England) for a total length of ~300 km of road were investigated.

The study investigated the capabilities of three machine learning techniques and their performance compared to those of the linear regression performed on the same data. In particular, the developed machine learning models are a SVM, a RF and an ANN (Perrotta, Parry and Neves, 2017b). The models contain 14 out of 56 variables initially available that include the gross vehicle weight, the road gradient, radius of curvature of the road, the vehicle speed, average acceleration, engine parameters such as revolutions and torque (at start and end of the record), gear used, activation of cruise control (0/1), measurements of road unevenness at three, ten and thirty metres wavelength (i.e. LPV03, LPV10 and LPV30) and measurement of the macrotexture of the road pavement

(SMTD). These have been identified to significantly impact the fuel consumption of the considered fleet of vehicles (Perrotta, Parry and Neves, 2017b) by using the random forest algorithm for variable selection (Breiman, 2001).

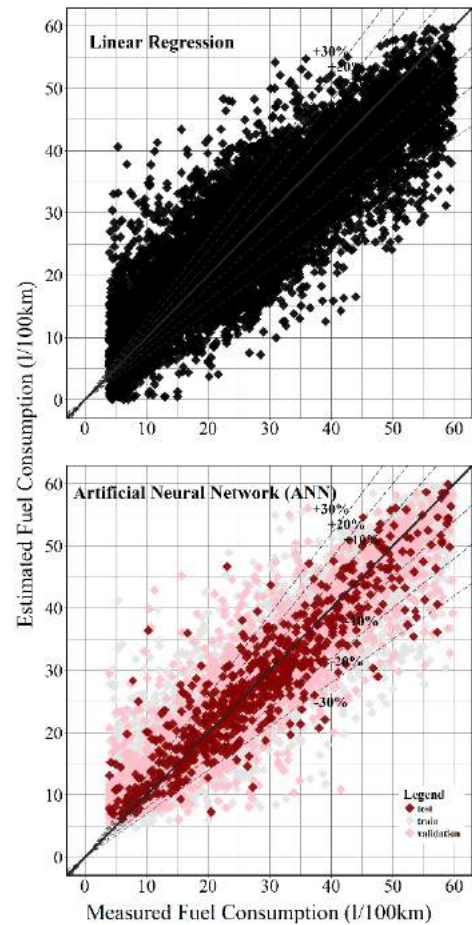


Figure 2. Fit of the ANN model published in (Perrotta, Parry and Neves, 2017b) and comparison with a linear regression model developed using the same data.

Figure 2 reports the fit of the developed ANN model and compares it to the fit of linear regression for the same data. Ten-fold crossvalidation is performed on the machine learning models for training but only one of the models is shown in the Figure. Due to the fact that machine learning algorithms need training before they can be used for making any estimate on new situations three colors are used in order to distinguish estimations made by the developed model on the training, validation and test sets.

Performance of the models in terms of RMSE, MAE and R^2 (for test sets and averaged on the ten crossvalidation processes for the ANN) are summarized in Table 2.

The authors show also that the RF model gives the highest performance in terms of RMSE, MAE and R^2 , slightly better than the ANN (i.e. $R^2 = 0.87$). However, this is also the model that requires the highest crossvalidation time for training (double that required by the ANN).

Table 2. Summary of performance of the ANN model presented in (Perrotta, Parry and Neves, 2017b) and comparison with performance of a linear regression model built on the same data.

Model	RMSE	MAE	R ²
Linear reg.	6.02	4.42	0.76
ANN	4.88	3.46	0.85

Finally, estimation of the effect of road surface conditions on fuel consumption can be computed by performing a parametric analysis. Figure 3 reports some examples of parametric analysis performed on the linear regression and ANN model developed.

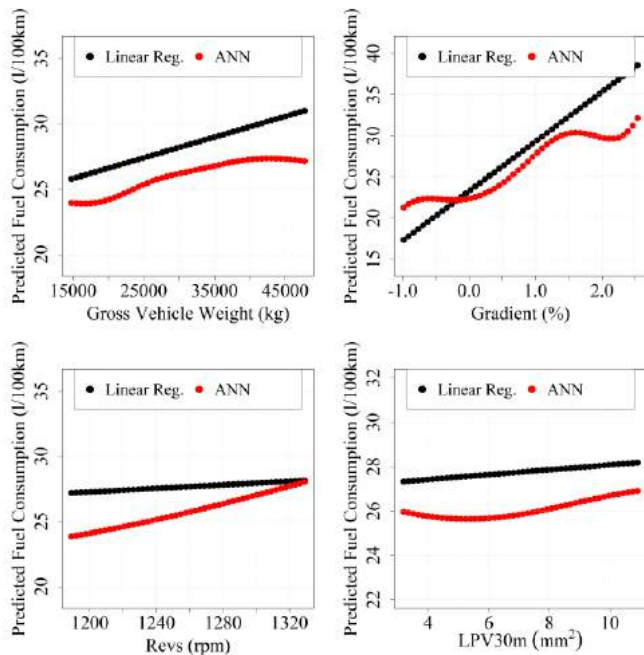


Figure 3. Examples of a parametric analysis and comparison of estimates between the linear regression and machine learning models developed in (Perrotta, Parry and Neves, 2017b).

This allows to compute the effect of each of the considered variables on vehicle fuel consumption for the fleet of trucks analyzed and also makes the developed SVR, RF and ANN partially interpretable.

5 CONCLUSIONS

Results of the project show great potential for the ‘Big Data’ approach to be used for modelling the fuel consumption of road vehicles including the possibility of estimating the influence that road surface characteristics have on this.

Initial results showed that a linear regression of the variables is able to predict the fuel consumption of the considered fleet of trucks and that this is able to estimate the impact of each of the single variables used as predictors on fuel consumption. This allows to estimate the impact of road surface properties on vehicle fuel economy that has been assessed at approximately 3% - 4% for road unevenness (LPV10) and at 1.25% - 5% for macrotexture (SMTD)

(Perrotta et al., 2017; Perrotta, Parry and Neves, 2017a). This substantially confirms results reported by experimental studies (Sandberg, 1990; Beuving et al., 2004; Chatti and Zaabar, 2012) and gives more confidence in the used approach.

However, the fact that linear regression is not reliable for very large quantities of data, it does not allow to identify and estimate non-linear effects and it cannot consider non-numerical or non-continuous variables, represent limitations that can be overcome by using machine learning. This is why in the second part of the project performance of SVR, RF and ANN have been investigated.

Results show that machine learning is able to outperform linear regression, in terms of RMSE, MAE and R² and that inclusion of more data and types of measurements could allow the developed models to further improve in precision, accuracy and reliability of estimates.

One issue presented by machine learning algorithms is the time required for training that increase with 1) the number of repetitions used for crossvalidating the model, 2) quantity of data analyzed and 3) complexity of the structure of the model used. However, this remains lower than the time required to organize, perform and analyze data from experiments that was the approach used in the past (e.g. Chatti & Zaabar, 2012).

Exploration of a wider range of vehicle types and investigation of a more extensive road network could help in obtaining results representative of real driving conditions in UK. That will improve applicability of the study and may help engineers in justifying a review of the current road design and maintenance strategies that may help highway authorities in reducing the emissions of pollutants from the road transport industry and save significant costs.

Also, performing a sensitivity analysis (Cortez and Embrechts, 2013) could allow to improve interpretability of the results helping in further testing the reliability of the obtained estimates.

In future, when data for different vehicle types will be available and accessible, this approach could help engineers in estimating the excess costs and environmental impact that the conditions of the road surface have on vehicle fuel economy and inform their decisions towards road design and maintenance of the road surface. That would be important to consider also for electric vehicles since batteries could last longer on smoother road pavements and possibly increase the distance that a vehicle can travel with a single charge.

ACKNOWLEDGEMENTS



This project has received funding from the European Union Horizon 2020 research and innovation programme under the Marie Skłodowska-Curie grant agreement No. 642453 and it is part of the Training in Reducing Uncertainty in Structural Safety project (TRUSS ITN, www.trussitn.eu).

REFERENCES

- Akaike, H. (1974) ‘A new look at the statistical model identification’, *IEEE Transactions on Automatic Control*, 19(6), pp. 716–723. doi: 10.1109/TAC.1974.1100705.
- Baker, M. (2016) *Statisticians issue warning over misuse of P values*, *Nature*. Macmillan Ltd. doi: 10.1038/nature.2016.19503.
- Benbow, E., Brittain, S. and Viner, H. (2013) *Potential for NRAs to provide energy reducing road infrastructure*. MIRAVEC - Deliverable D3.1.
- Benbow, E., Nesnas, K. and Wright, A. (2006) *PPR131 - Shape (surface*

- form) of *Local Roads*. Crowthorne (London).
- Beuving, E. et al. (2004) 'Environmental Impacts and Fuel Efficiency of Road Pavements', (March).
- Breiman, L. et al. (1984) *Classification and Regression Trees, The Wadsworth Statistics/Probability series*. doi: 10.1371/journal.pone.0015807.
- Breiman, L. (2001) 'Random forests', *Machine Learning*, 45(1), pp. 5–32. doi: 10.1023/A:1010933404324.
- Chatti, K. and Zaabar, I. (2012) 'Estimating the Effects of Pavement Condition on Vehicle Operating Costs', *NCHRP Report 720*. Washington, D.C.: Transport Research Board.
- Cortez, P. and Embrechts, M. J. (2013) 'Using Sensitivity Analysis and Visualization Techniques to Open Black Box Data Mining Models', *Information Sciences, Elsevier*, (225), pp. 1–17. doi: <http://dx.doi.org/10.1016/j.ins.2012.10.039>.
- CRAN (2017) *R ver. 3.4.1 'Single Candle', the Comprehensive R Archive Network*. Available at: <https://cran.r-project.org/bin/windows/base/old/3.4.1/> (Accessed: 24 April 2017).
- EP (2014) 'EU road surfaces: Economic and safety impact of the lack of regular road maintenance', *Policy Department for Structural and Cohesion Policies, European Parliament*.
- Friedman, J. et al. (2017) 'R Package: glmnet, Ver. 2.0-13'.
- Fritsch, S. et al. (2016) 'R Package: neuralnet, Ver. 1.33'.
- Goh, A. T. C. (1995) 'Back-propagation neural networks for modeling complex systems', *Artificial Intelligence in Engineering*, 9(3), pp. 143–151. doi: 10.1016/0954-1810(94)00011-S.
- Gunn, S. R. (1998) *Support Vector Machines for Classification and Regression, Faculty of Engineering, Science and Mathematics, School of Electronics and Computer Science*. Southampton. doi: 10.1039/B918972F.
- Hotelling, H. (1933) 'Analysis of a complex of statistical variables into principal components', *Journal of Educational Psychology*, 24(6), pp. 417–441. doi: 10.1037/h0071325.
- James, G. et al. (2013) *An Introduction to Statistical Learning, Springer Texts in Statistics*. New York, NY: Springer Science+Business Media New York (Springer Texts in Statistics). doi: 10.1007/978-1-4614-7138-7.
- Kuhn, M. (2017) *R Package: caret - Classification and Regression Training, Ver. 6.0-76*, <https://Cran.R-Project.Org/Package=Caret>. Available at: <https://github.com/topepo/caret/>.
- Kursa, M. B. and Rudnicki, W. R. (2010) 'Feature Selection with the Boruta Package', *Journal Of Statistical Software*, 36(11), pp. 1–13.
- Laxhammer, R. and Gasc'on-Vallbona, A. (2015) 'D4.3. Vehicle models for fuel consumption', *Seventh Framework Programme - COMPANION*, (610990), pp. 1–13. doi: 610990.
- Lew, M. J. (2013) 'To P or not to P: on the evidential nature of P-values and their place in scientific inference', (December 2012). Available at: <http://arxiv.org/abs/1311.0081>.
- Liaw, A. et al. (2017) 'R Package: randomForest, Ver. 4.6-12'. doi: 10.5244/C.22.54.
- Meyer, D. et al. (2017) *R Package: e1071, Ver. 1.6-8*. Available at: <https://cran.r-project.org/web/packages/e1071/e1071.pdf>.
- Ng, A. (2018) *Machine Learning Yearning - Technical Strategy for AI Engineers in the Era of Deep Learning*. Stamford, CA, USA: Draft.
- Pearson, K. (1901) 'On Lines and Planes of Closest Fit to Systems of Points in Space', *Philosophical Magazine*, 2(11), pp. 559–572. doi: 10.1080/14786440109462720.
- Perrotta, F. et al. (2017) 'Route level analysis of road pavement surface condition and truck fleet fuel consumption', in Al-Qadi L., I., Ozer, H., and Harvey, J. (eds) *Pavement Life-Cycle Assessment*. Champaign, Illinois: CRC Press, pp. 51–57. doi: 10.1201/9781315159324-7.
- Perrotta, F., Parry, T. and Neves, L. C. (2017a) 'A big data approach to assess the influence of road pavement condition on truck fleet fuel consumption', in Dell'Acqua, G. and Wegman, F. (eds) *Transport, Infrastructure and Systems: Proceedings of the AIIT International Congress on Transport, Infrastructure and Systems*. Rome, Italy: CRC Press, pp. 33–38. doi: <https://doi.org/10.1201/9781315281896-7>.
- Perrotta, F., Parry, T. and Neves, L. C. (2017b) 'Application of Machine Learning for Fuel Consumption Modelling of Trucks', *2017 IEEE International Conference on Big Data*.
- Perrotta, F., Parry, T. and Neves, L. C. (2017c) 'Using truck sensors for road pavement performance investigation', in Čepin, M. and Briš, R. (eds) *Safety and Reliability – Theory and Applications, Proceedings of 27th annual European Safety and Reliability Conference, ESREL 2017*. Portoroz, Slovenia: CRC Press Taylor & Francis Group, pp. 392–396. doi: 10.1201/9781315210469-343.
- Perrotta, F., Parry, T. and Neves, L. C. (2018) 'Evaluation of road pavements fuel efficiency using truck sensors data', in *TRAVISIONS Young Researchers Competition 2018, Transportation Research Arena (TRA) 2018*. Vienna (16–19 April, 2018).
- SAE International (2016) 'SAE J1939-71, Vehicle Application Layer - Surface Vehicle Recommended Practice', *SAE International Standards*. SAE International. Available at: http://standards.sae.org/j1939/71_201610/.
- Sandberg, U. (1990) 'Road macro-and megatexture influence on fuel consumption', in Meyer, W. E. and Reichert, J. (eds) *Surface Characteristics of Roadways: International Research and Technologies*. Philadelphia, pp. 460–479. doi: 10.1520/STP23382S.
- Song, F., Guo, Z. and Mei, D. (2010) 'Feature Selection Using Principal Component Analysis', *2010 International Conference on System Science, Engineering Design and Manufacturing Informatization*, pp. 27–30. doi: 10.1109/ICSEM.2010.14.
- The Highways Agency (2008) 'HD 30/08 Maintenance Assessment Procedure', *Design Manual for Roads and Bridges, Volume 7, Section 3*.
- Tibshirani, R. (1996) 'Regression Shrinkage and Selection via the Lasso', *Journal of the Royal Statistical Society. Series B (Methodological)*, 58(1), pp. 267–288. doi: <http://dx.doi.org/10.1111/j.1467-9868.2011.00771.x>.
- Viner, H. et al. (2006) *PPR148 - Surface Texture Measurement on Local Roads*. Crowthorne (London).
- Xu, X. and Zhao, Y. (2010) 'Prediction of fuel consumption per 100km for automobile engine based on Gaussian processes machine learning', in *International Conference on Mechanical Engineering and Green Manufacturing 2010, MEGM 2010*, pp. 1951–1955. doi: 10.4028/www.scientific.net/AMM.34-35.1951.
- Zeng, W., Miwa, T. and Morikawa, T. (2015) 'Exploring trip fuel consumption by machine learning from GPS and CAN bus data', *Journal of the Eastern Asia Society for Transportation Studies*, 11(June 2016), pp. 906–921.

Automated bridge deck evaluation through UAV derived point cloud

Siyuan Chen¹, Linh Truong-Hong¹, Debra F. Laefer^{1,2}, Eleni Mangina³

¹Department of Civil Engineering, University College Dublin, Ireland

²Center for Urban Science and Progress and Department of Civil and Urban, New York University, US

³Department of Computer Science, University College Dublin, Ireland

Email : siyuan.chen@ucd.ie, linh.truonghong@ucd.ie, debra.laefer@nyu.edu, eleni.mangina@ucd.ie

ABSTRACT: Imagery-based, three-dimensional (3D) reconstructions from Unmanned Aerial Vehicles (UAVs) hold the potential to provide a safer, more economical, and less disruptive approach for bridge inspection. This paper describes a methodology using a low-cost UAV to generate an imagery-based, dense point cloud for bridge deck inspection. Structure from motion (SfM) is employed to create a three-dimensional (3D) point cloud. Outlier data are removed through a density-based filtering method. Next, the unsupervised learning algorithm k-means and an object-based region growing algorithm are compared for accuracy with respect to bridge deck extraction. Last, an automatic pavement evaluation method is proposed to estimate the deck's pavement condition. The procedure is demonstrated through an actual case study, in which a 3D point cloud of 16 million valid points was generated from 212 images. With that data set, the region growing method successfully extracted the deck area with an F-score close to 95%, while the unsupervised learning approach only achieved 76%. In the last, to evaluate the surface condition of the extracted pavement, a polynomial surface fitting method was designed to evaluate and visualise the damages.

KEYWORDS: UAV, Bridge inspection; Point cloud; Segmentation; Deck extraction; Pavement inspection; SfM.

1 INTRODUCTION

Bridge inspection has traditionally been conducted by highly-skilled inspectors but associated with safety problems, especially for those inspectors. While van- and robot-based inspection capabilities have been developed to replace in-person methods [1], ultimately those inspection methods still rely on the physical inspectors or machines on site, which cause traffic closure and/or high equipment costs.

Advances in the unmanned aerial vehicle (UAV) industry and in computer vision have enabled the introduction of low-cost UAVs into the market and affiliate image process techniques that can be paired for bridge documentation. This type of approach is attractive, because it involves non-contact measurement, no traffic closures, no heavy/special equipment, and no need for experienced inspectors on-site. Additionally, the state-of-the-art computer vision-based methods allow generation of accurate, highly dense point clouds from UAVs-images with a single digital camera, which shows UAV-based abilities to capture three-dimensional (3D) topographic data of structures. These new abilities coupled with lower costs have accelerated the adoption of UAVs for infrastructure documentation related tasks including building modelling [2], dam inspection [3], and road surface evaluation [4].

However, most existing UAV work is focused on 3D model generation and does not address the specific aspects related to inspection. To address these gaps, this study first presents a work flow of utilizing a Structure from Motion (SfM) approach to generate a point cloud from low-altitude, aerial images collected by a low-cost UAV. Then, a noise reduction algorithm is introduced. Next a comparison of two deck extraction methods is made (a machine learning clustering method and an object segmentation approach involving a

region growing algorithm). Finally a means is provided for automated deck inspection.

2 RELATED WORKS

2.1 UAV Based 3D Reconstruction and Noise Removal

In recent years, less expensive and more easily controllable UAVs have increased their popularity for low altitude, close-range infrastructure inspection [5]. To aid in such activities, a wide range of detectors have been applied, such as digital cameras [6], laser scanners [7], multi-spectral cameras [8] and thermal cameras [9]. Among those, the digital camera is the cheapest and most common. A straightforward approach to achieve documentation with this equipment involves capturing two-dimensional (2D) images for analysis. For example, Chen et al. collected 2D imagery for identifying highway bridge cracks [10]. However, 2D images do not provide depth information directly, which precludes calculating volumetric damage (e.g. spalling). An alternative solution involves using images captured from multiple view angles to reconstruct an object in three dimensions (3D). A common strategy to achieve this is through the application of SfM [11] to multiple images taken from a single camera. SfM has been extensively studied and widely applied for a range of related applications [e.g. 12-14].

In general, SfM detects key (i.e. unique) features from each image. As these images are taken from multiple viewpoints, by linking these key points together, a 3D structure can be assembled (e.g. [15]). Compared to the traditional 3D point cloud generation methods from laser scanning, the UAV imagery reconstructed point offers the opportunity to include data obtained from less restricted by view angles, than from many other means, thereby providing

better coverage at lower costs. However, imagery-based point clouds are often much noisier than those from laser scanning data. Noise typically occurs from structural artefacts in the acquisition process or mismatching of features in images during the reconstruction process [16]. Noisy points can affect further surface reconstruction or point classification for damage detection. To minimize these negative effects, post-processing is applied for noise reduction. A typical solution involves the Statistical outlier removal (SOR) filter, which assumes that noisy points have distinguishable characteristics from non-noisy point in a k-dimensional space when fitting the data to a standard probability distribution [17].

2.2 Possible Bridge Deck Extraction and Evaluation Approaches

The task of bridge deck extraction relies on point cloud segmentation. This can be achieved by numerous means, but two common approaches involve either (1) machine learning or (2) object-based segmentation [18]. While machine learning based clustering can include multiple methods such as k-means, mean shift, neural network, and deep learning, this paper uses the k-means clustering. This method is able to classify 3D points into K groups using different features. The grouping is done by minimizing the sum of squares of distances between the point and the corresponding cluster centroid [19]. In contrast, object-based segmentation can be described as belonging to a class of procedures involving model fitting and region growing methods [20]. The model fitting method uses geometric primitives like planes, cylinders, and spheres to fit the point cloud and decompose the object. The approach works well for simple structures but tends to perform poorly in the face of large data sets or complex geometries [18]. Thus, this method is not considered further in this study, as the bridge structure is likely to be too complex to decompose – a problem previously noted by researchers using laser scans [21, 22]. The region growing method uses local features extracted from a neighbourhood around each point to aggregate nearby points with similar properties and thereby segment a region of a point cloud [20].

However, aforementioned studies have been focused on processing point cloud data derived from laser scanning. Such point clouds differ from those derived from imagery in several important ways. First, the laser scanning data do not contain red-green-blue (RGB) values, unless captured with an integrated camera. Instead, they have affiliated intensity measurements based on the strength of the returning laser signal. Second, the distribution of laser scanning points tends to follow specified patterns based on the pre-programmed operational movements of the scanner. Conversely, the imagery derived points are more randomly distributed around the structure surface, especially when acquired from a UAV, even if the UAV is following a pre-programmed flight path. This difference in data acquisition leads to differences in density and normals.

In the case of a stationary laser scanner, density degradation is more predictable (e.g. if scanning from a river bank, the angle of incidence combined with the offset will impact the point yield, as described in detail in [23] and demonstrated by Truong-Hong in the case of a metal bridge in [24]). As features play important roles in the point cloud segmentation process, there is a need to prioritize finding robust and

relevant features in the derived heterogeneous point cloud. These issues have yet to be addressed systematically in the peer-reviewed literature.

3 WORKFLOW FOR UAV-BASED BRIDGE DECK INSPECTION

To overcome some of these difficulties, a new work flow is proposed, as shown in Figure 1. First, a low-cost, commercial UAV is employed for image acquisition. Then, SfM is applied to generate a 3D point cloud from the 2D images. Next, noise caused by shadows and water reflections are removed automatically with a novel, new algorithm. Then an automatic deck extraction step occurs. Finally, a health evaluation matrix is proposed for deck assessment. Notably, herein two deck extraction approaches are compared: k-means clustering and region growing.

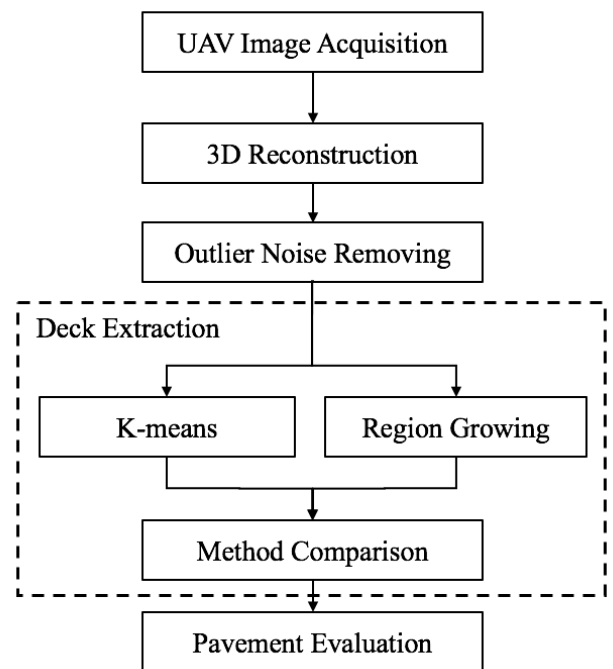


Figure 1. Flowchart of data processing of the developed bridge deck inspection system.

3.1 Image Acquisition

To validate the approach, a case study was conducted using the Blessington bridge in County Wicklow, Ireland. The bridge is of reinforced concrete and about 130 m long, 8 m wide, and situated 10 m above the water (Figure 2). A DJI Phantom 4 quadrotor was equipped with a 4K camera and a 3-axis gimbal; (total cost about 1,500 euros). To ensure full acquisition, 7 parallel flight paths along the bridge were undertaken (2 from each side of the bridge and 3 above the deck). Acquisition occurred from 10 to 20 m away. UAV operations were manually controlled by a remote pilot through a first-person view camera, with a safety inspector in attendance to watch for obstacles (e.g. trees, wires, birds). A total of 212 images were captured in a 1 hour duration.



a. Aerial image



b. Bridge deck

Figure 2. Blessington bridge.

3.2 3D Reconstruction

The 3D reconstruction process was performed in the commercial software PhotoScan [25] on a Dell XPS 15 laptop (i7 CPU with a clock speed 2.8Ghz, 4 cores, 16 Gb RAM, and the Microsoft Windows 10 operating system). The entire reconstruction processing took about 1 hour and generated a point cloud of approximately 16.8 million points (Figure 3). The achieved ground resolution was 8.18 mm/pix. See Table 1 for more details.



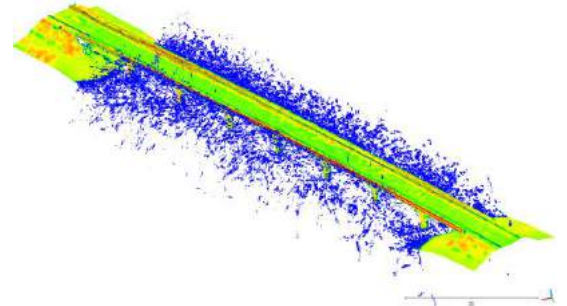
Figure 3. Original point cloud data with significant quantities of noise in evidence.

Table 1. 3D Reconstruction Result.

Number of images	212
Ground resolution	8.18 mm/pix
Spare points number	261,442
Spare reconstruction time	34 minutes
Dense points number	16,805,020 points
Dense reconstruction time	31 minutes

3.3 Outlier Noise Removing

Point clouds reconstructed from UAV images tend to be noisy. In this case study, much of noise appeared just beyond the bridge's boundaries, especially under the bridge. This was caused by waves, water reflection, and self-shadows. The noise greatly affects further point cloud processing. Therefore, an automatic denoising approach was devised. This involved calculating the volume density in a spherical neighbourhood of radius R (Figure 4a) for each point. In this case study, R was set to 0.5 m which must bigger than the regular size of noise clusters. If the density was less than the threshold K , the point was labelled as an outlier. The threshold K was automatically set to equal the average density of the entire dataset minus one standard deviation. In this instance, K equalled 1600 points in the specified neighbourhood.



a. Point density distribution



b. Point cloud after automatic noise removal

Figure 4. Input data.

3.4 Bridge Deck Extraction

As mentioned previously, two methods were compared herein: k-means clustering and region growing. The k-means processing is achieved by the blind-in function in the Matlab software [26]. While, the details of the implemented region growing algorithm can be found in reference [20]. For both methods, features of each point must be calculated prior to the extraction process. In this study, the geometric location (x y z), normal (N_x N_y N_z), colour information (R G B), density (with a searching radius $r = 0.25$ m), Gaussian curvature ($r = 0.25$ m), and Roughness ($r = 0.25$ m) were calculated within the software CloudCompare [27].

3.5 Extraction Performance Comparison

To evaluate the performance of two extraction methods, three metrics were employed to measure the overall accuracy and effectiveness of a segmentation. They were precision (Eqn 1), recall (Eqn 2) and F-score (Eqn 3). These metrics are based on the following values: (i) True Positives (TP), which represents proper segmentation that matches with a manually generated

ground truth benchmarked by human experts; (ii) False Positives (FP), which denotes over-segmentation within point cloud models that results in segmenting one ‘reference’ segment into several parts; and (iii) False Negatives (FN), which happens when two or more separate segments are wrongly grouped together leading to under-segmenting the 3D model.

$$Precision = \frac{|TP|}{|TP| + |FP|} \quad (1)$$

$$Recall = \frac{|TP|}{|TP| + |FN|} \quad (2)$$

$$F - score = 2 \times \frac{Precision \times Recall}{Precision + Recall} \quad (3)$$

3.6 Pavement Evaluation

To evaluate the surface condition of the extracted pavement, a second-order polynomial surface (Eqn 4) was generated to fit the dataset to simulate the original pavement surface. Then, for each point P_i , the distance D_i (Eqn 5) from the current surface to the artificial simulated surface was calculated to identify the wear condition of the deck surface.

$$sf(x, y) = P_0 + P_1 \times X + P_2 \times Y + P_3 \times X^2 + P_4 \times Y^2 + P_5 \times X \times Y \quad (4)$$

$$D_i = z_i - sf(x_i, y_i) \quad (5)$$

4 RESULT ANALYSIS

4.1 Extraction Result Analysis

First, the k-means clustering process was applied individually to each of the six sets of feature (see section 3.4). As shown in Table 2 and Figure 5, the result based on the ‘normal’ had a higher F-score, 0.76. When the normal was paired with other features (Figure 6 and Table 3), the combination of the normal and the z (elevation) produced the best outcome of the combined features. However, the top score 0.75 was slightly less than that produced using only the normal. Thus demonstrating that the presence of more features does not guarantee a more accurate result.

As the results could have been affected by the expected cluster numbers, k, a further test was conducted to segment the dataset into 6, 8, 9, 10 and 12 clusters, as shown in Table 4. Figure 7 shows that the k value does not have a significant effect on the results. However, a higher k value will decrease the recall rate, because of over-segmentation of the deck into small sections resulting in their exclusion from the main cluster.

Table 2. k-means Results with one feature

Features	K	Time (s)	Result		
			Precision	Recall	F-score
Normal	8	34.7	0.6279	0.9844	0.7667
Z	8	117.17	0.4876	0.6351	0.5516
RGB	8	161.37	0.7452	0.3025	0.4303
Curvature	8	114.19	0.3226	0.9988	0.4877
Residual	8	16.79	0.489	0.3920	0.4357
Density	8	28.18	0.1446	0.1544	0.1494

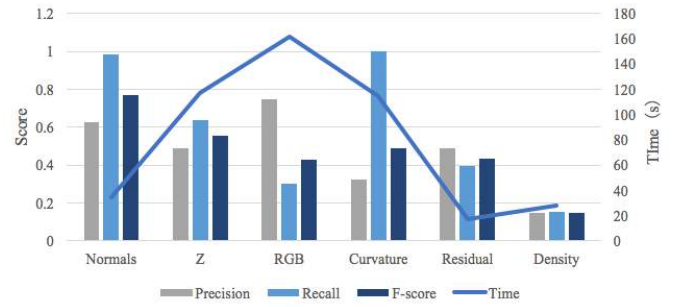


Figure 5. Single feature comparison.

Table 3. k-means Result with two features

Features	K	Time (s)	Result		
			Precision	Recall	F-score
Normal Z	8	64.37	0.6021	1	0.7516
Z RGB	8	195.56	0.7571	0.389	0.5139
Z Curvature	8	150.8	0.391	0.9985	0.562
Z Residual	8	28.51	0.5765	0.4735	0.52
Z Density	8	66.3	0.6618	0.6051	0.6322

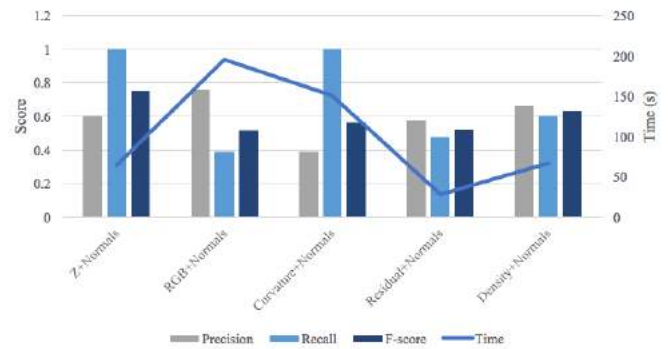


Figure 6. Multiple feature comparison.

Table 4. k-means results with different K values when using both the normal and z feature

K	Time (s)	Result		
		Precision	Recall	F-score
12	149.19	0.5855	0.6612	0.6211
10	186.29	0.5865	0.6752	0.6277
9	168.59	0.5933	1	0.7447
8	64.37	0.6021	1	0.7516
6	102.19	0.5934	1	0.7448

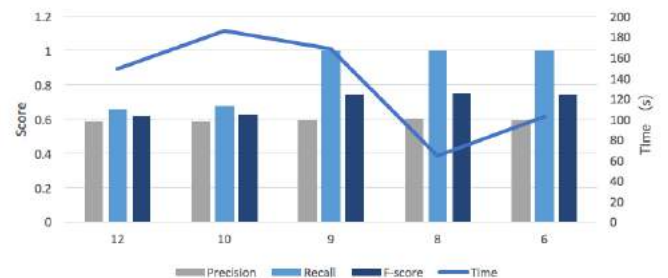


Figure 7. Comparison of different K values.

The results of the region growing method are shown in Table 5 and Figure 8. Normal feature, elevation (z), curvature, and residual were applied. The F-score reached 0.94 which was nearly 20% better than achieved by than the k-Means method, (Table 2 vs Table 5).

Table 5. The region growing method result

Time	Precision	Recall	F-score
188.61	0.9177	0.9809	0.9482

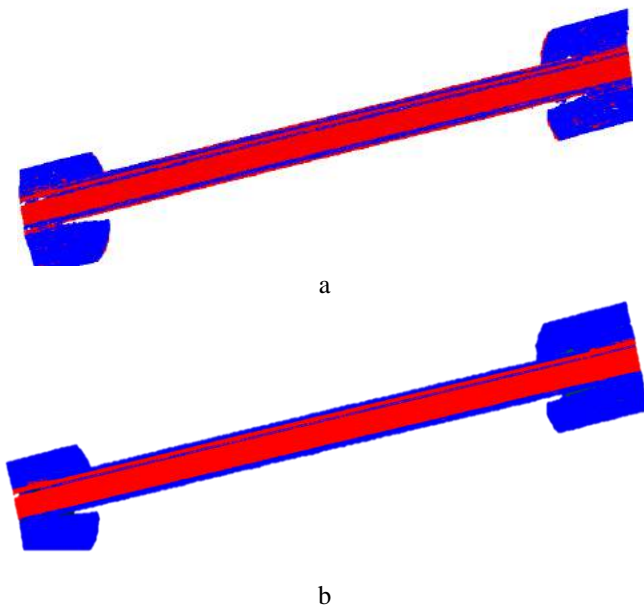


Figure 8. The extraction results a. k-means b. R growing.

4.2 Pavement Condition Analysis

The extracted bridge deck was then subjected to the pavement condition approach introduced in section 3.6. The result are shown in Figure 9. The condition map of the extracted pavement shows that the overall damage was heavier in the quarter span location, with small localized damage like potholes or erosions also visible.

5 CONCLUSIONS

Using UAV-based imagery, this paper introduces a complete workflow for bridge deck assessment, which involves prior steps of 3D point cloud reconstruction, noise reduction, deck extraction. Importantly, the proposed deck evaluation approach offers an automated means to estimate the surface conditions. This approach can be used for generating the health map as a reference for safety analysis. Additionally two bridge deck segmentation methods (k-means and region growing method) were compared, where the region growing method was able to generate an F-score close to 95% for bridge deck extraction, while the k-means only achieved 76%.

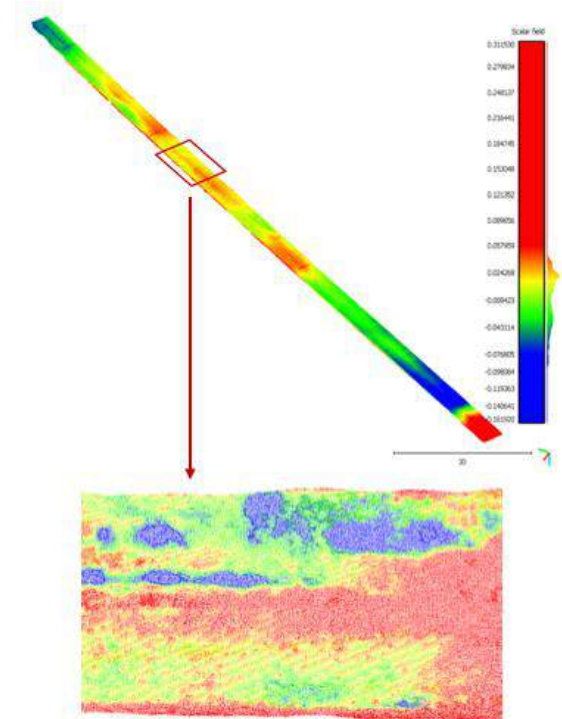


Figure 9. Pavement condition map showing damage and erosion.

ACKNOWLEDGMENTS



This project was made possible through the generous support of the European Union's Horizon 2020 Research and Innovation programme, Marie Skłodowska-Curie grant 642453, and UCD Seed funding grant SF1404.

REFERENCES

- [1] La, H.M., Gucunski, N., Dana, K. and Kee, S.-H. (2017), 'Development of An Autonomous Bridge Deck Inspection Robotic System', *J. F. Robot.*, Apr 2, no. arXiv:1704.07400v1, 1-25.
- [2] Byrne, J., O'Keeffe, E., Lennon, D. and Laefer, D.F. (2017), '3D reconstructions using unstabilized video footage from an unmanned aerial vehicle', *J. Imaging*, 3, 15.
- [3] Hallermann, N., Morgenthal, G. and Rodehorst, V. (2015), 'Unmanned Aerial Systems (UAS) – Case studies of vision based monitoring of ageing structures', *Int. Symp. Non-Destructive*, September, 15-17.
- [4] Distresses, S. and Zhang, C. (2012), 'An unmanned aerial vehicle-based imaging system for 3D measurement of unpaved road', 27, 118-129.
- [5] Chen, S., Laefer, D.F. and Mangina, E. (2016), 'State of Technology Review of Civilian UAVs', *Recent Patents Eng.*, 10(3) 201, 160-174.
- [6] Kim, H., Lee, J., Ahn, E., Cho, S., Shin, M. and Sim, S. (2017), 'Concrete Crack Identification using UAV incorporating Hybrid Image Processing', *Sensors (Basel)*, 17(9), 1-14.
- [7] Holz, D., Nieuwenhuisen, M., Droschel, D., Schreiber, M. and Behnke, S. (2013), 'Towards Multimodal Omnidirectional Obstacle Detection for Autonomous Unmanned Aerial Vehicles', *Int. Arch. Photogramm. Remote Sens. Spat. Inf. Sci.*, vol. XL-1/W2, September, 4-6.
- [8] Zhu, X., Li, X. and Yan, F. (2018), 'Design and implementation for integrated UAV multi-spectral inspection system', *Asia Conference on Energy and Environment Engineering*, 133, 1.
- [9] Omar, T. and Nehdi, M.L. (2017), 'Automation in Construction Remote sensing of concrete bridge decks using unmanned aerial vehicle infrared thermography', *Autom. Constr.*, June, 1-12.
- [10] Chen, S., Asce, M., Rice, C., Boyle, C. and Hauser, E. (2011), 'Small-format aerial photography for highway-bridge monitoring', *Journal of Performance of Constructed Facilities*, April, 25(2), 105-112.

- [11] Ullman, S. (1979), 'The Interpretation of Structure from Motion', *Proc. R. Soc. London. Ser. B, Biol. Sci.*, 203(1153), 405–426.
- [12] Moons, T., Vergauwen, M. and Van Gool, L. (2008), '3D reconstruction from multiple images', *Computer Graphics and Vision*, 4(4), 287-394.
- [13] Agarwal, S., Snavely, N., Simon, I., Seitz, S.M. and Szeliski, R. (2011), 'Building Rome in a day', *Commun. ACM*, 54(10), 105–112.
- [14] Micheletti, N., Chandler, J.H. and Lane, S.N. (2015), 'Structure from Motion (SfM) Photogrammetry', *Br. Soc. Geomorphol. Geomorphol. Tech.*, 2(2), 1–12.
- [15] Byrne, J., Laefer, D.L. and O'Keefe, E. (2017), 'Maximizing feature detection in aerial unmanned aerial vehicle datasets', *J. Appl. Remote Sens.*, 11(2), id. 025015.
- [16] Berger, M., Alliez, P., Tagliasacchi, A., Seversky, L.M., Silva, C.T., Levine, J.A. and Sharf, A. (2014), 'State of the art in surface reconstruction from point clouds', *urographics star reports*, 1(1), 161-185.
- [17] Nurunnabi, A., West, G. and Belton, D. (2015), 'Outlier detection and robust normal-curvature estimation in mobile laser scanning 3D point cloud data', *Pattern Recognit.*, 48(4), 1404–1419.
- [18] Nguyen, A. and Le, B. (2013), '3D point cloud segmentation: A survey', *6th International Conference on Robotics, Automation and Mechatronics (RAM)*, November.
- [19] Grilli, E., Menna, F. and Remondino, F. (2017), 'A review of point clouds segmentation and classification algorithms', *The International Archives of the Photogrammetry, Remote Sensing and Spatial Information Sciences*, vol. XLII-2/W3, March, 339–334.
- [20] Vo, A.V., Truong-Hong, L., Laefer, D.F. and Bertolotto, M. (2016), 'Octree-based region growing for point cloud segmentation', *ISPRS J. Photogramm. Remote Sens.*, October, 104, 88–100.
- [21] Laefer, D.F. and Truong-Hong, L. (2017), 'Automation in Construction Toward automatic generation of 3D steel structures for building information modelling', *Autom. Constr.*, 74, 66–77.
- [22] Truong-Hong, L. and Laefer, D.F. (2014), 'Application of terrestrial laser scanner in bridge inspection: review and an opportunity', *37th IABSE Symposium: Engineering for Progress, Nature and People*.
- [23] Laefer, D.F., Fitzgerald, M., Maloney, E.M., Coyne, D., Lennon, D. and Morrish, S. (2009), 'Lateral image degradation in terrestrial laser scanning', *Struct. Eng. Int.*, 19(2), 184–189.
- [24] Gyetvai, N., Truong-Hong, L., and Laefer, D.F. (2018), 'Laser scan-based structural assessment of wrought iron bridges : Guinness Bridge, Ireland', *Proc. Inst. Civ. Eng. Hist. Herit.*, 171, 76–89.
- [25] Agisoft, *Agisoft PhotoScan*, 2017.
- [26] Matlab, *k-means clustering*, 2018 [Online]. Available: <https://uk.mathworks.com/help/stats/kmeans.html>.
- [27] CloudCompare, *Stereo, V2.9, Open Source Project*, 2017 [Online]. Available: <http://www.danielgm.net/cc/>.



ARUP



AECOM



AALBORG UNIVERSITET



UNIVERSITÉ DE NANTES

Follow us on

